

**2007** *volume 9*

# Los Alamos Summer School Research Reports

## Sponsors

### Los Alamos National Laboratory

The National Nuclear Security Agency (NNSA) Nuclear Weapons Program, the Educational Program, Office and Department of Energy, Science Education and Nuclear Weapons Programs (Defense Programs)

### The Quantum Institute

### The University of New Mexico

Department of Physics and Astronomy and Extended University Graduate and Upper Division Programs, and the National Science Foundation: Research Experience for Undergraduates (REU)

### Contact

James Colgan, Theoretical Division, Mail Stop B283, Los Alamos National Laboratory, Los Alamos, NM 87545, [jcolgan@lanl.gov](mailto:jcolgan@lanl.gov)

### Publication

Sharon Mikkelson, Illustrator/Designer IRM-CAS/ADTSC

Vin LoPresti, Writer/Editor IRM-CAS/ADTSC

Pictures taken by Summer School Students

September 2007/LA-UR-07-6498





**2007** *volume 9*

## Los Alamos Summer School Research Reports

### *Table of Contents*

- Preface
- Class of 2007
- Mentors and Students
- Lectures
- Photos – Selected Scenes from Summer 2007
- Titles of Papers
- Student Papers





2007 *volume 9*

# Los Alamos Summer School Research Reports

## *Preface*

This year marked the seventeenth session of the Los Alamos Summer School in Physics, a joint educational project between the University of New Mexico and the Los Alamos National Laboratory (LANL). The National Science Foundation provides funding to the University side through its Research Experience for Undergraduates (REU) site, and the National Nuclear Security Agency (NNSA) supports the Laboratory component. In addition, this year we were pleased to receive support from the Los Alamos National Laboratory's Quantum Institute. The School recruits nationwide, and the majority of students were junior or senior undergraduates. Fifteen students, from a variety of backgrounds and locations, participated in this year's program.

As in previous years, the School employed a dual track of lectures on a wide variety of topics as well as student research projects to give the students their first taste of real research. The lecturers were distinguished scientists from LANL and from UNM and discussed topics as diverse as climate modeling, high-energy physics, and the latest developments in astrophysics. The research projects, each individually mentored by a LANL scientist, concentrated on a specific problem and allowed the student to experience how research is undertaken at a National Laboratory. Research projects were in many areas of science including atomic physics, high-energy physics, biophysics, and climate modeling. Many of the students presented their research at the annual Los Alamos Student Symposium, which was held at UNM-LA on August 1-2, 2007. One of the LASS students won an award for his research project. All the lecturers and mentors who participated in LASS were volunteers.

This report collates the research findings of the LASS students in their ten-week research experience. Although the short ten-week span of the school usually only allows the students to contribute to a project in progress, or to make a start on a new research project, this year, several of the projects are expected to lead to journal publications, leading to advances in the field. More importantly, this summer's experiences have allowed these students to participate in a working research environment, which will be of immense help in deciding their future career paths as they complete their undergraduate education within the coming year. We believe that these project reports demonstrate the remarkable achievements of all the students.

LANL

James Colgan  
Norm Magee  
Eddy Timmermans  
Gerd Kunde

UNM

Sally Seidel



**2007** *volume 9*  
**Los Alamos Summer School Class**

|                      |                                 |
|----------------------|---------------------------------|
| Michelle N. Adan     | Stetson University              |
| Sean R. Brannon      | Dickinson College               |
| Jacob W. Brock       | Eckerd College                  |
| Ethan W. Brown       | University of Oklahoma          |
| Emily A. Chouinard   | Michigan State University       |
| Samuel C. Fletcher   | Princeton University            |
| John K. Gamble       | The College of Wooster          |
| Tiffany R. Hayes     | University of New Mexico        |
| Mark Herrera         | University of Missouri-Rolla    |
| Tony Y Li            | Cornell University              |
| Andrew T. Mastbaum   | Lehigh University               |
| Jonathan D. Sperling | University of Wisconsin-Madison |
| Christine E. Suss    | Clarkson University             |
| Fuk S. Yeung         | Marlboro College                |
| Thomas G. Wong       | Santa Clara University          |





**2007** *volume 9*

## Los Alamos Summer School Mentors and Students

### *Mentor*

Stefan Eidenbenz (CCS-3)

Yongho Kim (P-24)

Dave Kilcrease (T-4)

Garrett Kenyon (P-21)

Siming Liu (T-6)

Gerd Kunde

Fernando Cucchietti (T-4)

Hanna Makaruk (P-22)

David C. Roberts and Natali Gulbahce (T-13/CNLS)

Justin Oelgoetz (X-1)

Andrew Hime (P-23)

Balu Nadiga (CCS-2)

Yi Jiang (T-7)

Hristo Djidjev (CCS-3)

Matt Foster (T-4)

### *Student*

Michelle N. Adan

Sean R. Brannon

Jacob W. Brock

Ethan W. Brown

Emily A. Chouinard

Samuel C. Fletcher

John K. Gamble

Tiffany R. Hayes

Mark Herrera

Tony Y Li

Andrew T. Mastbaum

Jonathan D. Sperling

Christine E. Suss

Fuk S. Yeung

Thomas G. Wong



**2007** *volume 9*

## Los Alamos Summer School Lectures

|                           |  |
|---------------------------|--|
| Mark Petersen (CCS-2)     | <i>Ocean and Climate Modeling</i>  |
| Alexander Heger (T-6)     | <i>Stellar nucleosynthesis; Life and Death of the First Stars; Explosions on the surfaces of neutron stars</i>         |
| Lon-Chang Liu (T-16)      | <i>Extract nuclear information from under the shadow of atomic Coulomb scattering</i>                                  |
| Brian O'Shea (T-6)        | <i>A Brief Introduction to Cosmology</i>   |
| Kent Budge (CCS-2)        | <i>Type II supernovae</i>  |
| Nick Hengartner (CCS-3)   | <i>Stochastic Modeling</i>   |
| Todd Ringler (T-3)        | <i>Predicting the Regional Impacts of Global Climate Change</i>  |
| Yi Jiang (T-7)            | <i>Multiscale, cell-based model for biological modeling I &amp; II</i>   |
| Justin Oelgoetz (X-1)     | <i>Introduction to Plasma kinetics &amp; Spectroscopy</i>  |
| Razvan Teodorescu (T-13)  | <i>Interface growth in two dimensions: from mathematics to biology and computer science- a physicist's perspective</i> |
| Dan Whalen (T-6)          | <i>Cosmological reionization</i>   |
| Tim Thomas (UNM)          | <i>High-Energy Physics</i>   |
| Cynthia Reichhardt (T-12) | <i>Computational models of DNA sorting</i>   |
| Andi Klein (P-22)         | <i>Computational Physics and the ROOT package</i>  |
| Gerd Kunde (P-22)         | <i>The Quark Gluon Plasma</i>  |
| Gerardo Chowell (T-7)     | <i>Understanding the spread of infectious diseases; linking models to data.</i>  |
| David Roberts (T-13/CNLS) | <i>Quantum weirdness at zero temperature: when superfluids are a drag</i>  |
| Steve Valone (MST-8)      | <i>Open system density functional theory and the Millikan oil-drop experiment</i>                                      |
| Balu Nadiga (CCS-2)       | <i>An introduction to turbulence in the ocean-atmosphere system</i>  |
| Ilya Nemenman (CCS-3)     | <i>Biophysics of cellular regulatory networks</i>  |
| Dan Horner (T-4)          | <i>Non-perturbative treatments of photoionization of atoms and molecules</i>   |
| Susan Atlas (UNM)         | <i>In Search of H: Two lectures on density functional theory</i>   |
| Takeyasu Ito (P-25)       | <i>Symmetries in Nuclear Physics</i>   |
| Dale Tupa (P-25)          | <i>Interferometry on Shock Waves</i>   |
| David Dunlap (UNM)        | <i>Transport and tunneling phenomena</i>   |
| Bill Louis III (P-DO)     | <i>Neutrino Physics</i>  |
| Eli Ben-Naim (T-13)       | <i>Statistical Physics of Competitions, Statistical Physics of Granular Materials</i>                                  |
| Hans Ziock (EES)          | <i>Carbon neutral energy system concepts</i>   |
| Garrett Kenyon (P-21)     | <i>Computational Neuroscience</i>  |



2007 *volume 9*

Los Alamos Summer School Photographs



*LASS Class of 2007*



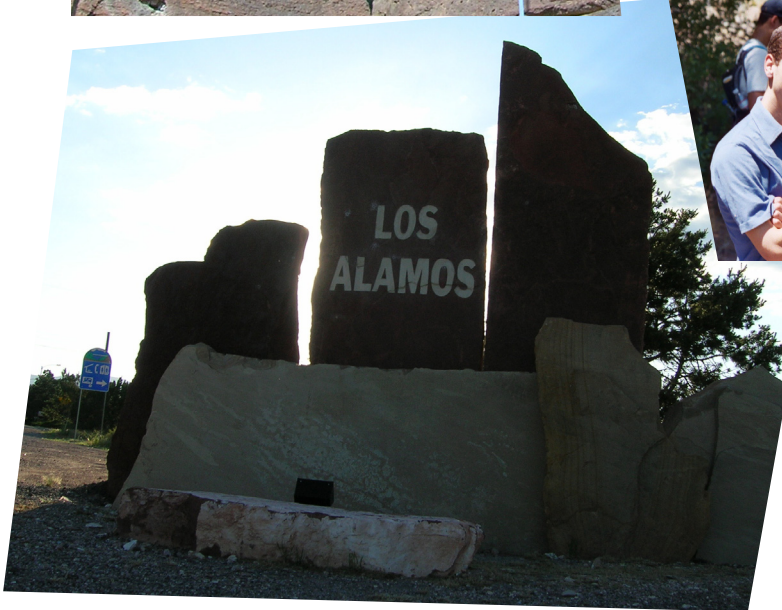
# 2007 *volume 9* Los Alamos Summer School Photographs





2007 *volume 9*

# Los Alamos Summer School Photographs





2007 *volume 9*

## Los Alamos Summer School Titles of Papers

|  |     |
|--|-----|
| <i>Non-thermal Plasma Effects on Hydrogasification of Coal</i><br>Sean R. Brannon  | 1   |
| <i>Time Dependent Electron-Positron Populations in High Energy Plasmas</i><br>Jacob Brock  | 10  |
| <i>Invariant Feature Recognition Using Dendritic Processing</i><br>Ethan Brown   | 15  |
| <i>Modeling Electron Distributions and Radiation Spectra Produced in Gamma Ray Bursts</i><br>Emily Chouinard   | 23  |
| <i>Visualizing Complex Networks</i><br>Fuk S. Yeung  | 31  |
| <i>Simulating a quantum Ising chain on a liquid-phase NMR quantum computer</i><br>John Gamble  | 45  |
| <i>Deriving the Electron Temperature of Short-Lived Plasma</i><br>Tiffany Hayes  | 58  |
| <i>Complex Networks and Scientific Ideas: The Road to Revolution</i><br>Mark Herrera   | 67  |
| <i>Simulation and Characterization of a Dark Matter Detector</i><br>Andy Mastbaum  | 75  |
| <i>Testing the Wire Integrity of Silicon Detector Cables</i><br>Michelle Adan  | 89  |
| <i>Jet Measurements for QGP Experiments at CMS</i><br>Samuel C. Fletcher   | 92  |
| <i>Linear Stability Analysis of the Bickley Jet</i><br>Jonathan Sperling   | 104 |
| <i>SARS Infection Dynamics in Lung Epithelial Tissue</i><br>Christine Suss   | 114 |
| <i>Calculation of Elastic Differential Cross Sections for Proton-Helium Collisions Through the Use of High Performance Computing</i><br>Thomas G. Wong | 120 |
| <i>Simulations of the <math>L\alpha</math> Spectra of Fe Ions</i><br>Tony Li   | 130 |



# Non-thermal Plasma Effects on Hydrogasification of Coal

Sean R. Brannon\*      Yongho Kim†

August 14, 2007

## Abstract

As oil reserves continue to be depleted and energy prices continue to rise, the search for viable alternative energy sources is taking on an increasing importance. One such alternative energy source is hydrogen and methane fuel produced by coal gasification. Los Alamos National Laboratory has developed the ZEC (Zero Emission Coal) concept, which utilizes methane produced by the hydrogasification reaction. ZEC comes with many benefits, including the plentiful supply of coal (enough for more than 100 years even assuming increasing rates of consumption), potential energy efficiencies of >65% (as compared with <35% for traditional coal-fired plants), and the possibility for zero carbon emissions. However, the technology is still mostly undeveloped commercially and needs significant improvement before it will become economically viable. In particular, hydrogasification reactions currently proceed far too slowly, and accelerating the reaction with traditional catalysts is not possible due to the highly abrasive environment inside the reactor. Thus, the key to making coal gasification a practical alternative is to increase the rate of reaction without using traditional catalysts. Our project involved investigating how a non-thermal plasma might be used in a catalytic role. Specifically, our method is to use a non-thermal plasma to create radical species of hydrogen, which can interact with the feedstock in the reactor to increase the rate of reaction and the percentage of feedstock conversion, and possibly allowing us to decrease the temperature and pressure in the reactor. To study these effects, we built a small-scale reactor to test both the background and plasma-enhanced methane production of the hydrogasification reaction.

## 1 Introduction to energy production

Ever since the advent of the Industrial Revolution, human society has been dependent on one variety or another of fossil fuels to power our economic growth.

---

\*Undergraduate, Department of Physics & Astronomy, Department of Mathematics, Dickinson College, Carlisle, PA 17013, e-mail: brannons@dickinson.edu

†Plasma Physics Group (P-24), Los Alamos National Laboratory, Los Alamos, NM 87545; e-mail: yhkim@lanl.gov

The two primary reasons for this become obvious upon inspection: first, fossil fuels (also known as hydrocarbons) are, kilo for kilo, one of the most concentrated energy sources on Earth; and second, they are one of the easiest and cheapest sources from which to extract energy. These two properties, when combined, have made hydrocarbons, and specifically petroleum, the most economical solution to our growing energy needs.

Unfortunately, like any resource that is extracted from the Earth, petroleum is in finite supply and cannot continue to meet our demands into the indefinite future. Just how finite these resources are is currently the subject of much debate, yet the overall consensus is clear: eventually, the cost of using petroleum will force it out of use due to economic reasons, leaving industrialized nations in need of a cost-effective replacement energy source. Several alternatives have already been proposed to meet this need. These include some old standards, such as hydroelectric, solar and wind generators, and nuclear plants, as well as some newer proposals, fusion reactors tidal power, and biofuel among them. Many of these proposed alternatives are attractive in that they rely on sources that are renewable (or at least sufficiently large to meet our demands for the foreseeable future) and relatively clean as compared with current energy production.

Many of them also have potential downsides, however: expensive equipment (solar), environmental impacts (hydroelectric, wind, biofuel, and nuclear), and the need for future research and innovations (fusion). Further, none of these sources can easily provide a mobile source of fuel in the form of hydrogen, for fuel cell-based vehicles. One attractive proposed solution which may circumvent some or all of these problems is the Los Alamos National Laboratory's proposed Zero Emission Coal (ZEC) program.[1] ZEC proposes using a process known as hydrogasification, which reacts carbon with hydrogen to produce methane. The methane is then run through a process known as steam-reforming, which reacts the methane with water and produces double the original amount of hydrogen and a pure stream of carbon dioxide. Half the produced hydrogen is used back in the hydrogasification reactor, while half can be used to produce electricity at the plant or stored to be used in a fuel-cell vehicle. The carbon dioxide, meanwhile, is produced in such a way that it can be easily sequestered, meaning that the plant releases no carbon dioxide to the atmosphere.

## 2 Motivation for our work

A proposed ZEC plant relies on several chemical reactions, as illustrated in Figure 1. The first, and arguably the most critical, reaction in the process is hydrogasification:



This reaction, also known as the methane production step, was our primary focus for further study. It is an exothermic reaction, producing 90 kJ of energy per mole of methane created, and thus the reaction theoretically requires no energy input to sustain. It should be noted, however, that Eq. (1) is a global



plant. One way around this problem is to simply operate the reactor at high temperatures ( $>500\text{ }^{\circ}\text{C}$ ), thus raising the feedstock energy to a sufficient degree to push it over to activation energy. However, as we found earlier, high temperatures quickly lower the conversion efficiency, and thus high pressures ( $> 50\text{ bar}$ ) are required.

Another way around the slow reaction rate is to lower the activation energy. Traditionally this is the role of a catalyst, which serves as an assistant substance in the feedstock, temporarily lowering the activation energy and allowing the reaction to proceed before moving on to the next. The mark of a good catalyst is that it significantly increases the rate of reaction and is not consumed by the reaction. Unfortunately, the hydrogasification reactor is not a friendly environment towards any traditional catalyst. The high temperatures and pressures, which are required to some degree even with the use of a catalyst, as well as a toxic environment due to sulfur, ash, and other impurities in the coal, lead to rapid degradation of traditional catalysts. Since these catalysts are expensive to replenish, it is clear that some other mechanism is required to increase the rate of reaction.

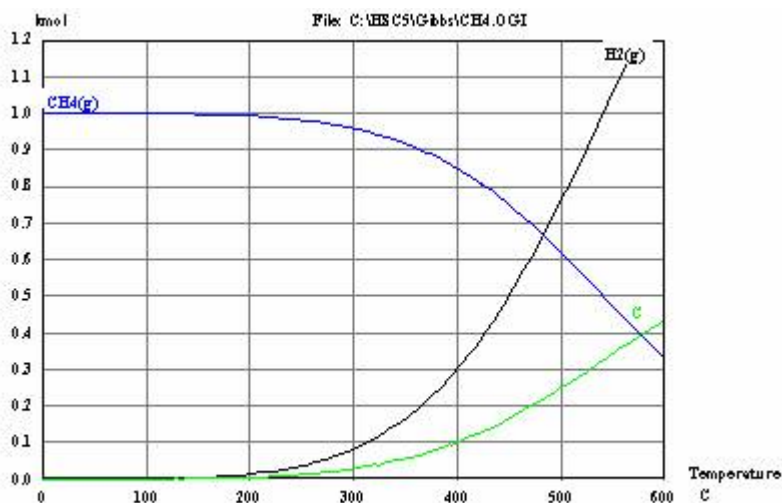


Figure 2: Chemical equilibrium composition of hydrogasification for 0-600 °C at 1 bar.

### 3 Radical species as substitute catalysts

A radical is a chemical species that has a single unpaired electron; for example, H is a radical form of hydrogen, as opposed to H<sub>2</sub> which is hydrogen dimer. What is interesting to note is that, in many cases, the activation energy of a

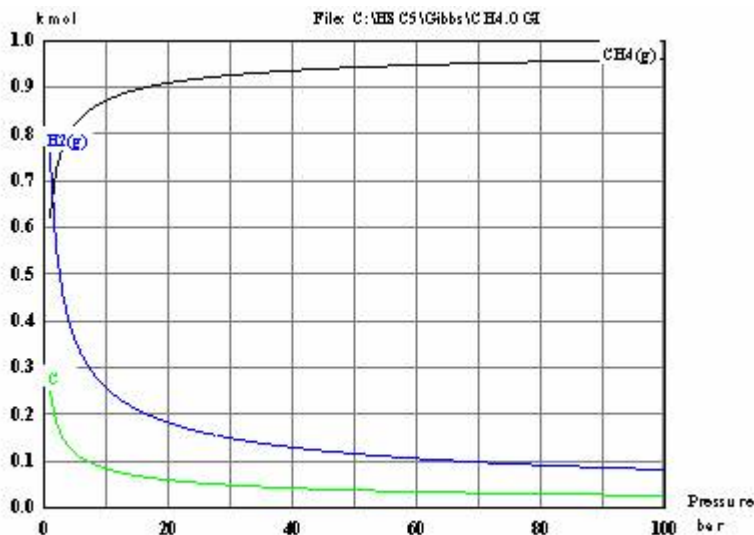


Figure 3: Chemical equilibrium composition of hydrogasification for 0-100 bar at 500 °C.

reaction using radical species is lower than that of its non-radical partner. For hydrogasification, the reaction



has an activation energy of only 30-40 kJ/mol, as compared with 210-335 kJ/mol for Eq. (1) above.[4] This lowering of the activation energy acts in a similar manner to that of a catalyst, but without the environmental degradation effects experienced by traditional catalysts.

An excellent way to generate radicals within the reactor itself is to use high voltage electrodes to create a non-thermal plasma from the hydrogen feedstock. The plasma breaks the  $\text{H}_2$  molecules into H radicals, which are then free to react with the carbon as in Eq. (2). The presence of the H radicals means that more reactions will occur for a given treatment time, and thus we should be able to measure a higher methane content from a sample taken from the plasma condition compared to a sample from the background, non-plasma condition.

## 4 Experimental setup

For our experiment we used a specially designed quartz tube, as shown in the cutaway view in Figure 4. This tube actually consists of two nested quartz tubes: within the smaller tube an electrode may be inserted. Approximately 0.2 grams of fine carbon powder is loosely placed at the bottom of the larger

tube. At one end is a filter which is porous to hydrogen and other gases, but will not permit carbon to drift past it. At the other end, quartz wool is used to keep the carbon in place. An outer electrode is coiled around the outer tube, and both ends are capped with gas-tight assemblies and connected to inlet and outlet gas lines. The entire assembly is then placed within an oven unit, as shown in Figure 5.

At one end we connected our electrical equipment, including the high voltage power supply, and the voltage and current leads to our oscilloscope. The oscilloscope was in turn connected to a computer which calculated the total power, allowing us to maintain a plasma of a constant power. We used a plasma of  $\sim 5$  W power, which corresponded to about 2.8-3.2 kV RMS, with a frequency of  $\sim 450$  Hz. The oven was held at a constant 400 °C, and hydrogen gas flow was controlled by a mass flowmeter ranging from 0-500 ccm. Samples were collected from a by-pass valve downstream of the reactor, which were then analyzed using a Star 3800 gas chromatography station.

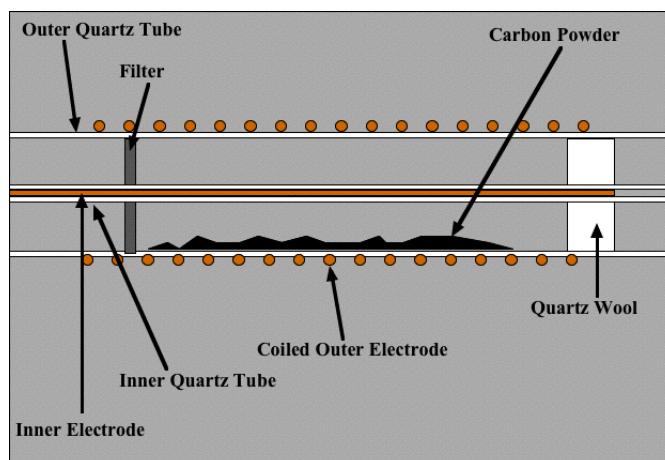


Figure 4: Cutaway diagram of the reactor. Note that hydrogen is flowed from right to left.

## 5 Results & Analysis

The graph in Figure 6 summarizes one particular set of methane production measurements collected from the reactor. These points represent four different runs at two different flow rates, 50 ccm and 500 ccm, and for each flow rate we collected a background sample and a plasma condition sample. Based on the size of the reactor, we calculated that the treatment times, i.e the amount of time the hydrogen spent in the reactor, for 50 ccm and 500 ccm were 80 s and 8 s, respectively. The x-axis of the graph in Figure 6 is the treatment time in seconds, and the y-axis is the  $\text{CH}_4$  concentrations in parts per million (ppm).



Figure 5: Photograph of the entire assembly. Note gas line hookups and electrical connections.

We can clearly see that the plasma condition produces more methane than the background. Further, we note that while the background remains constant with respect to treatment time, the plasma condition appears to react favorably to longer treatment time, producing significantly more methane for the 80 s treatment time as compared with the 8 s, where it is barely above background.

## 6 Discussion & Conclusions

As noted above, the reactor appears to perform more efficiently while operating in the plasma condition compared with background measurements. Moreover, as might be expected, this efficiency is enhanced significantly by a longer treatment time, increasing by  $\sim 10x$  for a  $10x$  increase in treatment time. We believe this effect to be due to the presence of radical species generated by the plasma, which react with the carbon and increase the rate of reaction well above its natural level.

## 7 Future Research

Although the reactor performed as expected, there were a variety of potential issues that will need to be addressed in the future. These include imprecise control over the plasma conditions, with constant monitoring required to ensure stable plasma; carbon residue obscuring inside of the quartz tube, preventing a clear view to interior conditions; incomplete heating or heat loss of hydrogen

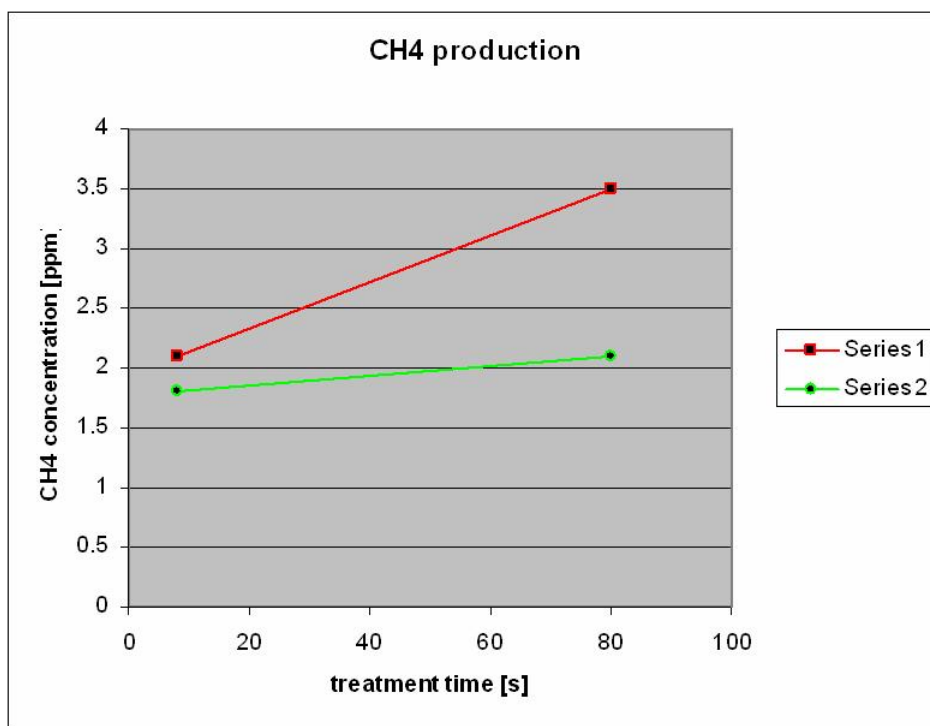


Figure 6: Graph of methane production in ppm for different treatment times, for both background and plasma conditions.

gas, possibly leading to lower reaction rates; and finally a "dancing carbon" effect, where particles of carbon dust would rise up in the tube and "dance" around. This last was likely an effect of the electric field inside the tube and may have partially been responsible for the higher reaction rates in the plasma condition, rather than the presence of radicals.

## 8 Acknowledgements

Sean Brannon would like to thank: Yongho Kim, his mentor at the Los Alamos Summer School; Louis Rosocha, the team lead; Richard Renneke and Sara Abbate, for their technical support on the project; Hans Ziock, for his work in creating the ZEC project; and Norm Magee and James Colgan, without whom life in Los Alamos would have been much more difficult.

## References

- [1] Ziock & Lackner *Zero Emission Coal*, 5<sup>th</sup> International Conference on Greenhouse Gas Technologies, Cairns, Australia, August 14-18 (2000)
- [2] Haasz & Davis *Synergistic methane formation kinetics for hydrogen impact on carbon*, J. Chem. Phys. (85) (1986)
- [3] Kim et al. *Experimental Characterization of Carbon Hydrogasification in an Atmospheric Pressure Microwave Plasma*, 5<sup>th</sup> International Symposium on Non-thermal Plasma Technology, Oleron Island, France, June 19-23 (2006)
- [4] Veprek, S. *Chemical Evaporation and Deposition of Solids in a Non-Isothermal Plasma; Chemical Transport of Carbon*, Journal of Crystal Growth (17) (1972)

# Time Dependent Electron-Positron Populations in High Energy Plasmas

Jacob Brock

*Eckerd College, Saint Petersburg, Florida, USA and  
T-4 Division, Los Alamos National Laboratory*

Dave Kilcrease

*T-4 Division, Los Alamos National Laboratory*

(Dated: August 10, 2007)

The electron-positron density in a plasma causes Compton scattering, increasing the plasma's opacity. In certain laboratory experiments too little time passes for the equilibrium population to occur, so we need to know the time dependence of the electron-positron populations. Although the equilibrium electron-positron population of plasma is well known, the time dependant population has not been described as thoroughly. In this paper we examine the electron-positron content of a plasma as determined by the initial electron content and the rate of creation based on one pair production process. Future work will include another process and the inverses of each for annihilation. By setting up the rate equations for the creation of these particle pairs, we can obtain the time dependence for the electron-positron population from the creation process in the plasma. Finally we apply this to approximate the time required for equilibrium to occur.

## I. INTRODUCTION

The relationship between a plasma's opacity and its temperature is important to understand. Knowing this relationship we can take the temperature of astrophysical plasmas, and of plasmas in the lab by measuring their opacities. Electron-positron content is one of the most important factors affecting plasma opacity. Due to Compton scattering, electron-positron content causes a plasma to be more opaque. Since the electron-positron population of a plasma is so important to its opacity, it is crucial to know the populations. While the equilibrium populations are well known, the time-dependent population for recently created plasmas is less well understood, and is important to understand in certain contexts.

In this paper we present a previous derivation of an equation for production rates based on a single photon decaying into an electron-positron pair, and show a new derivation based on the Born approximation for the same process's cross section. This new derivation using the more precise Born approximation gives very different results than the old derivation from a 1973 technical report by Harvey<sup>[3]</sup>.

## II. PAIR PRODUCTION PROCESSES

The two processes below can create electron-positron pairs. At lower photon energies Process A is more common for production and the inverse of Process B is more common for annihilation. This study is primarily concerned with the time dependent creation terms associated with Process A. In order for Process A to occur, the photon must pass close enough to a heavy nucleus to borrow momentum from it. Of course, the photon must also contain enough energy to produce an electron and a positron, so the threshold energy for this reaction is  $h\nu = 2m_e c^2$ . Future work will include creation and destruction associated with both processes and their inverses.

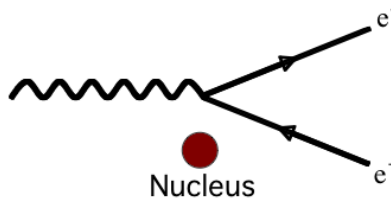


Figure 1: Process A<sup>[3]</sup>

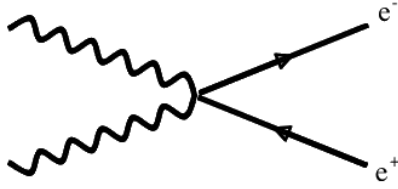


Figure 2: Process B<sup>[3]</sup>

### III. CROSS SECTION APPROXIMATIONS

Process A's occurrence depends on the charge of the nucleus, as well as the photon's energy and its proximity to the nucleus. The cross section describes the size of the target that the photon must "hit" in order for pair production to take place. While the exact form of the cross section is known<sup>[5]</sup>, its use would be prohibitively computationally taxing. For this reason we use approximations for the cross section. Harvey's approximations<sup>[3]</sup> are shown in Equations 1 and 2. The Born approximation<sup>[4]</sup> is shown in Equation 3, and all three approximations are displayed in Figure 3 (for iron). While the slight overshooting of Harvey's linear approximation may at first appear inconsequential, it turns out to drastically alter the result for the pair production rate because it is integrated with a photon flux which is typically larger at these lower photon energies. The drastic overshooting of the same approximation at higher photon energies is surprisingly inconsequential at higher photon energies. These points are illustrated in Figure 4.

$$\sigma_h \approx \begin{cases} Z^2 r_0^2 \alpha \frac{2\pi}{3} \left(\frac{k-2}{2}\right)^3 & k \ll 3 \\ Z^2 r_0^2 \alpha \left[ \frac{28}{9} \ln(2k) - \frac{218}{27} \right] & k \gg 1 \end{cases}, \quad k \equiv \frac{h\nu}{m_e c^2} \quad (1)$$

$$\sigma_l \approx 0.171 Z^2 r_0^2 \alpha k \quad (2)$$

$$\sigma_b \approx \begin{cases} Z^2 r_0^2 \alpha \frac{2\pi}{3} \left(\frac{k-2}{k}\right)^3 * \left[ 1 + \frac{1}{2} \left(\frac{2k-4}{2+k+2\sqrt{2k}}\right) + \frac{23}{40} \left(\frac{2k-4}{2+k+2\sqrt{2k}}\right)^2 + \frac{11}{60} \left(\frac{2k-4}{2+k+2\sqrt{2k}}\right)^3 + \frac{29}{960} \left(\frac{2k-4}{2+k+2\sqrt{2k}}\right)^4 + \dots \right] & k \lesssim 4 \\ Z^2 r_0^2 \alpha \left\{ \frac{28}{9} \ln 2k - \frac{218}{27} + \left(\frac{2}{k}\right)^2 \left[ 6 \ln 2k - \frac{7}{2} + \frac{2}{3} \ln^3 2k - \ln^2 2k - \frac{1}{3} \pi^2 \ln 2k + 2\zeta(3) + \frac{\pi^2}{6} \right] - \left(\frac{2}{k}\right)^4 \left[ \frac{3}{16} \ln 2k + \frac{1}{8} \right] - \left(\frac{2}{k}\right)^6 \left[ \frac{29}{9*256} \ln 2k - \frac{77}{27*512} \right] + \dots \right\} & k \gtrsim 4 \end{cases} \quad (3)$$

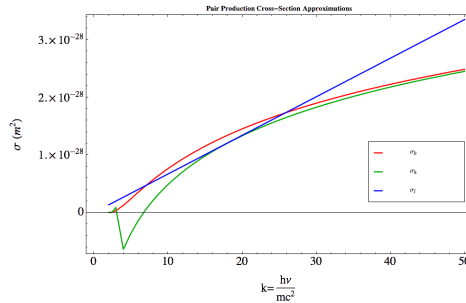


Figure 3: Comparison of Three Cross Sections

#### IV. PAIR PRODUCTION RATES

In order for a pair to be produced by Process A a photon must pass through the cross section around a nucleus. For this reason the pair production rate is based on the number density of heavy nuclei ( $N$ ), the cross section, and the differential flux at allowed photon energies as shown in Equation 4. While the cross section for a given photon energy is determined by the above equations, the magnitude of the photon flux is determined by the blackbody emission of the plasma itself. This photon flux goes by the equation  $dF = 3.9 * 10^{27} \frac{k^2 (m_e c^2)^3}{\exp[\frac{m_e c^2}{\theta} k] - 1} dk$  where the units of the flux are  $\frac{1}{m^2 \text{ sec}}$ . Figure 4 illustrates how the integrand of Equation 4 changes with varying photon energies at a temperature of 22,000 eV for iron. The shape of the curves is very similar for other elements and temperatures. At low photon-energies the linear approximation's overestimation of the cross section causes a huge overestimate of the specified integrand. Consequentially, our results are much different than Harvey's.

$$\frac{dn_p}{dt} = N \int_2^\infty \sigma(k) dF(k) \quad (4)$$

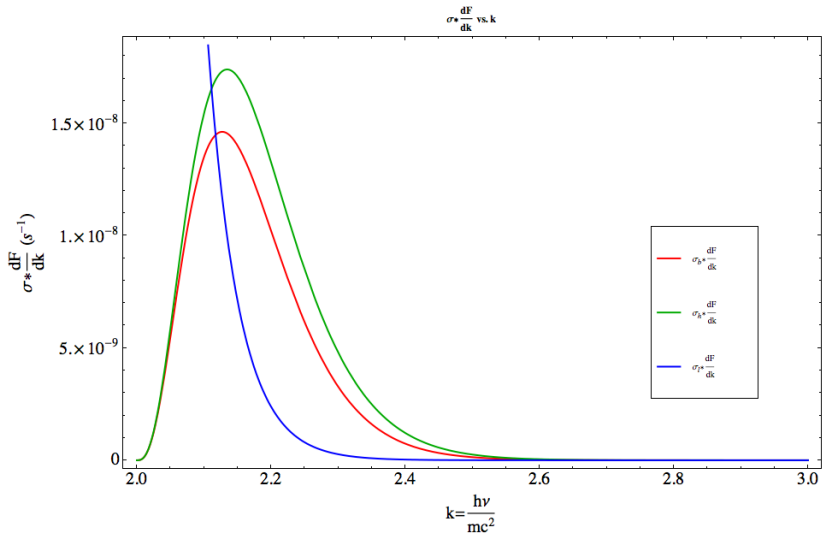


Figure 4: Comparison of Three Integrands in Equation 4

#### V. TIME TO REACH EQUILIBRIUM

It will be useful to consider how long it would take for populations to reach an equilibrium state since the motivation for this research is that equilibrium takes a significant amount of time to reach. Although there are more creation and annihilation processes that can be considered, using our creation rates from Process A will give us a rough estimate of the time required to reach equilibrium. Of course, destruction rates will only increase the time required to reach equilibrium. For now we will simply calculate the time required for the equilibrium number of electrons/positrons to be created by Process A, but future work will consider equilibrium to exist when the production and annihilation rates are equal.

Figures 5 and 6 show the times required for Process A to reach equilibrium based on Harvey's approximation and the Born approximation, respectively, for heavy nucleus number density of  $10^{24} m^{-3}$ . Note that with Harvey's approximation we reach the equilibrium much quicker than with the Born approximation (the shapes of the graphs are similar due to the linearity of both pair production rates). The drastic difference between the times highlights the importance of Harvey's cross section overestimation noted above. Because our results give a lower production rate than Harvey's, they also suggest that equilibrium will not be reached as quickly. Since our results suggest that equilibrium will not be reached for a much longer time, they indicate that it is more important than previously thought to understand the time dependent case for electron-positron population.

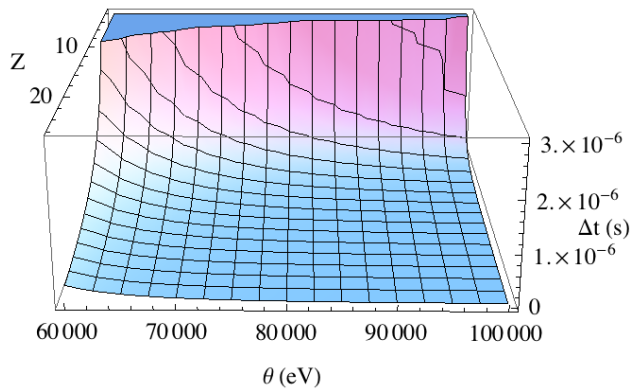


Figure 5: Time to Equilibrium Using Harvey's Approximation

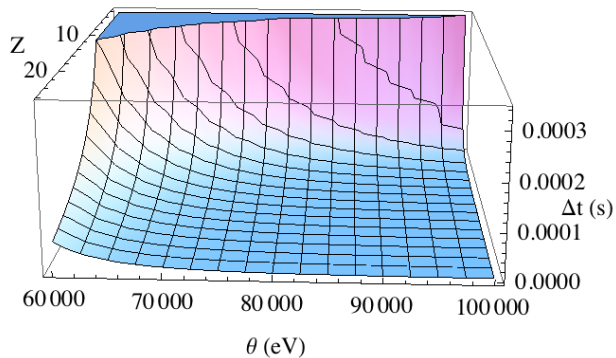


Figure 6: Time to Equilibrium Using Born Approximation

## VI. CONCLUSIONS

Our results are very different from those obtained by Harvey. The reason for this is that our more detailed approximation of the cross section for Process A approaches zero as the photon energy approaches the production threshold of  $2m_e c^2$ , while Harvey's approximation approaches a significantly greater value. Our results do, however, correspond to Harvey's in that the relationships between atomic number, temperature, plasma density, and pair production rates are similar. In order to obtain a more accurate description of the electron-positron populations, we must do further work to include Process B, and the inverse of both Processes A and B. Once we have a better description of the time-dependent electron-positron populations for evolving plasmas, this theory can be applied to the study of plasma opacities and its applications.

## Acknowledgments

This work was done under the supervision of Dave Kilcrease with support from the Los Alamos Summer School, headed by James Colgan and Norm Magee. Sponsorship for the program was provided by the NSF through the University of New Mexico, as well as Los Alamos National Laboratory. Other support was lent to this research by John Gamble.

## VII. REFERENCES

- [1] Clayton, Donald D., *Principles of Stellar Evolution and Nucleosynthesis*, McGraw-Hill, Inc., 1968.
- [2] Cowan, Robert D., "The Theory of Atomic Structure and Spectra", University of California Press, 1981, p.525.
- [3] Harvey, James M., Katz, I., and Vik, Robert C., *A Study of Equations of State/Opacity of Ionized Gases*, 1973.
- [4] Hubbel, J.H., Gimm, H.A., and Øverbø, I., J. Phys. Chem Ref. Data, Vol 9, No. 4, 1980.
- [5] Øverbø, I., Mork, Kjell J., Olsen, Haakon A., Physical Review, Vol. 175, No. 5, 25 November 1968.
- [6] Padmanabhan, T., *Theoretical Astrophysics, Volume I: Astrophysical Processes*, Cambridge University Press, 2000.

# Invariant Feature Recognition Using Dendritic Processing

Ethan Brown

*The University of Oklahoma, Norman, Oklahoma*

Garrett Kenyon, Mark Flynn

*Los Alamos National Laboratory, Los Alamos, New Mexico (P-21)*

The fundamental building blocks of the mammalian visual system are cortical edge detectors—simple cells in V1 that respond selectively to short line segments of a preferred orientation. Hubel and Wiesel proposed that these cells receive their input from optimally aligned sets of LGN relay neurons. However, current feed-forward models of layer 4 visual cortex simple cell edge detectors fail to account for the experimentally measured low aspect ratio (between 1:1 to 2:1) of the input LGN receptive fields. We hypothesize that non-linear dendritic subunits of higher aspect ratio could enable good orientation selectivity for V1 simple cells despite the low aspect ratio of their retinotopic input. First with passive dendritic structure at high aspect ratio, we confirm our model reproduces those results present in current experimental results, i.e. orientation tuning, contrast invariance, spatial frequency tuning, and weak small spot responses. Next, we show at low aspect ratios, passive dendritic structure is incapable of reproducing the measure response properties of V1 simple cells. Finally, we initialize dendritic spiking through non-linear subunits in order to once again regain the experimentally observed behavior. Furthermore, non-linear dendritic subunits could provide a general mechanism whereby neurons in higher visual areas acquire selective responses to very specific features regardless of scale, translation, or rotation. In all modelling, we utilize the NEURON environment to simulate a biophysical model of V1 layer 4 simple cells.

## INTRODUCTION

Orientation selectivity is a ubiquitous property throughout the primary visual cortex of most mammalian carnivores. Indeed, it has become the most comprehensively studied and debated characteristic of retinal cells due to its strong link to visual functionality and ease of measurement. Nevertheless, it is still not entirely well understood. Commonly, simple cells which are orientation selective are referred to as "edge detectors" since they respond exclusively to well-oriented edges or bars. It is the accumulation of all the edge detectors in the primary visual cortex which formulate basic vision before higher level functions can perform more complex tasks.

Over 40 years ago, Hubel and Wiesel first proposed a model for orientation selective retinal ganglion cells in which each V1 cell receives input from a line of lateral geniculate nucleus (LGN) neurons along the axis of its receptive field [3]. This "feed-forward" model received extraordinary experimental support and has been repeatedly augmented with various types of inhibitory contributions in order to mimic other physiological characteristics such as invariance to changes in stimulus contrast and broad spacial frequency tuning.

However, recent experiments have shown the receptive field of edge detectors to be as low as 1.5:1 [1]. This almost square LGN input is not sufficient for the feed-forward model alone to reproduce the sharp orientation tuning curves seen in experiment. With enough inhibition, good orientation tuning is possible, yet such levels of inhibition create non-physiological spacial frequency tuning curves. Thus it seems at low aspect ratio, the model breaks down.

So, how can V1 neurons respond selectively to oriented edges given their essentially un-oriented input without the need for extensive shaping by intracortical input? One solution to this paradox is dendritic spiking. For decades, electrophysical recordings of hippocamel neurons have documented the existence of fast prepotentials [8]. However, it was not until 10 years ago that direct recordings found such potentials to be generated in individual dendrites [9]. Further study showed that dendritic spikes initiated in functionally isolated dendritic compartments can propagate as action potentials to the soma despite continuous synaptic activity [11]. Moreover, dendrites have been shown to exhibit direction-selectivity to various light stimuli, a property formerly thought to belong primarily to somatic activity [6].

The model we are proposing to solve the dilemma of low aspect ratio orientation selectivity is that, while the total input to the V1 neuron is 1.5:1, each section of dendrite receives high aspect input. For a dendritic subunit to signal the presence of an appropriately oriented edge, it needs to amplify its input by spiking. Therefore dendritic subunits must integrate their input independently, and if the membrane potential exceeds threshold, generate an action potential [4]. If the dendrites passively propagated their input to the soma, only input that activated the majority of the dendritic tree would be sufficient to produce somatic spiking.

While it is likely that in an intact cortical network, both feed-forward and feed-back mechanisms contribute to V1

FIG. Model Schematics

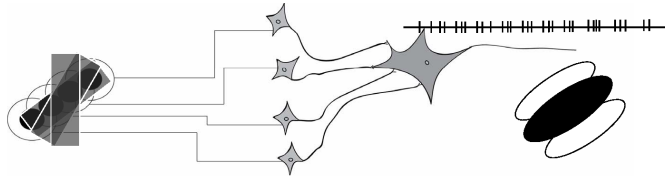


FIG. 1: A schematic of the feed-forward model as described by Hubel and Wiesel. A line of LGN cells provides input to the dendrites of a neuron. This input is then passively transferred through the cell to the axon where it is integrated. If the axon then spikes, an action potential is back-propagated throughout the cell. On the far right, we depict the "on" and "off" regions of the edge detector given by the "on" and "off" regions of the line of LGN cells. Our model differs from this approach in that instead of passive dendrites, we propose a spiking dendritic structure which may integrate its own input.

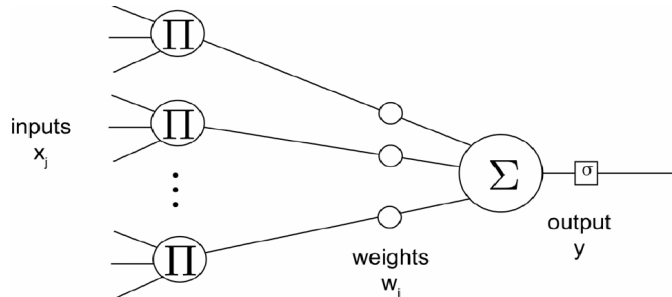


FIG. 2: A schematic of dendritic subunits integrating their input independently, which is then summed at the soma. Each subunit is weighted according to its relative position in the total receptive field of the edge detector.

orientation selectivity, our model shows that dendritic spiking can take relatively un-oriented LGN input and produce sharply tuned V1 edge detectors.

## CONCEPTUAL MODEL

In order to simulate an edge detector, we imagine a grid of LGN neurons being overlaid by a light bar or grating at various orientations. This grid then forms the total receptive field of a single neuron as prescribed in the feed-forward model, (FIG. 1). However, this total receptive field is divided into non-linear subunits of higher aspect ratio (3:1), (FIG. 2). Synaptic weight for each subunit is weighted by a double gaussian curve, while each the weight within each subunit is divided evenly among thalamic input. Each subunit then synapses to a particular dendrite on the excitatory cell, which in turn integrates its input and fires accordingly.

This grid is then copied for each of three inhibitory sites, each with six different preferred orientations. In this way, we establish cross-orientation inhibition, where two of the inhibitory sites flank the excitatory cell, while the third completely overlays it. As mentioned, each inhibitory site has six orientations which synapse at the soma directly to each other. The flanking inhibition running parallel to the excitatory receptive field directly synapses to the excitatory cell's soma while the parallel overlaying inhibition synapses to somas of its inhibitory neighbors. As one can imagine, this push-pull process helps give rise to the contrast invariance seen in the edge detector model.

Inhibitory strengths may vary based on whether the synaptic connection is inhibitory-inhibitory or inhibitory-excitatory. Furthermore, the synaptic strength of each LGN cell may vary depending on whether its target is inhibitory or excitatory. When these parameters are controlled properly, the entire edge detector should reproduce proper baseline and excited firing rates of 1-10 Hz and 30-50 Hz, respectively [2].

## COMPUTATIONAL MODEL

For all computational modeling, the NEURON environment was used. NEURON is a simulation environment for modeling individual neurons and networks of neurons. It provides tools for conveniently building, managing, and using models in a way that is numerically sound and computationally efficient. It is particularly well-suited to problems that

FIG. Model Neuron

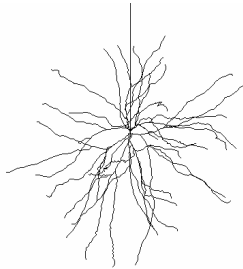


FIG. 3: Here we show an image of the Mainen and Sejnowski model cat V1 layer 4 spiny stellate as depicted in the modeling environment NEURON. One can see the varied dendritic arborization with the myelinated axon extended vertically from the soma. The entire cell is approximately a millimeter in diameter.

are closely linked to experimental data, especially those that involve cells with complex anatomical and biophysical properties.

For our particular problem, we utilize the Mainen and Sejnowski model spiny stellate for both excitatory and inhibitory neurons (the latter with spines removed), (FIG. 3). The electrophysical properties of the cell were reconstructed ad hoc from in vivo electrical recordings. Sodium channel densities were designed to do stuff, thus we have a certain buffer when testing the cell [5].

All LGN input was simulated with integrate and fire Poisson spike generators. Each is given a specific synaptic weight depending upon its target and a certain firing rate depending upon its relation to the overlaying stimulus.

## RESULTS

In our presentation of our results, we first show that at high aspect ratio (3:1) with passive dendritic structure, the model is completely physiological, i.e. it exhibits good orientation selectivity with contrast invariance, broad spacial frequency tuning, and a weak response to small spots. We then show that at low aspect ratio (3:2), the model breaks. This is demonstrated by showing sharp orientation selectivity and broad spacial frequency tuning are mutually exclusive. Finally, we bring the model "back to life", by enabling dendritic spiking and breaking the total receptive field into dendritic subunits.

### 3:1 Aspect Ratio with Passive Dendrites

As mentioned our first test of the model was with a total receptive field aspect ratio of 3:1. With these elongated receptive field we demonstrate our model to have good orientation selectivity with a preferred orientation of 0 degrees. (FIG. 4) This is seen by the sharpness of the curves about 0, with a solid baseline of 1 - 3 Hz. Furthermore, the model is shown to exhibit consistency with varying levels of contrast (10% to 100%). This is a necessary feature of any edge detector since a high contrast bar at a poor orientation should not outperform a low contrast bar at the preferred orientation.

Next we see our model behaves as predicted when presented a grating at varying spacial frequency. (FIG. 5) At low spacial frequency, we see a broad spectrum of positive response while at high spacial frequency there is a sharp cutoff. This response drop-off may be seen as the resolution of our edge detector model which makes intuitive sense since it is clear our visual system can only detect edges of a certain size.

To complete our model, we examine its response to a small spot stimulus. (FIG. 6) This result is found by shining a small (relative to the total receptive field) spot onto the a random location of the receptive field. Clearly because we are examining an edge detector, there should be limited response to such a stimulus. What we find is a response approximately 1/5th that of the response to a well-oriented bar, which is precisely what we would expect for a cat V1 simple cell edge detector.

With all these physiological characteristics confirmed, the passive model at 3:1 aspect ratio is complete. It is also important to note that the passive model was also shown to be physiologically reliable at an aspect ratio of 5:1 as

FIG. 3:1 Aspect Ratio, Passive Dendrites

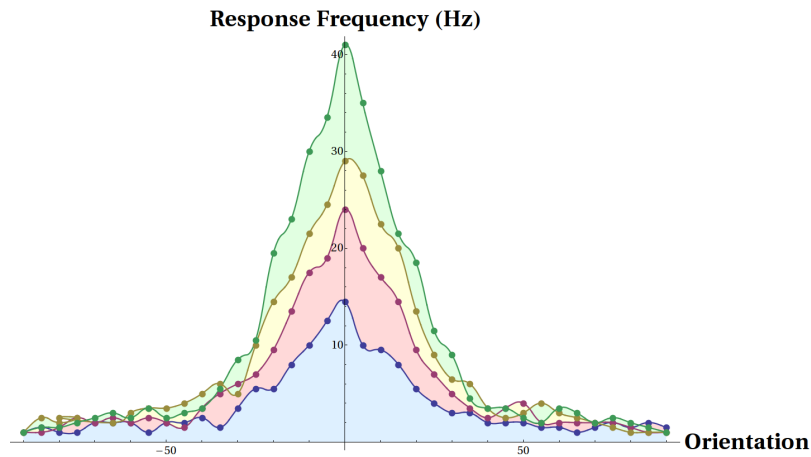


FIG. 4: Orientation tuning measures the response of a cell to different oriented stimuli. With a 3:1 aspect ratio, the model exhibits sufficient orientation selectivity (0 degrees being the preferred orientation). Also as shown, the model displays resilience to changes in contrast, varying primarily at the preferred orientation while keeping a solid baseline of 1 - 3 Hz. This is achieved through the use of cross-orientation inhibition in which orientation-tuned inhibitory flanks are synapsed to the soma of the excitatory cell. Contrast varies from 10% (blue) to 40% (red) to 70% (yellow) to 100% (green).

### Normalized Response

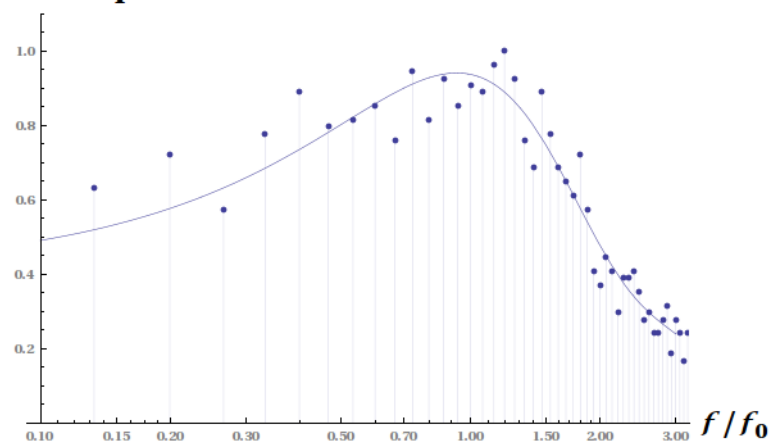


FIG. 5: The above depicts the spacial frequency tuning for the model cell which appears very close to what is expected for cat primary visual cortex edge detectors. The broad domain and sharp upper cutoff are characteristic of such simple cells. Spatial frequency tuning was measured by passing drifting gratings across the receptive field of the target cell. Noise arises from baseline the membrane potential which ranges from 1-10 Hz.

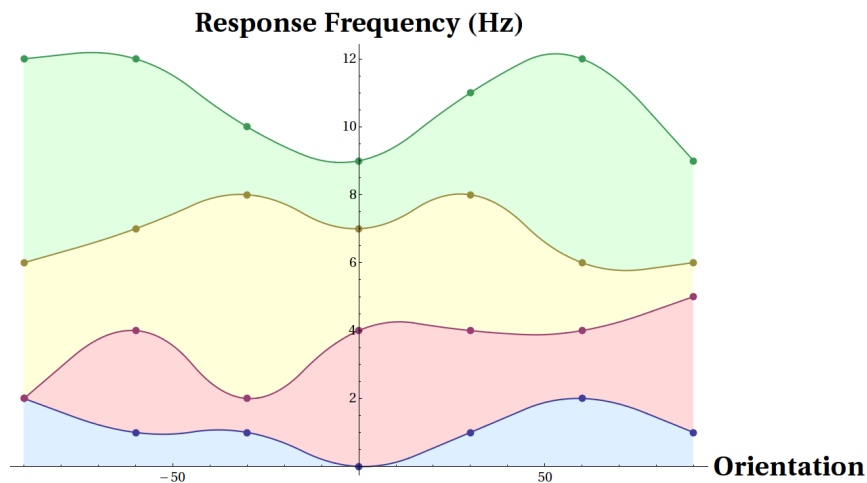


FIG. 6: This result is found by shining a small (relative to the total receptive field) spot onto the a random location of the receptive field. Clearly because we are examining an edge detector, there should be limited response to such a stimulus. The model has a small spot response 1/5th that of a well-oriented bar. This ratio is very close to the measured value for cat V1 simple cell edge detectors.

FIG. 3:2 Aspect Ratio, Passive Dendrites

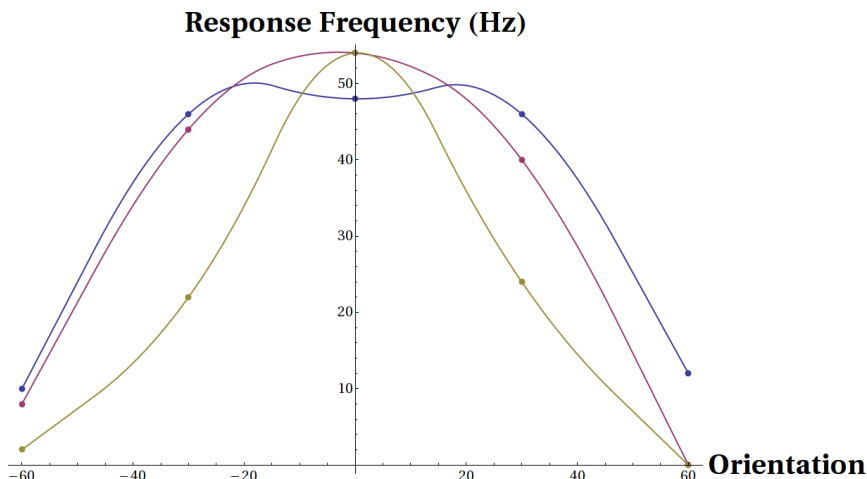


FIG. 7: At a 3:2 aspect ratio, good orientation tuning is difficult, perhaps impossible, to achieve with a passive dendritic structure. In order to display even decent orientation selectivity, inhibition needs to be increased to 5x that required in the 3:1 passive model. Such levels of inhibition are uncharacteristic for V1 simple cell neurons. Additionally, increased inhibition produces non-physiological spacial frequency tuning curves, as shown below. Inhibitory strength varies from 3X (blue) to 4X (red) to 5X (yellow) that of the 3:1 passive model.

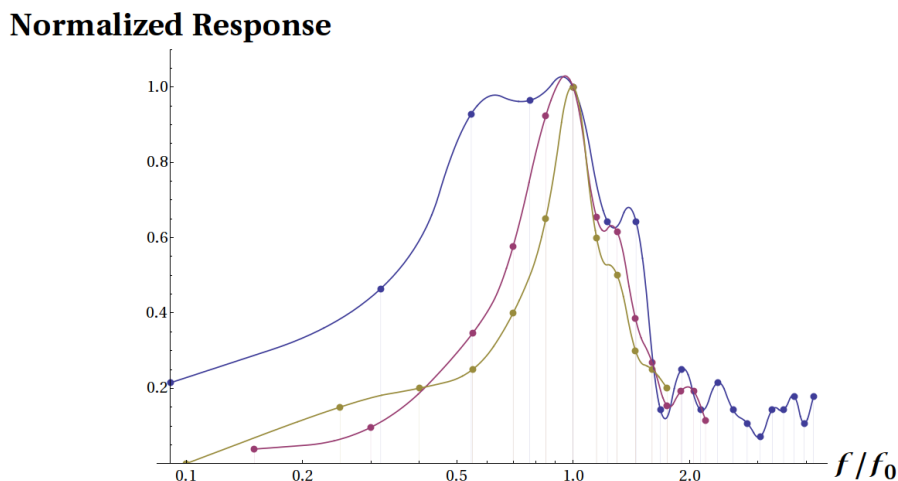


FIG. 8: Spacial frequency tuning becomes sharp as inhibition is raised to non-physiological levels. Thus it appears that at 3:2 aspect ratio, with passive dendritic structure, the edge detector breaks, i.e. orientation selectivity and spacial frequency tuning are mutually exclusive. Inhibitory strength varies from 3X (blue) to 4X (red) to 5X (yellow) that of the 3:1 passive model.

well.

### 3:2 Aspect Ratio with Passive Dendrites

Next, we reduce the total receptive field aspect ratio to 3:2. This is a value of interest since it has been measured experimentally, but not recreated computationally [7].

First, we find that at this low aspect ratio, simple orientation selectivity is not easy to come by. In fact, even decent orientation selectivity requires approximately 5X the flanking inhibitory contribution compared to that required at 3:1. Such levels of inhibition produce uncharacteristic firing rates for both the inhibitory and excitatory centers.

Furthermore, when we next examine the spacial frequency tuning of the passive 3:2 cell, we see a non-physiological effect due to such strong levels of inhibition. At low inhibition, spacial frequency tuning is decently representative of

FIG. 3:2 Aspect Ratio, Spiking Dendrites

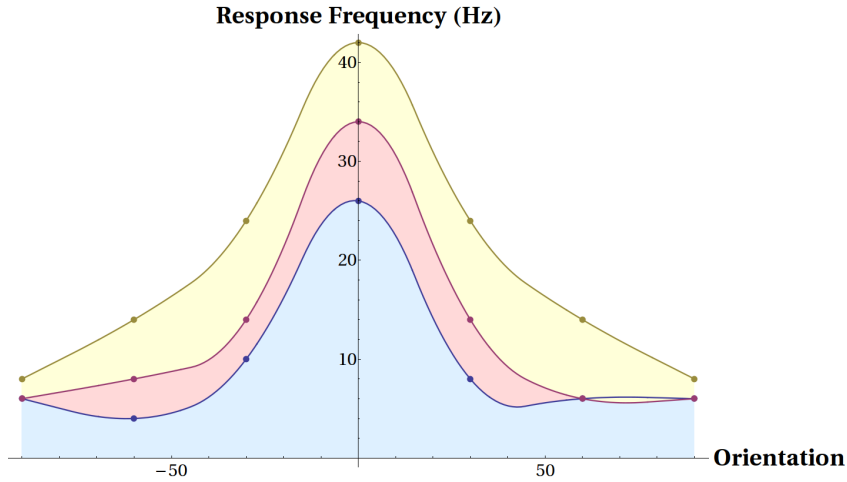


FIG. 9: With a 3:2 aspect ratio (now with spiking dendritic subunits), the model exhibits sufficient orientation selectivity (0 degrees being the preferred orientation). Also as shown, the model displays resilience to changes in contrast, varying primary at the preferred orientation while keeping a solid baseline of 10 - 13 Hz. This is achieved through the use of cross-orientation inhibition in which orientation-tuned inhibitory flanks are synapsed to the soma of the excitatory cell. It should be noted that this is higher than the baseline seen in the 3:1 passive model. This is due to the overlaid image taking up a greater percentage of the receptive field no matter its orientation. If a lower baseline was desired, one could effectively lower the entire plot 10Hz by shrinking the image width. Contrast varies from 10% (blue) to 40% (red) to 70% (yellow).

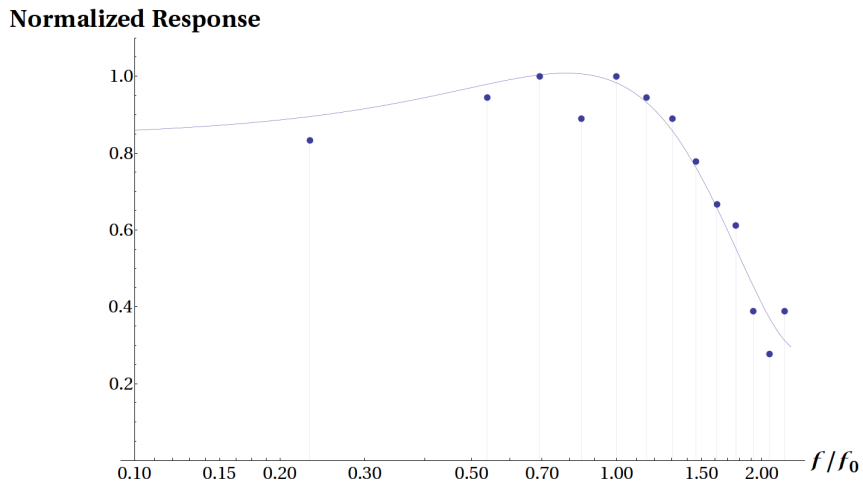


FIG. 10: The above depicts the spacial frequency tuning for the model cell which appears very close to what is expected for cat primary visual cortex edge detectors. The broad domain and sharp upper cutoff are characteristic of such simple cells. Notice the low spatial frequency response is broader here than compared to that of the 3:1 passive model. This results from lower inhibition. If we desired, we could achieve both sharper orientation tuning as well as spatial frequency tuning by once again raising inhibitory levels. Spatial frequency tuning was measured by passing drifting gratings across the receptive field of the target cell. Noise arises from baseline the membrane potential which ranges from 10-13 Hz.

a cat V1 edge detector, with a fairly broad low spatial frequency response. However, as inhibition is raised in order to achieve orientation selectivity, we find the spacial frequency tuning becomes sharp. This would imply that in order to have orientation tuned edge detectors, they would have to be tuned at a specific spacial frequency. We know this not to be true since our visual system can detect a spectrum of low spacial frequencies easily. Thus it appears that at 3:2 aspect ratio, with passive dendritic structure, the edge detector breaks, i.e. orientation selectivity and spacial frequency tuning are mutually exclusive.

### 3:2 Aspect Ratio with Spiking Dendrites

In order to resolve our dilemma, we now enable dendritic spiking. To do so, we raise the global  $Na^+$  -channel density from  $\sim 20$  ps  $\mu m^2$  to  $\sim 100$  ps  $\mu m^2$ . Likewise, to eliminate window currents from hyperpolarization, we raise the  $K^+$  -channel density at the soma from 200 ps  $\mu m^2$  to 600 ps  $\mu m^2$ . Doing so allows the dendrites to create individual action potentials which first propagate to the soma and then back-propagate throughout the cell. This process creates doublet spiking peaks which are characteristic of dendritic spiking.

It is important to note that this raising of ion concentration is physiologically possible because the model we are using included only a low density of both  $Na^+$  and  $K^+$  -channels in order to reproduce firing rates seen in similar neurons [5]. In other words, these numbers are by no means measured nor fixed. In fact it has been shown that physiological values for these densities range from  $\sim 50$  ps  $\mu m^2$  to  $\sim 180$  ps  $\mu m^2$  for  $Na^+$  -channels and from  $\sim 200$  ps  $\mu m^2$  to  $\sim 800$  ps  $\mu m^2$  for  $K^+$  -channels [10].

Finally, we test our model's orientation tuning at various contrasts, now with spiking dendrites. What we find is that, as predicted, we can retrieve contrast invariant orientation tuning using approximately the same inhibitory levels found in the passive 3:1 model. (FIG. 9) We can confirm that this is a direct result of dendritic subunit spiking, by noticing that even at small deviations from preferred, response is considerably lower. Furthermore, the model once again retains good spacial frequency tuning, (FIG. 10).

## CONCLUSIONS

At 3:1 aspect ratio with passive dendritic structure, our model matches all physiological characteristics found in cat V1 layer 4 edge detectors, including orientation selectivity, contrast invariance, spacial frequency tuning, and weak small spot response. At 3:2 aspect ratio with passive dendritic structure, our model breaks, i.e. orientation selectivity and spacial frequency tuning are mutually exclusive. Finally, once enabling dendritic spiking, at 3:2 aspect ratio with 3:1 subunits, our model regains all expected physiological characteristics simultaneously.

## FUTURE RESEARCH

Though the main result of our research has been given proof, we still have much to confirm. For example, membrane potentials for each cell must be measured and compared to the expected experimental values. Such background noise is vital for any edge detector considering the amount of intracellular input received. The small spot response at 3:2 aspect ratio should also be measured. Additionally, we must show our model is robust. To do so, we will find what range of values (e.g. ion channel densities, synaptic weight, synaptic placement, etc.) still produce said results.

Another measurement should be made regarding the receptive fields of the various models. We must confirm that the total receptive field of the 3:1 model is actually 3:1, the 3:2 model actually 3:2, etc. To do so, we will recreate the method used by most experimentalists when measuring receptive field aspect ratio; we will shine small spots, at random, upon the system and record the response. From this data, we will reconstruct the receptive field.

It should also be noted that raising global ion concentrations creates a variety of firing characteristics in the dendritic structure depending on individual compartmental morphologies. In doing this research, this was an area of much concern since the result hinges on each dendritic subunit being electrotonically compact. Making dendritic spiking more homogeneous will most likely require a mapping of input impedances as well as a measurement of electrotonic lengths in order to determine the necessary ion channel densities. This will be an interesting topic of study, not only for the research discussed in this paper, but also for all studies of dendritic spiking, especially as intercellular measurements become increasingly precise.

Finally, even though the data collected from our model was sufficient for a proof of concept. It would be advantageous to perform the above computations for smaller steps sizes in order to further confirm our results. Clearly this would be an expensive computation on an ordinary computer, thus it would seem advantageous to do so only if we were granted access to a super computer or large computing cluster.

## REFERENCES

---

- [1] Alonso et al. Complex receptive fields in primary visual cortex. *The Neuroscientist*. 9, No. 5, 317-331, 2003.
- [2] Carandini, M. & D. Ferster. Membrane potential and firing rate in cat primary visual cortex. *J Neurosci* 20: 470-484, 2000.
- [3] Hubel, D.H. & T.N. Wiesel. Receptive fields, binocular interaction and functional architecture in the cat's visual cortex. *J. Physiol.* 160: 106-154, 1962.
- [4] Losonczy, A. & J.C. Magee. Integrative properties of radial oblique dendrites in hippocampal CA1 pyramidal neurons. *Neuron*. 50, No. 10, 291-307, 2006.
- [5] Mainen, Z.F. & T.J. Sejnowski. Influence of dendritic structure on firing pattern in model neocortical neurons. *Nature*. Vol 382. 25 Jul 1006.
- [6] Oesch, N. et al. Direction-Selective dendritic action potentials in rabbit retina. *Neuron*. 47, No. 5, 739-750, 2005.
- [7] Pei et al. Receptive field analysis and orientation selectivity of postsynaptic potentials of simple cells in cat visual cortex. *J Neurosci*. 14: 7130-7140, 1994.
- [8] Spencer, W.A. & E.R. Kandel. Electrophysiology of hippocampal neurons. IV. Fast prepotentials. *J Neurophysiol* 24: 272-285, 1961.
- [9] Turner, R.W. et al. Localization of tetrodotoxin-sensitive field potentials of CA1 pyramidal cells in rat hippocampus. *J. Neurophysiol*—. 62: 1375-1387, 1989.
- [10] Vetter, Philipp, et al. Propagation of Action Potentials in Dendrites Depends on Dendritic Morphology. *J Neurophysiol*. 85: 926-937, 2001.
- [11] Williams, S.R. Spatial compartmentalization and functional impact of conductance in pyramidal neurons. *Nat. Neurosci*. 81: 1412-1417, 1999.

# Modeling Electron Distributions and Radiation Spectra Produced in Gamma Ray Bursts

Emily A. Chouinard and Siming Liu

## ABSTRACT

Gamma Ray Bursts (GRBs) have become one of the most interesting astrophysical phenomena during the past few decades. Their detection was quite accidental, and scientists have continuously studied them to unravel their mystifying nature. It is generally accepted that the gamma rays are produced by relativistic electrons through the synchrotron processes. The process of electron acceleration and the radiative characteristics of relativistic electrons in a turbulent magnetic field are therefore of great importance and interest. These processes are critical for us to uncover the underlying dynamical processes producing the GRBs with the observed radiation spectrum and its variation with time. A code was developed to model the evolution of the electron distribution function under the influence of a turbulent magnetic field, which can be produced during the energy release of GRBs. This turbulent magnetic field can not only accelerate electrons to very high energies at the site of very efficient energy conversion, but also cool the electrons through the radiative processes in a more extended region, where most of the observed gamma-rays are presumably produced. There are three basic processes involved, namely the acceleration of electrons by turbulence, the escape of electrons from the acceleration site into a cooling region, the cooling of electrons through radiation. These processes can be characterized by three time scales. The electron distribution is then determined by three basic parameters: the injection energy, the ratio of the acceleration to escape times, and the lifetime of the cooling region. The observational data can be compared with the model predicted synchrotron self-Comptonization spectrum to constrain the magnetic field, electron energy and density, and the size of the emitting region, which will lead to a better understanding of the progenitors and their environments.

## 1 Introduction

Gamma Ray Bursts were first discovered in the 1960s by the Los Alamos National Laboratory with the Vela Satellites as part of the US Nuclear Detection Program. When scientists realized that the gamma rays they were detecting did not come from the Earth they looked to space for an answer. Gamma ray bursts are burst of gamma ray photons produced by powerful explosions in space. They are by far the most vibrant and bright objects in the known universe and can on average produce more energy than the Sun can in its 10 billion year lifetime. There are two types of GRBs, short term and long term. Short term GRBs last from a few milliseconds to a few seconds with no prominent afterglow emissions. They are rare and hard to detect with current instruments thus making them by far the most elusive and unknown type of GRBs. On the other hand, long term GRBs last a few seconds to a few hundred seconds. On average, 2-3 long term GRBs are detected each week and most of the observational data are collected from this type of GRBs. They also produce strong afterglows that can last a few days to a few weeks. There are many theories about the origin of long term GRBs, from massive stars, black hole collapsars or supernovas; most theorists believe that the source of long term GRBs, in general, is an explosion triggered by the death of massive stars. The physical processes of producing the observed gamma rays can be different for short term and long term GRBs. Here we only consider long term GRBs.

It is generally accepted that the observed gamma rays are produced by relativistic electrons as they move around magnetic field lines producing synchrotron radiation. The same electrons can inverse Compton scatter the synchrotron photons and produce the so-called synchrotron self-Comptonized emission. Phenomenological modeling of some of the observed gamma ray spectra shows that the gamma rays are produced in an attenuated medium, where the Coulomb collision time scale among electrons is much longer than other relevant time scales. The electrons need to be accelerated via a collision-less process. A turbulent magnetic field is perhaps the most natural agent for such particle acceleration. The same magnetic field may also be responsible to the emission processes.

The high luminosity of the observed emission implies that the electrons are cooled very efficiently via the radiative processes. The electron acceleration by a turbulent magnetic field should be at least as efficient as the cooling to energize electrons from a low energy background to relativistic energies. It is also likely that most of the relativistic electrons lose their energy in a region much more extended than the region where they are accelerated. There are therefore three basic processes, namely the acceleration of electrons by a turbulent magnetic field, the escaping of electrons from the acceleration region into a cooling region, and the cooling of electrons in both the acceleration and cooling regions. In the simplest model, these three processes can be described by three time scales. The cooling time is inversely proportional to the energy of the electrons. We will assume that the acceleration and escape times are independent of the electron energy. Their ratio then determines the spectral index of the electron distribution function. Above the energy, where the cooling time crosses the acceleration time, the electron distribution cuts off exponentially. These three time scales and the injection energy of the electrons then determine the electron distribution function in the acceleration region.

Assuming that the electron density and magnetic field do not change dramatically from the acceleration region to the cooling region, the distribution of electrons in the cooling region then only depends on its lifetime. The model predicted synchrotron self-Comptonization (SSC) spectrum can be compared with the observed GRB spectra to infer the electron energy and density, magnetic field, and the size of the emission region, which can be used to guide our modeling of the progenitors.

## 2 Electron Acceleration by Turbulent Magnetic Fields

The initial explosion of GRBs can drive a relativistic outflow, which carries a significant amount of kinetic and/or magnetic energy. The interaction of this outflow with the surrounding media causes very efficient energy dissipation. The energy carried by the outflow is converted into the internal energy of the plasma at the working surface between the outflow and the media. Coulomb collisions cannot convert the energies efficiently. We postulate that the energy dissipation first generates a turbulent magnetic field that then accelerates the electrons. This electron acceleration process can then be described with three time scales, i.e. the acceleration time ( $\tau_{\text{acc}}$ ), the escape time ( $T_{\text{esc}}$ ) from the acceleration region, and the energy loss time ( $\tau_0$ ). The ratio of the acceleration to

the escape time, described by  $\delta$ , determines the index of the electron distribution, which cuts off at the energy  $\gamma_{cr}$ , where the cooling time is equal to the acceleration time. Note here that we use  $\gamma$ , the Lorentz factor of the electrons, to denote its energy. Following Liu et al. (2006b) the kinetic equation describing the evolution of the electron distribution function  $N(\gamma, t)$  can be written as,

$$\frac{\partial N}{\partial t} = \frac{\partial}{\partial \gamma} \left[ \frac{\gamma^2}{\tau_{ac}} \frac{\partial N}{\partial \gamma} + \left( -\frac{2\gamma}{\tau_{ac}} + \frac{\gamma^2}{\tau_0} \right) N \right] - \frac{N}{T_{esc}} + \dot{Q}, \quad (1)$$

where  $N/T_{esc} + \dot{Q}$  are the source terms, describing the fluxes of electrons escaping and entering the acceleration region, respectively. The acceleration and synchrotron cooling times are given by the following, respectively,

$$\tau_{ac} = \frac{2\gamma^2}{\langle \Delta\gamma\Delta\gamma\Delta t \rangle} = \frac{C_1 3R_c}{v_A^2}, \quad (2)$$

$$\tau_{syn} = \frac{\tau_0}{\gamma} = \frac{9m_e^3 c^5}{4e^4 B^2 \gamma}, \quad (3)$$

where the Alfven velocity,  $v_A = B/(4\pi n_p)^{1/2}$  and  $C_1$  is a dimensionless quantity of order 1. The source size, the magnetic field strength and electron density are given respectively by  $R$ ,  $B$  and  $n$ . Once one specifies the energy  $\gamma_{inj}$ , where electrons are injected into the acceleration region, equation (1) can be solved to obtain  $N$  in the acceleration region, which also leads to the flux of electrons escaping from the acceleration region and injected into a cooling region. Since the acceleration time scale is much shorter than the dynamical time of the system, we consider the steady-state solution. Then the electron distribution function only depends on,  $\gamma_{inj}$ ,  $\tau_{acc}$ ,  $T_{esc}$ , and  $\tau_0$ .

For a given injection flux  $N/T_{esc}$  into the cooling region, which has the same magnetic field and gas density as the acceleration region, the electron distribution function in the cooling region only depends on its lifetime  $\tau_{life}$ . The designed code gives the steady-state electron distribution function described by equation (1) and adds it up to the electron distribution in the cooling region. The energy of the distribution function is scaled with respect to the cutoff energy  $\gamma_{cr}$ , which can be determined observationally. In figures 1, 2, and 3 the dashed lines represent the electron distribution in the acceleration region, the thin solid lines represent the electron distribution in the cooling region, and the thick solid lines are the sum of the electron distributions in the acceleration and the cooling regions. Figure 1 displays the impact of varying  $\gamma_{inj}$ . In the left panel of figure 1 the injection energy (with a logarithm of -2.5) is greater than the energy in the right panel (-4.0) and as  $\gamma_{inj}$  increases the peak of the electron distribution decreases since we normalize the electron distribution at higher energies.

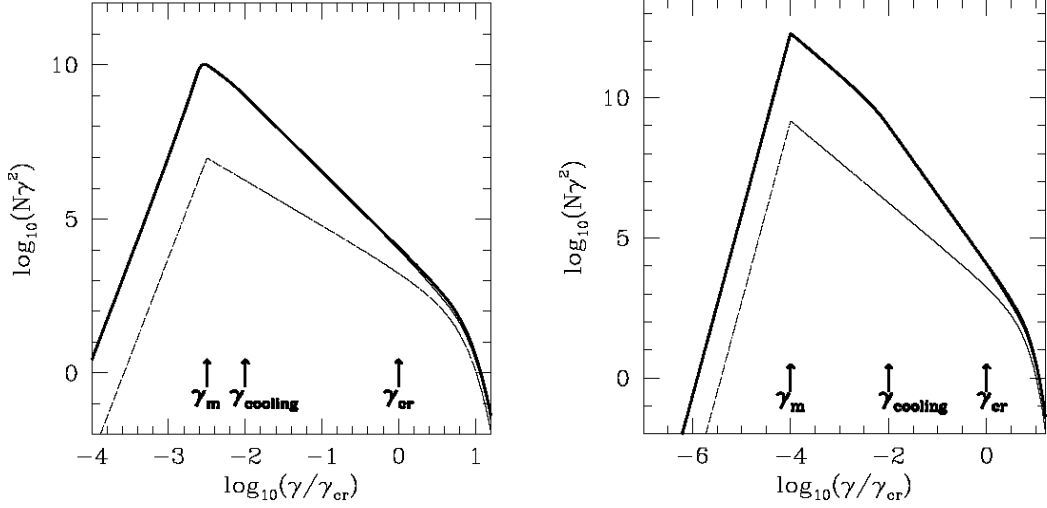


Figure 1: The impact of varying the injection energy of the electrons. *Left*:  $\log(\gamma_{\text{inj}}/\gamma_{\text{cr}})=-2.5$  or  $\gamma_{\text{inj}}/\gamma_{\text{cr}}\sim 1/300$ . *Right*: Same as the left except  $\gamma_{\text{inj}}=\gamma_{\text{cr}}/10,000$ .

The second parameter is the ratio of the acceleration time to the escape time, also denoted as

$$\delta = \left( \frac{9}{4} + \frac{2\tau_{ac}}{T_{esc}} \right)^{1/2} - 1.5. \quad (4)$$

One can tell that the longer the acceleration time is, the larger  $\delta$  is. When the acceleration time is longer, the probability of electron escaping is relatively higher, and the acceleration process is slower. Likewise, if the acceleration time is shorter, the probability of electron escaping is lower, and the acceleration process is faster. Figure 2 demonstrates how increasing  $\delta$  makes the electron distribution softer and the index of the electron distribution greater. The left panel of figure 2 shows a faster acceleration process than the right panel.

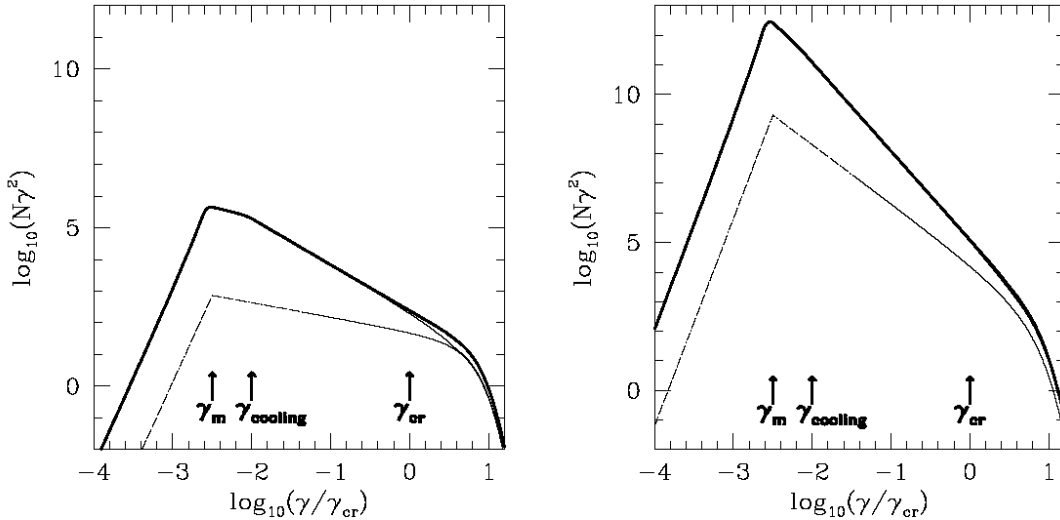


Figure 2: *Left*: For  $\delta=1.46$ , which determines the index of the acceleration region electron distribution. *Right*: Same as the left except  $\delta=3.0$ .

The third parameter is the lifetime of the cooling region. Because the cooling time of electrons is inversely proportional to their energy, the cooling is less important at lower energies. At low energies, where the cooling time is longer than the lifetime, the cooling effects can be ignored and the electron distribution will be the same as that in the acceleration region except that the number of particles at a given energy increases linearly with the lifetime due to the accumulation of these particles in the cooling region. At high energies, where the cooling time is shorter than the lifetime, particles injected into the cooling region at an earlier time have already lost most of its energy and will not contribute to the particle distribution function at these high energies. Particles injected very recently from the acceleration region dominate the particle distribution function in this energy range. These result in a spectral break in the electron distribution function in the cooling region at the energy, where the electron cooling time is equal to the lifetime. As the lifetime of the cooling region increases, this break energy decreases. Figure 3 shows how the effective electron distribution function depends on the lifetime of the cooling region in units of the acceleration time. For a lifetime equal to 0, the electron will not have had any time to accumulate in the cooling region, i.e. there are not particles in the cooling region, the thick solid line, the sum of the acceleration and cooling region electron distributions, and dashed line, the acceleration region electron distribution, will be identical.

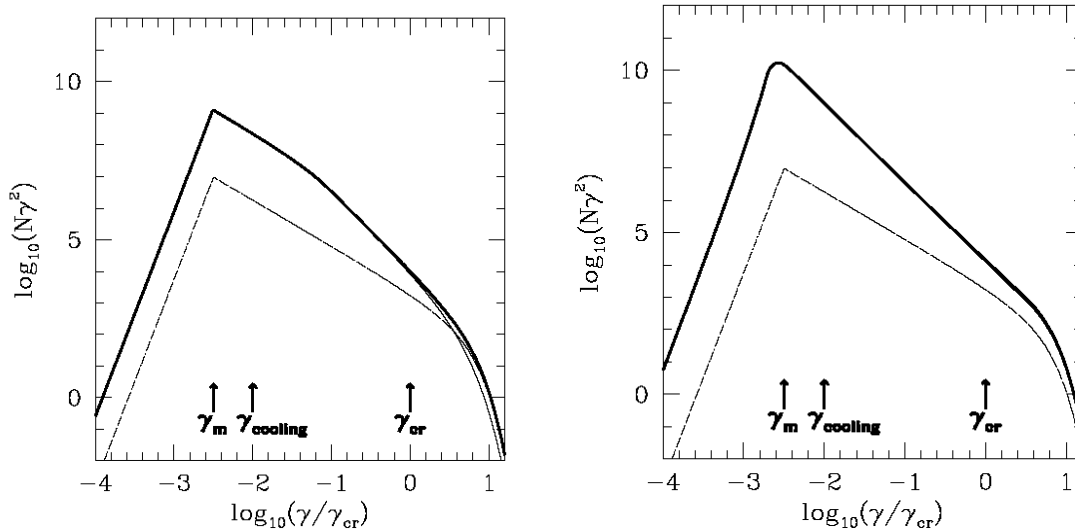


Figure 3: *Left*: For a lifetime 10 times longer than the acceleration time. We note that there is a spectral break at one-tenth of the cutoff energy. *Right*: Same as the left except for a 20 times longer lifetime and the spectral break is located at one-200<sup>th</sup> of the cutoff energy.

The left panel of figure 3 illustrates that as the lifetime of cooling region is short the energy where the cooling time is equal to the acceleration time is relatively high. For a longer lifetime, as shown in the right panel, the energy, at which the cooling time is equal

to the acceleration time, is less. The lifetime of the cooling region is the time since the electrons started to be injected from the acceleration region into the cooling region, and it also gives the time when the oldest electrons have evolved in the cooling region.

### 3 Radiation Spectra

The second code calculates the synchrotron and SSC spectra from both the acceleration and cooling regions, which can be compared with the observed GRB spectra directly to constrain the magnetic field, electron energy and density, and the source size.

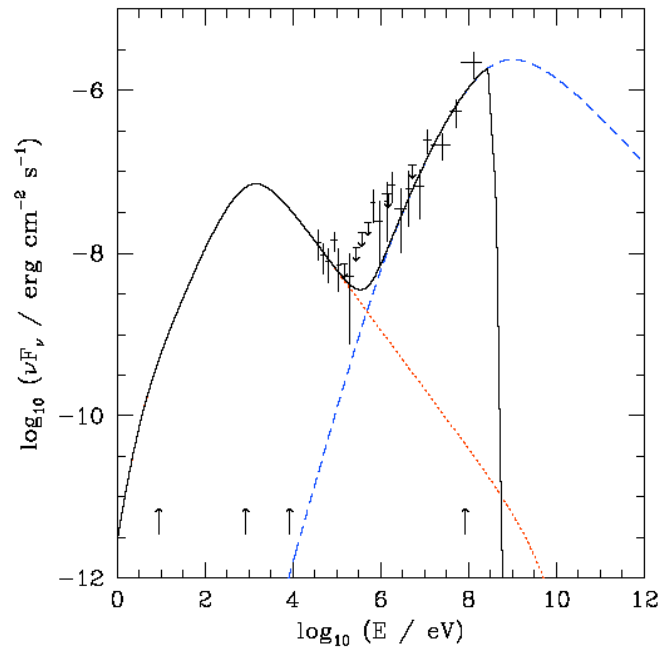


Figure 4: In this graph the dotted red line represents the synchrotron radiation and the blue dashed line represents the SSC spectrum, and the solid black line is the sum of the two with the effects of gamma ray attenuation by electron position pair production included. The crosses are actually data points from GRB observations. The magnetic field is 500G, the source size is  $3.5 \times 10^{13}$  cm and the  $\gamma_{cr}=126500$  for this model.

Figure 4 is the radiation spectra produced from the electron distribution function with parameters  $\gamma_{inj}=-2.5$ ,  $\delta=2.46$  and lifetime=100. Four arrows are labeled on the figure to signify four important characteristics of this radiation spectrum. The arrows from left to right correspond to spectral breaks caused by synchrotron self-absorption, (as the frequency increases, the object, GRB in this case, will go from optically thick to an optically thin object),  $\gamma_{inj}$ ,  $\gamma_{cooling}$ , where the electron cooling time is equal to the lifetime of the cooling region, and  $\gamma_{cr}$ , respectively. The radiation spectrum is smoother than the electron distribution function because it has been integrated over the energy of the electrons. When the data from actual GRB observations are fitted with the model

predicted radiation spectra, we obtain the magnetic field, the source size, and the electron density and energy.

## 4 Conclusions

The evolution of the electron distribution function in a GRB can be described by the time-dependent kinetic equation discussed in §2. The electrons can produce the observed gamma rays through synchrotron and SSC processes. By comparing the model predicted spectra with the observed radiation spectra from the GRB, one can constrain properties of the emitting plasma in the GRB source, which help to infer the characteristics of the progenitor and its environment.

GRBs can originate from some of the most distant objects in the universe, and can have ages of  $1/12$  of the present age of the universe. Understanding the emission mechanisms and the electron acceleration processes in GRBs provides critical constraints on the origin of the GRB. Although the model agrees with current data, more observations need to be made in order to validate/reject the model. In November 2007, NASA will launch GLAST (the Gamma Ray Large Area Space Telescope), which will also house the Gamma-ray Burst Monitor (GBM). The GBM was selected as a complementary instrument for the GLAST mission and will be sensitive to X-rays and gamma rays with energies between 8 keV and 25 MeV. The combination of the GBM and GLAST provides a powerful tool for studying gamma-ray bursts, particularly for time-resolved spectral studies over a very wide energy band. With observations and data received from this telescope our model can be modified to better portray the GRB.

## References

- Abramovitz, M. Stegun, I.A.: 1970, Handbook of Mathematical Functions, National Bureau of Standards, Washington
- Blumenthal, G.R., & Gould, R. J. 1970, Rev. Mod. Phys., 42, 237
- Bittner, J. M., Liu, S., Fryer, C.L., & Petrosian, V, 2007, ApJ, 662
- Gonzalez, M. M., Dingus B. L., Kaneko, Y., Preece, R. D., Dermer, C. D. & Briggs, M.S., 2003, Nature, 749
- Liu, S., & Melia, F. 2002 ApJ, 566, L77
- Liu, S., Melia, F., & Peterosian, V. 2006a, ApJ, 636, 798
- Liu, S., Peterosian, V., Melia, F., & Fryer, C. L. 2006b, ApJ, 648, 1020
- Schlickeiser, R. 1984, A&A, 136, 227

## Acknowledgments

I would like to thank first, my mentor, Siming Liu, for answering questions, even horribly easy and obvious ones, guiding me and giving me a great research learning experience. I would also like to thank the coordinators of the Los Alamos Summer School; James Colgan for keeping track of all of us and offering real world advice and Norman H. Magee for his support and for University of New Mexico for providing a

wonderful educational experience. Finally, I would like to thank all my colleagues of the Los Alamos Summer School for providing a memorable summer experience.

# Visualizing Complex Networks

Fuk S. Yeung      Hristo Djidjev

6 August 2007

## 1 Introduction

A complex network is an intricate interconnected system characterized by connections that are neither random nor geometrically regular. Research into complex networks incorporates the use of graphs dominant in graph theory. These are graphs which pattern pairwise relations between points in a collection. A graph is made up of vertices, sometimes referred to as “nodes,” and edges which connect the vertices. [4] This is the simplest type of network and it can quickly increase in complexity. Often, edges need not be uniform. Each type of edge can represent a particular type of relationship between two vertices. For example, a directed edge can represent a one sided relationship between two vertices whereas an undirected edge can represent a mutual relationship between two vertices. Graphs with these kinds of vertices are respectively called directed and undirected graphs. [4]

Furthermore, graphs can be partitioned into clusters, or “communities.” Graph partitioning involves dividing the vertices of a network into different groups with roughly the same size while minimizing the number of edges between groups. The methods for partitioning clusters go beyond the scope of this paper but, it is a continuing topic in computer science. [5]

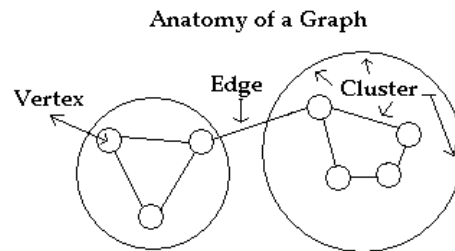


Figure 1: A simple undirected graph with seven vertices and eight edges separated into two clusters

Another ongoing topic in mathematics and computer science, and the subject of this paper, is the visualization of complex networks. The problem is simply, given a set of vertices and edges, to calculate the positions of the vertices and edges to be drawn. A graph is defined by how it is drawn. Different ways of drawing a graph can emphasize the different characteristics of a graph. These are often motivated by the intended application from circuit schematics to bioinformatics. [3] In this paper, I will describe our design for a unique graph drawing algorithm used in the visualization of a complex network.

## 2 Motivation

I have already addressed the importance of graph drawing and acknowledged the diversity of graph types. In short, there is no definite way to draw a graph. However, there are certain instances when a data set needs to look a certain way. In figure [2] below, the same graph is presented in two different ways, each with its strengths and weaknesses. Graph A emphasizes vertex placement preserving

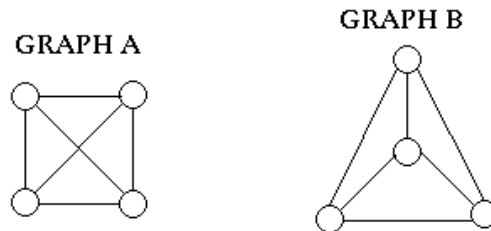


Figure 2: Two equal graphs visualized in two ways

an observable geometry while Graph B emphasizes edge placement preventing edge crossings. Both of these instances can be important when analyzing and designing real world networks.

Although there are many graph drawing programs currently in use, and many that provide very flexible visualization rules, there are few, if any, that make cluster communities visually relevant. Our graph drawing algorithm is designed to maximize the emphasis on vertex relationships and cluster groupings.

## 3 Execution

The complexity of the graphs we are dealing with are clearly defined. We are analyzing simple undirected graphs that have been partitioned into defined clusters. In these graphs, all the vertices are treated as equal units and every edge is treated as an equal relationship. However, the difficulty comes from the

size of our graphs, specifically the number of vertices and edges. We are using graphs with a size in the order of hundreds of vertices and edges, numbers that complicate our task.

There are many ways to calculate the geometric layout of simple undirected graphs. The most common method and our method of choice is in the use of force directed algorithms. In this method, each vertex is treated as a unit and the interaction between each unit and its neighboring units produce forces that drive the positions of every unit in the graph. [1]

### 3.1 The Basics

The force directed algorithm we use in our visualization is the Fruchterman-Reingold(FR) force directed layout. In our research, we discovered many force directed algorithms but we chose the FR algorithm because of its application of both attractive and repulsive forces. The Fruchterman-Reingold force directed algorithm works by modeling each edge as a spring and each vertex as a charged particle point. Because every vertex is treated equally in a simple undirected graph, every vertex is charged equally and a repulsive force is constantly acting between each and every vertex. Similarly, every edge is treated as a spring with the same spring constant resulting in a spring force acting between neighboring vertices, those vertices with connecting edges. The FR algorithm is an iterative function influenced mainly by a variable, temperature. During each iteration, the forces are calculated and applied to each vertex but, the motion of the vertex, or the maximum displacement, is limited by the temperature. As the temperature falls, vertices are able to move through shorter and shorter displacements. When the temperature reaches a minimum, the iteration ends. [1] The pseudocode for the algorithm is given below.

---

**Algorithm 3.1.1** Fruchterman Reingold Force Directed Algorithm

---

**Require:**  $G(E,V)$  { graph  $G$  with set of edges  $E$  and vertices  $V$  }  
 $Area = W * H$  { frame size }  
 $f_a(d)$  { attractive force function with displacement input }  
 $f_r(d)$  { repulsive force function with displacement input }  
 $cool(t)$  { cooling function with temperature input }

**Ensure:**  $t \leq t_{min}$

```
for  $i = 0$  to iterations do
  {calculate repulsive force}
  for  $v \in V$  do
     $\Delta v = 0$ ;
    for  $u \in V$  do
      if  $u \neq v$  then
         $\delta = v.pos - u.pos$ ;
         $\Delta v = \Delta v + (\delta/|\delta|) * f_r(|\delta|)$ ;
      end if
    end for
  end for
  {calculate attractive force}
  for  $e \in E$  do
    { edge  $e$  is from two vertices, here  $u$  and  $v$  }
     $v = e.source$ ;
     $u = e.target$ ;
     $\delta = v.pos - u.pos$ ;
     $\Delta v = \Delta v - (\delta/|\delta|) * f_a(|\delta|)$ ;
     $\Delta u = \Delta u + (\delta/|\delta|) * f_a(|\delta|)$ ;
  end for
  {limit displacement to temp and prevent  $v$  moving outside frame}
  for  $v \in V$  do
     $v.pos = v.pos + (\Delta v/|\Delta v|) * \min(\Delta v, temp)$ ;
     $v.pos_x = \min(W/2, \max(-W/2, \Delta v))$ ;
     $v.pos_y = \min(L/2, \max(-L/2, \Delta v))$ ;
  end for
   $temp = cool(temp)$ ;
end for
```

---

Our implementation of the FR algorithm is through the Boost Graphing Library. The Boost Graphing Library implementation of this algorithm uses a linear cooling schedule for reducing the temperature to the minimum temperature, zero. It also uses the repulsive and attractive forces defined in the FR paper. The time complexity for this algorithm is at worst  $O(|V|^2 + |E|)$ . [2] For the most part, we used the default settings of the BGL algorithm. The only necessary changes we made were with the settings that calculated the attractive and repulsive force in certain instances. We altered these forces and eventually the source code to suit our conditions.

### 3.2 The Algorithm

As mentioned, our data contains vertices with predefined clusters. To emphasize the cluster relationships, we use a dual layered application of the FR algorithm to localize the vertices in a cluster shape. For reasons I will touch on later, the cluster shape was chosen to be a circle with a radius directly proportional to the number of vertices within that cluster.

To optimize our graph space, we decided to apply a modified force directed layout to the clusters themselves. First, we create virtual vertices acting as the geometric centers of the cluster circles and virtual edges between these vertices with weights equal to the number of real edges shared by the clusters. Next, we apply our modified FR algorithm to the graph consisting of the virtual members. The modified FR algorithm takes into account the physical geometry of the clusters. Because the clusters are geometric circles of different radii, we must set conditions for the attractive and repulsive forces to prevent the circles from assimilating each other.

This alone is sufficient for most graphs however, in certain cases where the cluster sizes are dramatically different, a clear bug is encountered. The smaller clusters are actually prevented from moving into a section of the frame by larger clusters. The repulsive force of the arrangement of clusters can actually hinder the movement of a smaller cluster and thus reduce the approach to an optimal layout. This is clearly shown in the figure below. To prevent this, we ran the default FR algorithm first and then applied our reconditioned algorithm to the virtual vertices. This solution allowed for an optimal preplacement layout complimenting the final application of the FR algorithm.

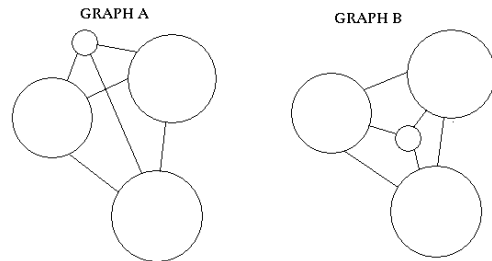


Figure 3: In Graph A, the smaller cluster is excluded from moving to an optimal position. In Graph B, the smaller cluster is preplaced near its optimal position.

After the cluster layout is determined, we add the real vertices and edges to the graph. In addition, to maximize the space available within the cluster circle, we add an edge from the center of a cluster to each real vertex within that cluster. The graph now consists of the virtual vertices connected by virtual edges to the real vertices and edges. Finally, we apply another modified FR algorithm to this graph with one strict condition, the virtual cluster centers do not move.

---

**Algorithm 3.2.1** Localized Vertex Drawing Algorithm

---

**Require:**  $G$  { empty graph  $G$  }  
**Require:**  $V$  { set of all real vertices  $v$  }  
**Require:**  $E$  { set of all real edges  $e$  }  
**Require:**  $C(V)$  { set of cluster vertices for each real vertex in  $V$  }  
 $G = \text{NULL};$   
{ find the virtual vertices with internal radii }  
**for**  $v \in V$  **do**  
     $u = C(v);$   
    **if**  $u \in G$  **then**  
         $u.\text{radius}++;$  { increase size of cluster centered at  $u$  }  
    **else**  
         $G.\text{add-vertex}(u);$   
    **end if**  
**end for**  
{ find the virtual edges with internal weight }  
**for**  $e \in E$  **do**  
     $v_1 = e.\text{source};$   
     $v_2 = e.\text{target};$   
    **if**  $C(v_1) == C(v_2)$  **then**  
        continue;  
    **else**  
        **if**  $e \in G$  **then**  
             $e.\text{weight}++;$  { increase weight of edge between clusters }  
        **else**  
             $G.\text{add-edge}(e);$   
        **end if**  
    **end if**  
**end for**  
 $FR_1(G);$  { default FR algorithm }  
 $FR_2(G);$  { modified cluster graph FR algorithm }  
{ add the real vertices and edges }  
**for**  $v \in V$  **do**  
     $G.\text{add-vertex}(v);$   
     $G.\text{add-edge}(v, C(v));$   
**end for**  
**for**  $e \in E$  **do**  
     $G.\text{add-vertex}(e);$   
**end for**  
 $FR_3(G);$  { modified total graph FR algorithm }

---

The key to this algorithm is in the layered development of the graph. The layers take advantage of the three separate instances of the FR function which are each designed for a specific purpose. I will now move onto a discussion of these modified FR functions.

### 3.3 The Forces

The main difference between the three instances of the FR layout function in the main drawing algorithm is in the application of the repulsive and attractive forces to the vertices among the graph. I will layout these three instances in sequential order and provide some reasoning for the chosen forces. The forces are applied in three graph scenerios following the path of our algorithm: the default, the cluster graph, and the total graph.

The first application of the FR function is upon the graph consisting solely of the virtual vertices, the cluster centers, and edges. It uses the default Boost Graphing Library algorithm which is faithful to the algorithm in the FR paper. In this default state, the attractive and repulsive forces require one parameter,  $d$ , the displacement between the involved vertices. There is also a constant,  $k$ , which is a visual displacement constant equal to the square root of the area of the frame divided by the number of vertices,  $k = \sqrt{W * H / |V|}$ . The default attractive and repulsive forces are respectively as follows:

$$f_a(d) = \frac{d * d}{k} \tag{1}$$

$$f_r(d) = \frac{k * k}{d}. \tag{2}$$

The default force is mainly used to counter the exclusion oddity mentioned previously in the main drawing algorithm.

The second application of the FR function is again upon the cluster vertices and edges but, this second application takes into account the cluster shape to influence the final layout. In the force functions, we must use the internal properties of the cluster edges and vertices. The attractive force involves only edges so, we use the internal weight of the cluster edge to directly affect the force. Larger edge weights produce larger attractive forces. The reasoning behind this was purely the intuitive sense that clusters with more real edges between them have a stronger connection than clusters with less real edges between them. The algorithm below shows how this can be applied to the attractive force using the fact that each cluster edge weight is directly related to the number of real edges between the clusters.

---

**Algorithm 3.3.1** Cluster Attractive Force

---

**Require:**  $d$ ; {displacement between vertices}

**Require:**  $k$ ; {again,  $k = \sqrt{W * H / |V|}$ }

**Require:**  $w$ ; {weight of edge connecting vertices}

return  $d * d * w / k$ ;

---

However, the attractive force must be balanced by a repulsive force that also takes into account the geometry of the cluster shape. The calculation is surprisingly simple if we choose a circle to be the cluster shape. Every cluster

vertex is given an internal radius property directly proportional to the number of real vertices within that cluster. We give the condition that if the distance between two cluster vertices reaches a maximum point, analogous to infinity in electrical physics, the repulsive force vanishes. Furthermore, if the distance reaches a minimum point, the repulsive force explodes in magnitude. This is to keep the cluster circles from intersecting. If none of these extremes are met, we provide a variation of the default force that connects the two extremes.

---

**Algorithm 3.3.2** Cluster Repulsive Force

---

**Require:**  $d$ ; {displacement between vertices}  
**Require:**  $C$ ; {constant of maximum distance}  
**Require:**  $c$ ; {constant of minimum distance}  
**Require:**  $u, v$ ; {involved cluster vertices  $u$  and  $v$  }  
**Require:**  $w.rad$ ; { radius of cluster with center vertex  $w$  }  
 $min = v.rad + u.rad$ ;  
**if**  $d \geq C * min$  **then**  
    return 0;  
**else if**  $d \leq c * min$  **then**  
    return 1000000000;  
**else**  
    { at this point, the range is:  $C * min > R > c * min$  }  
    return  $1/(d - c * min)$ ;  
**end if**

---

The final application of the FR function is upon the final graph consisting of both the cluster and real vertices and edges. This is the trickiest application of the FR function because of its focus on maintaining the cluster placement while optimizing the geometry of the cluster shape. The involved vertices are first divided by whether they are in the same cluster. Then, attractive force maintains that if they are in the same cluster and one of the vertices is a cluster vertex, there are three options. There is a maximum, the radius of the cluster circle and any vertex that moves outside this radius experiences an explosive force. There is a range from this maximum to a minimum point where the attractive force is slightly weaker, being inversely proportional to the difference between the maximum and the displacement. Finally, there is the range from the cluster vertex to the minimum point where the force is the weakest, the default force. This is a layered approach to keep the layout centered around the cluster vertices. Furthermore, if the involved vertices are in the same cluster and are both real vertices or if they are not in the same cluster, they also follow the default force.

---

**Algorithm 3.3.3** Final Attractive Force

---

**Require:**  $d$ ; {displacement between vertices}  
**Require:**  $u, v$ ; { cluster and/or real vertices  $u$  and  $v$  }  
**Require:**  $c$ ; { decimal constant of minimum distance }  
**Require:**  $C[V]$  { set of cluster indices for all vertices }  
**Require:**  $w.rad$ ; { radius of cluster with center vertex  $w$  }

```
if  $C[v] == C[u]$  then  
   $max = -1$ ;  
  if  $v$  is cluster vertex then  
     $max = v.rad$ ;  
  else if  $u$  is cluster vertex then  
     $max = u.rad$ ;  
  end if  
  if  $d \geq max$  and  $max \geq 0$  then  
    return 100000000;  
  else if  $d \geq c * max$  and  $max \geq 0$  then  
    return  $d * d / ((d - max) * k)$ ;  
  else  
    return  $d * d / k$ ;  
  end if  
else  
  if  $v$  is cluster vertex or  $u$  is cluster vertex then  
    return 0;  
  else  
    return  $d * d / k$ ;  
  end if  
end if
```

---

The repulsive force does not follow this layered pattern. It simply maintains that if the involved vertices are in the same cluster, the repulsive force is inversely proportional to the radius. However, if one of the involve vertices is a cluster vertex, we apply a condition that if the real vertex moves beyond the radius of its cluster, the repulsive force vanishes. There is no repulsive force between cluster vertices and real vertices of different clusters. However, real vertices are acted on by the repulsive force of other real vertices in an inversely proportional manner.

---

**Algorithm 3.3.4** Final Repulsive Force

---

**Require:**  $d$ ; {displacement between vertices}  
**Require:**  $u, v$ ; { cluster and/or real vertices  $u$  and  $v$  }  
**Require:**  $c$ ; {constant of minimum distance}  
**Require:**  $C[V]$  { set of cluster indices for all real and virtual vertices }  
**Require:**  $w.rad$ ; { radius of cluster with center vertex  $w$  }

```
if  $C[v] == C[u]$  then
   $r = -1$ ;
  if  $v$  is cluster vertex then
     $max = v.rad$ ;
  else if  $u$  is cluster vertex then
     $max = u.rad$ ;
  end if
  if  $d \geq max$  and  $r \geq 0$  then
    return 0;
  else
    return  $k/d$ ;
  end if
else
  if  $v$  is cluster vertex or  $u$  is cluster vertex then
    return 0;
  else
    return  $k/d$ ;
  end if
end if
```

---

The most important thing about the final FR function is that it does not affect the positions of the cluster vertices. The real vertices and edges are forcibly contained within the cluster shape. This visually emphasizes the placement of the clusters themselves as well as the size of the cluster through their positions among the graph layout.

## 4 Conclusion

To conclude, the purpose of this paper was to present a reasonable graph drawing algorithm that emphasized cluster relationships. In doing so, I have presented the devices to implement this algorithm along with the algorithm itself. The algorithm is rough in its use of the linear FR algorithm and not fully tested in terms of capacity. However, it accomplishes the goal of creating a visually impressive 2-D layout while emphasizing the desired characteristics. I will end this paper with my results,

## 5 Epilogue

This section is intended to present my own viewpoints concerning the LASS program. For two months, I have been pushing C++ code in designing a drawing program from scratch. The future state of my written code is not clear to me at this point. I am actually not sure how my code will be handled and how it will be used as it is just a subset of a larger program. Furthermore, I am not content with the completeness of my code. First and foremost, I do not believe I have tested the program enough to call it complete. Although I have written and rewritten various aspects of the layout, there is still much to be done in terms of the graphical implementation of the layout. My knowledge of OpenGL, the 3-D graphics engine I used to draw the layout, is still limited and my knowledge in computer graphics even moreso. The most important feature I could not provide efficiently was the final 3-dimensional camera. This would allow for a more efficient viewing of the 3-D graph. The 3-D graph uses a height map to create a simple terrain. Its blocky but usable. I have written the height map output in the program to be easily configurable and extremely flexible. This gives it some hope for future use. Other incarnations of my program would include a working GUI and multfile and variable file inputs, especially for the graphics portion. That being said, the final product isn't a complete waste considering the results below.

All in all, though, I must say that as a C++ programmer I have improved drastically. I have now surpassed the barrier of the C++ programmer who programs like a C programmer with fancy structs.

## References

- [1] Thomas M. J. Fruchterman and Edward M. Reingold. Graph drawing by force-directed placement. *Software - Practice and Experience*, 21(11):1129–1164, 1991.
- [2] Doug Gregor. C++ boost. [http://www.boost.org/libs/graph/doc/fruchterman\\_reingold.html](http://www.boost.org/libs/graph/doc/fruchterman_reingold.html), 2004.
- [3] Ivan Herman, Guy Melançon, and M. Scott Marshall. Graph visualization and navigation in information visualization: A survey. *IEEE Transactions on Visualization and Computer Graphics*, 6(1):24–43, /2000.
- [4] M. Newman. The structure and function of complex networks, 2003.
- [5] M. E. J. Newman. Detecting community structure in networks. *European Physical Journal B*, 38:321–330, 2004.

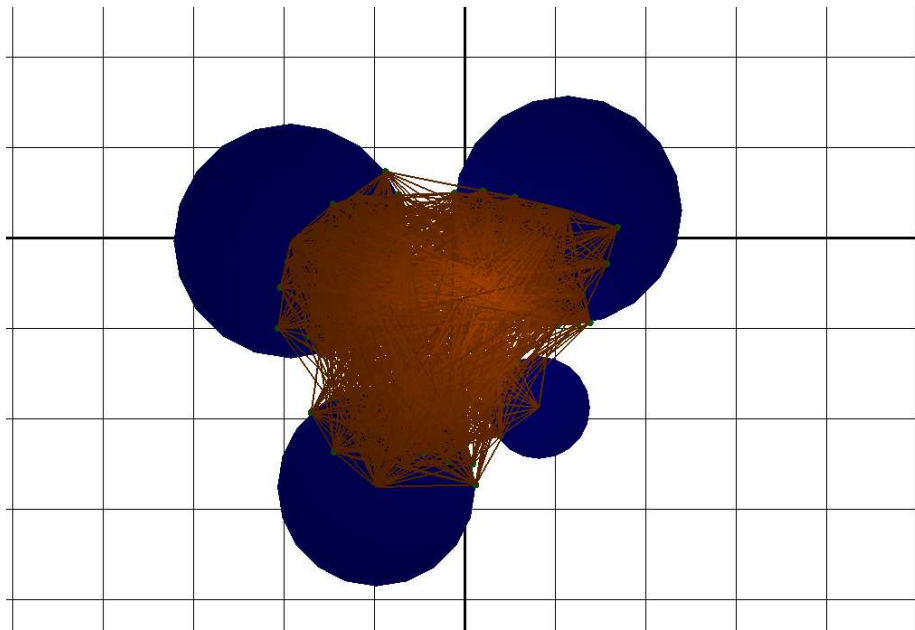


Figure 4: Graph 1: graph with 120 vertices and 1673 edges

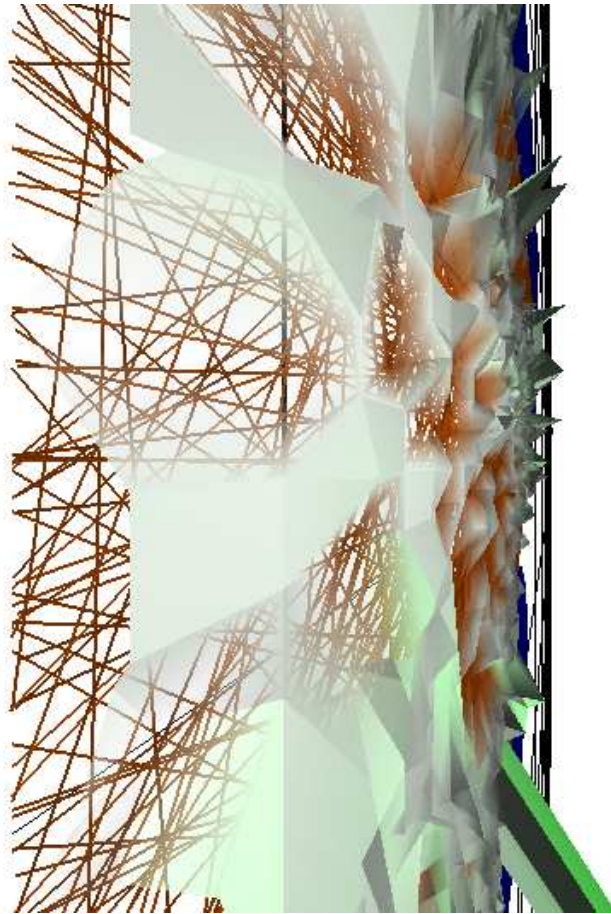


Figure 5: Side view of Graph 1

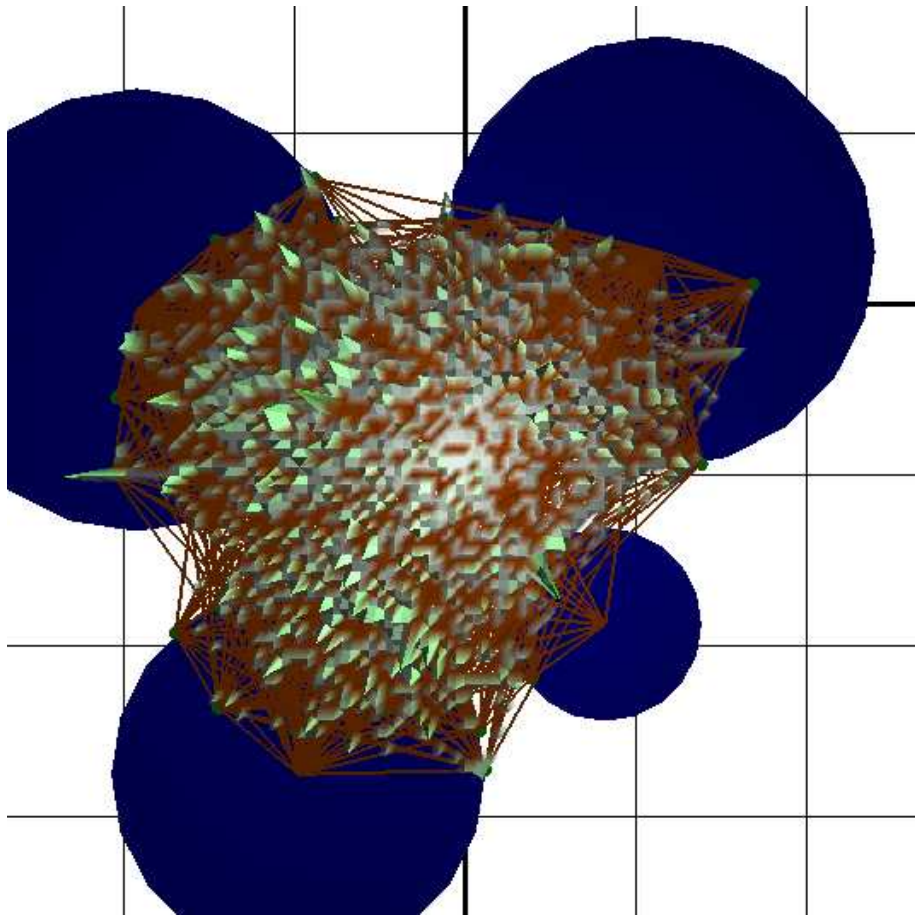


Figure 6: Graph 1: 3-D heightmap of edge density

# Simulating a quantum Ising chain on a liquid-phase NMR quantum computer

John Gamble

*Physics Department, The College of Wooster, Wooster, Ohio 44691, USA*

(Dated: August 10, 2007)

Quantum simulation is an important topic to the physics community, and the simulation of certain simple systems is currently within the grasp of experiment. An algorithm for simulating a transverse field seven-spin Ising chain on an NMR experiment using liquid crotonic acid was developed. The fidelity of the algorithm was then tested and found to be acceptable for times up to about 40 ms. Next, experimental measurement possibilities for the algorithm were assessed, and easily measurable correlation functions were found to show good promise. Care was taken to provide experimental feasibility in that only eight pulses per simulation step were used.

## I. INTRODUCTION

Until recently, everything we knew about information processing did not take advantage of the fundamental quantum-mechanical effects that are manifest on small scales. Rather, we confined ourselves to the realm of classical computing, based on the laws of classical physics. Quantum computation uses quantum properties such as entanglement and superposition states to attain efficiency that is not possible on the classical computers of today[1]. To date, there are a number of efficient quantum algorithms for which there exist no classical analogue. These algorithms include Deutsch's algorithm for simultaneously evaluating a function twice, Grover's fast search of an unsorted database, and Shor's algorithm for factoring an integer into primes[1].

Of the many possible applications of quantum computation in existence today, one of the most intriguing to physicists is quantum simulation. On a classical computer, simulations of quantum systems in general require exponentially increasing resources; memory and time increase exponentially with system size. Thus, physicists are forced to make crude approximations or use large amounts of computer time. Richard Feynman first proposed the idea of using a quantum system to simulate another quantum system in the 1980's, but the field is still primitive compared to conventional computation[1].

One of the problems is the difficulty of building a scalable quantum computer. Because of this, we cannot expect to be able to factor 1000 digit prime numbers on a real quantum computer anytime soon. However, certain interesting quantum simulations are currently within our experimental grasp. The simulation of a seven-spin Ising chain with a transverse field, the topic of this paper, is one of these interesting systems.

## II. QUANTUM COMPUTING

### A. The Qubit

The fundamental unit of information in classical computing is the *bit*. A bit can take values of either 0 or 1, and is manipulated by structures called *gates*, outlined in section II B. Quantum bits, or qubits, are the fundamental unit of quantum computation. Physically, a qubit is any two-level quantum system, such as particle spin or the ground and excited states of an atom. Like the classical bit, the qubit has two orthogonal basis states, usually denoted as  $|0\rangle$  and  $|1\rangle$ . However, unlike the bit, the qubit can also exist as any normalized linear combination of its basis states, giving it a continuum of possible values[1]. A general state of a qubit  $|\psi\rangle$  can thus be written as

$$|\psi\rangle = \alpha|0\rangle + \beta|1\rangle, \quad (1)$$

where  $\alpha$  and  $\beta$  are complex scalars. It is important to note that while a qubit may exist in any linear combination of  $|0\rangle$  and  $|1\rangle$ , measurement of the qubit will result in *either*  $|0\rangle$  or  $|1\rangle$ , but not both, a general result of quantum mechanics called wavefunction collapse.

As mentioned above, we constrain the wavefunction by normalization

$$1 \equiv \langle\psi|\psi\rangle = |\alpha|^2 + |\beta|^2, \quad (2)$$

which can be interpreted as requiring that the measurement of a qubit always yield either  $|0\rangle$  or  $|1\rangle$  with probability  $|\alpha|^2$  or  $|\beta|^2$ , respectively. This constraint on a qubit allows us to visualize the state of any one qubit on the closed, two dimensional surface of a two-sphere, known in quantum information as a Bloch sphere, as shown in figure 1. The vector of a qubit on a bloch sphere is given by solving[1]

$$|\psi\rangle = \cos \frac{\theta}{2} |A\rangle + e^{i\phi} \sin \frac{\theta}{2} |B\rangle, \quad (3)$$

where  $|A\rangle$  is defined as the basis state ( $|0\rangle$  or  $|1\rangle$ ) for which the corresponding scalar coefficient ( $\alpha$  or  $\beta$ ) is real and non-negative, and  $\theta$  and  $\phi$  are the familiar polar and azimuthal angles in polar-spherical coordinates. This representation will be useful for understanding the rotation pulses examined in section IV D.

## B. Quantum Gates

In classical computing, bits are manipulated in a computer using *gates*. These gates, given certain input, yield certain output. For example, one of the simplest classical gates is the NOT gate. The NOT gate takes one bit as input and gives one bit as output. The state of the output (either 1 or 0) is the complement of the input, as shown in table I. Throughout this paper, we will use three specific quantum gates, although many more exist. These quantum gates are formed by exponentiating the familiar Pauli matrices, which are[3]

$$\begin{aligned} \mathbf{X} &= \begin{pmatrix} 0 & 1 \\ 1 & 0 \end{pmatrix}, \\ \mathbf{Y} &= \begin{pmatrix} 0 & -i \\ i & 0 \end{pmatrix}, \\ \mathbf{Z} &= \begin{pmatrix} 1 & 0 \\ 0 & -1 \end{pmatrix}. \end{aligned} \quad (4)$$

We can represent our general qubit in eq. 1 as a column vector,

$$|\psi\rangle = \begin{pmatrix} \alpha \\ \beta \end{pmatrix}. \quad (5)$$

Using this notation, we can easily observe the effects of a quantum gate on a qubit. Since the Pauli matrices happen to be unitary, we can also think of them as the exponential of some other matrix, and thus also as quantum gates.

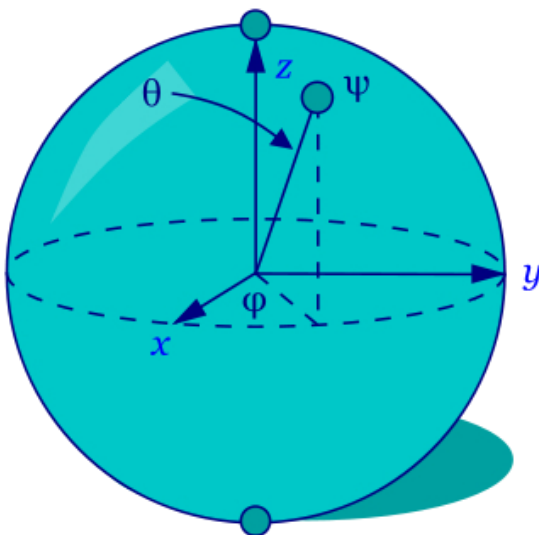


Figure 1: Single qubits can be visualized as being vectors on a two-sphere, known in quantum information as the Bloch sphere[2]. The angles  $\phi$  and  $\theta$  are defined in eq. 3

Table I: Truth table for a classical NOT gate.

| Input | Output |
|-------|--------|
| 1     | 0      |
| 0     | 1      |

For example,

$$\mathbf{X}|\psi\rangle = \begin{pmatrix} 0 & 1 \\ 1 & 0 \end{pmatrix} \begin{pmatrix} \alpha \\ \beta \end{pmatrix} = \begin{pmatrix} \beta \\ \alpha \end{pmatrix}. \quad (6)$$

Thus, we find that  $\mathbf{X}$  is merely a generalization of the classical NOT gate.

### C. Multiple Qubits

The main system we will consider in this paper (introduced in section III) contains seven qubits. However, so far we have only addressed a single qubit system. Fortunately, the generalization to multiple qubits is fairly straightforward. If we consider the case of seven qubits, we find we an arbitrary state  $|\psi\rangle$  must have the form

$$|\psi\rangle = \alpha_1 |0000000\rangle + \alpha_2 |0000001\rangle + \dots + \alpha_{128} |1111111\rangle, \quad (7)$$

where the  $\alpha_i$ s are complex scalars, and we have  $2^7 = 128$  total basis states[1]. As in the single-qubit case, we enforce  $1 \equiv |\langle\psi|\psi\rangle|^2$  for normalization. In general, we can represent multiple qubits as vectors and gates acting on multiple qubits as matrices. This time, however, each vector representing  $n$  qubits must now have  $2^n$  dimensions, and so a corresponding gate must be a  $2^n \times 2^n$  matrix.

For our purposes, we will never need to consider a true multiple qubit gate. That is, we will never need a gate that manipulates qubit  $i$  in a certain way based on the value of qubit  $j$ . Rather, we need to apply multiple single-qubit gates in a multiple-qubit setting. For instance, we might wish to apply the operators  $\mathbf{Z}$  and  $\mathbf{Z}$  to the 2nd and 3rd qubits in a seven qubit chain, while leaving the rest of the qubits undisturbed. To accomplish this, we consider the Kronecker product of the operations we wish to perform in a bitwise fashion. seven qubit operator described above is then[4]

$$\mathbf{I} \otimes \mathbf{Z} \otimes \mathbf{Z} \otimes \mathbf{I} \otimes \mathbf{I} \otimes \mathbf{I} \otimes \mathbf{I}, \quad (8)$$

where  $\mathbf{I}$  is the identity. To get a better handle on this process, let us consider a simple two qubit system. Say that we want to “NOT” the first qubit but not the second. As noted previously, the quantum analogue of the classical NOT gate is the  $\mathbf{X}$  Pauli matrix. If we denote the final operator by  $\mathbf{X}_1$ , indicating we want to operate  $\mathbf{X}$  on only the first qubit, we find that

$$\mathbf{X}_1 = \mathbf{X} \otimes \mathbf{I} = \begin{pmatrix} 0 & 1 \\ 1 & 0 \end{pmatrix} \otimes \begin{pmatrix} 1 & 0 \\ 0 & 1 \end{pmatrix} = \begin{pmatrix} 0 & 0 & 1 & 0 \\ 0 & 0 & 0 & 1 \\ 1 & 0 & 0 & 0 \\ 0 & 1 & 0 & 0 \end{pmatrix}. \quad (9)$$

Now, we take our system of qubits to be in the state

$$|\psi\rangle = \alpha |00\rangle + \beta |01\rangle + \gamma |10\rangle + \delta |11\rangle \leftrightarrow \begin{pmatrix} \alpha \\ \beta \\ \gamma \\ \delta \end{pmatrix}. \quad (10)$$

Thus, when we operate  $\mathbf{X}_1$  on  $|\psi\rangle$ , we get

$$\mathbf{X}_1 |\psi\rangle = \begin{pmatrix} 0 & 0 & 1 & 0 \\ 0 & 0 & 0 & 1 \\ 1 & 0 & 0 & 0 \\ 0 & 1 & 0 & 0 \end{pmatrix} \begin{pmatrix} \alpha \\ \beta \\ \gamma \\ \delta \end{pmatrix} = \begin{pmatrix} \delta \\ \gamma \\ \alpha \\ \beta \end{pmatrix} \leftrightarrow \alpha |10\rangle + \beta |11\rangle + \gamma |01\rangle + \delta |00\rangle. \quad (11)$$

So, we see that for each coefficient, the first qubit has been flipped, while the second has remained the same. We will use this process extensively in section IV D for a system of seven qubits.

### III. QUANTUM ISING MODEL

#### A. The Hamiltonian

The Hamiltonian of the quantum Ising model with a transverse field for a system of seven spins is [5]

$$\mathcal{H}_I = \mathcal{H}_{int} + \mathcal{H}_{zee} = \sum_{i \neq j}^7 J_{ij} \mathbf{Z}_i \mathbf{Z}_j + \sum_{i=1}^7 g \mathbf{X}_i, \quad (12)$$

where  $\mathcal{H}_{int}$  is an interaction term,  $\mathcal{H}_{zee}$  is a Zeeman (field) term, the  $J_{ij}$  terms are interaction constants, and  $g$  is a field coupling constant.

To understand the meaning of these terms, let's turn again to our simple two qubit system, for which the Hamiltonian reduces to

$$\mathcal{H}_2 = J_{12} \mathbf{Z}_1 \mathbf{Z}_2 + g (\mathbf{X}_1 + \mathbf{X}_2). \quad (13)$$

First, we investigate the interaction term. If we evaluate  $\mathbf{Z}_1 \mathbf{Z}_2$ , we find

$$\mathbf{Z}_1 \mathbf{Z}_2 = (\mathbf{Z} \otimes \mathbf{I}) (\mathbf{I} \otimes \mathbf{Z}) = \begin{pmatrix} 1 & 0 & 0 & 0 \\ 0 & -1 & 0 & 0 \\ 0 & 0 & -1 & 0 \\ 0 & 0 & 0 & 1 \end{pmatrix}. \quad (14)$$

This clearly has eigenvalues of  $\pm 1$ . If we assume  $J_{12} > 0$ , we have a degenerate ground state energy of  $-J_{12}$  and ground states  $|01\rangle$  and  $|10\rangle$ .

We treat the Zeeman term similarly. If we write it as a matrix, we have

$$\mathbf{X}_1 + \mathbf{X}_2 = \begin{pmatrix} 0 & 1 & 1 & 0 \\ 1 & 0 & 0 & 1 \\ 1 & 0 & 0 & 1 \\ 0 & 1 & 1 & 0 \end{pmatrix}, \quad (15)$$

which has eigenvalues of  $-2, 0$ , and  $2$ . Thus, if we assume  $g > 0$ , we have a ground state energy of  $-2g$  and a ground state of  $1/2 (|00\rangle - |01\rangle - |10\rangle + |11\rangle) = 1/2 (|0\rangle - |1\rangle) (|0\rangle - |1\rangle)$ , which physically corresponds to the spins lining up parallel to the  $\hat{x}$  axis. Since the ground states of the interaction and Zeeman Hamiltonians are not the same, the ground state of the total system must depend on the value of  $J_{12}$  and  $g$ . So, if we tune  $g$ , we should be able to generate both ground states, and at some point there should be a phase transition between the two. This is called a quantum phase transition and is what makes the quantum Ising model interesting to study.

### IV. QUANTUM SIMULATION

#### A. The Problem

The core issue in quantum simulation is, given a system's Hamiltonian  $\mathcal{H}$ , how do we model some other Hamiltonian of interest  $\mathcal{H}'$ ? In our case, we need to know how we can start from the NMR Hamiltonian and convert it to the Hamiltonian for the Ising spin chain. We accomplish this through the judicious use of unitary operators through a series of qubit rotations. However, before we can delve into the details, we need to develop some background details in quantum mechanics. First, we will investigate the two pictures of time dependence in quantum mechanics: the Schrödinger and Heisenberg pictures. Then, we will develop the two tools we will use to perform a quantum simulation: the Trotter expansion and qubit rotation.

## B. Schrödinger and Heisenberg pictures

Quantum evolution can be viewed from two distinct perspectives, called the Schrödinger and Heisenberg pictures. In the Schrödinger picture, the wavefunction of a system is viewed as time-dependent, while any observable one wishes to measure is viewed as constant with time. This is a useful and logical way to look at things, since we can visualize individual qubits as rotating in Bloch spheres with time. So, in the Schrödinger picture, the expectation value of an observable  $\hat{O}$  is written as

$$\langle \hat{O} \rangle (t) = \langle \Psi(t) | \hat{O} | \Psi(t) \rangle, \quad (16)$$

where we note that the time dependence of the expectation value is expressed entirely through the wavefunction  $\Psi(t)$ . While this interpretation provides a good intuitive feel for the problem, for our purposes it is practical to use the second picture of time dependence in quantum mechanics, the Heisenberg picture. Essentially, we will separate the time dependence from the wavefunction and bundle it with the observable. To do this, first we need to solve the Schrödinger equation. It is

$$\mathcal{H} |\Psi(t)\rangle = i\hbar \frac{d}{dt} |\Psi(t)\rangle, \quad (17)$$

and it has solutions of the form

$$|\Psi(t)\rangle = e^{-i\mathcal{H}t/\hbar} |\Psi(0)\rangle, \quad (18)$$

where  $|\Psi(0)\rangle$  is the wavefunction evaluated at some initial time, and we have assumed that  $\mathcal{H}$  is constant with time. For simplicity of notation, we set  $\hbar = 1$ , and denote  $|\Psi(0)\rangle$  as  $|\psi\rangle$ , giving us

$$|\Psi(t)\rangle = e^{-i\mathcal{H}t} |\psi\rangle. \quad (19)$$

Note that we now have separated all of the time dependence of the wavefunction into an exponential coefficient, known as the time-evolution operator. This suggests that we can write

$$\langle \hat{O} \rangle (t) = \langle \Psi(t) | \hat{O} | \Psi(t) \rangle = \langle \psi | e^{i\mathcal{H}t} \hat{O} e^{-i\mathcal{H}t} | \psi \rangle \equiv \langle \psi | \hat{O}'(t) | \psi \rangle, \quad (20)$$

where we have implicitly defined some new time-dependent observable  $\hat{O}'(t) = e^{i\mathcal{H}t} \hat{O} e^{-i\mathcal{H}t}$ . Thus, we have transferred the time dependence of the problem from the wavefunction in the Schrödinger picture to the operator in the Heisenberg picture. This is a bit harder to visualize, as there is no great way to “see” an operator evolve. However, it will be a valuable mathematical tool when we start doing quantum simulations.

## C. The Trotter Expansion

If we return to the problem outlined in section IV A, recall that our object is to simulate a new hamiltonian  $\tilde{\mathcal{H}}$ . Suppose that we can decompose  $\tilde{\mathcal{H}}$  in two simpler Hamiltonians  $\mathbf{G}_1$  and  $\mathbf{G}_2$ . That is, suppose

$$\tilde{\mathcal{H}} = \mathbf{G}_1 + \mathbf{G}_2. \quad (21)$$

Now, consider the time-evolution operator introduced in the previous section,

$$e^{-i\tilde{\mathcal{H}}t} = e^{-i(\mathbf{G}_1 + \mathbf{G}_2)t}. \quad (22)$$

Normally, we can only write an exponential sum as a product of exponentials if the summands commute. In this case, that would mean  $e^{-i(\mathbf{G}_1 + \mathbf{G}_2)t} = e^{-i\mathbf{G}_1t} e^{-i\mathbf{G}_2t}$  if and only if  $[\mathbf{G}_1, \mathbf{G}_2] = 0$ . Of course, since  $\mathbf{G}_1$  and  $\mathbf{G}_2$  are operators, this is not generally true.

Fortunately, the Trotter expansion guarantees us that[4]

$$\lim_{t \rightarrow 0} \left( e^{-i(\mathbf{G}_1 + \mathbf{G}_2)t} \right) = \lim_{t \rightarrow 0} \left( e^{-i\mathbf{G}_1t} e^{-i\mathbf{G}_2t} \right), \quad (23)$$

even if  $\mathbf{G}_1$  and  $\mathbf{G}_2$  do not commute. Thus, we know

$$e^{-i(\mathbf{G}_1 + \mathbf{G}_2)t} \underset{t \ll 1}{\approx} e^{-i\mathbf{G}_1t} e^{-i\mathbf{G}_2t}. \quad (24)$$

This will prove valuable in allowing us to combine Hamiltonians that do not commute, a problem which we will come across when we attempt to simulate the Ising Hamiltonian. If we can construct  $e^{-i\mathbf{G}_1t}$  and  $e^{-i\mathbf{G}_2t}$  separately, then we can simulate  $e^{-i\tilde{\mathcal{H}}t}$  through the use of a Trotter expansion for short times.

## D. Qubit Rotations

The Trotter expansion tells us how to combine two simple Hamiltonians into a larger, more complex one. However, we have not yet dealt with the creation of these simpler Hamiltonians. We mentioned in section II A that qubits could be represented as vectors in the Bloch sphere. Similarly, any normalized linear combination of the Pauli matrices can be represented as a vector on the Bloch sphere, as defined in figure 2[3].

Now that we have defined the Pauli matrices geometrically, we want to be able to transform one into another, e.g. by a rotation. If we consider the time-evolution operator of the operator associated to some Hamiltonian  $\mathbf{S}$  that is a normalized linear combination of Pauli matrices, we can write[1]

$$e^{-i\mathbf{S}t} = e^{-i\mathbf{A}\theta/2} e^{-i\mathbf{Z}\theta} e^{-i\mathbf{A}\theta/2}, \quad (25)$$

where we have rotated the  $\mathbf{Z}$  Pauli matrix to  $\mathbf{S}$ . In the rotation formula,  $\mathbf{A}$  is a normalized linear combination of Pauli matrices that indicates the axis of rotation in the Bloch sphere, and  $\theta$  is the angle of rotation about that axis.

Note that the angle is divided by two because we are dealing with spin one-half particles. In practice, this relation is approximate, rather than exact, because of the physical origin of the rotation pulses. In an experiment, each exponential rotation term is a magnetic pulse, which takes some amount of time to complete. However, we take this pulse time to be much less than  $t$ , the evolution time of the Hamiltonian, so we neglect its time component altogether.

This rotation concept is rather abstract, so let us consider a simple example. Suppose we start with some Hamiltonian  $\mathcal{H} = \mathbf{Z}$ . If we want to rotate it such that  $\tilde{\mathcal{H}} = -\mathbf{Z}$ , as shown in figure 3, we can construct a rotation of  $\pi$  about  $\mathbf{Y}$ . This is

$$e^{-i\mathbf{Z}t} = e^{-i\mathbf{Y}\pi/2} e^{-i\mathbf{Z}t} e^{-i\mathbf{Y}\pi/2}. \quad (26)$$

In an experiment, we would apply a pulsed magnetic field in the  $\hat{y}$  direction such that its intensity times its duration equals  $\pi$  (this is called a  $\pi$  pulse), then allow the natural Hamiltonian  $\mathbf{Z}$  to evolve for a time  $t$ . Next, we would invert our original pulse, and we would be left with the same result as if the Hamiltonian  $-\mathbf{Z}$  had evolved for a time  $t$ . These pulses are good to use for simulations, since they are easy to execute in a practical experiment. In an experimental NMR setup, the pulses are just electrical impulses in appropriately oriented coils. These impulses generate bursts of magnetic field that cause the desired rotation.

## E. Example of a Simple Simulation

Before we delve into simulating the actual Ising chain, let's try an easier problem first to cement some of the methodology we covered above. Suppose we let  $\mathcal{H} = \mathbf{Z}$  and we want to simulate  $\tilde{\mathcal{H}} = \mathbf{I}$ , the identity operator. We start with

$$|\Psi(t)\rangle = e^{-i\mathbf{Z}t} |\psi\rangle, \quad (27)$$

and we want to have

$$|\tilde{\Psi}(t)\rangle = |\psi\rangle, \quad (28)$$

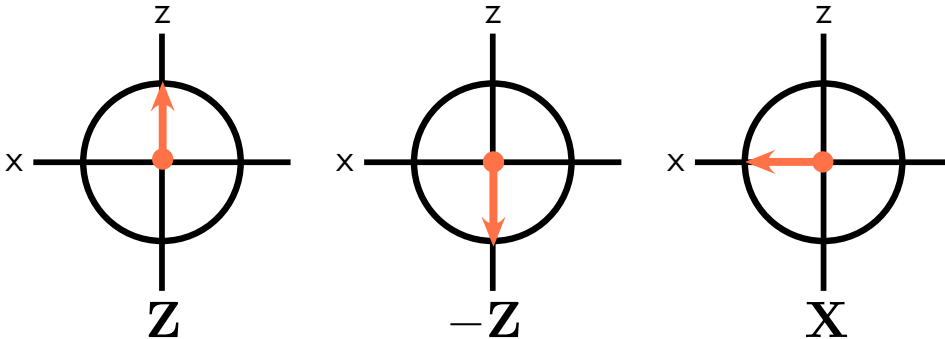


Figure 2: The quantum gates  $\mathbf{Z}$ ,  $-\mathbf{Z}$ , and  $\mathbf{X}$  correspond to vectors  $\hat{z}$ ,  $-\hat{z}$ , and  $\hat{x}$  on the Bloch sphere.

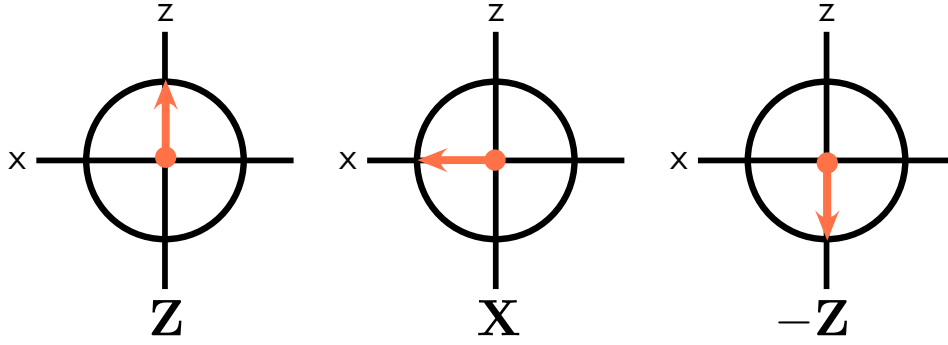


Figure 3: A quantum gate is rotated through an angle  $\pi$ .

a static system. We can write

$$\left| \tilde{\Psi}(t) \right\rangle = e^0 |\psi\rangle = e^{i(\mathbf{Z}-\mathbf{Z})t} |\psi\rangle = e^{-i(-\mathbf{Z})t/2} e^{-i\mathbf{Z}t/2} |\psi\rangle. \quad (29)$$

But, we know the rotation to move  $\mathbf{Z}$  to  $-\mathbf{Z}$ . This is

$$e^{-i\mathbf{Z}t} = e^{-i\mathbf{Y}\pi/2} e^{-i\mathbf{Z}t} e^{-i\mathbf{Y}\pi/2}, \quad (30)$$

so

$$\left| \tilde{\Psi}(t) \right\rangle = e^{-i(-\mathbf{Z})t/2} e^{-i\mathbf{Z}t/2} |\psi\rangle = e^{-i\mathbf{Y}\pi/2} e^{-i\mathbf{Z}t/2} e^{-i\mathbf{Y}\pi/2} e^{-i\mathbf{Z}t/2} |\psi\rangle. \quad (31)$$

In practice, this translates to:

1. Allow the system to evolve naturally for a time  $t/2$ .
2. Execute a  $\pi$  pulse about the  $\hat{y}$  axis.
3. Allow the system to evolve a time  $t/2$ .
4. Execute a  $-\pi$  pulse about the  $\hat{y}$  axis.

Experimentally, in NMR, the pulses take the form of magnetic field generated from a wire in the  $\hat{y}$ .

## V. ALGORITHM IMPLEMENTATION

### A. Goal for Simulating the Ising Chain

The goal of our simulation is to simulate the Hamiltonian of the quantum Ising chain on an NMR quantum computer. The particular molecule we will be using is crotonic acid, drawn schematically in figure 4 with physical parameters defined in table II. The Hamiltonian of the NMR machine is approximately[6]

$$\mathcal{H} = \sum_{i \neq j}^7 J_{ij} \mathbf{Z}_i \mathbf{Z}_j + \sum_i^7 \omega_i \mathbf{Z}_i, \quad (32)$$

which is identical to the Ising hamiltonian in eq. 12 except for the  $\mathbf{Z}$  Pauli matrix in the field term rather than the  $\mathbf{X}$  Pauli matrix and the spin-dependence of the magnetic field coupling (in NMR, there  $\omega_i$ s are called chemical shifts). We aim to transform the NMR Hamiltonian into the Ising model's Hamiltonian through the clever use of several rotations and Trotter expansions, which are outlined below.

## B. Schematic of the Algorithm

We can form the correct sequence of pulses by carefully sequencing rotations and Trotter expansions logically, rather than temporally, as show in figure 5. This can then be converted into a temporal sequence, shown in figure 6 Note that the algorithm does not eliminate the spin dependence of the chemical shifts in the Zeeman term, as we would have hoped. Rather this spin dependance must be taken care of by viewing each spin in a distinct rotating coordinate frame and absorbing this rotation into the applied pulses[7]. The precise working of this coordinate change is left for future work. We will now outline and examine the properties of all of the lettered gates used in our schematic.

Gate A uses the same trick we performed in the example in section IV E. The specific pulse sequence is

$$e^{-i\mathbf{Y}_{all}\pi/2}e^{-i\mathcal{H}t/2}e^{i\mathbf{Y}_{all}\pi/2}e^{-i\mathcal{H}t/2}, \quad (33)$$

where  $Y_{all} = \sum_i \mathbf{Y}_i$ , a rotation on all qubits. Because each qubit is being rotated, the resultant Hamiltonian is

$$\mathcal{H}_1 = \frac{1}{2} \sum_{i \neq j}^7 J_{ij}(-\mathbf{Z}_i)(-\mathbf{Z}_j) - \frac{1}{2} \sum_i^7 \omega_i \mathbf{Z}_i + \frac{1}{2} \sum_{i \neq j}^7 J_{ij} \mathbf{Z}_i \mathbf{Z}_j + \frac{1}{2} \sum_i^7 \omega_i \mathbf{Z}_i = \sum_{i \neq j}^7 J_{ij} \mathbf{Z}_i \mathbf{Z}_j, \quad (34)$$

where we have eliminated the field term.

Gate B is a bit more complex, and requires an approximation. In crotonic acid, we label the the atoms the spin numbers given in figure 4. Now, we note that the strongest interaction coefficients ( $J_{ij}$ s), as indicated in table II, are between nearest neighbor spins. Thus, if we only consider these strong interactions and neglect the distant ones, we construct the B pulse sequence as

$$e^{-i\mathbf{Y}_{246}\pi/2}e^{-i\mathcal{H}_1t}e^{i\mathbf{Y}_{246}\pi/2}e^{-i\mathcal{H}t}, \quad (35)$$

where  $\mathbf{Y}_{246}$  indicates a rotation of  $\pi$  on the second, fourth, and sixth spins. Since exactly one of those spins is present in each strong nearest-neighbor correlation, we write the new Hamiltonian as

$$\mathcal{H}_2 \approx -\mathcal{H}_1 + \mathcal{H} = -\sum_{i \neq j}^7 J_{ij} \mathbf{Z}_i \mathbf{Z}_j + \sum_{i \neq j}^7 J_{ij} \mathbf{Z}_i \mathbf{Z}_j + \sum_i^7 \omega_i \mathbf{Z}_i = \sum_i^7 \omega_i \mathbf{Z}_i. \quad (36)$$

Now that we have eliminated the interaction term, we are free to rotate  $\mathbf{Z}$  to  $\mathbf{X}$ . This is done by gate C with a pulse sequence of

$$e^{-i\mathbf{Y}_{all}\pi/4}e^{-i\mathcal{H}_2t}e^{i\mathbf{Y}_{all}\pi/4}, \quad (37)$$

where we have rotated all the spins by  $\pi/2$ . Thus, our resultant Hamiltonian is

$$\mathcal{H}_3 = \sum_i^7 \omega_i \mathbf{X}_i. \quad (38)$$

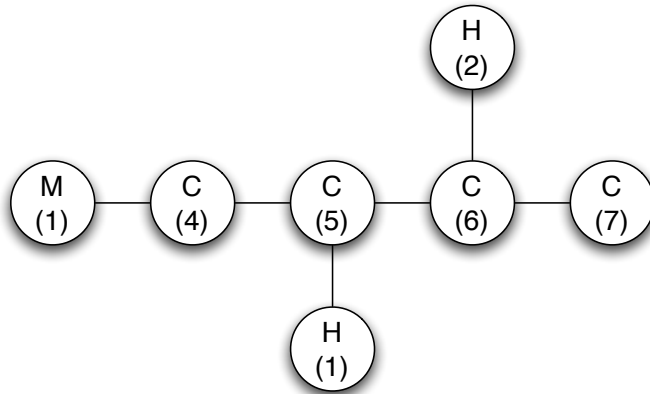


Figure 4: The crotonic acid molecule. It consists of a four carbon chain with two hydrogens and a methyl group.

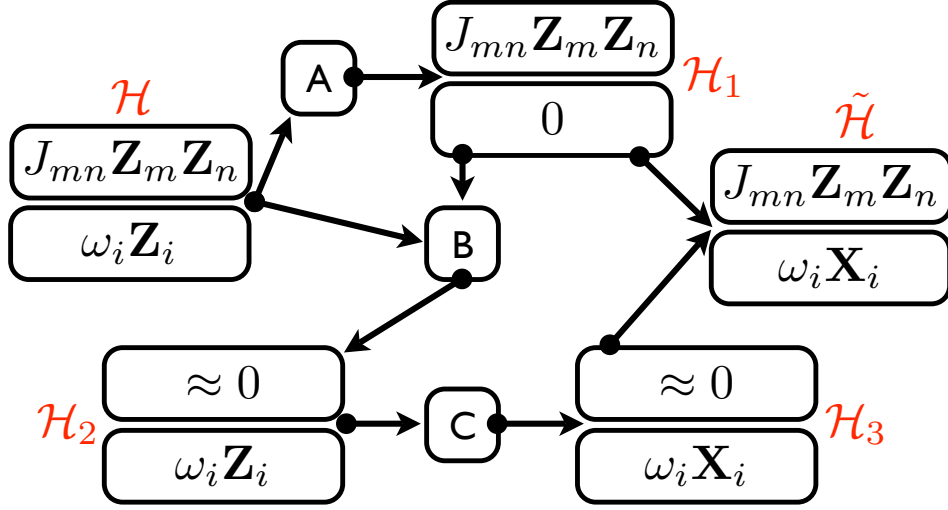


Figure 5: Logical schematic of the algorithm. The rotations are denoted by lettered gates, which are addressed in section V B. The two cells of each node are representative of the interaction term (top) and the field term (bottom) of the Hamiltonian as it undergoes rotations and combinations.

Next, we form a Trotter expansion for the total Ising Hamiltonian. This has the form

$$\begin{aligned}
e^{-i\tilde{\mathcal{H}}t} &\approx e^{-i\mathcal{H}_1t}e^{-i\mathcal{H}_3t}, \\
&= e^{-i\mathbf{Y}_{all}\pi/2}e^{-i\mathcal{H}t/2}e^{i\mathbf{Y}_{all}\pi/2}e^{-i\mathcal{H}t/2}e^{-i\mathbf{Y}_{all}\pi/4}e^{-i\mathcal{H}_2t}e^{i\mathbf{Y}_{all}\pi/4} \\
&= e^{-i\mathbf{Y}_{all}\pi/2}e^{-i\mathcal{H}t/2}e^{i\mathbf{Y}_{all}\pi/2}e^{-i\mathcal{H}t/2}e^{-i\mathbf{Y}_{all}\pi/4}e^{-i\mathbf{Y}_{246}\pi/2}e^{-i\mathcal{H}_1t}e^{i\mathbf{Y}_{246}\pi/2}e^{-i\mathcal{H}t}e^{i\mathbf{Y}_{all}\pi/4} \\
&= e^{-i\mathbf{Y}_{all}\pi/2}e^{-i\mathcal{H}t/2}e^{i\mathbf{Y}_{all}\pi/2}e^{-i\mathcal{H}t/2}e^{-i\mathbf{Y}_{all}\pi/4}e^{-i\mathbf{Y}_{246}\pi/2}e^{-i\mathbf{Y}_{all}\pi/2}e^{-i\mathcal{H}t/2}e^{i\mathbf{Y}_{all}\pi/2}e^{-i\mathcal{H}t/2}e^{i\mathbf{Y}_{246}\pi/2}e^{-i\mathcal{H}t}e^{i\mathbf{Y}_{all}\pi/4},
\end{aligned} \tag{39}$$

which has a total maximum of eight pulses necessary. However, the adjacent pulses could be combined together, giving a sequence of only six pulses. This is an original result and is the main accomplishment of this paper. The remaining sections develop methods for verifying this simulation algorithm experimentally.

## VI. MEASUREMENT AND RESULTS

While the results in the previous sections are certainly mathematically interesting, they would be of little use if they could not be tested with experiment. We will now investigate what could be measured in an experiment so that an experimentalist could verify that the simulated Hamiltonian was indeed the Ising Hamiltonian. In section V, we noted that if we perform a change of coordinates into a rotating reference frame for each spin individually, it is possible to

Table II: The values for interaction and chemical shift terms for crotonic acid. The values for chemical shift ( $\omega_i$ s) are listed on the diagonal, while the other values are interaction terms ( $J_{ij}$ s). Note that the strongest interactions are between nearest neighbors.

|       | M (1)  | H (2)   | H (3)   | C (4)   | C (5)    | C (6)    | C (7)    |
|-------|--------|---------|---------|---------|----------|----------|----------|
| M (1) | -969.4 |         |         |         |          |          |          |
| H (2) | 6.9    | -3560.3 |         |         |          |          |          |
| H (3) | -1.7   | 15.5    | -2938.2 |         |          |          |          |
| C (4) | 127.5  | 3.8     | 6.2     | -2327.0 |          |          |          |
| C (5) | -7.1   | 156.0   | -0.7    | 41.6    | -18599.2 |          |          |
| C (6) | 6.6    | -1.8    | 162.9   | 1.6     | 66.7     | -15412.8 |          |
| C (7) | -0.9   | 6.5     | 3.3     | 7.1     | 1.4      | 72.4     | -21685.1 |

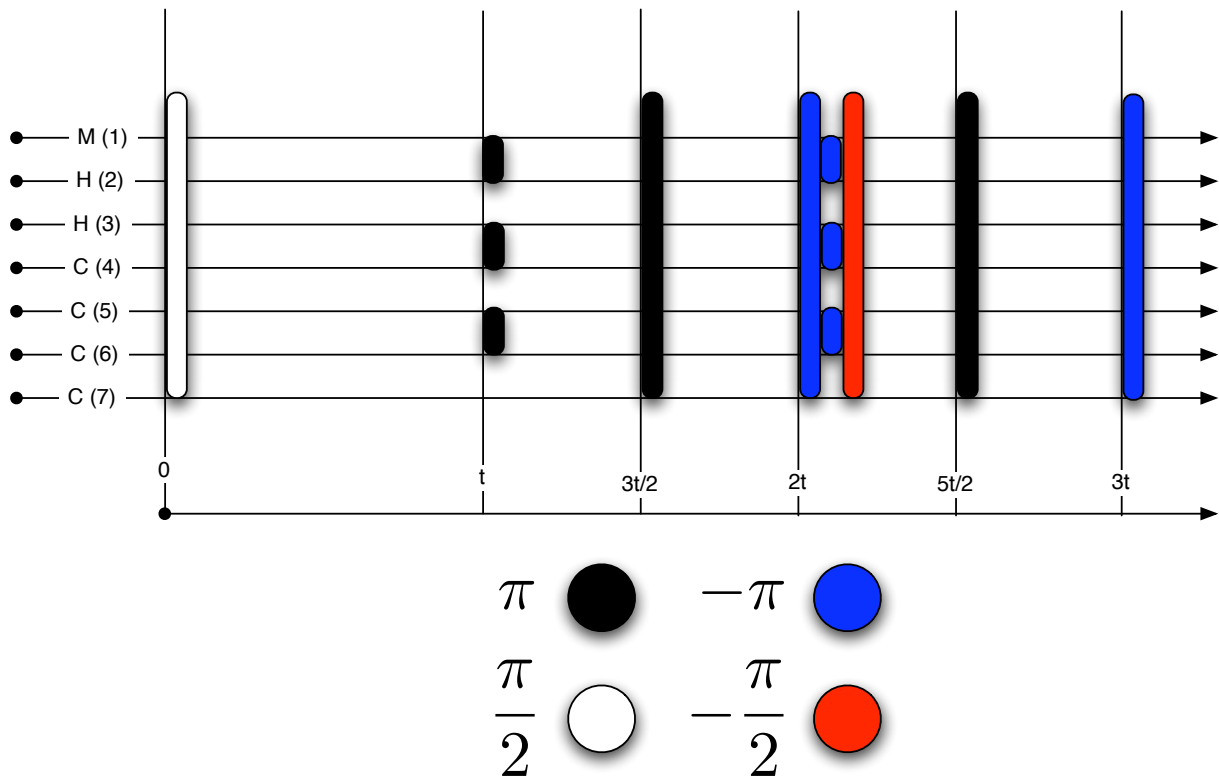


Figure 6: Temporal diagram of the algorithm that runs the Ising Hamiltonian for time  $t$ . Note that running the Ising Hamiltonian for time  $t$  requires  $3t$  of experimental time. Each spin is represented by a labeled line, and time passes from left to right. All rotation pulses are about the  $\hat{y}$  axis.

write

$$\omega_i = g = 50 \forall i, \quad (40)$$

where the precise details of this transformation have been left for future work. For measurement purposes, we assume that this has been applied and that all of the chemical shifts are numerically 50. Further, since the Trotter expansion is valid only for small times, we can play tricks with our pulse sequence. Experimentally, less than 100 pulses is a reasonable number. Since we only have eight in our sequence, we can pulse our whole sequence ten times in a row. This is equivalent to allowing the simulation to run for time  $10t$ , but it will give use much better results.

The most natural test for the simulation is to measure the simulated Hamiltonian's fidelity with respect to the ideal Ising Hamiltonian. That is, we can investigate

$$F(t) = \left| \langle \psi | (e^{-i\mathcal{H}_{ideal}t})^\dagger e^{-i\mathcal{H}_{sim}t} | \psi \rangle \right|^2, \quad (41)$$

or, if we pulse ten times,

$$F(t) = \left| \langle \psi | (e^{-i\mathcal{H}_{ideal}t})^\dagger (e^{-i\mathcal{H}_{sim}t/10})^{10} | \psi \rangle \right|^2, \quad (42)$$

which is shown in figure 7 when  $\langle \psi | = \langle 0000000 |$ . This plot shows that for low times, our simulation performs quite well, as the fidelity is nearly one. As time progresses, the fidelity gets worse, which we expect due to the Trotter expansion we used when making the simulation. However, while this gives us an idea of how good our Hamiltonian is and a reasonable time scale for our simulation, it is not easy to measure experimentally.

To find an experimentally measurable quantity, we looked at the expectation values of correlation functions of the form

$$\langle \mathbf{Z}_i \mathbf{Z}_j \rangle (t) = \langle \psi | e^{i\mathcal{H}t} \mathbf{Z}_i \mathbf{Z}_j e^{-i\mathcal{H}t} | \psi \rangle, \quad (43)$$

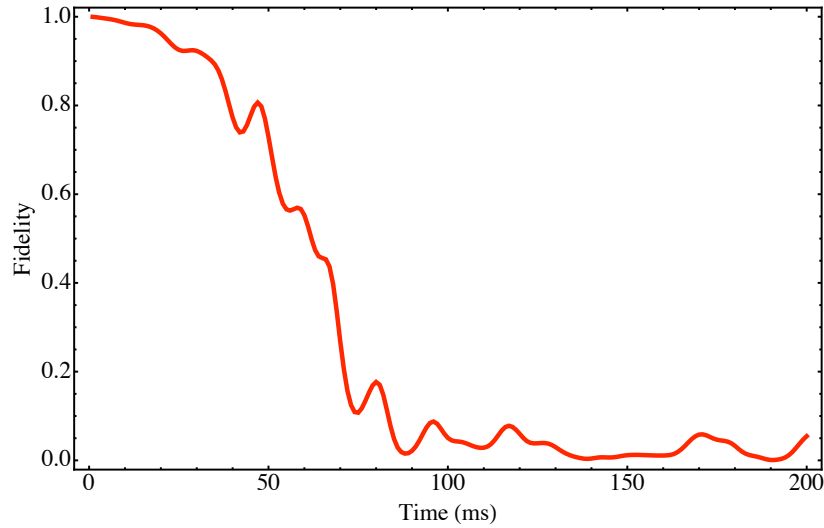


Figure 7: The fidelity over time for a the simulated Ising system with respect to the target Hamiltonian. In this plot, the chain starts with all spins pointed in  $|0\rangle$ . The system is run for a time of 20 ms, and the sequence is pulsed ten times, giving a total time of 200 ms.

which are easy to measure experimentally. The original NMR Hamiltonian had constant expectation value for all interactions, which was

$$\langle \mathbf{Z}_i \mathbf{Z}_j \rangle_{NMR}(t) = 1. \quad (44)$$

The expectation values of the correlation function for the simulated and ideal Ising models showed great promise in being a good experimental tag to verify that the Ising Hamiltonian was being simulated. Examples of the 1-7, 1-4, and 6-7 correlation functions are shown in figures 8, 9, and 10, where we see that the correlation ranges from about 1.0 to less than 0.5, a very large fluctuation. Also, the ideal and simulated curves stay together very well until about 40 ms, as we might expect from the fidelity plot. Because of the large time scales and the large fluctuation compared to the NMR Hamiltonian, this measurement would be an ideal choice for experimental measurement.

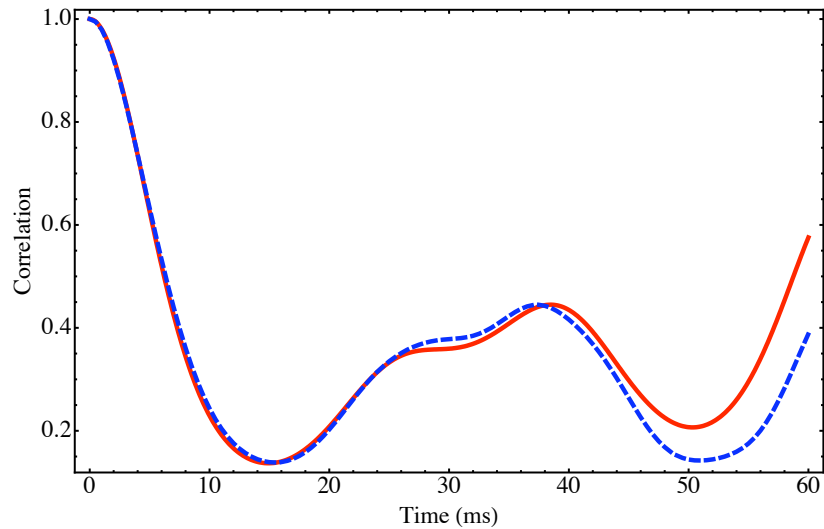


Figure 8: The expectation value of the correlation function  $\langle \mathbf{Z}_1 \mathbf{Z}_2 \rangle(t)$  over time. The target Hamiltonian is indicated by a solid red line, while the Hamiltonian simulated using sequence 39 is a dashed blue line. The system runs for 6 ms, and the pulse sequence is applied 10 times, giving a total time of 60 ms.

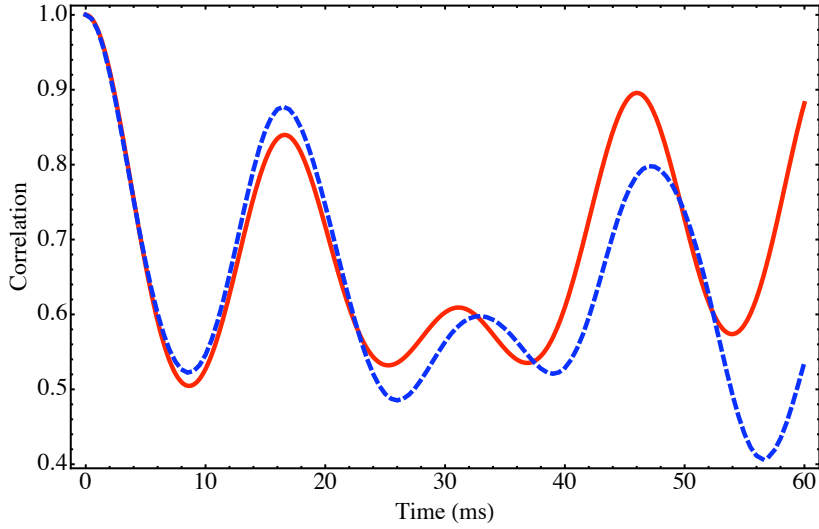


Figure 9: The expectation value of the correlation function  $\langle \mathbf{Z}_1 \mathbf{Z}_4 \rangle(t)$  over time. The target Hamiltonian is indicated by a solid red line, while the Hamiltonian simulated using sequence 39 is a dashed blue line. The system runs for 6 ms, and the pulse sequence is applied 10 times, giving a total time of 60 ms.

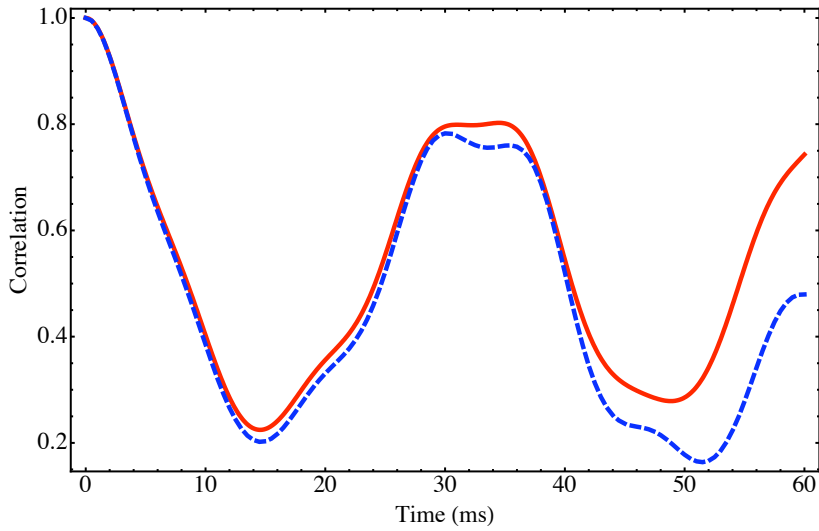


Figure 10: The expectation value of the correlation function  $\langle \mathbf{Z}_6 \mathbf{Z}_7 \rangle(t)$  over time. The target Hamiltonian is indicated by a solid red line, while the Hamiltonian simulated using sequence 39 is a dashed blue line. The system runs for 6 ms, and the pulse sequence is applied 10 times, giving a total time of 60 ms.

## VII. CONCLUSIONS AND FUTURE WORK

Small quantum simulations are practical on today's quantum computers, and are some of the most interesting practical algorithms that can be run on the required small numbers of qubits. We first introduced some of the basic concepts in quantum computing. Then, we analyzed the quantum Ising chain and its Hamiltonian. After that, we worked through the technicalities of performing a quantum simulation in detail.

Next, we proposed an algorithm to simulate the quantum Ising chain on an NMR Hamiltonian, working through the components of this algorithm rigorously. Then, we tested the simulation numerically by examining its fidelity, and found that it stayed close to unity until about 40 ms. We next extended the numerical tests to find a suitable measurement that could be performed experimentally. We found that the correlation functions of the form  $\langle \mathbf{Z}_i \mathbf{Z}_j \rangle(t)$  produced large fluctuations for the Ising model Hamiltonian, while staying constant in the NMR Hamiltonian. Further, the simulated Ising Hamiltonian stayed close to the ideal Hamiltonian for about 40 ms as expected.

Some progress still needs to be made to finish this project. First, the coordinate transformation into rotating frames of reference needs to be worked out precisely. Second, a more realistic simulation, including temperature effects and nonzero time pulses should be included to give an accurate estimate of the noise of the system. After these steps are completed, this work will be proposed to an experimental group for implementation.

### VIII. ACKNOWLEDGMENTS

I would like to thank Fernando Cucchietti for mentoring this project; his guidance was invaluable. I would also like to thank Norm Magee and James Colegan for putting together the Los Alamos Summer School program and helping tremendously with the logistics all summer. Finally, I would like to thank Los Alamos National Laboratory and the National Science Foundation for the funding for this project.

- 
- [1] M. A. Nielsen and I. L. Chuang, *Quantum Computation and Quantum Information* (Cambridge University Press, 2000).
  - [2] MuncherOfSpleens, *Blochsphere.svg* (2006), URL <http://en.wikipedia.org/wiki/Image:Blochsphere.svg>.
  - [3] F. M. Cucchietti, *Quantum computing*, Los Alamos Summer School Public Lecture (2007).
  - [4] H. D. Raedt, A. H. Hams, and K. Michielsen, *Computer Physics Communications* **132**, 1 (2000).
  - [5] S. Sachdev, *Quantum Phase Transitions* (Cambridge University Press, 1999).
  - [6] X. Peng, J. Du, and D. Suter, *Phys. Rev. A* **71** (2005).
  - [7] C. P. Slichter, *Principles of Magnetic Resonance* (Springer, 1990).

# Deriving the Electron Temperature of Short-Lived Plasma

Tiffany Hayes<sup>1,3</sup>  
Hanna Makaruk<sup>2</sup>

<sup>1</sup>T-4/LASS, Los Alamos National Laboratory, Los Alamos, NM  
<sup>2</sup>Mentor: P-22, Los Alamos National Laboratory, Los Alamos, NM  
<sup>3</sup>University of New Mexico, Albuquerque, NM

Plasma makes up 99% of normal matter in the Universe, and most of the matter seen in astrophysics falls into this category. However, properties of plasma are not fully understood, and so experiments are conducted. Plasma produced from inertia confined fusion (ICF) stays together for nanoseconds. Due to the shortness of the process a normal spectrometer is unable to be used. Instead, images are taken every four picoseconds using a special camera. This paper will present the image analysis methods used to derive the temperature.

## 1. Introduction

A question arose during the last couple of years: how well do we understand the physics of plasma? Plasma is a gas of free electrons and ions, but this does not directly mean that the gas is very hot or very dense. Plasma actually spans a range of physical properties. Plasma can have a density as low as  $10^{-4} \text{ cm}^{-3}$ , and as high as  $10^{30} \text{ cm}^{-3}$ , with temperatures varying from around zero Kelvin to temperatures into the millions of Kelvin. It also conducts electric fields, and creates magnetic fields. What makes plasma so important is that it makes up 99% of normal matter in the Universe. The material seen when looking around the Earth is considered normal matter, and it was only recently that plasma was made a “fourth” state. It is very new ground, and so the physics is also new. However, there are already many potential uses, one of the most important being a clean, efficient energy source.

The center of the Sun has a mass density of  $150 \text{ g/cm}^3$ , and a temperature around 15 million Kelvin [1]. It expels energy in the form of light at a rate of  $3.8 \cdot 10^{26}$  joules every second [1]. The fuel source of this energy is fusion, in the form of hydrogen fusing into helium, or more exactly, deuterium and tritium fusing into helium. The Sun is a large, gravitationally confined plasma and fusion center, though confining plasma and fusion is a very difficult process that still eludes us. Today, people are looking to confine fusion to create a new energy source that would be more efficient than fossil fuels. One gram of deuterium and tritium burned by fusion would be equivalent to burning 8.4 tons of oil [2]. However, fusion is not easily contained.

Three methods of confinement are known: gravitational confinement, magnetic confinement, and inertial confinement. Gravitational confinement as seen in stars is proven to work, but this method is impractical for human use. The size of the container must be on order of magnitude with the Sun, and so physicists started to look towards magnetic confinement

fusion. This method has been studied since the 1950's, and is still studied today. Magnetic confinement uses magnetic fields to contain plasma and fusion. The method could theoretically keep plasma confined indefinitely [2], however building and maintaining the magnetic field creates difficulties. The method has made progress since it was first started in the 1950's, but it is still not complete.

The third method was not studied until several years later. Inertial confinement fusion (ICF) uses the inertia of mass to confine plasma long enough for fusion to occur. During the process of ICF, a spherical shell of gas is shot with a laser. The laser destroys most of the shell, which expands outwards. Due to conservation of momentum, the inside material collapses in on itself. The heat from the laser on the outside and the compression of the gas at the center turns the gas into plasma and sparks fusion. This method has been tested with the OMEGA laser at Rochester University in New York. This laser shoots 40,000 joules of energy onto a 1 mm sphere, which then collapses to 50 microns. The density in the center is currently around  $10 \text{ g/cm}^3$ , and is around  $10^7$  Kelvin, while the confinement time is around one nanosecond. Currently, this process is not efficient enough for to be used as an energy source and a new laser is currently being constructed at the National Ignition Facility (NIF). The NIF laser will shoot pulses that are 1.8 million joules at a 1 mm target.

## 2. The Experiment

With the construction of the NIF laser, the opening question has returned: how well do we understand the physics that is occurring during the implosion? In order to test their understanding, physicists have created an experiment to check their models via computer simulations. There is very little deviation from the normal experiment. However, the capsule has an added amount of krypton, argon or xenon. These contaminants were chosen because it requires more energy than average to remove all of their electrons. This means that when the rest of the gas is ionized, these atoms will retain some of their electrons which may then jump up and down levels, and produce spectra lines.

Instruments are set up to analyze the process, which occurs within a hundred picoseconds. This fast process makes it difficult to observe parameters, and in some cases, the normal means cannot be used. This paper will describe the process of discerning the electron temperature of the plasma throughout the process. Normally, a spectrometer would be used to analyze the temperature of the plasma. However, due to how quickly the process ensues, that is not possible. Using a streak camera, images are taken every four picoseconds throughout the process, and using these images, we developed a method for measuring the electron temperature from the continuous spectrum.

## 3. Data Processing

A sample image is shown on the left in figure one. The image obtained from a streak camera is not in terms of space coordinates, but time is on the horizontal axis, and increasing photon energy is on the vertical one. There are also several features to be noticed. One, there is a continuous spectrum running through from top to bottom of the image. This spectrum is caused by the free electrons. On top of this spectrum are two spectra lines from the contaminate, in this case krypton. Third, there is an artifact that was produced by the camera.

The first step in the process is to cut the image down to keep as many of the spectra lines, and as much of the background as possible while eliminating any artifacts that are present.

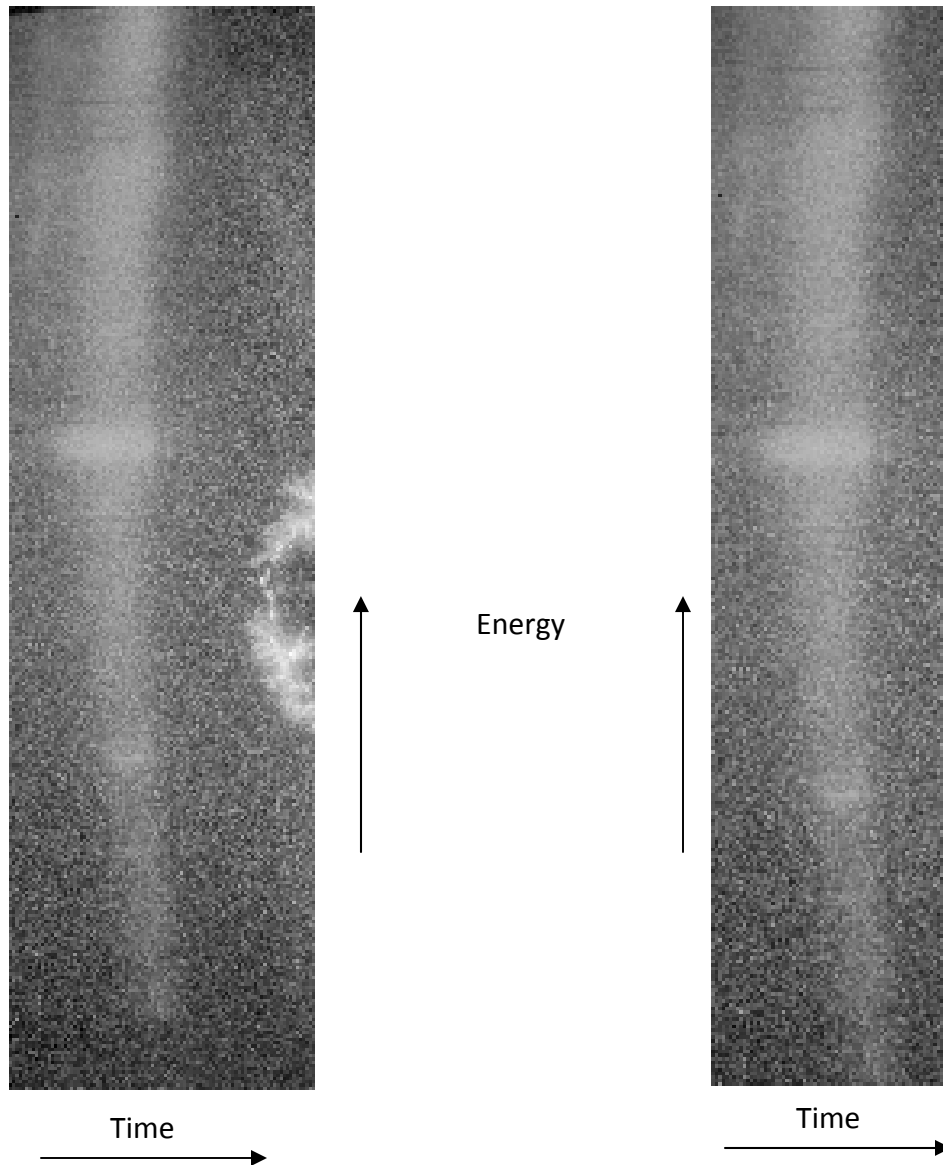


Figure 1: The figure on the left is the original image taken from the camera, while the image on the right is the image after it has been trimmed to cut out any artifacts or areas that do not have part of the spectrum.

Using Mathematica and its image processing package, we view each image and correct it as follows. As can be seen in the figure above, there is an obvious curvature of the spectrum line. This curvature is caused by the imperfections of the camera lense, and must be removed. This is actually a relatively easy process. A line is fitted through the center of the spectrum line. This gives a measurement of the curvature. From there, it is easy to subtract this curvature, and leave a straight spectrum line, as seen in figure two.

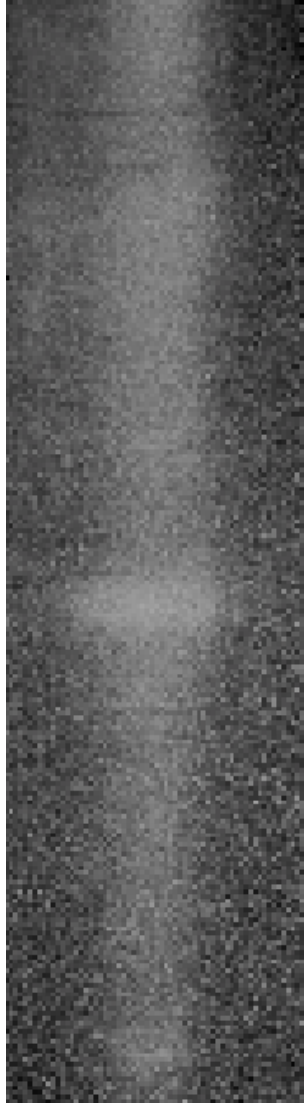


Figure 2: Sample of an image after the curvature has been removed.

Generally, the next step would be to subtract the background to remove any fluctuations. All of the fluctuations in these images are caused by the experiment, and not from the image processing techniques. Fluctuations occur for at least three different reasons. The first is from the laser pulse that is fired at the beginning of the process. The second is caused by the implosion itself: fusion and heat occur, and the hotter areas tend to be brighter than others. And last, from the electrical discharges from the camera, which show up as artifacts. It has been vigorously attempted to remove the background from the images, but it consistently ruins the images, and gives data that is incomprehensible. In general, this step is skipped.

Instead, the next step is to change the scale of the image. Remember that the images are energy vs. time. However, we need to know how much energy there is per pixel (we know how much time there is per pixel). The spectra lines help to find a pixel-to-wavelength ratio that is assumed to be constant from image to image. This would only be incorrect if the camera were moved from image to image, or a different camera were used. In general, the ratio is

found whenever possible, and has proved to be constant. Figure three helps demonstrate how the pixel-to-wavelength ratio is calculated.

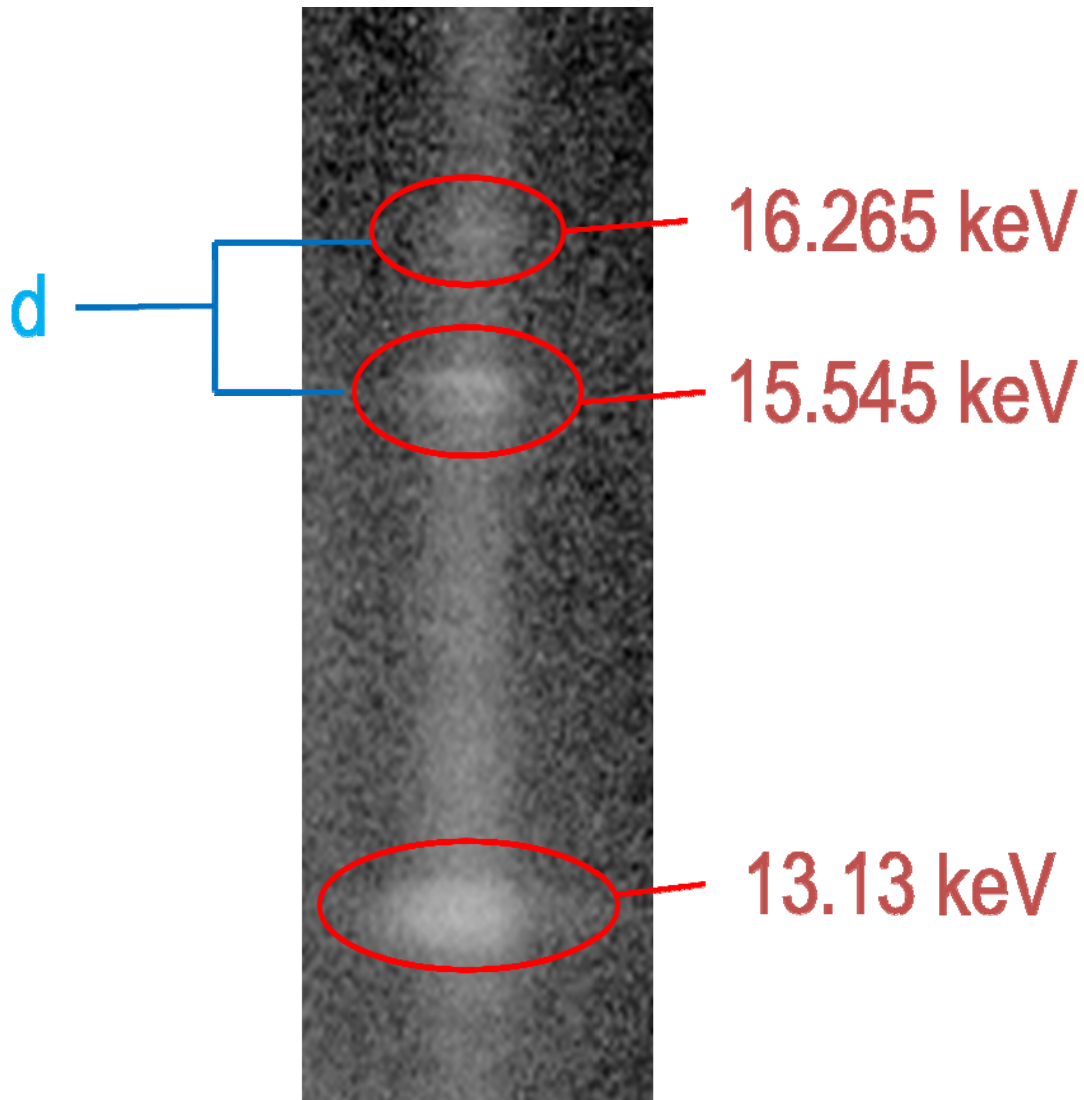


Figure 3: The three spectrum lines are used to determine the pixel-wavelength ratio. The energy of the three lines is known, and is easily converted to wavelength.

Generally, only one spectrum line appears over the continuous spectrum. These lines only occur when the plasma reaches a sufficiently high temperature. On rare occasions two spectra lines occur, and on even rarer occasions, the third spectra line is visible. It is known that these lines occur from the krypton, and the energy of the three spectra lines is known, and shown above. The energy is easily calculated into wavelength, and then the distance in pixels is taken between two wavelengths. An average of the pixel-to-wavelength scale is taken, and this average is used to change the image scale to wavelength.

Figure four shows the next correction. This figure shows the response function of the camera. A response function is place dependent measurement. It shows how an individual area reacts, in this case to energy. That is to say, in the case of a CCD camera, the response function would show how each individual chip on the CCD camera reacts to receiving a photon of different energy. This is a theoretical measurement, though it can be determined from images as well. The response function of our camera was derived from information provided by the camera company. Once the function is determined, the inverse of that is applied to the image.

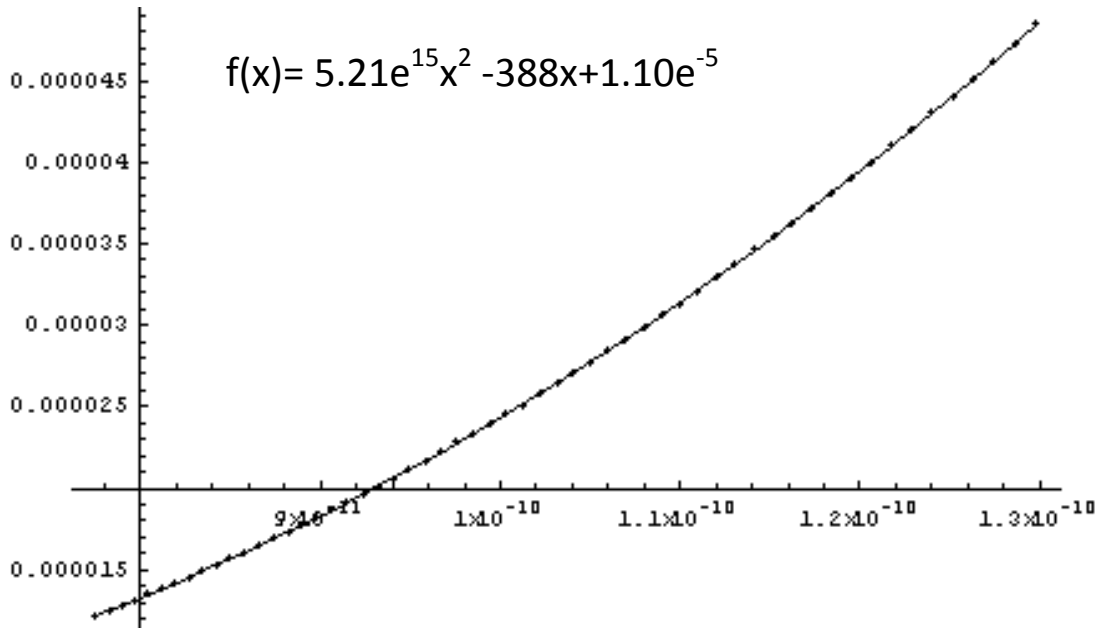


Figure 4: The response function of the camera. This is a theoretical prediction that was calculated using data from the camera company.

Up until now everything has been a step in correcting the image. We now have a corrected image, and are ready to calculate the temperature. In order to do this, we start with a few simple calculations. First, we define a few parameters,  $J$ ,  $x$ ,  $y$ ,  $r$ , and  $A$ ,  $a$ ,  $b$ .

$$\begin{aligned}
 J(\lambda,t) &= \text{original intensity} \\
 x(\lambda,t) &= \text{measured intensity} \\
 y(\lambda,t) &= \text{intensity from image} \\
 R(\lambda) &= \text{Response function} + \text{calibration} \\
 A_i, a, b &= \text{constants}
 \end{aligned}$$

Then we write the following definition. The original intensity is equal to the measured intensity divided by the response function of the camera. We take this definition, and for reasons that will be shown later, we take the natural log of, and we are left with the following equations.

$$J(\lambda) = \frac{x(\lambda)}{R(\lambda)} \longrightarrow \ln(x) = \ln(J) + \ln(R) \quad (1), (2)$$

Next, we define the intensity of the image as follows:

$$y = a[b + \ln(x)] \longrightarrow \ln(x) = \frac{y}{a} - b \quad (3), (4)$$

Combining the equations (2) and (4), we are left with the following expression:

$$\frac{y}{a} - b = \ln(J) + \ln(R) \longrightarrow \ln(J) = \frac{y}{a} - b - \ln(R) \quad (5), (6)$$

We step away from the top equation, and go back to a theoretical prediction of the original intensity as a function of wavelength and temperature. The Boltzmann equation states that:

$$J(\lambda) = A_o e^{\frac{-hc}{\lambda kT}} \quad (7)$$

which reduces to:

$$\ln(J) = A_1 - \frac{hc}{\lambda kT} \quad (8)$$

Now we can combine equation (6) with equation (8), and we find the following:

$$\frac{y}{a} - b - \ln(R) = A_1 - \frac{hc}{\lambda kT} \quad (9)$$

It is found that the response function, R, has a variation that is less than .5%, and therefore we can consider it a constant. Combining all of the constants, we find that:

$$y(\lambda) = A_2 - \frac{A_3}{\lambda T} \quad (10)$$

Using a corrected image, we fit a line through the spectrum that has the same form as equation (10), where  $\lambda$  is changing, and T becomes part of the coefficient. We know all of the constants in the coefficient of lambda, except for T. It is trivial to extract those from the coefficient. Figure five shows the exact equation plotted versus the intensity and wavelength extracted from the image. As can be seen, the curve fits the data rather well. Figure six shows a plot of the temperature.

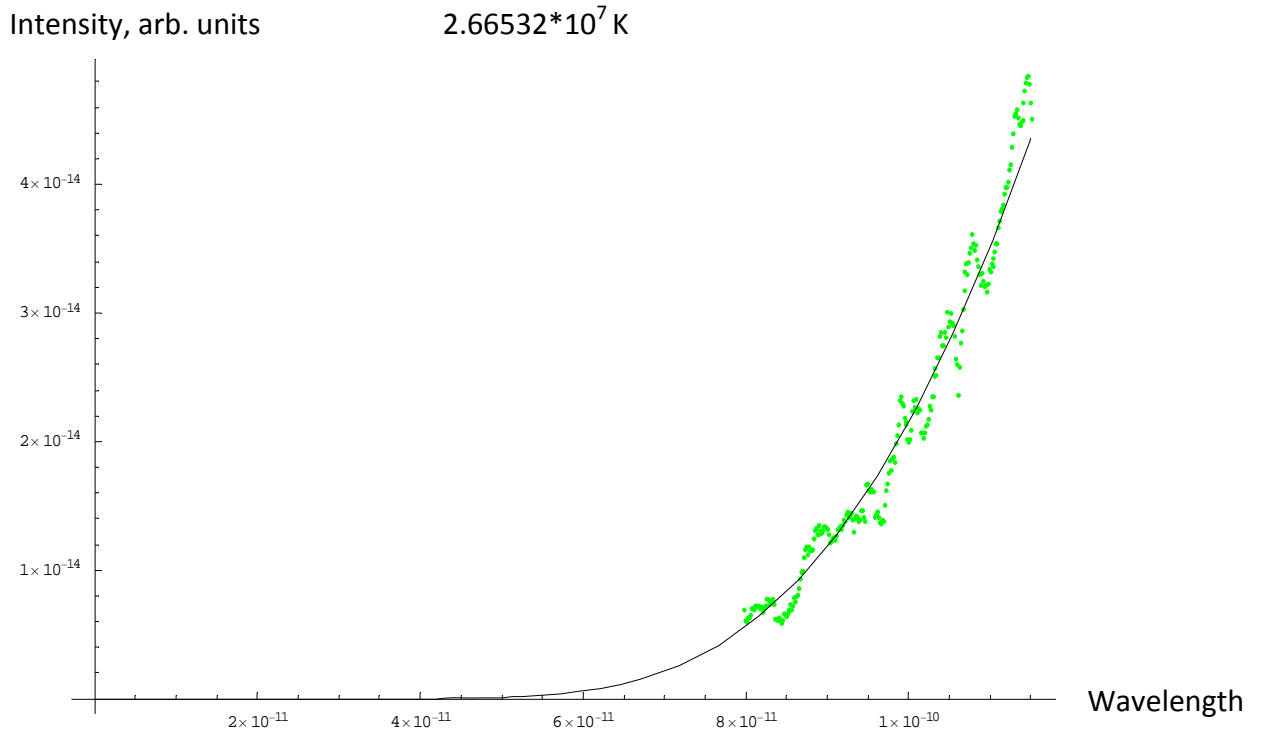


Figure 5: This graph shows the fitted equation for a particular image, and the actual data plotted against that function. As can be seen, the fitted function matches the data.

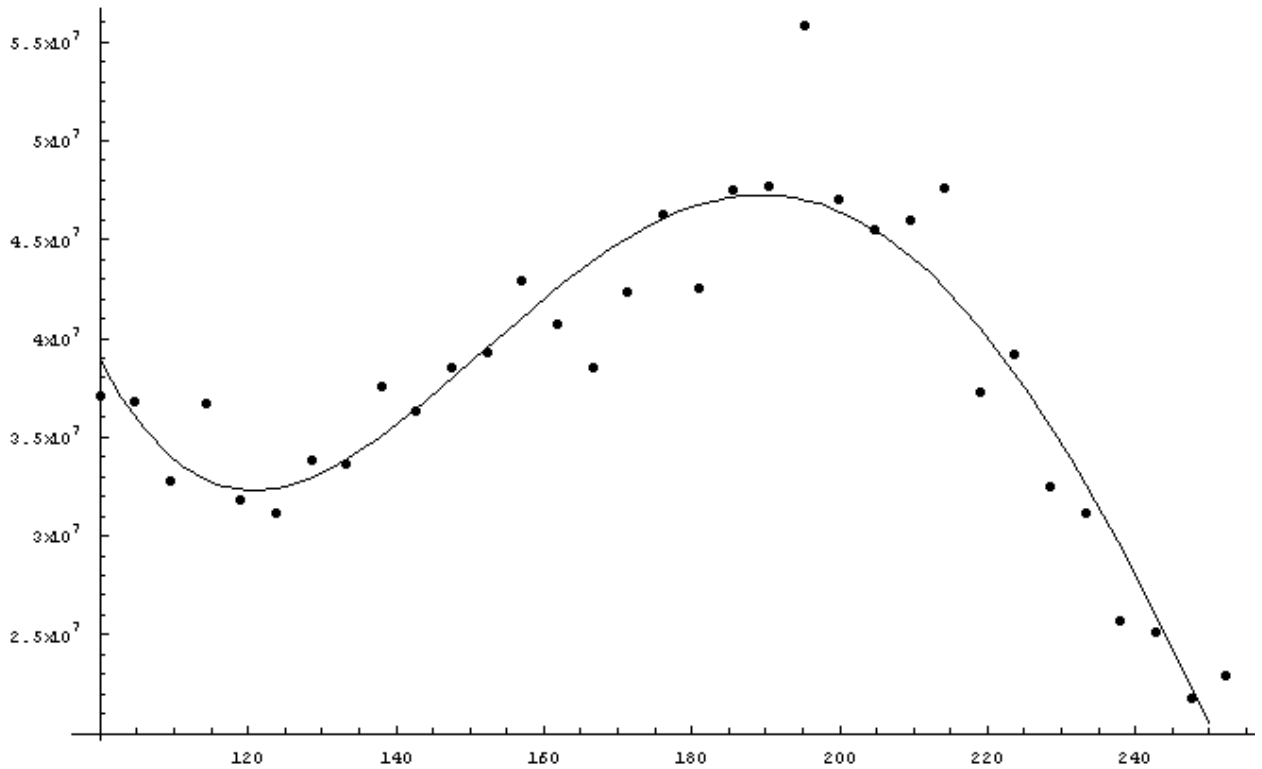


Figure 6: This image is the temperature in Kelvin plotted against the time in picoseconds. As can be seen, the peak temperature is around  $10^7$  Kelvin

## 4. Conclusion

The electron temperature of all of the images has been in the range of orders of magnitudes  $10^7$  -  $10^8$  Kelvin. This measurement is in agreement with temperature that was theoretically expected and temperature which for some images was measured from the appearance of spectral lines.

## Acknowledgments

I, Tiffany Hayes, would like to thank John Benage who provided background information and insight into the usefulness of this project. Also, thanks to LASS, and Norm Magee, who did not mind rescuing stranded students, and James Colgan for organizing our program.

## Bibliography

- [1] Carroll, B., Ostlie, D., *An Introduction to Modern Astrophysics*. (Pearson Addison Wesley, New York, 2007)
- [2] Colombo, U., and Farinelli, U., *Annu. Rev. Energy Environ.* **17**, 123-159, (1992)
- [3] Dharma-wardana, M.W.C., Perrot, Francois, *Physical Review E*, **58**, 3, (1998)
- [4] Gericke, D.O., Murillo, M. S., Schlanges, M., *Laser and Particle Beams*, **20**, 543-545, (2002)
- [5] Gericke, D.O., Murillo, M. S., Schlanges, M., *Physical Review E*. **65**, (2002)
- [6] Hazak, G., *et al*, *Physical Review E*, **64** (2001)
- [7] Lindl, John D., *Inertia Confinement Fusion*. (Springer-Verlag, New York, 1998)
- [8] Keefe, Denis, *Ann. Rev. Nucl. Part. Sci.*, **32**, 391-441, (1982)

# Complex Networks and Scientific Ideas: The Road to Revolution

M. Herrera<sup>1,2,\*</sup>, D. Roberts<sup>2</sup>, and N. Gulbahce<sup>2</sup>

(1) *Department of Physics, University of Missouri–Rolla, Rolla, MO 65409 and*

(2) *Center for Nonlinear Studies, Los Alamos National Laboratory, Los Alamos, NM 87545*

(Dated: August 10, 2007)

Network theory has allowed for the study of many complex systems in computer science, physics, and even biology; e.g. the Internet, protein-protein interaction and social relationships. The goal of this project is to apply the well developed analytical tools of network theory, such as degree distribution and community finding, to a network of scientific ideas. Some ideas are expected to form communities of distinct fields, such as solid state physics, information theory, or quantum mechanics. By building and analyzing data on these idea networks, this project aims to gain insight into the topology of scientific ideas, how they relate to each other, and how they may merge to form new, independent subfields

## Introduction

From time to time, different fields in science come together in a scientific revolution. An illustrative example is the merger of quantum mechanics and information theory into quantum information in the 1980s. Two networks of scientific ideas were built, where data had been gathered from two scientific paper databases: The American Physical Society, and the Inspec Database. Both networks were classified according to their degree distributions, as well as their average clustering coefficient. In addition, we extracted various communities and fields from the networks and analyzed how various disciplines in physics relate to each other.

## Background

It is important to introduce the terminology of network theory before considering an idea network.

- A **node** is an individual agent in a network. For example, if one considers a social network, individual nodes can be made to represent persons.
- **Edges** are links or connections between two nodes. Edges can be assigned weights in a network, which characterize how strongly connected two nodes are. For example, if again we consider a social network, persons A and B can have an edge between them if they are acquaintances, and the weight associated with the edge could represent the amount of time A and B have known each other.
- The **degree ( $k$ )** is simply the number of edges a node has. Thus, the higher the degree of a node, the more connected it is to other nodes in the network. The weights of an edge can also contribute to the overall degree of a node: i.e. if a node has two edges, both with weight four, then the total degree for that node is eight.

Other terminology will be defined as needed. In many networks, edges can also have a direction, a starting node and an end node. This is useful in studies where a directional flow of information is being considered. For this study, all edges are not directed, and there are no self-loops (edges that begin and end on the same node).

## Building the Network

Data was collected from two sources: The American Physical Society (APS) and the Inspec Database. Papers in the APS Database are classified by their *authors* according to the Physics and Astronomy Classification System (PACS) and are assigned a set of PACS numbers. PACS numbers represent the main topics associated with a paper, such as Brownian motion or quantum computing. A network of scientific ideas can be constructed where the nodes of the network are the individual PACS numbers. An edge between two PACS numbers can be said to exist if those two PACS numbers appear in the same paper. Further, the edges are weighted by the number of times a pairing of two PACS numbers occurs in the database. The Inspec Database is a broader collection of scientific papers on physics, electrical engineering, and computing. Inspec papers are reviewed externally by *expert reviewers* and are assigned INSPEC classifications. It is important to note the difference in assigning classification between APS and Inspec: in

one database authors assign classifications, in the other classifications are assigned via external reviewers. Much like PACS numbers, these classification codes characterize the main ideas of a paper. Again, individual classification codes can be mapped onto nodes of a network, and an edge exists if two classification codes appear in the same paper. Like before, weights of edges are determined by the number frequency of pairing between two classification codes. Table I presents node and edge information on both idea networks. Like any data, some noise is present in the network data. These small irregularities stem from imperfections in the databases, such as mis-transcribed classification codes, or irregular data formatting. An attempt was made to find and correct these irregularities as to minimize the impact on the overall network.

|       |        |         |
|-------|--------|---------|
|       | APS    | Inspec  |
| Nodes | 4737   | 3492    |
| Edges | 187370 | 1315613 |

TABLE I: The number of nodes and edges in both the APS and Inspec networks

### Degree Distributions

Once a network has been built, one can find the degree distribution  $p(k)$ , the probability that a node has degree  $k$ . Another way to represent degree data is the **cumulative degree distribution**  $P(k)$  where

$$P(k) = \sum_{k'=k}^{\infty} p(k')$$

measures the probability of a node having degree  $k$  or higher. The functional form of the cumulative degree distribution allows one to classify the network. For example, networks whose degree distribution follow a power-law are said to be scale free [2]. These networks are often characterized by a number highly connected nodes, called "hubs" [1]. The Barabási-Albert model of a scale free network models network growth by assuming new nodes have a higher probability of forming an edge to already well connected nodes.

The cumulative degree distributions for both the full APS and full Inspec networks were calculated, and are displayed in Figures 1 and 2. Further, one can ignore the weight of the edges and calculate the cumulative degree distributions for both networks. The degree distributions for both networks clearly do not appear to follow scale-free behavior. Rather, the functional form of all the cumulative degree distributions roughly follows an exponential stretched/squeezed distribution:  $f(k) \sim \exp\left[-\left(\frac{k}{\tau}\right)^{\beta}\right]$ . For both full networks,  $\beta \sim 0.5$ . When the weights of the edges are ignored, the parameter  $\beta$  increases in both cases;  $\beta_{APS}$  increases to 0.763, and  $\beta_{Inspec}$  increases to 1.588. Our qualitative argument for the lack of scale-free behavior is as follows. Both databases have a dynamically evolving classification system, that is, new classifications are periodically introduced to account for new fields. More importantly, classification systems attempt to avoid forming hubs by introducing classification codes that are related to the forming hub. This ensure that the classifications assigned are specific enough to be useful. Thus, both processes lower the connectivity of forming hubs, disallowing scale free behavior.

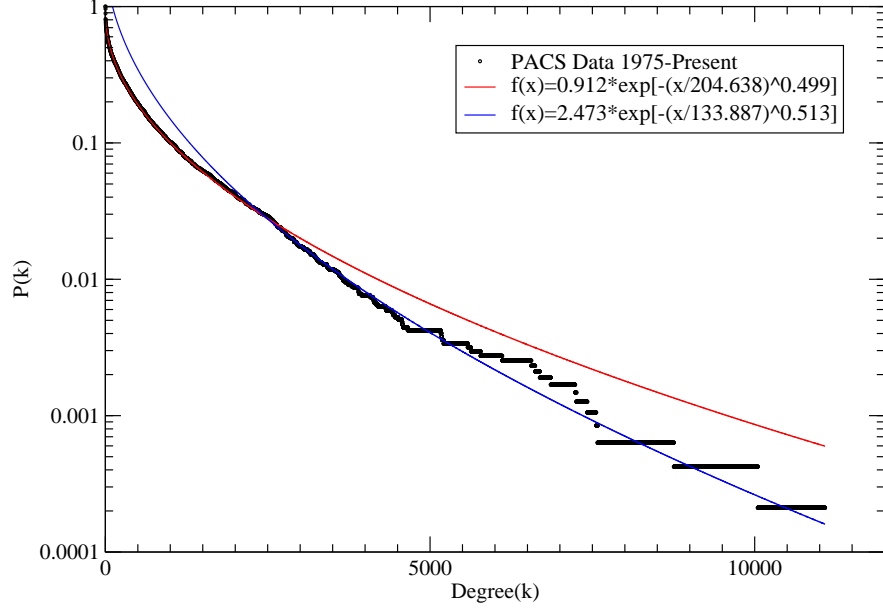
### Clustering

Consider three nodes in a network: A, B, and C. If an edge exist between A and B, and another edge exist between B and C, then in many networks there is a higher probability that an edge between A and C will exist. This measure can be quantified by the clustering coefficient  $C_j$  where

$$C_j = \frac{\text{number of triangles containing node } j}{\text{number of triples centered on node } j}$$

One can calculate  $C(k)$ , the average clustering coefficient for all nodes of degree ( $k$ ).  $C(k)$  allows one to study the degree of hierarchy in the network. A hierarchical structure occurs when there is a regularly iterated pattern in the network. If a network has no hierarchical structure, then  $C(k)$  should have no degree dependence. At the opposite end of the spectrum, if a network is purely hierarchical, then  $C(k) \sim k^{-1}$  [1]. The average clustering per degree

### PACS 1975-Present Cumulative Degree Distribution



### PACS Data 1975-Present Cumulative Degree Distribution (Collapsed Edges)

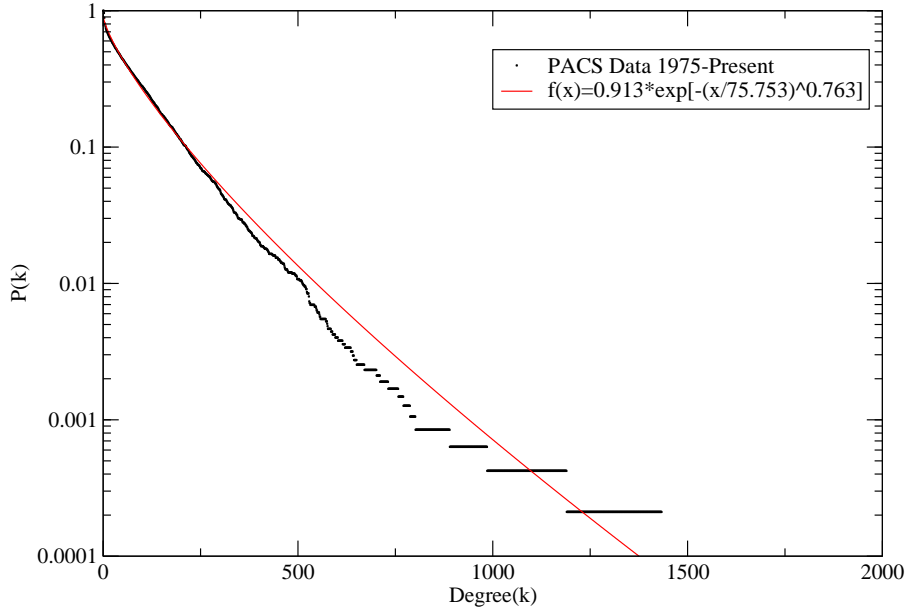
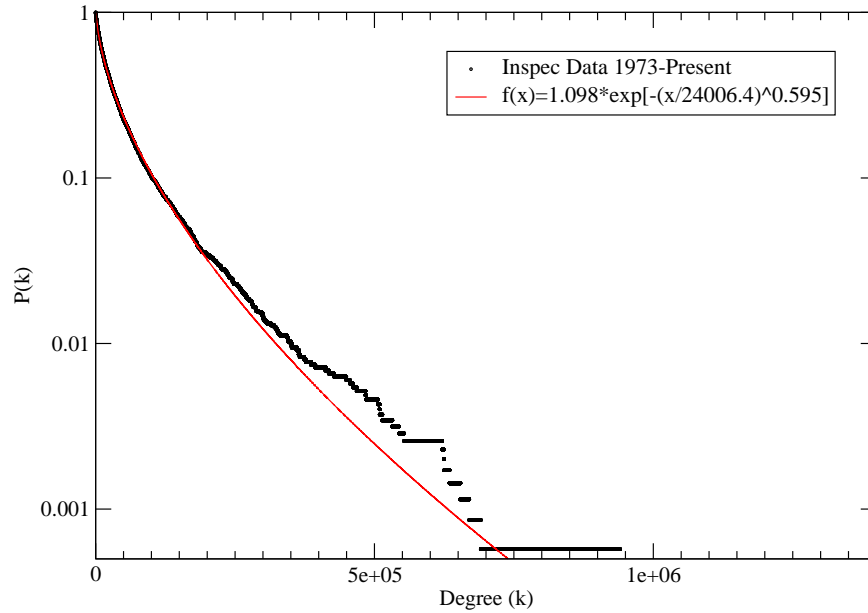


FIG. 1: Cumulative degree distributions  $P(k)$  of the APS network for both full degree, as well as collapsed edges (ignoring weights). The colored lines are fits to the data. Both cases do not exhibit scale-free behavior.

was calculated for both APS and Inspec networks, and results are shown in Figure 3. In both cases, the clustering coefficient demonstrates some degree dependence. Fitting both to a power-law functional form,  $f(x) \sim k^{-\alpha}$ , we find  $\alpha_{APS} = 0.279$  and  $\alpha_{Inspec} = 0.182$ . While,  $\alpha < 1$ , demonstrating that the networks are not purely hierarchical, there is still some hierarchical structure apparent in the network, which is consistent with intuition given the inherent hierarchical structure of the classification systems.

## Inspec 1973-Present Cumulative Degree Distribution



## Inspec Data 1973-Present Cumulative Degree Distribution (Collapsed Edges)

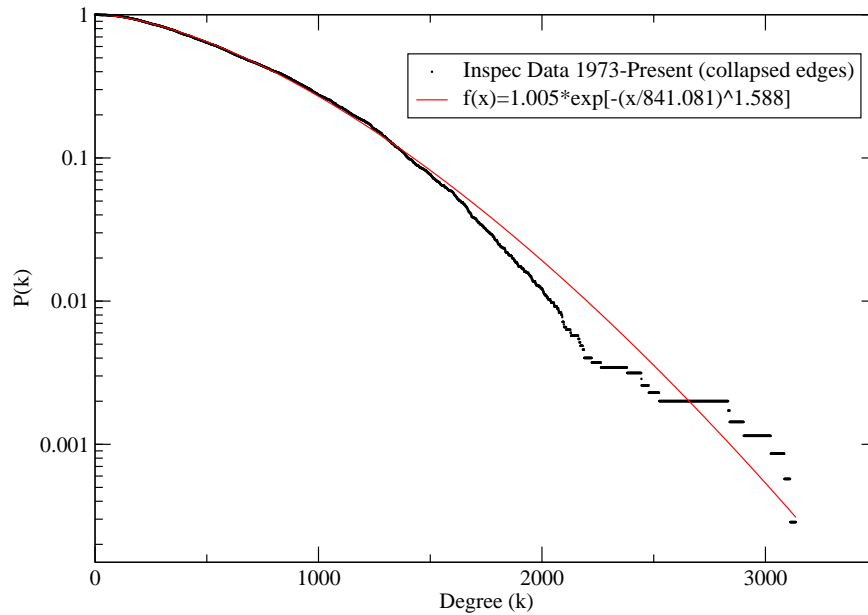


FIG. 2: Cumulative degree distributions  $P(k)$  of the Inspec network for both full degree, as well as collapsed edges (ignoring weights). The colored lines are fits to the data. Both cases do not exhibit scale-free behavior

## Community Finding

To predict the merger of fields into new revolutions, one must be able to identify these fields inside of an idea network. In order to extract these fields, the **CFinder** Community Finding Algorithm was applied to two-year periods of data in the APS Database. The CFinder Algorithm works by finding complete subgraphs called  $k$ -cliques. A  $k$ -clique is a fully connected set of  $k$  nodes. A community is then defined as the set of adjacent  $k$ -cliques where adjacency means sharing  $k-1$  nodes [3]. Figure 4 shows the overlap of two communities. A network of communities can be constructed, where each community is represented by a node, and edges exist between communities if they

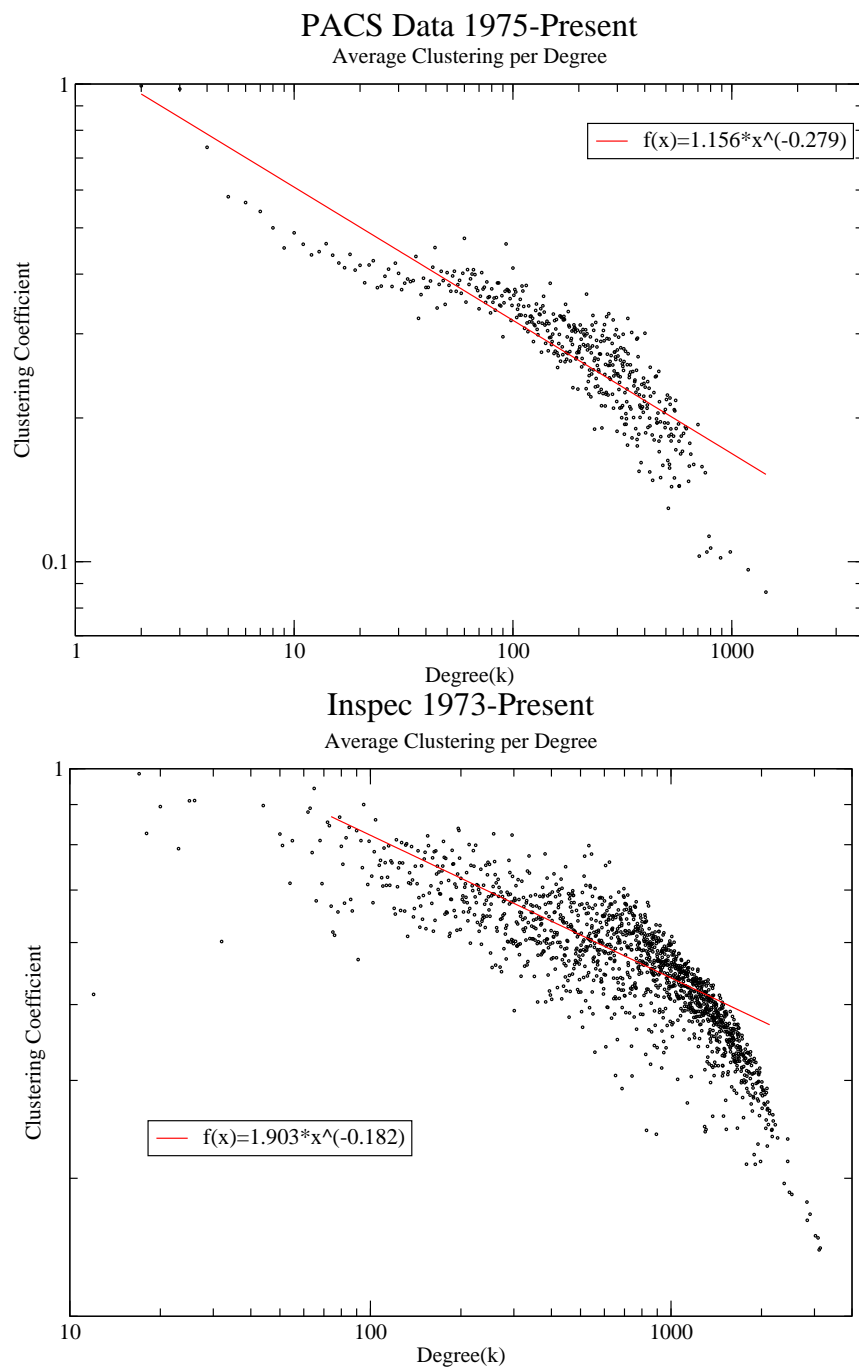


FIG. 3: Average Clustering vs Degree for both APS and Inspec Both demonstrate that  $C(k)$  has some dependence on degree. Thus, there is some hierarchical structure present in both networks

have overlapping nodes. Further, the weight of an edge can be defined as the number of nodes two communities share. Figures 5 and 6 show the extracted fields from 1999-2000, and again from 2000-2001. The structure of the fields is apparent from the CFinder results. The actual grouping into fields was devised by looking at the individual PACS numbers making up each community. The structure of these fields reconstruct the current fields of physics. For example, one notices that nuclear physics is a smaller community that is not connected to the other fields. This result is reasonable, given that nuclear physics is a more mature field in which the number of publications has decreased. Further, where each field comes into contact with other fields is also consistent with intuition. For example, quantum computing comes into contact with quantum optics in a region representing laser cooling and trapping. These results

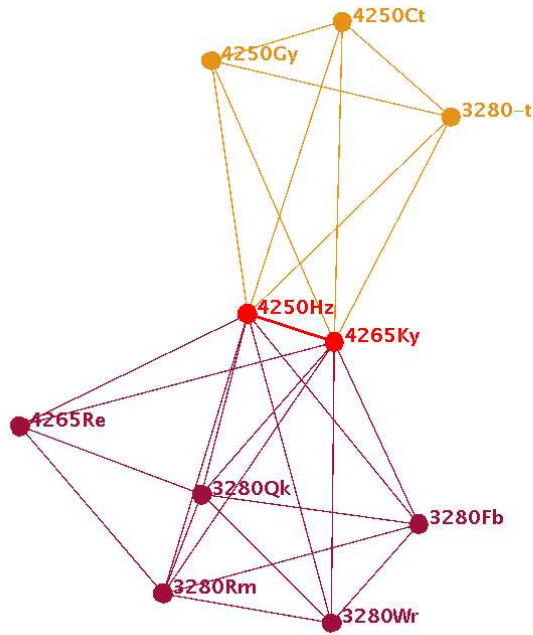


FIG. 4: The intersection of two communities.

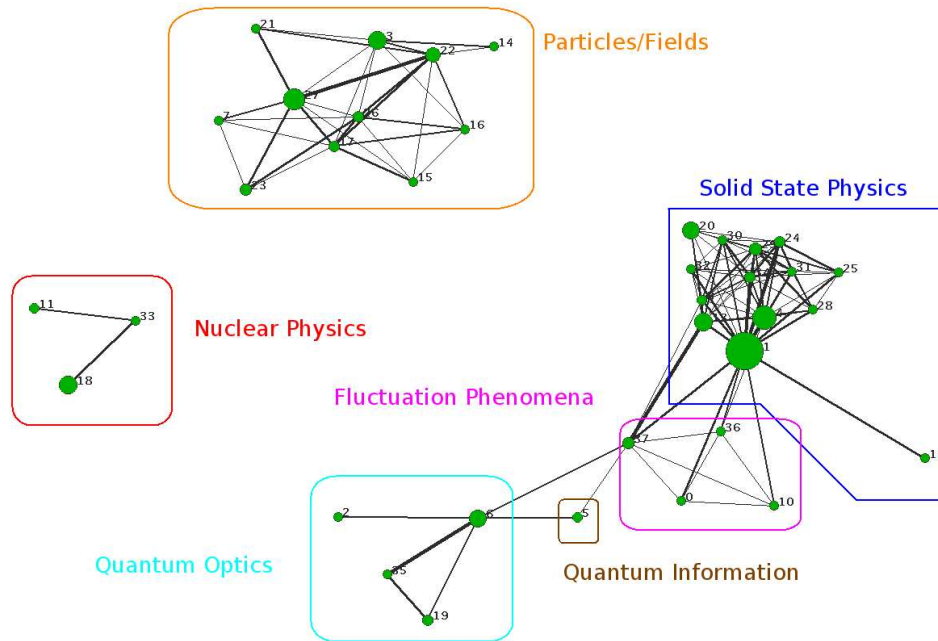


FIG. 5: A snapshot of the different fields in the APS database during 1999-2000.

are promising as they allow for the decomposition of a very complex network into the intersections of various fields.

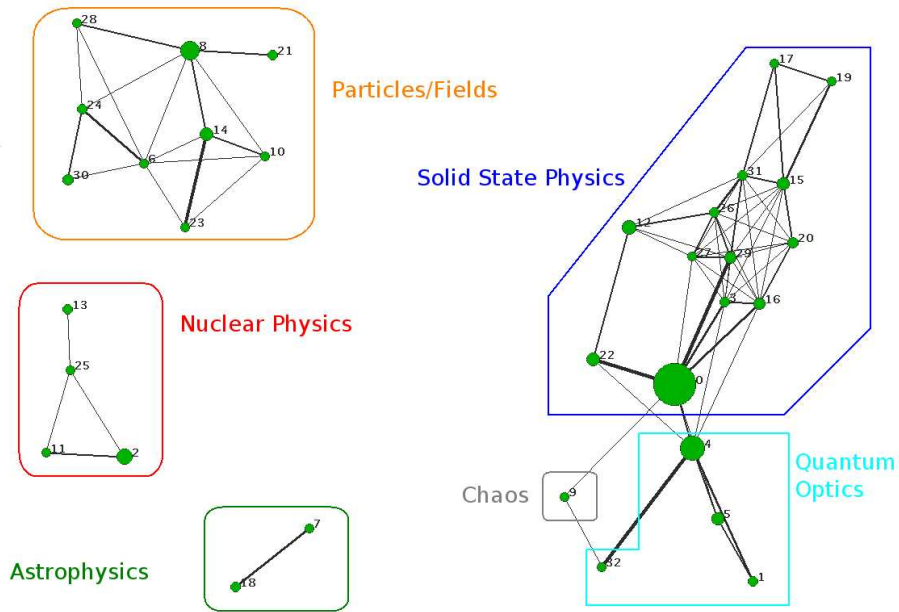


FIG. 6: A snapshot of the different fields in the APS database during 2001-2002.

### Conclusions

The various properties of both the APS and Inspec networks allow us great insight into their structure and topology. Both APS and Inspec networks do not appear to exhibit scale free behavior. We qualitatively explain this result by noting that both networks have a dynamically evolving classification system. In addition, the functional dependence of the clustering coefficient demonstrates that there is some hierarchical structure in the network. This result is in accordance with intuition when one considers the hierarchical structure of the classification systems. Finally, communities and fields were successfully extracted from the APS network, and the way in which fields interact reflects the current situation in physics. This new understanding of these idea networks is critical to developing a method that would allow one to predict the merger of different fields.

### Future Work

Ongoing work includes using different community finding algorithms, as well as tracking the merger and growth of communities. An attempt was made to correlate network properties such as betweenness centrality to citation data. As of yet, no correlation has been found, but there are still various other network properties to calculate and attempt to correlate. Future work also includes the development and implementation of edge and node prediction algorithms in order to attempt to predict the merger of fields.

### Acknowledgments

The authors would like to thank the Los Alamos Physics Summer School, specifically Norm Magee and James Colgan, as well as the University of New Mexico. Further thanks to the Center for Nonlinear Studies, Aric Hagberg, Hristo Djidjev, and Luis Bettencourt. Thanks to the American Physical Society and Inspec for the use of their data, as well as James Powell, Frances Knudson and the rest of the LANL Research Library. This work was funded by the Los Alamos Physics Summer School, a joint program between Los Alamos National Laboratory and the University of New Mexico.

- 
- \* Electronic address: [mherrera@lanl.gov](mailto:mherrera@lanl.gov); URL: <http://www.umr.edu/~mrh9rb>
- [1] A.L. Barabási and Z N. Oltvai, *Nature Rev. Genet.* **5**, 101-113 (2004)
  - [2] M.E. J. Newman, *SIAM Rev.* **45,167** (2003)
  - [3] G. Palla, I. Derényi, I. Farkas, and T. Vicsek, *Nature*(London) **435**,814 (2005)

# Simulation and Characterization of a Dark Matter Detector

Andy Mastbaum

August 7, 2007

## Abstract

It is now firmly established that the matter content of the Universe is largely comprised of an unknown and non-luminous form. Astronomical observations and particle theory place WIMPs (Weakly Interacting Massive Particles) among the foremost of dark matter particle candidates. LANL scientists are currently leading efforts to develop a novel tonne-scale dark matter detector, which will observe WIMPs directly through recoils in a cryogenic noble liquid scintillation medium. Full detector simulations, supported by experimental tests of detector components (photomultiplier tubes, data acquisition systems, etc.) are key to the success of this project. An overview of this project will be presented, and results of detector simulations and photomultiplier tube testing will be shown.

## 1 Introduction

The search for dark matter (DM) is well-motivated by both cosmological and particle physics concerns. Originally postulated in astronomy as an explanation for apparently missing matter in galaxies and globular clusters, dark matter currently provides the best explanation for a wide array of astronomical phenomena, providing an excellent model for previously inexplicable gravitational lensing and cluster dynamics data. The Bullet Cluster (1E 0657-56) provides an illustrating example; the interaction that took place during this two-cluster collision provides much support for the existence of dark matter [1]. Modified Newtonian Dynamics (MOND) fails to adequately explain the Bullet Cluster. Other DM evidence is provided by anomalous velocities in numerous galaxies and star clusters [2]. In many cases, these systems achieve angular velocities far exceeding that which would cause radial disintegration given Einstein's theory of gravity and the amount of visible matter present.

From the particle physics perspective, dark matter is motivated by many of the supersymmetric extensions to the Standard Model (SM); it has long since been clear that DM requires physics beyond the SM. WIMP dark matter is predicted by the MSSM (Minimal Supersymmetric Standard Model), wherein it is the lightest superparticle (LSP), i.e. the lightest neutralino ( $\tilde{\chi}_1^0$ ) [2]. This

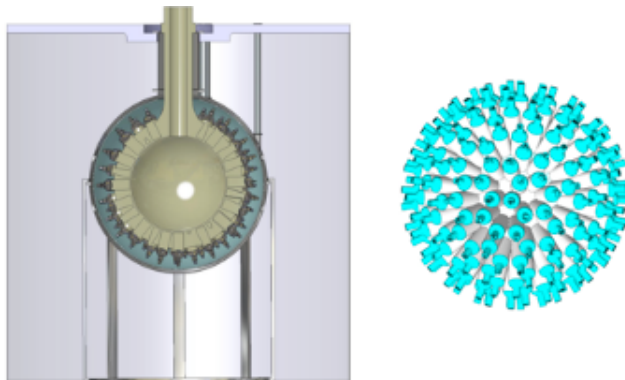


Figure 1: The DEAP/CLEAN detector concept (left) and “sea urchin” model lightguide geometry (right)

particle interacts only via the weak and gravitational forces (explaining astronomical phenomena), and current limits place the mass at approximately 100-150 GeV [3]. MSSM is a well-established extension to the SM, much simpler than most other supersymmetry theories and SM extensions, awaiting confirmation through either the discovery of LSP WIMP dark matter or the genesis of predicted superpartners in large accelerators (i.e. CERN’s LHC) [4].

The detector currently under development at Los Alamos National Lab (LANL) aims to directly detect WIMP dark matter particles directly through nuclear recoils in a noble liquid scintillation detector.

## 2 The DEAP/CLEAN Detector Concept

Building off of the DEAP (Dark matter Experiment with Argon and Pulse-shape discrimination) and CLEAN (Cryogenic Low Energy Astrophysics with Noble gases) experiments, the DEAP/CLEAN detector concept consists of a tonne-scale noble liquid scintillator detector contained within an acrylic vessel, surrounded by 266–366 photomultiplier tubes (PMTs). This entire unit will be surrounded by water (with additional structural supports) or ice, and enclosed in a stainless steel cylindrical volume [5].

When any event occurs in the cryogenic scintillator material, the recoil excites a dimer state in the molecules of the medium [6]. These dimer excitations are difficult to analyze, as it becomes difficult to distinguish between WIMP events and events due to other (background radiation) sources. To make this determination, a pure and well-characterized scintillator must be used, such that individual excited states can be mapped to recoil energies; hence the use of liquid argon (LAr) and liquid neon (LNe) in the DEAP/CLEAN detector. WIMP

interactions in LAr and LNe (and also LXe<sup>1</sup>) produce either a quickly-decaying (via  $\gamma$ ) singlet dimer state  $^1\Sigma$  (2.2 ns in LNe, 6 ns in LAr) or a longer-lived triplet dimer state  $^3\Sigma$  (2.9  $\mu$ s in LNe, 15  $\mu$ s in LAr). Both states result in the emission of an ultraviolet (UV) photon (of 128 nm for LAr), and both occur on a much faster scale than purely electronic state decay. By correlating event energy (determined by the number of observed photoelectrons) and event time, and employing Pulse-Shape Discrimination (PSD), distinguishing WIMP events from other nuclear interactions becomes possible [8] [9].

The UV light created in the scintillator medium by an event passes through a wavelength-shifting coating of TPB (tetraphenyl butadiene) before entering the surrounding UV-transparent acrylic (polymethyl methacrylate) vessel (AV) (shifting the light into the visible range to match PMT response). Coupled to the AV are mirror-coated light guides, each bonded to a PMT. Figure 1 shows the detector as a whole (left) and the lightguide geometry alone (right). Photons travel a total 30 cm through acrylic from TPB to PMT. PMT data is read through a digital data acquisition system (DAQ), and the event is characterized through numerous computational models including PSD, proven effective in the microCLEAN and DEAP experiments [10] [9].

The WIMP-nucleon cross section is believed to be about  $10^{-46}$  cm<sup>2</sup>, requiring sensitivity never before achieved for adequate signal/noise discrimination, and likely resulting in only one event per year (per tonne) [4]. Hence, low background is critical to the DEAP/CLEAN experiment. Figure 2 summarizes current dark matter detection experiments in terms of sensitivity.

## Background Analysis

Background radiation in DEAP/CLEAN comes from a number of sources, both natural and integral to the detector itself. Since the minimum background possibly achievable in physical materials is too great for the sensitivity of the experiment, much care must go into understanding these sources, engineering the detector to minimize exposure, and establishing methods for rejecting background events.

The primary sources of background radiation are:

**PMT Glass** Fast neutrons from decaying isotopes in the the silica-based glass envelope of the PMT. These neutrons are effectively attenuated by an acrylic vessel between the scintillator material and PMT; see section 3.2.1.

**<sup>39</sup>Ar** When the LAr is used in the detector, there is inevitably a small fraction of the <sup>39</sup>Ar isotope, which spontaneously undergoes  $\beta$ -decay. Electronic events are discernable via PSD, however this effect provides motivation for the use of LNe in favor of LAr. Simulations of this effect are in progress; see section 3.3.

---

<sup>1</sup>More information on the XENON LXe dark matter search can be found in reference [7]

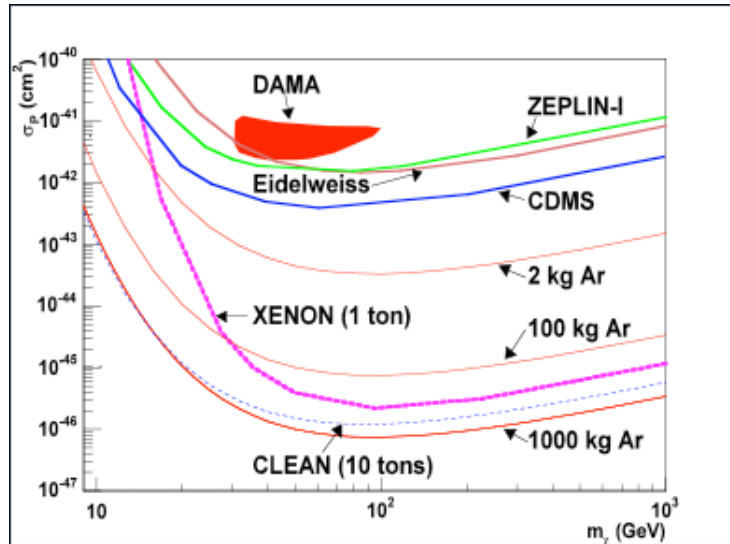


Figure 2: Current experiments and their mass limits. N.B. Only CLEAN/DEAP (“CLEAN” and “1000 kg Ar”) reach the  $10^{-46}$   $\text{cm}^2$  mass limit.

**Radon** Radon gas is ubiquitous, particularly underground and in uranium-rich locales. As this detector must be placed far underground to be isolated from cosmic rays and high-energy gammas, radon is an important concern. Tests have shown that in a radon-rich environment, Rn daughters will plate onto surfaces, creating a problem during construction while the detector is unfilled. Work is ongoing to determine methods for either removing Rn daughters from the surface, or sealing the AV during construction to avoid deposition.

**Cosmic Rays** The detector will be placed kilometers below Earth’s surface, so as to attenuate cosmic rays and high-energy gammas.

**Neutrinos** Neutrinos are impossible to attenuate in such an experiment, but their small masses allow easy discrimination. The DEAP/CLEAN detector, in fact, will double as a  $pp$ -solar  $\nu$  observatory with no modification.

**Rock** The detector’s location in a cave or mine will introduce additional background, as all natural rock contains radioactive uranium and thorium, among other isotopes. This effect cannot be fully characterized until a location is chosen, however, water shielding will attenuate much of this noise.

**Detector Components** Technically the entire detector, consisting of physical materials, is a background source. The TPB wavelength shifter, the water and stainless steel vessel surrounding the detector, the acrylic, etc., are all

potential contributors. Measures will be taken to ensure that substances are as radio-pure as possible, but these sources must also be considered in calculations and simulations as the net noise contribution may be significant.

### 3 DEAP/CLEAN Detector Component Characterization

Due to the large scale of the detector, preliminary theoretical and experimental work must be done, in addition to extensive simulation, to fully characterize the detector and its components before construction begins.

#### 3.1 Acrylic Vessel and Lightguides

The primary goal of the AV and lightguides is to transport photons as efficiently as possible from the noble liquid to the PMT faces while maintaining a requisite separation between these components. A major source of radioactive background in this experiment is residual uranium and thorium present in the PMT glass. Though efforts are made to minimize isotope concentration, some fast neutron emission from the PMT surface is inevitable. According to theoretical calculations (confirmed by simulations), a 30 cm separation is sufficient to attenuate all fast neutrons from the PMTs. Hence, this has been adopted as the total acrylic thickness. Simulations are underway to determine whether 20 cm would suffice, as it is advantageous in terms of light loss to minimize photon path length through acrylic.

##### 3.1.1 AV Thickness/Lightguide Length RAT Simulations

A series of simulations was run to test the DEAP/CLEAN tonne-scale detector with various waveguide/wall thickness parameters, to confirm that thinner AV walls correspond to higher PE counts per keV. The simulations were run in Braidwood RAT 0.3 (in conjunction with GEANT4 and ROOT 5.14) on the LANL Weak Interactions team (WI) Xserve cluster [11] [12] [13].

Simulations were run with the geometries listed in Table 1. Note that each of these correspond to a total thickness of 30 cm. The extreme final case (30cm wall thickness) refers to the “golfball” model, which uses no waveguides (PMTs are bonded directly to the AV). In all cases, simulations used the *sno-standard* acrylic for the AV (acrylic vessel), shown to be superior to *sno-good* acrylic in previous simulations [17]. All simulations in this study were run using models including a reflective coating on the outer radius of the AV. The PMTs used in the simulations were Hamamatsu model R5912. The results indicate that:

- Higher photoelectron yield per keV is achieved with longer reflecting waveguides (i.e. thinner AV walls)

| Wall Thickness | Waveguide Length | PE count per keV | Uncertainty |
|----------------|------------------|------------------|-------------|
| 5              | 25               | 7.88             | 0.04        |
| 7.5            | 22.5             | 7.84             | 0.03        |
| 10             | 20               | 7.66             | 0.02        |
| 15             | 15               | 7.24             | 0.03        |
| 20             | 10               | 6.67             | 0.03        |
| 25             | 5                | 6.07             | 0.03        |
| 30             | 0                | 4.99             | 0.03        |

Table 1: Geometries Simulated with 30 cm Total Straight Path Length

- Photoelectron (PE) count falls with increasing rapidity at higher wall thicknesses
- The maximum possible PE/keV yield is  $\approx 8$

The PE count versus waveguide length function follows a  $1 - \frac{1}{e^{\alpha x}}$  functional form, implying that attenuation in the acrylic is responsible for the photon loss in higher-thickness AVs. Extracting the  $\alpha$  fitting parameter,  $\frac{1}{\alpha}$  is an “effective attenuation length” for the AV material (*sno-standard*) with a particular reflector configuration. Here,  $\frac{1}{0.0642191} = 15.572$ . That is, every 15.572 cm of wall thickness, a factor of  $e$  is lost through attenuation. Hence, it is important to minimize the photon path length through the acrylic.

### 3.1.2 20 cm Simulations

In order to gain a more comprehensive understanding of the attenuation effects of the acrylic, a series of simulations with a total straight path length (distance from cryogen liquid to PMT surface)  $l_{AV} + l_{waveguide} = 20$  cm were run. Maintaining a many-cm gap is important to the detector as it prevents excitations in the scintillator due to decays of radioactive contaminants in PMT glass, but it is possible that 20 cm is sufficient.

The simulations run with a 20 cm total showed a significant improvement over the 30 cm simulations; PE count per keV increased by about 15-50%. The geometries simulated are summarized in Table 2.

| Wall Thickness | Waveguide Length | PE count per keV | Uncertainty |
|----------------|------------------|------------------|-------------|
| 5              | 15               | 9.14             | 0.04        |
| 7.5            | 12.5             | 9.09             | 0.04        |
| 10             | 10               | 8.81             | 0.04        |
| 15             | 5                | 8.30             | 0.04        |
| 20             | 0                | 7.35             | 0.04        |

Table 2: Geometries Simulated with 20 cm Total Straight Path Length

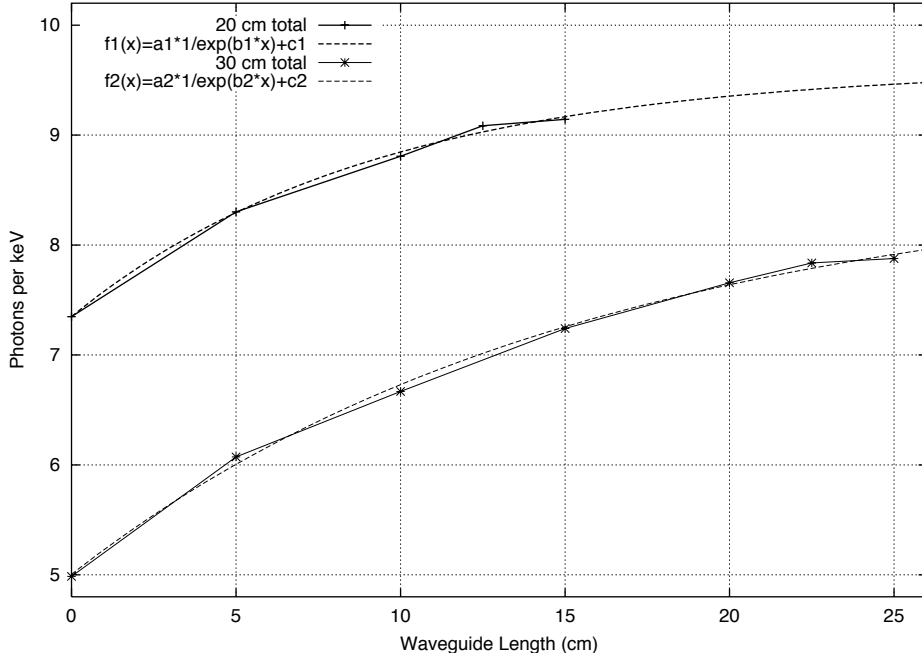


Figure 3: RAT simulation data, 20cm/30cm comparison. Statistical errors are too small to be seen.

Figure 3 compares the 20 and 30 cm results. The analytical fits obtained for both data sets through gnuplot’s fitting routines show very good agreement with the above-stated inverse-exponential form. In the case of the 20 cm model, the “effective attenuation length” is  $\frac{1}{0.108167} = 9.2450$  cm. Table 3 summarizes the fit parameters for the function  $\frac{A}{e^{Bx}} + C$ .

|                       | 20 cm   | 30 cm   |
|-----------------------|---------|---------|
| $A$                   | -2.23   | -3.64   |
| $B$                   | 0.108   | 0.0642  |
| $C$                   | 9.61    | 8.65    |
| RMS of Residuals      | 0.0517  | 0.0576  |
| Variance of Residuals | 0.00267 | 0.00332 |

Table 3: Fit parameters for lightguide simulations

### 3.1.3 Conclusions from AV Thickness Simulations

Clearly, thinner AV walls correspond to higher PE counts per keV. Signal is further increased when the total thickness of material between the cryogenic liquid and PMT is minimized. According to these simulations, a 20 cm total thickness, or a 30 cm total thickness with a waveguide length of about 15 cm or more, should be sufficient to obtain at least 7 photoelectrons per keV. If it is feasible from an engineering standpoint and sufficiently thick to attenuate fast neutron emission from PMT glass, a 20 cm total thickness is ideal. Further simulation and testing must be done to determine the effects of the lower quantum efficiency of the Hamamatsu R5912-02-MOD PMTs slated for use in the experiment; these simulations were run using a standard Hamamatsu R5912<sup>2</sup>.

### 3.1.4 Acrylic Vessel Attenuation Length Simulation

Simulations were also run with various attenuation properties of the acrylic. The purpose of these tests was to determine the degree of precision to which the acrylic’s optical properties must be characterized experimentally. As with the AV thickness simulations, RAT 0.3 was used. The wavelength-dependent attenuation length curve was shifted down by 60%, in 2–10% steps. This series of simulations showed a strong trend relating AV attenuation length to the resultant number of photoelectrons per keV; Losses greater than one photoelectron per keV were seen when attenuation length was halved. However, only  $\approx 0.1$  PEs/keV were lost when this value was changed by 10%. Therefore, it appears that measurement of the acrylic’s attenuation length to within 10% is sufficient. Table 4 and Figure 4 summarize these results.

| % Attenuation Length | PEs/keV | % Change |
|----------------------|---------|----------|
| 100                  | 7.9     | —        |
| 90                   | 7.8     | 1.3      |
| 80                   | 7.6     | 3.8      |
| 70                   | 7.4     | 6.3      |
| 60                   | 7.3     | 7.6      |
| 50                   | 6.9     | 12.7     |
| 40                   | 6.5     | 17.2     |

Table 4: Attenuation Length Simulation Results

## 3.2 Photomultiplier Tubes

Clearly, the photon detecting elements themselves are critically important to the experiment. The PMTs to be used are 8-inch Hamamatsu R5912-02-MOD, a large spherical glass PMT with a quantum efficiency (QE) of approximately 15%

<sup>2</sup>Hamamatsu claims quantum efficiency of the R5912 to be 19% at 440 nm, while WI tests indicate that the R5912-02-MOD is about 15%

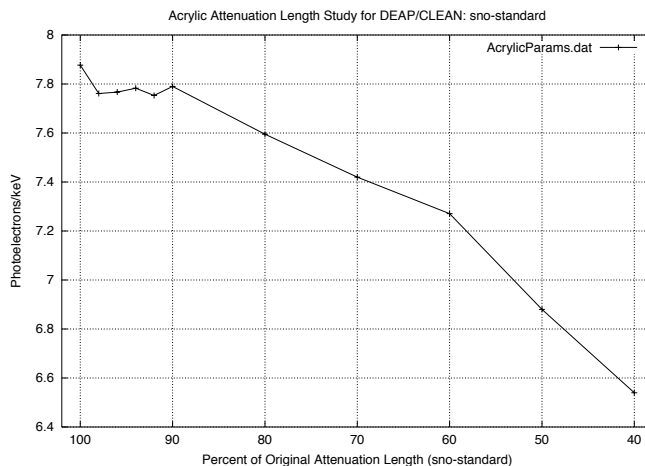


Figure 4: Attenuation Length Simulation Results

(according to the manufacturer). This PMT is much like the standard R5912 model, but feature a platinum coating on the inner face and total 14 dynodes, intended to improve low-temperature performance, and a “frosty” surface; sand-blasting is intended to reduce reflections. Work is ongoing in determining the effects of the platinum and sandblasting; future experiments will allow side-by-side comparisons with and without these features.

Accurate measurements of QE, variations among individual PMTs, and the effects of angle and temperature on QE are critical to a complete understanding of the detector and an accurate determination of its feasibility. Experimental tests cover each of these aspects of PMT performance.

### 3.2.1 Quantum Efficiency Tests

Recent work by K. Myers of the WI team determined the efficiency of a small sample set of R5912-02-MOD [14]. The results, obtained by comparison with a PMT from the Milagro experiment<sup>3</sup>, are shown in Table 5. This data corresponds to an average QE of  $14.8 \pm 1.1\%$ , close to Hamamatsu’s reported 15%. Recent work by collaborators at University of Texas ran similar tests with an <sup>90</sup>Sr source rather than a (blue diode) laser as used by Myers, and found a QE of 15.09% on the single PMT tested.

Variations among individual PMTs are a concern for the experiment, and differences will have to be compensated for through individual tuning in the final setup.

<sup>3</sup>Milagro is an all-sky high-energy gamma ray observatory; more information can be found at the collaboration website, <http://umdgrb.umd.edu/cosmic/milagro.html>.

| PMT | Efficiency<br>Relative to Milagro | Absolute<br>Efficiency |
|-----|-----------------------------------|------------------------|
| 25  | 80.3%                             | 15.3%                  |
| 26  | 77.0%                             | 14.6%                  |
| 27  | 79.1%                             | 15.0%                  |
| 29  | 80.3%                             | 15.3%                  |
| 31  | 78.1%                             | 14.8%                  |
| 34  | 72.2%                             | 13.7%                  |

Table 5: Absolute efficiency of R5912 MOD PMTs at 440nm [14]

### 3.2.2 Angular Testing

Since interactions occur uniformly throughout the spherical volume, light incident on the PMT faces will almost certainly be at oblique angles. Hence, it is important to understand the effects of non-normal photon incidence [15]. To study this, an experiment was designed in which the PMT can be rotated to any azimuthal and polar angle, and the laser made incident on any position on the PMT face. The spherical symmetry of the R5912-02-MOD reduces the number of measurements necessary, and so tests will be done within one quadrant of the PMT face.

The apparatus constructed for these tests consists of a miniature lab jack, upon which is mounted a small rotation stage. A custom-designed 2 cm thick aluminum plate with slots bored lengthwise mounts to this rotation stage, and supports a steel post. Attached to the post is another rotation stage, and on the rotation stage mounts a custom acrylic PMT clamp.

Using the rotation stages for angular adjustment (with single-degree precision), the jack and post for vertical translation, and movement of the post along the slots in the aluminum plate for horizontal adjustment, efficiency measurement of any incident angle on any surface point is possible.

### 3.2.3 Cold Testing

The DEAP/CLEAN detector will operate at very low temperatures (27 K for LNe, 87 K for LAr), and the PMTs are not thermally isolated from the cryogenic liquid. Therefore, study of PMT properties at low temperature is critical [16]. A series of experiments was designed to explore this topic, using a specially-designed vacuum refrigerator (based on a CTI Cryogenics/Helix vacuum cryostat) capable of 17 K temperatures and  $< 10^{-10}$  torr vacuum.

Once the full testing setup is complete (present work went to research and development), PMTs will individually placed in a smaller chamber within the vacuum cryostat, and noble gases (chiefly Ne) flowed through while slowly being chilled. This way, the PMT can be slowly and evenly cooled to the desired temperature.

A high-power film resistor (Caddock Electronics MP9100-50.0-1%) and power

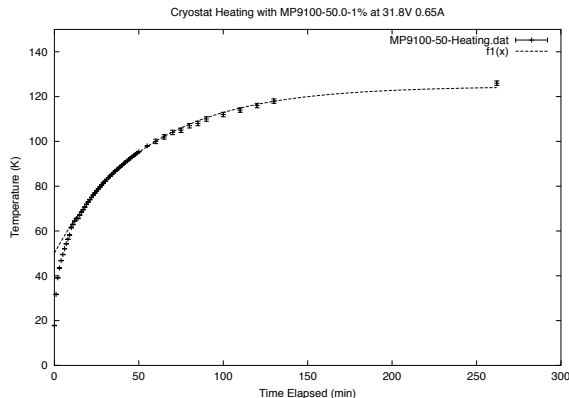


Figure 5: Heating potential of MP9100-50.0-1% at 20.7 W

supply (Lambda Americas GENH-40-19) will be used to resistively heat the cryostat’s cold head and control the PMT temperature within the 17–300 K range. The present work explored the heating potential of a number of resistors, and determined that the MP9100-50.0-1% is suitable. A number of tests were carried out to ensure the integrity of this component in a high vacuum, low-temperature environment. Figure 5 shows a sample heating curve, indicating the temperature range available when powering the resistor at 20.7 W.

This setup faces a number of challenges. The lack of commercially available resistors designed to operate at the power and temperature desired has forced extensive characterization of components not designed for cryogenic usage. According to the manufacturer, Caddock Electronics, Inc., the Sn95Ag5 solder used internally may fail with repeated chilling cycles; tests are currently underway to evaluate this possibility, but no failures have been observed thus far [18].

Results thus far indicate that resistance is slightly dependent on temperature in the MP9100-50.0-1%. Over the 293K–17.8K temperature range, a 1.23  $\Omega$  variation in the resistance value was observed. The results of this experiment are summarized in Figure 6.

### 3.3 Background Simulations: $^{39}\text{Ar}$

An important source of background when the detector uses LAr will be  $\beta$ -decay of  $^{39}\text{Ar}$  isotopes. These isotopes are present even in the purest Ar currently attainable. A simulation is underway to determine the interaction properties and detector signature of these events, through analysis of prompt light (*fPrompt*) and photoelectron pulse shape. The hope is that the energy spectrum of these events will not overlap with that of the WIMPs. Simulation time is on the order of months, due to inefficient photon tracking in GEANT4; results are forthcoming.

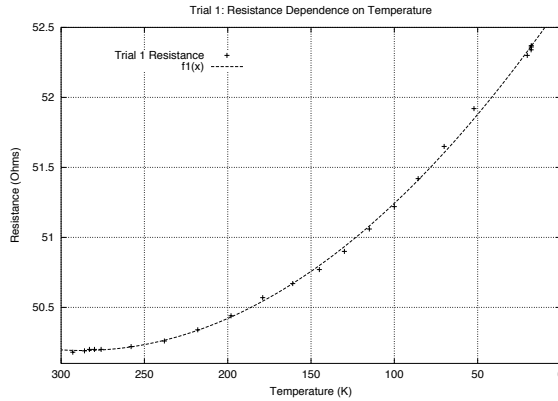


Figure 6: (Quadratic) resistance dependence on temperature in the Caddock MP9100-50.0-1%

## 4 Challenges

The DEAP/CLEAN project faces a number of interesting and unique challenges. A dark matter detection project of this type and scale has not yet been attempted, and though many formerly-unconfronted difficulties have appeared, careful research and development, extensive simulation, sound theoretical models can ultimately confront these issues successfully. A few of the main problems faced by the project are:

**Low Background** The sensitivity of the DEAP/CLEAN detector must be unprecedentedly low, pushing the current experimental energy limits down by some three orders of magnitude. Characterization of background noise must be more thorough and accurate than ever before achieved, and detector component radio-purity requirements will push the limits of material sciences.

**Low Temperature** LNe and LAr require very low temperatures (27K and 87K, respectively). Low temperature operation raises the risk of mechanical and structural failure, elevates operational costs, and introduces a multitude of safety concerns. Much work must be done to understand the properties of all detector elements at low temperature, and analysis must be done to ensure safe handling of catastrophic cryogen boil-off or other such disasters.

**Engineering Constraints** Safety and structural integrity concerns are of great importance here, as in all experiments. All design considerations must be evaluated by a team of engineers, and the balance between an ideal detector and a safe, well-engineered one is often difficult to achieve.

## 5 Conclusions

The acrylic vessel and photomultiplier tubes are key pieces of the detector, and the present work has resulted in quantitative models for optimizing light collection efficiency as well as supporting ongoing experimental research regarding angular response and cryogenic performance of the photomultiplier tubes. Simulations currently underway will be the first to fully characterize the  $^{39}\text{Ar}$   $\beta$ -decay as a background source, giving insight into the problem of overlap in the prompt light signal of electronic and nuclear events. Through this analysis, the DEAP/CLEAN collaboration will gain a better understanding of the detector at the component level, and in turn build and operate a more successful experiment.

Developing the DEAP/CLEAN dark matter detector is a challenging task, but is possible through careful characterization and simulation work, accurate experimental observations, and thorough analysis. Direct observation of the  $\tilde{\chi}_1^0$  MSSM neutralino requires sensitivity approximately 2.5 orders of magnitude below any existing experiments; the WIMP-nucleon interaction cross-section is predicted to be  $\approx 10^{-46}$  cm<sup>2</sup>. The corresponding event rate of 1 event per tonne per year makes background characterization and precise event signature analysis critical. However, extensive Monte Carlo simulations and experimental tests of detector components are helping to ensure that once constructed, the detector will perform as expected. The existence of WIMP dark matter, in particular MSSM neutralinos, is a fundamental question of basic science. The goal of this work is to help ensure that the DEAP/CLEAN detector can make that determination as clearly as possible; elimination of unknowns in detector components and a firm understanding of detector response will make WIMP event determination much easier and in turn contribute to the credibility of the results.

This work was generously supported by Los Alamos National Laboratory grants and LDRD (Los Alamos Directed Research and Development) funds. Special thanks to Andrew Hime, LANL P-23 Weak Interactions team leader, Laura Stonehill and Keith Rielage of the Weak Interactions team, James Colgan and Norm Magee of the Los Alamos Summer School, and Stan Seibert, James Nikkel, Franco Guiliani, and the entire DEAP/CLEAN collaboration.

## References

- [1] M. Markevitch, et al. *Astrophys. J.*, 606:819-824, 2004.
- [2] Richard J. Gaitskill *Annu. Rev. Nucl. Part. Sci.*, 54:315-59, 2004.
- [3] Vernon Barger, et al. *AIP Conf. Proc.*, 805:306-309, 2006.
- [4] Richard W. Schnee. *AIP Conf. Proc.*, 903:8-15, 2007.

- [5] Frank Lopez, et al. Engineering Design Document for Vacuum Cryostat Based Dark Matter Detector, DEAP/CLEAN Internal Report, 2007.
- [6] George Fuller, Andrew Hime, et al. arXiv: nucl-ex/0702031, 2007.
- [7] J. Angle, et al. arXiv: 0706.0039v1 [astro-ph], 2007.
- [8] M.G. Boulay and A. Hime. arXiv:astro-ph/0411358 v1, 2004.
- [9] Kevin Coakley. Micro-CLEAN: Pulse Shape Modeling and PSD, DEAP/CLEAN Internal Report cl0707003, 2007.
- [10] M.G. Boulay, et al. Demonstration of Scintillation Pulse-Shape Discrimination in Liquid Argon, DEAP/CLEAN Internal Report, 2007.
- [11] RAT Framework
- [12] ROOT Framework
- [13] GEANT4 Framework
- [14] Kirby Myers. Quantum Efficiency Measurements of R5912-02MOD Photomultiplier Tubes, DEAP/CLEAN Internal Report cl0707004 (2007).
- [15] M.D. Lay. *Appl. Optics*, 36:232-239, 1997.
- [16] James A. Nikkel, W. Hugh Lippincott, and Daniel N. McKinsey. arXiv:astro-ph/0702202v1, 2007.
- [17] Rohit Hegde. Simulating CLEAN in RAT, DEAP/CLEAN Internal Report cl0706004, 2007.
- [18] Richard Drawz. Personal email, 2007.

# Testing the Wire Integrity of Silicon Detector Cables

Michelle Adan

*T-04/LASS, University of New Mexico and Los Alamos National Laboratory  
Stetson University*

Gerd Kunde (mentor)

*P-25, Los Alamos National Laboratory*

## I. Abstract

The silicon detectors that will be used in the LHC at CERN transmit information via small pitch, high density connectors. These connectors are comprised of many cables that could individually contain undetected shorts in the wires. The focus is on testing each individual cable, enabling one to analyze the integrity of the connectors and properly prepare them for data measurement.

## II. Introduction

Silicon detectors are the optimal detectors for both low energy and high accuracy experiments. Due to its properties as a semi-conductor, it has a relatively low activation energy. When a particle interacts with the silicon, it displaces valence electrons in the silicon. In its place is a vacancy (hole) in the valence band. These electron-hole pairs, in a strong electric field, migrate to the edges of the detector to collect at a p-n junction, which is an edge of doped silicon that has much higher conductivity. This junction ensures that there is no drift of electrons across the surface other than the ones displaced by the particle. The detector then sends a time-stamped signal proportional to the displaced energy. When multiple detectors lie in the path of the incoming particle, the responses indicate the energy and track of the particle. From this, one can determine the type of the particle along with its initial position.

Millions of these very small detectors will line the LHC (Large Hadron Collider, ready 2008), all of which transmit their signals with 50-pin, .05 inch pitch connectors. Because of the high degree of accuracy necessary for the projects to be conducted at CERN, each wire must be rigorously tested for errors in data transmission. Spacing between the wires is particularly small; therefore, a very precise method is necessary to test each wire individually.

## III. Experimental Setup

In order to test fifty wires in parallel, the use of a serial-input, parallel-output shift register is necessary. The shift registers used translate a single signal into many parallel outputs. Three signals - clock, clear pulse, and input - are fed into the shift register. The input signal is shifted onto a series of D-type flip flops, which only change upon the rising edge of the clock signal. After a set amount of clock pulses - in this case, fifty - the entire signal is viewable in parallel on all fifty flip-flops. The signals feed through the connector cable, and only usable wires will transmit the signal.

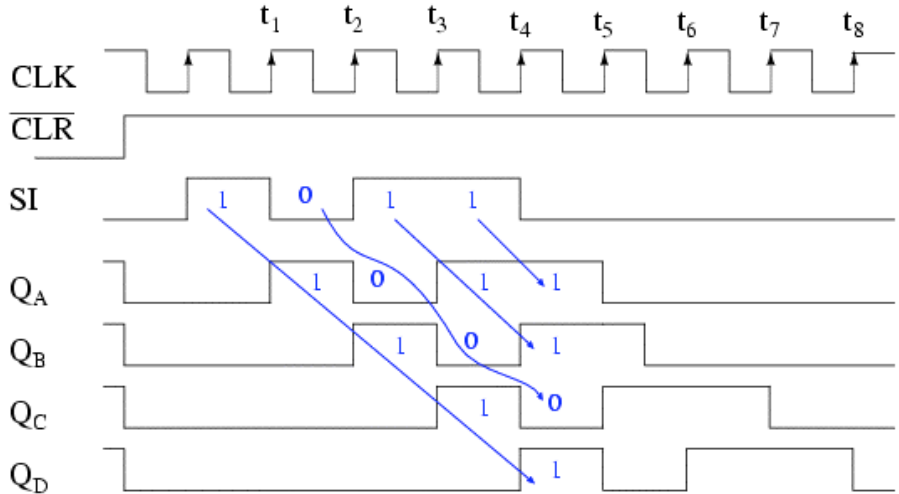


**Fig. 1 – Waveforms of the input/output of the shift register. When viewed at time  $t_4$ ,  $Q_A$  through  $Q_D$  show the entire signal (SI) in parallel.**

Experimentally, there is no shift register in existence with fifty outputs; however, eight shift registers in series is an equivalent setup. The last signal of the prior shift register feeds into the input signal of the next, which cascades the subsequent signals. All of them keep in time with the other via the clock signal, which is connected to all of the shift registers.

The experimental task is split between two boards: a FPGA (field-programmable gate array) and a PCB (printed circuit board). The PCB is used to connect the shift registers to the 50-pin connector, and the 50-pin connector to the FPGA. A hard-wired board is necessary because of the large number of connections made, and the differing specifications of the connectors.

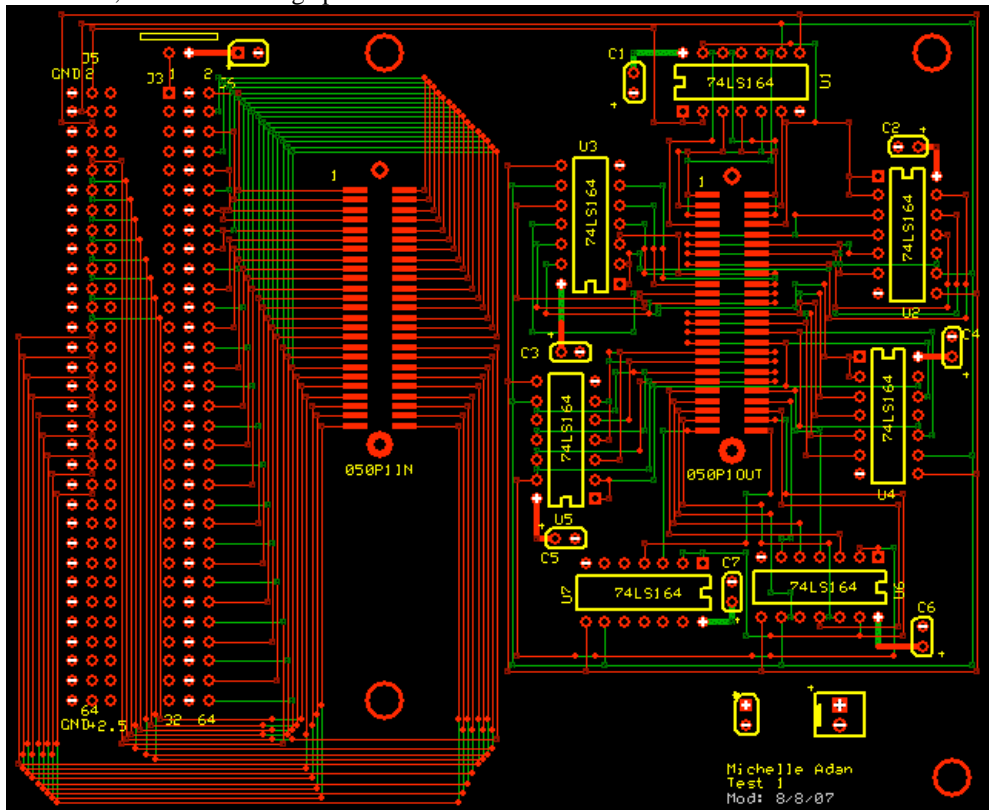


**Fig. 2 – Layout for the PCB. To the right, the signal is fed through the shift registers into the 50-pin connector. It is then fed into the FPGA at left.**

After receiving the signals from the connector, the FPGA – a Virtex-4 - tests each wire against fifty internally reproduced shifted signals. If any one signal fails an XOR test (which runs positive if two incoming signals do not match), the FPGA records the change and encodes it within a scalar data output. The FPGA is necessary for this stage because the methods of data analysis may change over time, and requires variable logic gates.

At this point, the final signal is viewed on an oscilloscope. The oscilloscope receives both the input signal and the output. It triggers upon the initial pulse, and by looking at the corresponding output signal, one can measure the spacing of individual peaks as failures in the connector.

#### IV. Conclusion and Future Research

Using a combination of boards and shift registers, a method was developed to effectively test 50-pin low-pitch connectors. The PCB board allows for a precise configuration for shifting the input through the shift registers, and feeding the data through the connectors and into the FPGA. The FPGA code analyzes the 50 raw signals to determine which wire has failed while allowing for further analysis if necessary.

At this point, the board is in the production process, and the wires themselves have not been tested. Once the board is complete, then it can be used to experimentally test the integrity of the wires. It is also hoped that a more thorough method of analysis is employed within the FPGA to more accurately determine the specific wires that have failed.

#### V. Acknowledgements

Much thanks to Gerd Kunde, for taking me on so late in the summer. Thanks also to Sergey Butsyk, Pat McGaughey, Gary Grim, and to James Colgan and Norm McGee. Thank you, John Rodgers, for prodding me into pursuing a project I enjoy, and Stephan Eidenbenz for letting me find that project.

#### References

- Ashenden, P. J. (2001). *The Designer's Guide to VHDL, Second Edition*.
- Christian, D. (2007). *FPIX2.1 Specification*, 1.13.
- Hall, B. K., Appel, J. A., Cardoso, G., Christian, D., Hoff, J., Kwan, S., et al. (2002). Development of a Readout Technique for the High Data Rate BTeV Pixel Detector at Fermilab. *2001 IEEE NSS/MIC conference*.
- Knoll, G. F. (2000). Semiconductor Diode Detectors. *Radiation Detection and Measurement*. 353-391.
- Kuphaldt, T. R. (1996). Serial-in, Parallel-out Shift Register. *All About Circuits, Volume IV: Digital*. Retrieved July 23, 2007, from [http://www.allaboutcircuits.com/vol\\_4/chpt\\_12/4.html](http://www.allaboutcircuits.com/vol_4/chpt_12/4.html).
- Xilinx. (2005). *Introduction to VHDL*.
- Xilinx. (May 2006). *ML401/ML402/ML403 Evaluation Platform*.

# Jet Measurements for QGP Experiments at CMS

Samuel C. Fletcher (scfletch@princeton.edu)  
Princeton University, Princeton, NJ 08544

August 10, 2007

## Abstract

Since the 1980s, experimentalists have sought to create in heavy ion collisions a new form of matter called quark-gluon plasma (QGP), in which the constituent quarks of highly energetic hadrons become deconfined amidst large numbers of gluons. Measurements of the QGP can serve not only as a test of non-perturbative aspects of quantum chromodynamics, but also illuminate the properties of the early universe, which is believed to have existed as a QGP at the first few microseconds after the Big Bang. We propose a new measurement with the Compact Muon Solenoid (CMS) at the Large Hadron Collider that uses the dileptonic decay of  $Z^0$  bosons to tag jets electromagnetically. Dileptons are unhindered by the QGP's strong color field, and thus allow for direct, model-independent measurements of jet energy loss. This is an improvement over previous experiments, which, in order to measure jet energy loss, required assuming the validity of certain QCD models. Here I will present some first studies of experimental feasibility of measuring the  $Z^0$  signal at CMS.

# 1 Introduction

Like a traditional plasma in which electrons become unbound from nuclei to create an electrically charged medium, a quark-gluon plasma (QGP) consists of quarks and gluons that are no longer confined to the boundaries of color-neutral hadrons, producing a strong color field.<sup>1</sup> To create a QGP, it requires high energy densities, which in turn cause a high multiplicity of quark-antiquark pair production and quark deconfinement. The usual channel for creating the multiplicities necessary for a QGP is heavy ion (e.g. Au or Pb nuclei) collisions using large accelerator facilities.

There are two principle reasons why physicists are interested in studying the properties of the QGP. One is further testing the theory of Quantum Chromodynamics (QCD), which describes the interactions of quarks via gluons, the strong-force-mediating boson. The predictions of this theory have been verified to within remarkable accuracy for few-body collisions through experiments using proton-proton (p-p) collisions. How the theory applies to many-body collisions is currently a topic of research, and so far the main experimental vehicle for this research has been the study of the QGP.

Another, perhaps even more important reason for studying the QGP is cosmological. The Big Bang theory predicts that the early universe, at an age of a few microseconds, had the high temperatures and densities necessary for existing entirely as a QGP. Thus by creating a QGP, physicists recreate for a brief moment this early state, and by measuring its properties, they at once measure those of the early universe. Knowing these properties, besides being in itself knowledge about an interesting piece of the universe's history, could allow cosmologists to better understand the details of the evolution of the early universe as it made the phase transition from QGP to hadronic gas.

## 2 QGP Experiments at RHIC

It has only been recently that the experimental facilities necessary for colliding heavy ions to make a QGP have been available. The first has been the Relativistic Heavy Ion Collider (RHIC) at Brookhaven National Lab, which began operations in 2000. At the various experiments at RHIC, physicists measured particle production rates in gold-gold (Au-Au) collisions, comparing them to what was already known about such rates in p-p collisions.<sup>2</sup> The idea was this: if RHIC creates a QGP, then its strong color field could attenuate and scatter the quarks and gluons that comprise many of the particles generated in such high energy collisions. Thus the hadrons produced would have on average a lower energy than those in simple p-p collisions, and this lower energy would correspond to a reduction in the number of observed particles. Since at lower energies fewer quark-antiquark pairs are likely to be produced, there would be fewer quarks to create the observed hadrons. On the other hand, particles without a color charge would be unaffected by the strong color field

---

<sup>1</sup>This is a notable difference with “traditional” plasmas, which by comparison are weakly-coupled plasmas—the kinetic energy of the constituent particles is much greater than their interaction energy. In a QGP the opposite is rather the case, giving it different properties that actually make it behave more like a liquid than a gas. Thus analogies between a QGP and a “traditional” plasma should not be pressed too strongly.

<sup>2</sup>As mentioned in §1, the results of these p-p collisions were successfully predicted by QCD, so physicists are very confident that they understand the physics of such collisions.

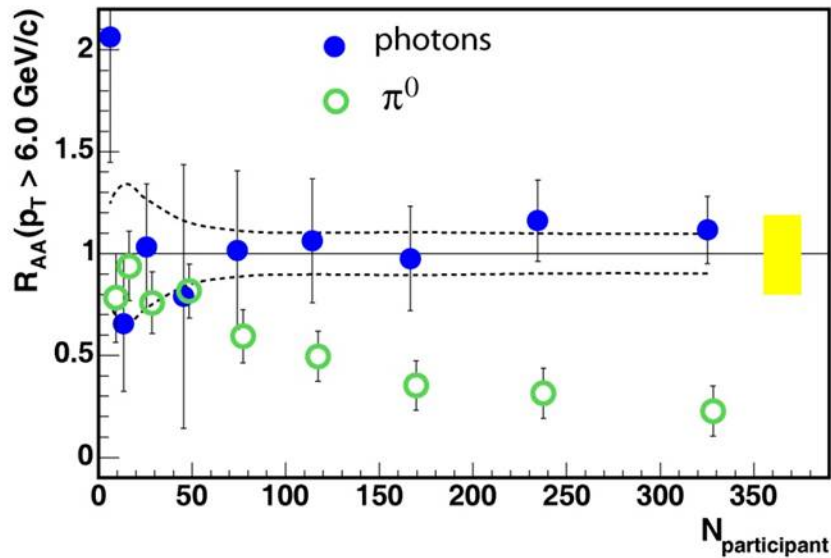


Figure 1: Plotted are the nuclear modification factors  $R_{AA}$  for photons and  $\pi^0$  mesons versus the number of participant nucleons in Au-Au heavy ion collisions, which varies because the two colliding overlap in their collision to varying degrees.  $R_{AA}$  is the ratio of observed particles to expected particles as scaled from p-p collision. For varying degrees of centrality,  $R_{AA} \sim 1$ , but for high centrality there is a suppression of  $\pi^0$  mesons by about a factor of five. [1]

and would pass through without attenuation. Thus one of the important values to examine for measuring of this suppression (or lack thereof) is the nuclear modification factor  $R_{AA}$ , defined as the ratio of observed to expected particles based upon scaling per nucleon the appropriate numbers for p-p collisions.

The results of such measurements are shown in Fig. 1, which indicates that the number of photons measured for varying degrees of centrality is around what is expected, since photons do not carry a color charge and are not thereby attenuated by the strong color field. The observation of  $\pi^0$  mesons, however, is increasingly reduced at higher centralities, up to a factor of five. This indicates that high-centrality collisions create the strong color field characteristic of a QGPs, whereas low-centrality collisions don't have enough multiplicity to result in any attenuation.

This result, while remarkable, has at least one experimental issue. In order to understand what it is, it is helpful to examine the physics of individual parton-parton collisions within heavy ion collisions. The initial hard scattering of partons produces a hadronic dijet, but if one of these jets points into the strong color field of a QGP, it will be attenuated. So, instead of observing a whole dijet, such an experiment would only measure one side thereof. In Fig. 2, we see that having the large multiplicity to create a strong color field, as in Au-Au collisions, entails the suppression of one side of the dijet, but without this multiplicity, as in p-p or even d-Au (deuterium-gold) collisions, there is very little such suppression; both sides of the dijet are observed.

Data from many of these collisions results in the overall suppression of hadronic production. While this allows for the observation of a phenomena indicative of a QGP, it also

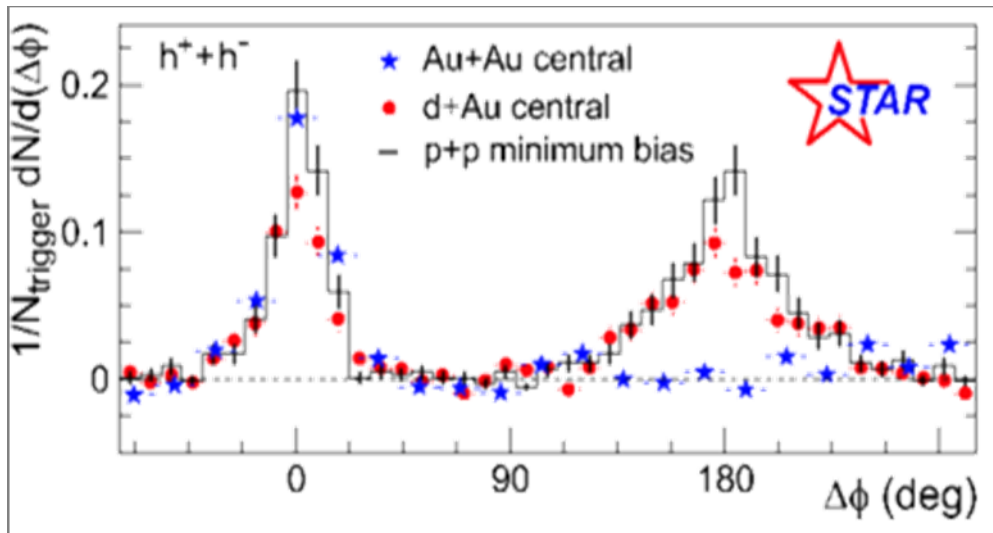


Figure 2: Plotted are observed charged hadrons, normalized by the number of trigger events, versus angular correlation, for Au-Au, d-Au, and p-p collisions. The peak at  $\Delta\phi = 0$  indicates an observed jet. For p-p and d-Au collisions, which have low multiplicities, there is very little suppression of the other side of the dijet, whereas in Au-Au collisions there is a very strong suppression. This is another indicator that a large multiplicity is needed in order to create a QGP. [2]

prevents a direct measurement of jet energy loss, a measurement which is necessary to determine the properties of the QGP. In these cases, the initial energy of scattering is known, and the energy of an observed jet can be made through calorimetry. But without a direct measurement of the energy of other jet, physicists have to rely on models of the QGP in order to determine jet energy loss. Direct, model-independent measurements would have an advantage in that they could be used to test the predictions of the QGP models, hence fulfill one of the objectives of QGP research: testing the application of QCD models to many-body collisions.

### 3 QGP Experiments at the LHC

An idea to improve upon the previous methodology used at RHIC is to tag using  $Z^0$  bosons instead of the second hadronic jet.  $Z^0$  bosons are extremely short-lived, and can decay dileptonically.<sup>3</sup> Fig. 3 displays the Feynman diagrams for this process.

The advantage of this is that leptons, not having a color charge, are unhindered by the strong color field of a QGP. Thus, unlike the usual hadronic jet, there is no attenuation, meaning that direct measurements of jet energy loss are possible. The energy of initial scattering is known, and measuring the energy of the dimuon pair and the hadronic jet then provide information on the energy loss of that jet in the QGP. This tagging method is an improvement precisely because it provides a model-independent way of measuring jet energy

<sup>3</sup>A dileptonic decay is one in which a single particle decays into a lepton and its corresponding antilepton. Thus a dilepton (e.g. dimuon) is a pair of leptons produced with a common origin.

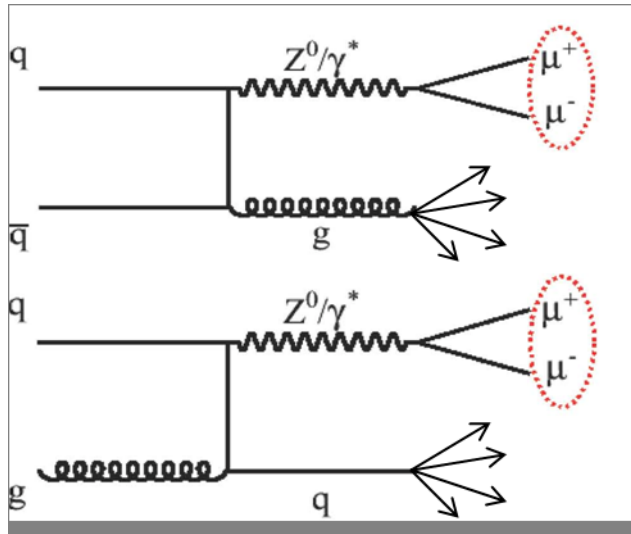


Figure 3: Feynman diagrams of the two parton-parton collisions that can produce  $Z^0$  bosons. The  $Z^0$  can then decay into a dimuon pair, and the remaining parton typically fragments into a hadronic jet.

loss, and hence the properties of the QGP.

While it is true that there are many other, often more abundant processes that produce dimuons, the decay of the  $Z^0$  boson is significantly more viable experimentally because its signal in invariant mass is peaked at its rest mass, which is about  $91 \text{ GeV}/c^2$ . In Fig. 4, we see that  $D\bar{D}$  and  $B\bar{B}$  decays, which mimic dileptonic decays, have exponential spectra in invariant mass. The invariant mass of virtual photons, though plotted with that of  $Z^0$  bosons, also has an exponential spectrum. Thus only the  $Z^0$  has a peak that is easily distinguishable from the background.

One might ask why  $Z^0$  tagging was not done at RHIC given its clear experimental advantage. The reason is that the desired kind of  $Z^0$  production (shown in Fig. 3) is exceedingly rare. At the energies achievable by RHIC (as well as older facilities), the cross-section for this process is small enough that there is not a reasonable running time that would produce enough  $Z^0$  bosons with the appropriate decay channel. Fortunately, the Large Hadron Collider (LHC), which is to be completed in May, 2008, is capable of the center-of-mass energies and beam luminosities necessary to make  $Z^0$  tagging feasible.

Fig. 5 shows a comparison in hadronic cross-section versus transverse momentum for three facilities. Because hadronic cross-section is related to the number of parton-parton collisions, of which a small fraction yield dileptonically decaying  $Z^0$  bosons, it is a good estimate of  $Z^0$  production. As the plot makes plain, the LHC has a much higher cross-section than previous facilities. The difference of a factor of  $10^4$  at  $p_T = 35 \text{ GeV}/c$ , for example, means that one needs only a year's worth of data for significant analysis when before 10,000 years' worth would have been needed.

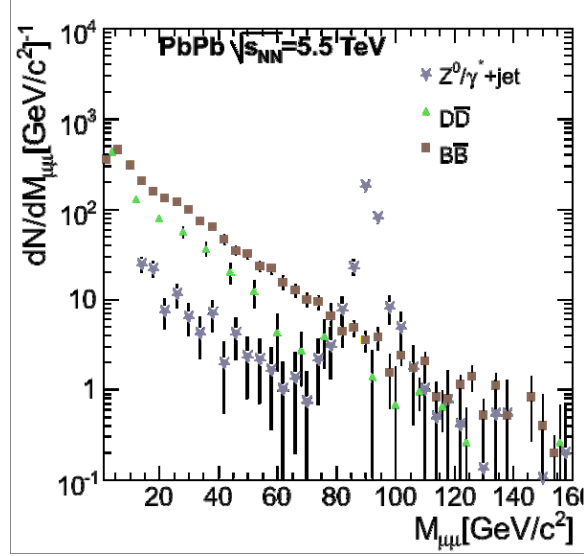


Figure 4: Number of particles producing a dileptonic signal versus invariant mass, assuming a beam luminosity of  $0.5 \text{ nb}^{-1}$  over one week of running Pb-Pb collisions at the expected LHC center-of-mass energy per nucleon of 5.5 TeV.  $Z^0$  bosons and virtual photons are grouped together because they both have true dileptonic decays ( $Z^0/\gamma^* \rightarrow \mu^+ + \mu^-$ ), whereas  $D\bar{D}$  and  $B\bar{B}$  decays only mimic dileptons. Data for  $Z^0/\gamma^*$  numbers were generated with PYTHIA, and those for  $D\bar{D}$  and  $B\bar{B}$  were done by MNR, which calculated next-to-leading-order cross-sections for heavy quark dynamics. [5]

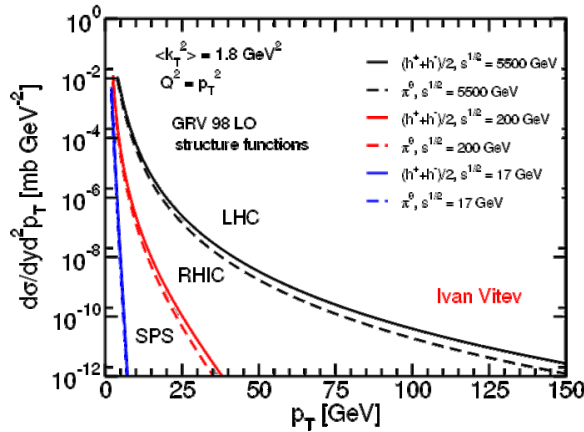


Figure 5: Cross-section per unit rapidity per unit transverse momentum versus particle transverse momentum for hadronic production at three facilities capable of heavy ion collisions. At 35 GeV/c, the LHC is capable of a  $10^4$  improvement in cross-section over RHIC, a gain which only improves at higher momenta. [3]

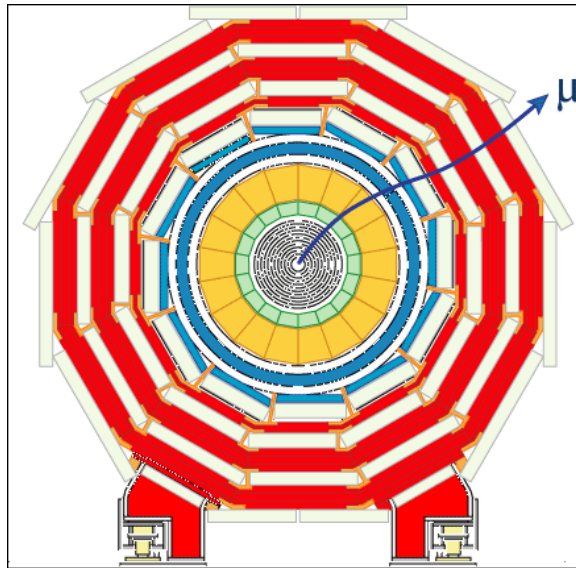


Figure 6: A cross-section of the CMS detector. At the very center is the beam pipe, and in order of increasing radius: the silicon tracker, shown by concentric circles, which, as its name says, tracks most particles from a collision; the electromagnetic calorimeter, shown in green, designed to stop and measure photons and electrons; the hadronic calorimeter, shown in pale yellow-orange, designed to stop and measure hadrons; the solenoidal magnets, shown in blue, with a diameter of 5.9 meters; and finally, muon chambers (in white) interspersed with layers of iron (in red), the latter of which is designed to funnel the return flux from the magnets. As the pictured muon passes through the various layers of the detector, it bends in a helical path according to the magnetic field along the axis of the beam; as the muon exits the diameter of the solenoid, the magnetic field changes direction, which is why its path has a point of inflection at that point. [4]

## 4 Methodology

The primary activity of this study has been to simulate the data relevant to using  $Z^0$  bosons as a tag for studying the QGP at the Compact Muon Solenoid in order to understand the latter's relevant experimental properties. Accordingly, below is a description of the solenoid itself, followed by details about the software methods used to simulate it.

### 4.1 The Compact Muon Solenoid

The experimental apparatus proposed for  $Z^0$ -tagged QGP experiments is the Compact Muon Solenoid (CMS), whose cross-section is shown in Fig. 6. CMS, as its name declares, is a superconducting solenoid designed to produce a uniform axial magnetic field of four Tesla at its center, the region of collision. Because electrically charged particles in the presence of such a magnetic field subtend a helical path with radius

$$r = \frac{p_T}{qB_z},$$

one can determine, using data from the tracking and muon chambers, the transverse momentum ( $p_T$ ) and electrical charge ( $q$ ) of such particles, even at very high energies. In particular, the silicon tracker, hadronic calorimeter, and muon chambers allow for all the necessary measurements in a QGP experiment tagging with  $Z^0$  bosons.

## 4.2 Simulating $Z^0$ Bosons in CMS

One of the first experimental steps in determining the feasibility of a QGP experiment at CMS, where the apparatus is already designed, is to examine how well the detector can reconstruct the  $Z^0$  signal. To that effect, we have simulated the production of  $Z^0$  bosons that decay into a dimuon pair inside CMS. These particles were generated using PYTHIA according to a Breit-Wigner distribution with a constraining pseudorapidity of  $|\eta| < 5$ . PYTHIA is a package which uses extensive data from p-p collisions to calculate the relevant cross-sections, probabilities, and distributions of particle dynamics. The dimuons were then used as input in the reconstruction code of CMSSW v1.5.2, a package of modules based on the ROOT high-energy physics C++ library, which simulates all of the physical details of CMS. The reconstruction code groups detected muons by event and generates combinatorically all possible pairs according to a few selection criteria. For example, pairs must consist of a muon and an antimuon and perhaps satisfy conditions on possible invariant mass values and differences in azimuthal angle.<sup>4</sup> In the case of the data simulated here, each event consisted only of a single  $Z^0$  boson and any particles produced by quantum mechanical vacuum fluctuations. If these fluctuations did not produce any muons or muon-like tracks, then each dimuon pair has three detection possibilities:

1. Both muons are detected; a  $Z^0$  is reconstructed.
2. Only one muon is detected; no  $Z^0$  is reconstructed.
3. Neither muon is detected; no  $Z^0$  is reconstructed.

Muons can be lost either because they are simply not detected, or because they are outside the acceptance range of CMS, which is  $|\eta| < 2.4$ . Because it is muons and not the  $Z^0$  bosons which are detected directly, it is entirely possible that a  $Z^0$  generated within the acceptance range of CMS not be detected because one or both of its dimuon pair are outside of the range. Conversely, a  $Z^0$  generated outside this range will never be detected, since at most only one of its muons could enter the acceptance range.

On the other hand, if the quantum fluctuations do produce a muon for a given event,<sup>5</sup> there are in fact six non-zero detection possibilities:

1. Three muons are detected; two  $Z^0$  bosons are reconstructed.<sup>6</sup>

---

<sup>4</sup>Besides merely detected the bare  $Z^0$  signal, it will be necessary in the future to find the data cuts – those criteria on selecting possible pairs – that optimize the strength of the signal with respect to the background while still maintaining a detectable  $Z^0$  yield.

<sup>5</sup>To first order there will be at most one muon generated per event by quantum fluctuations.

<sup>6</sup>Though combinatorically there seem to be three possible pairings, there will only ever be at most two viable ones since each pair must consist of a muon and an antimuon.

2. Three muons are detected; some reconstruction criterion is not met, and only one  $Z^0$  is reconstructed.
3. Two muons are detected; one  $Z^0$  is reconstructed.
4. Two muons are detected; some reconstruction criterion is not met, and no  $Z^0$  is reconstructed.
5. One muon is detected; no  $Z^0$  is reconstructed.
6. No muons are detected; no  $Z^0$  is reconstructed.

Of note is the fact that the first case always and the third case sometimes produces a false positive. The extent to which this happens can be measured by an examination of the purity (see §5) of the reconstructed signal, defined as the ratio of correct reconstructions to total reconstructions. In addition, another important factor is the efficiency, the ratio of detected (reconstructed) to detectable (reconstructable) particles. For muons, this is just the ratio of those detected over those generated within the acceptance range  $|\eta| < 2.4$ ; for  $Z^0$  bosons, it is the ratio of those detected to those whose muon decay products are within the acceptance range  $|\eta| < 2.4$ .

Also of interest is the invariant mass plot for reconstructed  $Z^0$  bosons, and the resolution in both transverse momentum and invariant mass, which determines to which percentage accuracy these values can be measured.

## 5 Results on CMS Signal Reconstruction

In Fig. 7, we see data points for both the generated  $Z^0$  bosons (in black) and the reconstructed ones (in red), both fitted with a Breit-Wigner distribution,

$$f(E) = \frac{\Gamma}{(2\pi)((E - E_0)^2 - (\Gamma/2)^2)^2}$$

where  $E_0$  is the maximum and  $\Gamma$  is the width at half-maximum. The fact that the reconstruction produces fitting parameters which are very close to the generated ones indicates that CMS can reconstruct the  $Z^0$  signal with high accuracy; the high ratio of reconstructed to generated  $Z^0$  bosons suggests a high efficiency; and the few points with significant residuals also suggests high purity, although we should note the asymmetry in this respect for invariant mass less than that of the peak.

We can investigate more quantitatively the hints provided by Fig. 7 about the various properties contributing to detector fidelity. Beginning with the efficiencies for both muons and  $Z^0$  bosons shown in Fig. 8, we see that the average muon efficiency is about 98%, and that for  $Z^0$  bosons is about 96% if we disregard those with  $p_T < 20$  GeV/c.<sup>7</sup> This means that very few muons are lost to the detector, and most of them are successfully reconstructed.

---

<sup>7</sup>The exclusion of low-momentum  $Z^0$  bosons is necessary in order to render negligible momentum error due to Fermi motions. If a  $Z^0$  boson's transverse momentum is high enough, then it will be approximately equal to that of the opposing hadronic jet immediately after a parton-parton collision.[6]

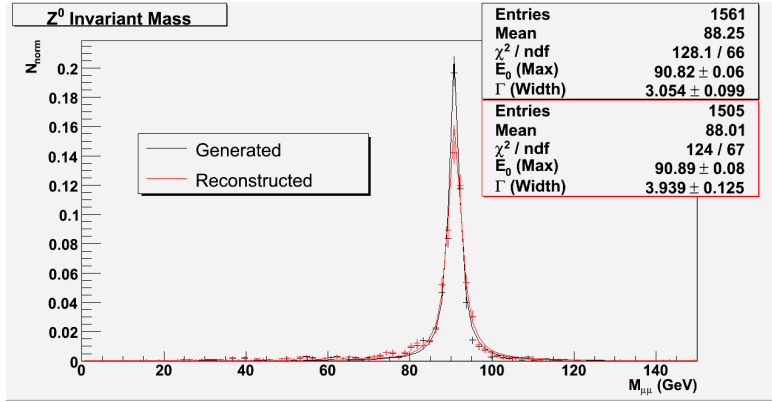


Figure 7: Number of reconstructed  $Z^0$  bosons, normalized by the total area of the histogram, versus invariant mass, for both generated and reconstructed  $Z^0$  bosons. Though 2500 such bosons were generated in the simulation, only 1561 of them had both of their muon decay products emitted within the acceptance range of the detector. The indicated fits are Breit-Wigner distributions.

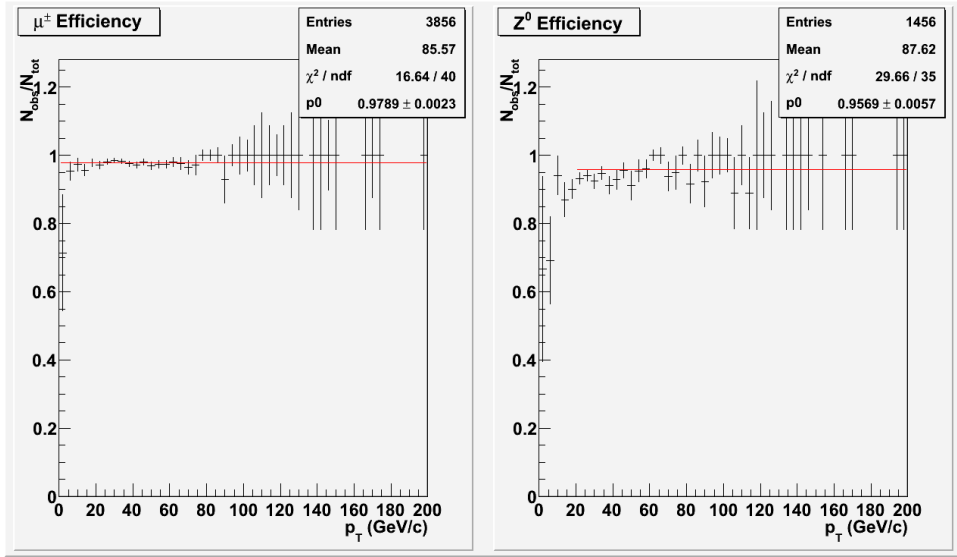


Figure 8: Muon and  $Z^0$  efficiency, defined as the ratio of observed to actual particles in the acceptance range, versus transverse momentum. For muons, the efficiency is simply the ratio of detected particles in  $|\eta| < 2.4$  to generated particles in  $|\eta| < 2.4$ . For  $Z^0$  bosons, it is the ratio of reconstructed bosons whose muon decay products are within the acceptance  $|\eta| < 2.4$  to total generated bosons whose muon decay products satisfy the same condition. The indicated fit is the average efficiency over all momenta for muons, and over  $p_T < 20$  GeV/c for  $Z^0$  bosons. See footnote 7.

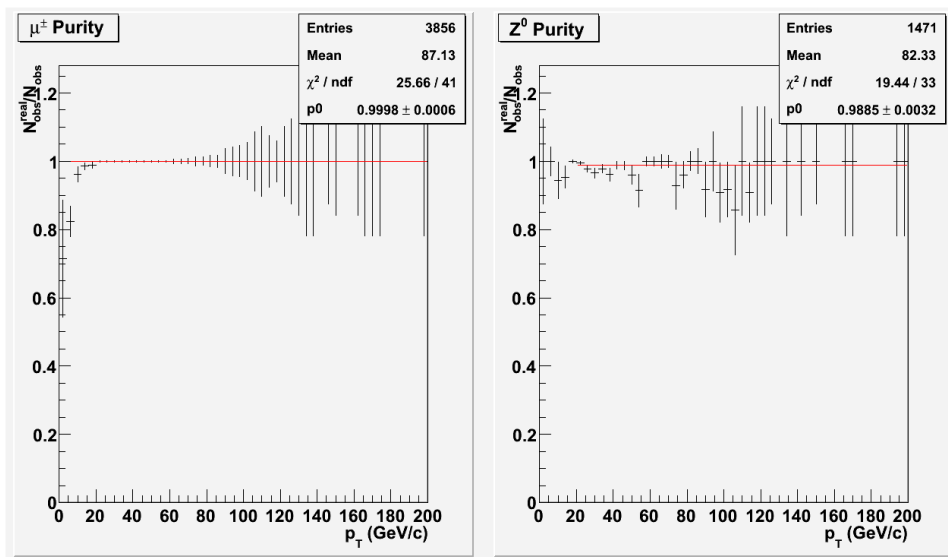


Figure 9: Muon and  $Z^0$  purity, defined as the ratio of true positives to total positives, versus transverse momentum. The departure from unity gives the total fraction of false positives. Since the only background in this study was PYTHIA-generated quantum fluctuations, muon false positives indicates, for example, high-energy pions that masqueraded as muons in the detector.  $Z^0$  false positives, on the other hand, are do to incorrect reconstruction.

Also, looking at Fig. 9, we see that the purity for muons is almost 100%, while that for  $Z^0$  bosons is nearly 99%. This indicates that there are very few false positives created from the background of quantum fluctuations.

Finally, looking at the resolutions in Fig. 10, we see small systematic errors since the means of the fitted Gaussians are both nonzero. This tendency to underestimate, seen as well in the assymetry of residuals in Fig. 7, is likely due to the presence of low energy muons engendered by the quantum vacuum fluctuations. Of note is the width of these Gaussians, which indicate a resolution at  $\pm 1\sigma$  of about  $\pm 4\%$  for the muons, but more importantly, a small  $\pm 1.5\%$  for the  $Z^0$  bosons.

## 6 Conclusions and Prospects

As seen in §5, CMS is able to reconstruct the  $Z^0$  signal to high degree of accuracy, efficiency, and purity when the background consists of quantum mechanical fluctuations. This is the first step towards a viable QGP experiment using CMS. The next step in the feasibility analysis is performing the same kinds of checks on accuracy, efficiency, and purity on the background (see Fig. 4). If CMS can recontruct the background to this signal to a sufficiently satisfactory degree, then we would proceed to analyze, given a certain signal, how much background CMS could tolerate before the signal would be irreperably degraded. In this context, we would need to develop the data cuts and selection criteria for muon pairing that would optimize the signal-to-background ratio. The final goal of this project is to determine, from the perspective of data analysis, how robust a QGP experiment at CMS can be.

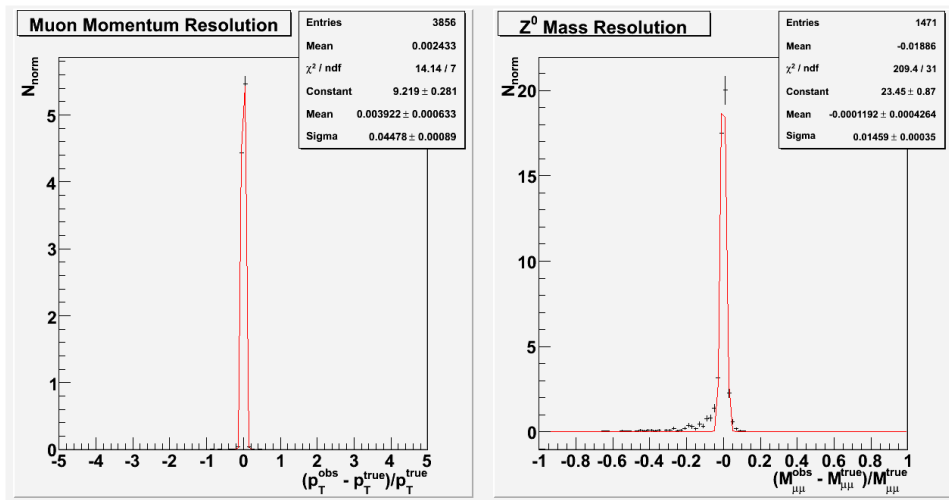


Figure 10: On the left, muon resolution versus transverse momentum, and on the right,  $Z^0$  resolution versus invariant mass. The resolution in a particular quantity is defined as the difference between the observed value of that quantity and its actual value, divided by its actual value. The fitted Gaussian (in both cases) is made only to estimate the width of the resolution, which can then be used as an approximation for the percentage error.

## 7 Acknowledgements

I would like to express my sincere gratitude to the following: Gerd Kunde, for his advice and friendship throughout the summer; Camelia Mironov, for the keen productivity of our collaborations; Maria Castro, for her help in finding programming resources and debugging; James Colgan, and especially Norm Magee for their indefatigable commitment to making the Los Alamos Physics Summer School as enjoyable and comfortable as possible; and finally, to Los Alamos National Lab and the National Science Foundation for the grants that made my being here possible.

## References

- [1] PHENIX Collaboration, Phys. Rev. Lett. 94, 232301 (2005)
- [2] STAR Collaboration, Phys. Rev. Lett. 91 (2003) 072304
- [3] I.Vitev, hep-ph/0212109
- [4] <http://cmsinfo.cern.ch/outreach/CMSdetectorInfo/MagneticField/page1.html>
- [5] C. Mironov, using PYTHIA and MNR
- [6] C. Mironov et al., CMS-Note (2006).

# Linear Stability Analysis of the Bickley Jet

Jonathan Sperling  
University of Maryland–College Park

August 9, 2007

## Abstract

The Bickley jet was subjected to linear stability analysis in the case of inviscid, incompressible, beta-plane flow. This paper delves into the derivation of the Rayleigh-Kuo equation under the aforesaid conditions, a discussion of the difficulties in analyzing the equation, and highlights the numerical methods that were brought to bear on the problem. Progress was made in developing a program to study the jet's stability, but limited computation time and numerical difficulties did not allow for a full-fledged stability analysis.

## 1 Introduction

The Bickley jet first arose in fluid dynamics as an approximate solution to Prandtl's boundary layer equations [5, 7],

$$\partial_t u + u\partial_x u + v\partial_y u = \partial_t U + U\partial_x U + \frac{\mu}{\rho}\partial_{yy}u \quad (1)$$

$$\partial_x u + \partial_y v = 0 \quad (2)$$

In the above,  $U$  is the mainstream velocity,  $u$  and  $v$  are secondary  $x$  and  $y$  flow velocities, respectively,  $\mu$  is the coefficient of viscosity, and  $\rho$  is the fluid density. These equations were derived from the two-dimensional Navier-Stokes equation as early as 1904 by Ludwig Prandtl, who introduced the notion of boundary layers, at which there is little or no relative velocity between a fluid and bounding solid [3].

Many intense atmospheric and oceanic currents have flow profiles that are centrally peaked and rapidly decay as one approaches the flow boundary. The Bickley jet, which has a velocity profile that goes as  $U(y) = \text{sech}^2 y$ , is often used to model these intense currents, and has as such drawn a great deal of interest regarding questions of jet stability. In this paper, we subject the Bickley jet to a linear stability analysis in the case of inviscid, incompressible, beta-plane flow.

## 2 Derivation of the Stability Equation

### 2.1 The Vorticity Equation

Our analysis begins with the two-dimensional Navier-Stokes equation:

$$\partial_t \tilde{\mathbf{u}} + \tilde{\mathbf{u}} \cdot \nabla \tilde{\mathbf{u}} = -\frac{1}{\rho} \nabla p + \nu \nabla^2 \tilde{\mathbf{u}} + \frac{1}{\rho} \mathbf{F} \quad (3)$$

$$\tilde{\mathbf{u}} = \tilde{u}(x, y, t) \mathbf{e}_x + \tilde{v}(x, y, t) \mathbf{e}_y$$

In the above equation,  $\tilde{\mathbf{u}}$  is the velocity vector,  $\rho$  is again the density,  $\nu$  is the kinematic viscosity (i.e.,  $\frac{\mu}{\rho}$ ),  $p$  is the pressure, and  $\mathbf{F}$  are other forces (per unit volume), such as gravity and fictitious forces due to the fluid's accelerating reference frame [6]. The first two terms compose what is called the substantive derivative of the velocity, commonly written  $\frac{D\tilde{\mathbf{u}}}{Dt}$ , while the last three forcing terms are derived from pressure gradients, viscous stress, and other sources, respectively. In this light, the Navier-Stokes equation is nothing more than a statement of Newton's Second Law.

By taking the curl of the Navier-Stokes equation (3), we arrive at the general vorticity equation:

$$\partial_t \tilde{\boldsymbol{\omega}} + \tilde{\mathbf{u}} \cdot \nabla \tilde{\boldsymbol{\omega}} - \tilde{\boldsymbol{\omega}} \cdot \nabla \tilde{\mathbf{u}} + (\nabla \cdot \tilde{\mathbf{u}}) \tilde{\boldsymbol{\omega}} = \nu \nabla^2 \tilde{\boldsymbol{\omega}} + \frac{1}{\rho} \nabla \times \mathbf{F} \quad (4)$$

In the above,  $\tilde{\boldsymbol{\omega}} = \nabla \times \tilde{\mathbf{u}}$  is the vorticity. For an incompressible flow, we have that  $(\nabla \cdot \tilde{\mathbf{u}}) \tilde{\boldsymbol{\omega}} = 0$ , and, for an inviscid fluid, we have that  $\nu = 0$ . We are thus led to the following simplified equation:

$$\partial_t \tilde{\boldsymbol{\omega}} + \tilde{\mathbf{u}} \cdot \nabla \tilde{\boldsymbol{\omega}} - \tilde{\boldsymbol{\omega}} \cdot \nabla \tilde{\mathbf{u}} = \frac{1}{\rho} \nabla \times \mathbf{F} \quad (5)$$

## 2.2 Perturbation of the Equilibrium Shear Flow

For the purpose of stability analysis, we separate the flow  $\tilde{\mathbf{u}}$  into the equilibrium shear flow of the Bickley jet,  $\mathbf{U}(y) = U(y) \mathbf{e}_x = \text{sech}^2 y \mathbf{e}_x$ , and a small perturbation,  $\mathbf{u}(x, y)$ . That is,

$$\tilde{\mathbf{u}} = \mathbf{U}(y) + \mathbf{u}(x, y) \quad (6)$$

We further observe that for an incompressible flow, with  $\nabla \cdot \tilde{\mathbf{u}} = 0$ , we may write the velocity as the curl of a streamfunction  $\tilde{\psi}$ . We may do the same for the perturbative flow velocity, because the equilibrium velocity is also divergenceless:

$$\tilde{\boldsymbol{\psi}}(x, y) = -\tilde{\psi}(x, y) \mathbf{e}_z, \quad \boldsymbol{\psi}(x, y) = -\psi(x, y) \mathbf{e}_z \quad (7)$$

$$\mathbf{u} = \nabla \times \boldsymbol{\psi} = -\partial_y \psi \mathbf{e}_x + \partial_x \psi \mathbf{e}_y$$

$$\begin{aligned} \tilde{\mathbf{u}} = \nabla \times \tilde{\boldsymbol{\psi}} &= -\partial_y \tilde{\psi} \mathbf{e}_x + \partial_x \tilde{\psi} \mathbf{e}_y \\ &= (U(y) - \partial_y \psi) \mathbf{e}_x + \partial_x \psi \mathbf{e}_y \end{aligned}$$

It follows that we may express the vorticity as the Laplacian of the stream function:

$$\boldsymbol{\omega} = \nabla \times \mathbf{u} = (\partial_{xx} \psi + \partial_{yy} \psi) \mathbf{e}_z \quad (8)$$

$$\begin{aligned}\tilde{\boldsymbol{\omega}} = \nabla \times \tilde{\mathbf{u}} &= (\partial_{xx}\tilde{\psi} + \partial_{yy}\tilde{\psi}) \mathbf{e}_z \\ &= (\partial_{xx}\psi + \partial_{yy}\psi - U'(y)) \mathbf{e}_z\end{aligned}$$

We now substitute (6,7,8) into (5). Starting from the left,

$$\partial_t \tilde{\boldsymbol{\omega}} = \partial_t(\omega - U'(y)) \mathbf{e}_z = \partial_t \boldsymbol{\omega} \quad (9)$$

$$\begin{aligned}\tilde{\mathbf{u}} \cdot \nabla \tilde{\boldsymbol{\omega}} &= \{[(-\partial_y\psi + U) \mathbf{e}_x + \partial_x\psi \mathbf{e}_y] \cdot [\partial_x\omega \mathbf{e}_x + (\partial_y\omega - U'') \mathbf{e}_y]\} \mathbf{e}_z \\ &= \{U\partial_x\omega + [(\partial_x\psi)(\partial_y\omega) - (\partial_x\omega)(\partial_y\psi)] - U''\partial_x\psi\} \mathbf{e}_z \\ &= [U\partial_x\omega - U''\partial_x\psi + J(\psi, \omega)] \mathbf{e}_z\end{aligned} \quad (10)$$

In (10), we have used  $J(\psi, \omega) = (\partial_x\psi)(\partial_y\omega) - (\partial_x\omega)(\partial_y\psi)$ . Continuing,

$$\tilde{\boldsymbol{\omega}} \cdot \nabla \tilde{\mathbf{u}} = (\omega - U')[\partial_z(U - \partial_y\psi) \mathbf{e}_x + \partial_z(\partial_x\psi)] = 0 \quad (11)$$

Taking (9,10,11) together, we may rewrite (5) as

$$[\partial_t\omega + U\partial_x\omega + J(\psi, \omega) - U''\partial_x\psi] \mathbf{e}_z = \frac{1}{\rho} \nabla \times \mathbf{F} \quad (12)$$

The above equation is nonlinear due to the term  $J(\psi, \omega)$ ; however, because the perturbation is assumed to be small at the outset, the other terms dominate. Neglecting the small nonlinear term, we have

$$[\partial_t\omega + U\partial_x\omega - U''\partial_x\psi] \mathbf{e}_z = \frac{1}{\rho} \nabla \times \mathbf{F} \quad (13)$$

### 2.3 The Coriolis Force in the $\beta$ -plane Approximation

We take the Coriolis force to be the dominant external force. The right-hand side of (12) is thus the curl of the Coriolis acceleration:

$$\frac{1}{\rho} \nabla \times \mathbf{F} = \nabla \times (-2\boldsymbol{\Omega} \times \tilde{\mathbf{u}}) \quad (14)$$

$$\boldsymbol{\Omega} = \Omega \mathbf{e}_\Omega = \Omega (\cos \theta \mathbf{e}_z + \sin \theta \mathbf{e}_y)$$

In the above,  $\boldsymbol{\Omega}$  is the angular rotational velocity of the Earth,  $\theta$  is the spherical polar angle,  $\mathbf{e}_z$  is the outward unit normal of the Earth's surface,  $\mathbf{e}_y$  is the northward unit tangent vector, and  $\mathbf{e}_x$  is the eastward unit tangent vector.

In making the  $\beta$ -plane approximation, we assume that the system under consideration subtends a small angle  $\Delta\theta$  from  $\theta = \theta_0$ . The spherical surface  $(\phi, \theta)$  may thus be described by a local map from the neighborhood of  $\theta_0$  to the  $\beta$ -plane  $(x, y)$ . Of interest to us is the following transformation:

$$\cos \theta = \cos \theta_0 + \frac{y}{a} \sin \theta_0 \quad (15)$$

In the above,  $a$  is the radius of the Earth at  $\theta_0$ .

With the velocity  $\tilde{\mathbf{u}}$  given by (3), the z-component of the curl of the cross-product in (14) evaluates to

$$\begin{aligned}
[\nabla \times (-2\boldsymbol{\Omega} \times \tilde{\mathbf{u}})] \cdot \mathbf{e}_z &= -2\Omega \left\{ \partial_x \left[ \tilde{u} \left( \cos \theta_0 + \frac{y}{a} \sin \theta_0 \right) \right] \right. \\
&\quad \left. + \partial_y \left[ \tilde{v} \left( \cos \theta_0 + \frac{y}{a} \sin \theta_0 \right) \right] \right\} \\
&= -2\Omega \left\{ [(\nabla \cdot \tilde{\mathbf{u}}) \cos \theta] + \frac{\tilde{v}}{a} \sin \theta_0 \right\} \\
&= -\frac{2\Omega}{a} \tilde{v} \sin \theta_0 = -\beta \tilde{v}
\end{aligned} \tag{16}$$

In the above,  $\beta = \frac{2\Omega}{a} \sin \theta_0$ .

Finally, recalling from (7) that  $\tilde{v} = \partial_x \psi$ , we substitute (16) into (13) to get an equation entirely in terms of  $U, \psi$ , and  $\omega$ :

$$\partial_t \omega + U \partial_x \omega = (U'' - \beta) \partial_x \psi \tag{17}$$

## 2.4 Fourier Decomposition of the Stream Function

The next step in the stability analysis is to Fourier decompose the stream function [2]:

$$\psi(x, y, t) = \hat{\psi}(y) e^{ik(x-ct)} \tag{18}$$

Substituting equation (18) into equation (17), we arrive at the following:

$$\partial_t \omega = \partial_t (\partial_{xx} \psi + \partial_{yy} \psi) \sim -i\omega (\hat{\psi}'' - k^2 \hat{\psi}) \tag{19}$$

$$U \partial_x \omega = U \partial_x (\partial_{xx} \psi + \partial_{yy} \psi) \sim ikU (\hat{\psi}'' - k^2 \hat{\psi}) \tag{20}$$

$$(U'' - \beta) \partial_x \psi \sim ik(U'' - \beta) \hat{\psi} \tag{21}$$

Next, we substitute equations (19,20,21) into equation (17), and then divide everything by  $ik$  to arrive at the following ordinary differential equation:

$$(U - c)(\hat{\psi}'' - k^2 \hat{\psi}) = (U'' - \beta) \hat{\psi} \tag{22}$$

This is the Rayleigh-Kuo equation, which, together with the appropriate boundary conditions, describes the linear stability of an inviscid, incompressible shear flow [1, 2].

## 2.5 Significance of the Rayleigh-Kuo Equation

With the Rayleigh-Kuo equation, the linear stability problem is reduced to a two-point boundary condition eigenvalue problem in  $c = c_r + ic_i$ . Returning to equation (18), we see that the stream function  $\psi$  is unstable over time if and only if  $c_i \neq 0$ .

Typical boundary conditions for (22) are  $\hat{\psi}(-L) = \hat{\psi}(L) = 0$ , with further constraints to specify the parity of the solution. Numerical analysis of the eigenvalue problem is discussed later on.

### 3 Smoothing of the Stream Function

#### 3.1 Scale and Boundary Condition Sensitivity

For large  $k$ , with  $k^2 \gg \frac{\beta}{c_r}$  and  $c_i \ll c_r$ , and for  $y$  such that  $U = \text{sech}^2(y) \ll |c|$ , the eigenfunction  $\hat{\psi}$  resembles exponential decay [1]:

$$\hat{\psi}'' \approx k^2 \hat{\psi} \quad (23)$$

Thus the solution is fairly insensitive to boundary conditions at  $y = \pm L$ , and the problem is correspondingly amenable to direct numerical techniques. However, for small  $k$ , the solution begins to deviate significantly from an exponential, and hence becomes very sensitive to boundary conditions. The eigenfunctions in this regime are very difficult to find numerically, and thus we must employ more powerful analytical tools to characterize the flow stability.

#### 3.2 The Smoothed Stream Function

The smoothed stream function  $\psi_s$  satisfies the following differential equation:

$$\nabla^2 \psi_s = \partial_{xx} \psi_s + \partial_{yy} \psi_s = \frac{1}{\alpha^2} (\psi_s - \psi) \quad (24)$$

Thus for  $\alpha^2 \ll 1$ ,  $\psi_s \rightarrow \hat{\psi}$ , whereas for  $\alpha^2 \gg 1$ ,  $\psi_s$  approaches a solution to Laplace's equation.

We assume a separable solution  $\psi_s$  of the form

$$\psi_s = \phi(y) e^{ik(x-ct)} \quad (25)$$

Substituting (25) and (18) into (24), dividing by  $e^{ik(x-ct)}$ , and multiplying by  $\alpha^2$ , we arrive at the equation

$$\hat{\psi} = -\alpha^2 \phi'' + (k^2 \alpha^2 + 1) \phi \quad (26)$$

In the limit that  $\alpha$  is large and  $k$  is small, the highly oscillatory nature of the solution is diminished, and hence the eigenfunction is smoothed.

We substitute equation (26) into equation (22) to arrive at the fourth order stability equation

$$\phi^{(4)} - \left[ \frac{2k^2 \alpha^2 + 1}{\alpha^2 (U - c)} + \frac{U'' - \beta}{U - c} \right] \phi^{(2)} + \left[ \frac{k^4 \alpha^2 + k^2 + (U'' - \beta)(k^2 \alpha^2 + 1)}{\alpha^2 (U - c)} \right] \phi \quad (27)$$

Unfortunately, due to time constraints, the solution to this higher-order problem could not be pursued numerically.

## 4 Numerical Analysis

### 4.1 Finite Difference Equations and Boundary Conditions

Equation (22) was solved numerically in Fortran 77 via the relaxation method, with code based heavily on examples provided in §16.3 and §16.4 of *Numerical Recipes*[4].

The complex, second order differential equation (22) was transformed into a system of six real, first order differential equations, which were then approximated by central finite differencing. The dependent variables were renamed  $y_1, y_2, \dots, y_6$ , with independent variable  $x$ . Because  $k$  was used for the index in the finite difference equations, the wavenumber was replaced by  $\kappa$ . The relationship between the components of (22) and the components of the system first-order differential equations (and FDEs) are given below:

$$\begin{aligned} y_1 &= \Re(\hat{\psi}), \quad y_2 = \Im(\hat{\psi}), \quad y_3 = y'_1, \quad y_4 = y'_2 \\ y_5 &= \Re(c) = c_r, \quad y_6 = \Im(c) = c_i, \quad k \rightarrow \kappa, \quad y \rightarrow x \end{aligned} \quad (28)$$

The six first-order differential equations are:

$$\begin{aligned} y'_1 - y_3 &= 0, \quad y'_2 - y_4 = 0 \\ (U - y_5)(y'_3 - \kappa^2 y_1) + y_6(y'_4 - \kappa^2 y_2) - (U'' - \beta)y_1 &= 0 \\ (U - y_5)(y'_4 - \kappa^2 y_2) - y_6(y'_3 - \kappa^2 y_1) - (U'' - \beta)y_2 &= 0 \\ y'_5 &= 0, \quad y'_6 = 0 \end{aligned} \quad (29)$$

The six corresponding finite difference equations are:

$$\begin{aligned} y_{1,k} - y_{1,k-1} - 0.5(x_k - x_{k-1})(y_{3,k} + y_{3,k-1}) &= 0 \\ y_{2,k} - y_{2,k-1} - 0.5(x_k - x_{k-1})(y_{4,k} + y_{4,k-1}) &= 0 \end{aligned} \quad (30)$$

$$\begin{aligned} [U &- 0.5(y_{5,k} + y_{5,k-1})][y_{3,k} - y_{3,k-1} - 0.5\kappa^2(x_k - x_{k-1})(y_{1,k} + y_{1,k-1})] \\ + &0.5(y_{6,k} + y_{6,k-1})[y_{4,k} - y_{4,k-1} - 0.5\kappa^2(x_k - x_{k-1})(y_{2,k} + y_{2,k-1})] \\ - &0.5(U'' - \beta)(x_k - x_{k-1})(y_{1,k} + y_{1,k-1}) = 0 \end{aligned}$$

$$\begin{aligned} [U &- 0.5(y_{5,k} + y_{5,k-1})][y_{4,k} - y_{4,k-1} - 0.5\kappa^2(x_k - x_{k-1})(y_{2,k} + y_{2,k-1})] \\ - &0.5(y_{6,k} + y_{6,k-1})[y_{3,k} - y_{3,k-1} - 0.5\kappa^2(x_k - x_{k-1})(y_{1,k} + y_{1,k-1})] \\ - &0.5(U'' - \beta)(x_k - x_{k-1})(y_{2,k} + y_{2,k-1}) = 0 \end{aligned}$$

$$y_{5,k} - y_{5,k-1} = 0, \quad y_{6,k} - y_{6,k-1} = 0$$

These six equations require six boundary conditions, of which, as discussed in §2.5, those at  $x = \pm L$  are most obvious. However, due to the nature of the problem, the most convenient boundaries for the finite difference equations are  $x_1 = -L$  and  $x_M = 0$ , where  $M$  is the number of points in the mesh.

The boundary conditions, which are given below, are necessarily different for even and odd eigenfunctions:

$$\text{Even and Odd Boundary Conditions :} \quad (31)$$

| <u>Odd</u>          | <u>Even</u>         |
|---------------------|---------------------|
| $y_{1,1} = 0$       | $y_{1,1} = 0$       |
| $y_{2,1} = 0$       | $y_{2,1} = 0$       |
| $y_{1,M} = 0$       | $y_{1,M} - A_r = 0$ |
| $y_{2,M} = 0$       | $y_{2,M} - A_i = 0$ |
| $y_{3,M} - B_r = 0$ | $y_{3,M} = 0$       |
| $y_{4,M} - B_i = 0$ | $y_{4,M} = 0$       |

In the above,  $A_r$ ,  $A_i$ ,  $B_r$ , and  $B_i$  are constants.

Taken together, equations (30) and (31) complete the finite difference approximation to the complex, second order, two-point boundary condition eigenvalue problem (22). However, these equations are still not easily solved over all ranges of  $\beta$ , and thus special attention must be given to the structuring of the mesh.

## 4.2 Singular Behavior and Variable Meshspacing

When  $c$  is real and  $(U - c) = 0$ , equation (22) exhibits singularities [1]. In such a case, the physical constraints of the system require that  $(U'' - \beta) \rightarrow 0$  as well. Thus, though we cannot know beforehand the value of  $c$ , we can nevertheless anticipate singular behavior in the vicinity of a point  $x = x_0$  such that  $(U''(x_0) - \beta) = 0$ . This condition can occur over the range  $-2 \leq \beta \leq \frac{2}{3}$ .

In order to compensate for singular behavior, it is desirable to concentrate sections of the FDE grid about the singular point. (Where singularities cannot occur, uniform meshspacing suffices.) The problem is first to locate  $x_0$ , and then to devise a consistent way to space the mesh.

In order to find  $x_0$ , we employed the simultaneous bisection / Newton-Raphson method in §9.4 of *Numerical Recipes*[4]. In order to set the variable meshspacing, we solved a separate finite differencing equation by the same relaxation methods described in §4.1 of this paper. The finite difference equations governing the meshspacing were the following:

$$x_k - x_{k-1} - h \left\{ 1 - \alpha \left[ \frac{0.25 (\Delta_k + \Delta_{k-1})^2 - [0.5(x_k + x_{k-1}) - x_0]^2}{0.25 (\Delta_k + \Delta_{k-1})^2 + [0.5(x_k + x_{k-1}) - x_0]^2} \right] \right\} = 0$$

$$\Delta_k - \Delta_{k-1} = 0 \tag{32}$$

In the above,  $0 < \alpha < 1$  and  $h$  is the meshspacing for a uniform mesh.

The two finite difference equations (32) were then constrained to match the two boundary conditions

$$x_1 = -L, \quad x_M = 0 \tag{33}$$

In this way, the problem of meshspacing was reduced to a two-point boundary condition eigenvalue problem. Meshspacing was confined to the range  $h(1 + \alpha) < \Delta x \leq h(1 - \alpha)$ , with many more points concentrated in the neighborhood of  $x_0$  than elsewhere.

The importance of variable meshspacing is poignantly demonstrated in Figure 1, on the top of the next page, where the solution with variable meshspacing resolves far more detail—even with far fewer datapoints—than does the solution with uniform meshspacing.

## 5 Results

Results from the numerical analysis were fairly limited, due to insufficient computation time and the difficulty of finding the eigenvalues for certain regions of the  $(\beta, k)$ -plane. There was insufficient time to sweep a large region of the

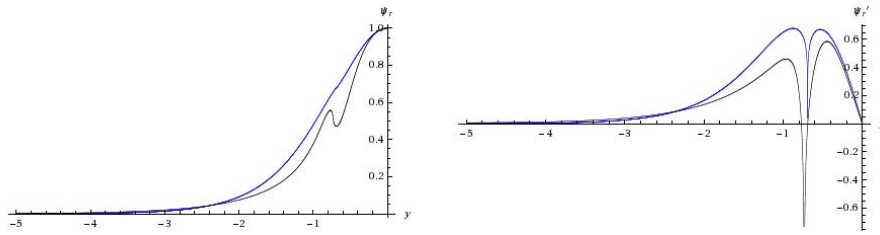


Figure 1: Plots of  $\psi_r(y)$  (left) and its derivative,  $\psi'_r(y)$  (right), both with variable meshspacing (black) and with uniform meshspacing (blue). Equation parameters for these even eigenfunctions were  $L = 5.0$ ,  $\beta = 0.0$ ,  $k = 1.9$ . The variable meshspacing solution required only 3,000 points, whereas the uniform meshspacing solution required as many as 10,000 points, and still failed to resolve detailed behavior at  $y_0$ .

plane with a small enough step size and large iteration number. Density plots of eigenvalues for both even and odd eigenfunctions are shown in Figure 2, located at the end of the paper.

It is clear from the density plots that the problem is computationally difficult for smaller values of  $k$ , especially in the region  $|k| < 0.5$ . This holds for both even and odd eigenfunctions, and is at least partially due to the reasons discussed in §3.1 of this paper. The linear stability analysis failed in that we were not able to identify and categorize regions of stability from our data.

## 6 Acknowledgments

I would first like to acknowledge my mentor, Dr. Balasubramanya Nadiga of CCS-2, for giving me the opportunity to work in fluid dynamics and learn about numerical methods. I would also like to thank Drs. Norm Magee and James Colgan of T-4 for doing such a great job as caretakers of the students of the Los Alamos Summer School.

Dr. Colgan deserves special thanks for all the help that he has given me in my mentor's absence. Without his help, it is doubtful that I would ever have had a working program for the numerical analysis.

## References

- [1] Balmforth NJ & Piccolo C. "The onset of meandering in a barotropic jet." *J. Fluid Mech.*, 449: 85-114, 2001.
- [2] Drazin PG & Reid WH. *Hydrodynamic Stability*. Cambridge University Press, Cambridge (1981).
- [3] McMahon, Niall. "Derivation of boundary-layer equations for two-dimensional flow." <http://student.dcu.ie/~mcmahon4/blderivation.pdf>. Downloaded July 6, 2007.
- [4] Press WH, et al. *Numerical Recipes: The Art of Scientific Computing*. Cambridge University Press, Cambridge (1986).

- [5] Swaters, Gordon. "The evolution of near-singular modes of the Bickley jet."  
Phys. Fluids, Vol. 11, No. 9, September 1999.
- [6] Tritton, D.J. *Physical Fluid Dynamics*, 2nd ed. Clarendon Press, Oxford (1988).
- [7] Weisstein, Eric W. "Prandtl's Boundary Layer Equations."  
From Mathworld—A Wolfram Web Resource.  
<http://mathworld.wolfram.com/PrandtlsBoundaryLayerEquations.html>.  
Downloaded July 6, 2007.

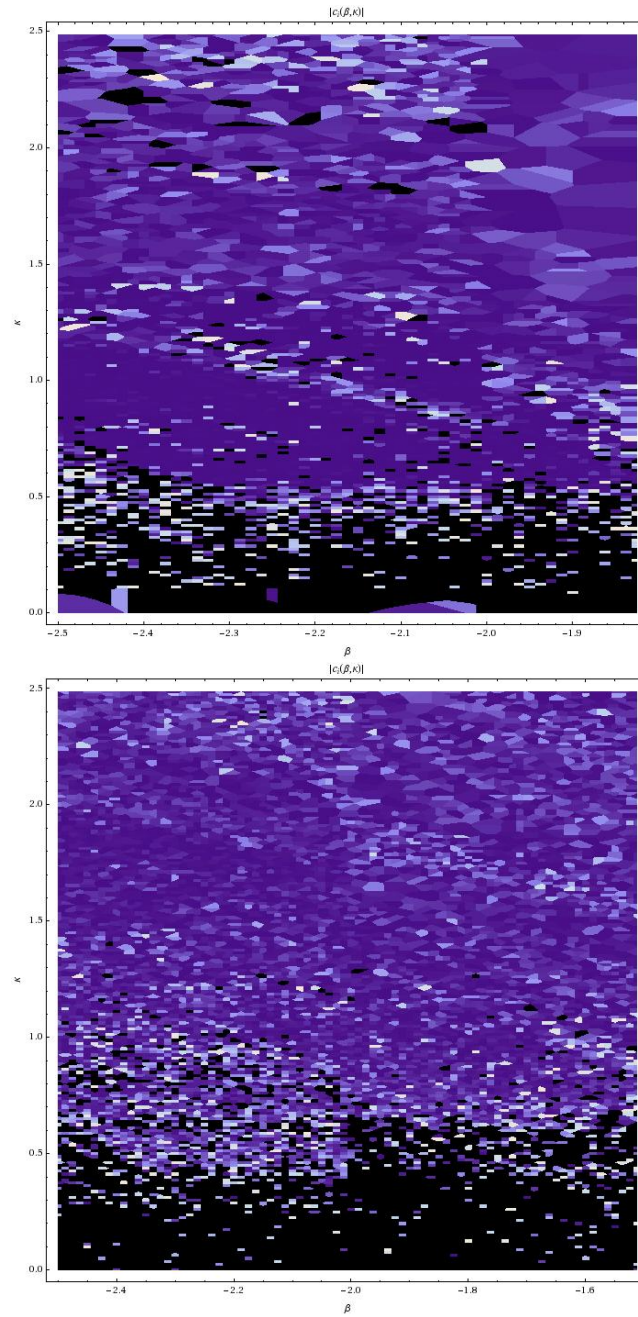


Figure 2: Density plots for the magnitude of imaginary eigenvalues for even (top) and odd (bottom) eigenfunctions. Lighter areas represent greater magnitude, with the exception of black, which represents missing data. The data shown is for  $L = 10.0$ .

# SARS Infection Dynamics in Lung Epithelial Tissue

Christine Suss

*Clarkson University, Potsdam, New York and  
T-7 Mathematical Modeling and Analysis, Los Alamos National Laboratory*

Kristin White

*T-7 Mathematical Modeling and Analysis, Los Alamos National Laboratory and  
Allegheny College, Meadville, Pennsylvania*

Mentor: Yi Jiang

*T-7 Mathematical Modeling and Analysis, Los Alamos National Laboratory*

(Dated: August 10, 2007)

In 2002 and 2003, there was a severe acute respiratory syndrome (SARS) outbreak where symptoms included oxygen desaturation, mechanical ventilation, diarrhea, hepatic dysfunction, and death [7]. With an infection like this, it is important to understand how the virus infects and spreads throughout the lung tissue. With this knowledge, we can prevent and control future outbreaks. Our model is based on an influenza model that models influenza dynamics on an epithelial cell monolayer in vitro. In addition to this existing model, we have added constant flow of periciliary liquid (PCL), driven by cilia beating, on the spread of the virus. With this new model we can better our understanding of how viruses interact with and penetrate our first line of defense, the epithelial tissue. As time progresses, the addition of more parameters will be necessary. The next step may be to focus on mucus flow as opposed to just PCL, and the force created by the cilia.

## I. INTRODUCTION

Severe acute respiratory syndrome is caused by the SARS coronavirus. Early symptoms are often flu-like. They may include fever, myalgia, lethargy, gastrointestinal symptoms, cough, sore throat and other non-specific symptoms. However, not all these symptoms are common among all patients. In fact, the only one they tend to share is a fever above 100.4 °F and often, a shortness of breath may occur later on after the infection has taken place. These symptoms usually appear within 2-3 days.

As the SARS outbreak advanced, the mortality rate approached 10%. Treatment seemed to be difficult. Antibiotics are ineffective. The only near solution provided was isolation.

With such a global threat, it is important for us to learn more about this syndrome. One thing we can do is gain knowledge about the viral dynamics in lung epithelial tissue. We will do this by creating an Agent-Based Model, which is a computer program that encodes the cell's behavior and laws for interacting with other cells and the environment.

We will start with an Influenza model provided by Beauchemin et al. This model is represented as a 2-D hexagonal lattice where each site signifies one epithelial cell. In addition, we will add a constant flow denoting mucus flow propelled by cilia beating. Recent results from in vitro experiments revealed that large numbers of virions were being trapped by the mucus<sup>[2]</sup>. This plays a critical role in controlling the rate of spread of the viral infection.

The cilia's primary purpose is to move fluid over the surface of the cell and propel single cells through a fluid. They also sweep layers of mucus, together with trapped particles of dust and dead cells, up toward the mouth, where they are swallowed and removed. For our purpose, we will look at the beating the cilia does on the periciliary fluid layer. The PCL provides a low viscosity medium, like water, between the cell surface and the mucus layer in which the cilia can beat and propel the mucus blanket<sup>[9]</sup>. The cilia extend into the PCL and only their tips are embedded in the mucus layer. Cilia move in two phases. The first phase is known as the effective stroke, which moves as a straight rod and generates thrust against strong viscous resistance. The second phase, the recovery stroke rolls close to the surface in tangential motion and avoids viscous resistance. The cilia can differ the type of their metachronism in response to changes in the environment, such as changed fluid viscosity, which can be caused by an infection.

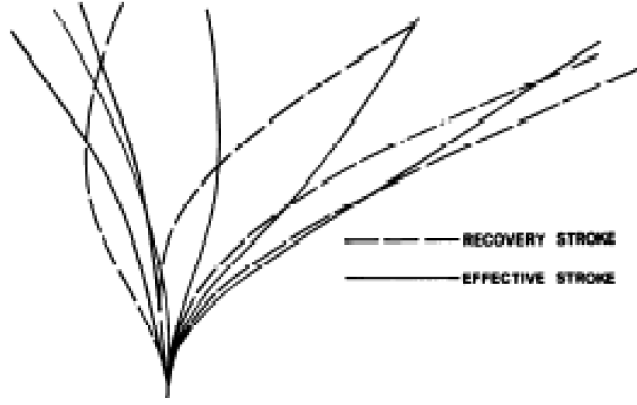


Figure 1: Image of the effective and recovery stroke of a cilium<sup>[6]</sup>

## II. ASSUMPTIONS

For the simplicity of our model, we will have to make a few assumptions. We will allow maximal spacing between cilia where they are still capable of influencing one another, and no changes of the beat patterns in the presence of neighboring cilia.

We will consider the beating of the cilia to be in an incompressible Newtonian fluid. This is a safe assumption because PCL is like salty water. In another words, we can neglect the effect of inertial forces in the Navier Stokes equation because the cilia are operating in a low Reynold's number environment. This now leaves us with the Stokes equation, which reads

$$0 = -\nabla p + \mu \nabla^2 \nu + f, \quad (1)$$

where  $\nabla \cdot \nu = 0$ ,  $-\nabla p$  is the pressure gradient,  $\mu \nabla^2 \nu$  represents the viscosity, and  $f$  indicates other forces. No-slip conditions will also be satisfied. This means that at a boundary, fluids have zero velocity relative to that boundary. We can think of the outermost molecule of a fluid sticking to the surfaces past which it flows.

In mucus movement in the lung, gravity, generally, is thought to be unimportant. When the serous layer becomes thin, less than the cilia length, then gravity is negligible<sup>[3]</sup>.

## III. INFLUENZA MODEL

In this model, the assumption is made that there is no cell division over the course of the infection<sup>[2]</sup>. The same assumption will be made with the SARS infection.

The diffusion of virions is modeled using a finite difference approximation on a hexagonal grid to the diffusion equation (Equation 2),

$$\frac{\partial V}{\partial t} = D_V \nabla^2 V \quad (2)$$

where  $V$  is the concentration of virions,  $D_V$  is the diffusion coefficient, which measures how fast virions spread; and  $\nabla^2$  represents the Laplacian.

In hexagonal coordinates  $(m, n)$  as a function of the 6 honeycomb neighbors, we can express the previous equation as a difference equation (Equation 3),

$$\frac{V_{m,n}^{t+1} - V_{m,n}^t}{\Delta t} = \frac{D_V}{(\Delta x)^2} \left[ -3V_{m,n}^t + \frac{1}{2} \sum_{nei} V_{nei}^t \right] \quad (3)$$

where  $V_{m,n}^{t+1}$  at time  $t+1$  is a function of  $V_{m,n}^t$  and  $\sum_{nei} V_{nei}^t$  is the sum of the virion concentration at all 6 neighbors at time  $t$ .

The grid spacing ( $\Delta x$ ) represents the diameter of the epithelial cells and  $\Delta t$  is a duration of a time step.

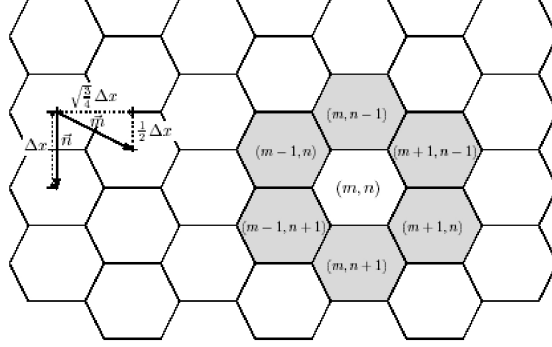


Figure 2: Geometry of the agent based model's hexagonal grid. The honeycomb neighborhood is represented in gray, and base vectors  $\vec{m}$  and  $\vec{n}$  are shown and expressed as a function of  $\Delta x$ , which identifies the grid spacing, the mean diameter of an epithelial cell<sup>[2]</sup>.

#### IV. APPROACH

The next addition to this model is to add a constant flow. In which case, our new equation will then read

$$\frac{\partial V}{\partial t} = D_V \nabla^2 V - (\vec{f} \cdot \vec{\nabla} V), \quad (4)$$

where  $\vec{f} \cdot \vec{\nabla} V$  is the flow or velocity field.

Before implementing this equation into our agent-based model, we must break down  $\vec{f} \cdot \vec{\nabla} V$ . We will first do the finite difference approximation for  $\vec{\nabla} V$  on a hexagonal lattice. Geometric definitions are the same as proposed in Figure 2. The partial derivative in  $x$  is

$$\frac{\partial V}{\partial x} = \frac{\sqrt{3}}{2} \left( \frac{V_{m+1,n-1} - V_{m-1,n+1}}{2\Delta x} + \frac{V_{m+1,n} - V_{m-1,n}}{2\Delta x} \right). \quad (5)$$

The partial derivative in  $y$  is

$$\frac{\partial V}{\partial y} = \frac{V_{m,n-1} - V_{m,n+1}}{\Delta x} + \frac{1}{2} \left( \frac{V_{m+1,n-1} - V_{m-1,n+1}}{2\Delta x} + \frac{V_{m-1,n} - V_{m+1,n}}{2\Delta x} \right). \quad (6)$$

We now have the definition for  $\vec{\nabla} V$ :

$$\vec{\nabla}V = \frac{\partial V}{\partial x} + \frac{\partial V}{\partial y}. \quad (7)$$

The next question is what is the proposed flow field? The flow field can be represented as

$$\vec{f} = r \sin(\omega t) \hat{\theta}. \quad (8)$$

The following definitions will aid in putting the flow into our code:

$$x = r \cos \theta \quad (9)$$

$$y = r \sin \theta \quad (10)$$

$$\hat{\theta} = -\sin(\theta)\hat{x} + \cos(\theta)\hat{y}. \quad (11)$$

We can change  $\vec{f} = r \sin(\omega t) \hat{\theta}$  into Cartesian coordinates and get

$$\vec{f} = -\frac{y^2}{\sqrt{x^2 + y^2}}\hat{x} + \frac{xy}{\sqrt{x^2 + y^2}}\hat{y}. \quad (12)$$

Now our flow field  $\vec{f} \cdot \vec{\nabla}V = f_x \frac{\partial V}{\partial x} + f_y \frac{\partial V}{\partial y}$  is ready to implement into our agent-based model.

## V. RESULTS

After programming in C and Matlab, we have some interesting, yet not surprising results. Our results can be seen on a 200 x 200 grid, which represents 40,000 epithelial cells. This site is like taking a square out of a circular experimental well.

The first step was to run the code with the SARS infection without flow being added. It is clear through the simulation that the viruses are freely diffusing. The spread is very homogeneous.

The next step was to run the code with the addition of flow. The infection pattern was greatly altered. This time, in the simulation, the observation was made that there was an indicated direction where the healthy cells were being infected. The viruses are being moved in one particular direction.

By viewing the simulations, and both figure 3 and 4, we can see that adding constant flow does significantly affect the infection pattern. Infection and the death of cells occurs much faster with the flow being added.

We can also change the infection pattern because of the flexibility of our code. We are capable of changing multiple parameters. For instance, as seen in figures 3 and 4, we decided to take a look at what would happen if we started with 100 viruses vs. 500. As predicted, the peak of infection affects a greater amount of cells early on with an initial number of viruses of 500 than with 100. As the initial number of viruses increases, the faster the healthy cells will be infected.

## VI. FUTURE WORK

This model is a simple one, but it is a start to modeling infectious diseases in lung epithelial tissue. For better accuracy, it will later be necessary to add the flow of mucus. Mucus is considered to be visco-elastic. This means that the fluid has both fluid and solid properties which is characterized by a relaxation that is fairly large in comparison to the beat frequency of the cilium. It is suggested that mucus flow rates of 10-20 mm/min in trachea. The movement

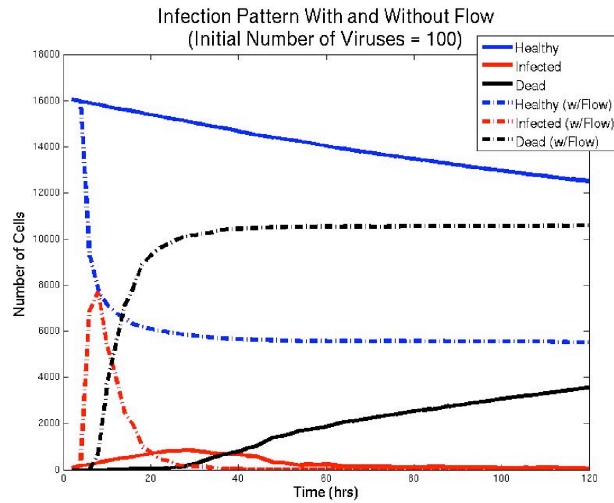


Figure 3: Infection Pattern With and Without Flow. The initial number of viruses placed in the square patch is 100. Infection and death of cells occurs much earlier in the 120 hour time period when flow is added to the model. The peak of infection is substantially greater with flow as opposed to without.

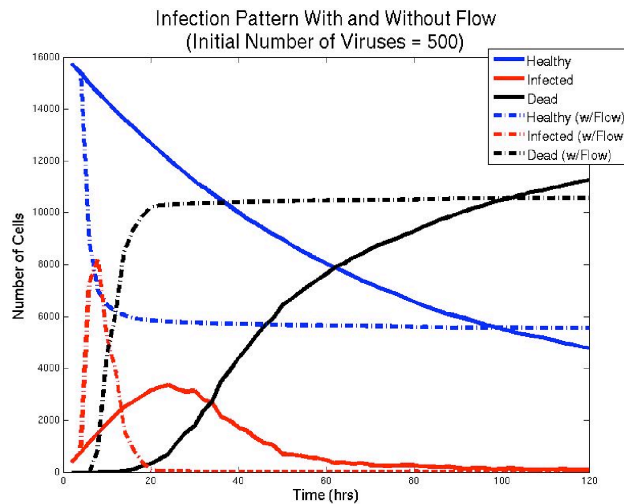


Figure 4: Infection Pattern With and Without Flow. The initial number of viruses placed in the square patch is 500. In this graph, it is clear that the curves between the infection with and without flow hold the same shape.

of the mucus depends on the viscosity and depth of the serous layer, therefore, gravity can also be an important factor to take into consideration<sup>[3]</sup>. As we push even further along, the model may also be extended to a two layer model: the PCL and mucus. This is an important consideration because the cilia interact with both layers. With cilia beating, there are many other factors that need to be considered. For instance, as the number of the cilia in the row increases, there is approximately a 3-fold decrease in the energetic cost in a beat cycle. So, as death occurs, the intercilia spacing will increase. This means that the interactions between the cilia weaken<sup>[5]</sup>.

## Acknowledgments

I would like to thank Yi Jiang in T-7 Mathematical Modeling and Analysis for mentoring us, and Yilin Wu of the University of Notre Dame for helping with specific questions that arose during research. Special thanks to colleague and partner Kristin White of Allegheny College for all of her additions to this project.

## VII. REFERENCES

- [1] Alberts, Bruce, Dennis Bray, Julian Lewis, Martin Raff, Keith Roberts, and James D. Watson. *Molecular Biology of the Cell*. 3rd ed. New York: Garland, 1994. 815-820.
- [2] Beauchemin, Catherine, Stephanie Forrest, and Frederick T. Koster. *Modeling Influenza Viral Dynamics in Tissue*. University of New Mexico, Lovelace Respiratory Research Institute. Springer-Verlag Berlin Heidelberg, 2006. 23-36.
- [3] Blake, John. *On the Movement of Mucus in the Lung*. Trinity College. Great Britain: Pergamon P, 1975. 179-190.
- [4] Gueron, Shay, and Konstantin Levit-Gurevich. "Computation of the Internal Forces in Cilia: Application to Ciliary Motion, the Effects of Viscosity, and Cilia Interactions." *Biophysical Journal* 74 (1998): 1658-1676.
- [5] Gueron, Shay, and Konstantin Levit-Gurevich. *Energetic Considerations of Ciliary Beating and the Advantage of Metachronal Coordination*. University of Haifa, Technion-Israel Institute of Technology. PNAS, 1999. 12240-12245.
- [6] Gueron, Shay, and Nadav Liron. "Ciliary Motion Modeling, and Dynamic Multicilia Interactions." *Biophysical Journal* 63 (1992): 1045-1058.
- [7] Hung, I.F.N., V.C.C. Cheng, A.K.L. Wu, B.S.F. Tang, K.H. Chan, C.M. Chu, et al. "Viral Loads in Clinical Specimens and SARS Manifestations." *Emerging Infectious Diseases* 10 (2004).
- [8] King, Malcolm. *Physiology of Mucus Clearance*. University of Alberta. 2006. s212-s214.
- [9] Samet, James M., and Pi-Wan Cheng. "The Role of Airway Mucus in Pulmonary Toxicology." *Environmental Health Perspectives* 102 (1994): 89-103. 26 June 2007 |<http://www.jstor.org>.
- [10] Smith, D J., A Gaffney, and J R. Blake. *A Viscoelastic Traction Layer Model of Muco-Ciliary Transport*. University of Birmingham. 2007. 289-327.

# Calculation of Elastic Differential Cross Sections for Proton-Helium Collisions Through the Use of High Performance Computing

Thomas G. Wong  
*Santa Clara University, Santa Clara, California 95053*

L. Matthew Foster and James P. Colgan  
*Theoretical Division, T-4, Los Alamos National Laboratory, New Mexico*

Don H. Madison  
*Physics Department, University of Missouri-Rolla, Rolla, Missouri, 65401*

## INTRODUCTION

Interest in ion-impact ionization has increased in recent years due to new applications in plasma physics, surface physics, and others. Foster *et al.* recently showed that a distorted wave treatment of electron-impact ionization is necessary to get accurate results for fully differential cross sections [1]. However, this has not been calculated for heavy ions due to the likely requirement that thousands of terms are needed to do a partial wave analysis since the number of terms scales with momentum [2]. This project uses the high performance computing resources available at Los Alamos National Laboratory to calculate the elastic differential cross sections for proton-helium collisions using a distorted wave treatment and partial wave analysis. By comparing the results with existing calculations, the feasibility of such a treatment for heavy ion-impact ionization can be determined.

## ATOMIC THEORY

### Classical Scattering Theory

In Fig. 1, a projectile is incident through an infinitesimal cross-sectional area,  $d\sigma$ , and scatters through a corresponding solid angle,  $d\Omega$ . This scattering can be described using the differential cross section,  $d\sigma/d\Omega$ . Importantly, this can be measured experimentally and can be used to test theory. Thus, the goal is to compute  $d\sigma/d\Omega$  using theory to see if it matches with experiment.

### Quantum Scattering Theory

Assuming azimuthal symmetry (i.e.,  $\phi$ -independence), the solution to the Schrödinger Equation is the superposition of an incident plane wave and an outgoing spherical wave, as shown in Fig. 2. That is,

$$\psi(r, \theta) = A \left[ e^{ikz} + f(k, \theta) \frac{e^{ikr}}{r} \right],$$

where A is a normalization constant and  $f(k, \theta)$  is called the scattering amplitude, which weights how much of the wave function is incident and how much is outgoing. The  $r$  in the denominator is for normalization purposes and is

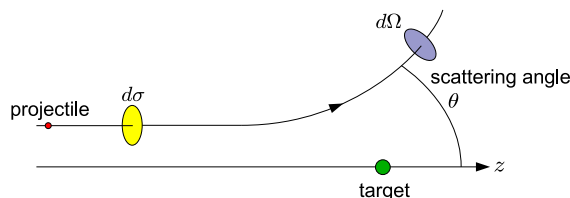


FIG. 1: Classical scattering of a projectile off a target.

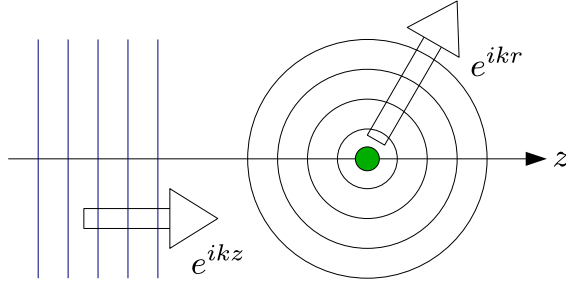


FIG. 2: Quantum scattering of a projectile off a target.

necessary for the wave function to integrate properly. Assuming a solution of this form results in

$$\frac{d\sigma}{d\Omega} = |f(k, \theta)|^2. \quad (1)$$

The idea is to find the scattering amplitude, then use Eq. (1) to calculate the differential cross section.

### Partial Wave Analysis

For a central potential,  $V(r)$ , the Schrödinger Equation yields separable solutions:  $\psi(r, \theta, \phi) = R(r)Y_l^m(\theta, \phi)$ , where  $Y_l^m$  is a spherical harmonic. Substituting  $u(r) = rR(r)$ , the radial equation becomes (in atomic units)

$$\left[ \frac{d^2}{dr^2} - \frac{l(l+1)}{r^2} - U(r) + k^2 \right] u = 0, \quad (2)$$

where  $U(r) = 2m \cdot V(r)$  and  $k = \sqrt{2mE}$ . This equation cannot be solved analytically. However, the asymptotic form can. As shown in Fig. 3, the potential far away goes to zero, leaving

$$\left[ \frac{d^2}{dr^2} - \frac{l(l+1)}{r^2} + k^2 \right] u = 0. \quad (3)$$

This potential-less radial equation has solutions  $u(r) = Arj_l(kr) + Brn_l(kr)$ , where  $j_l(x)$  and  $n_l(x)$  are the spherical Bessel and Neumann functions, respectively. Boundary conditions for the radial equation in Eq. (2) and its asymptotic form in Eq. (3) yields

$$f(k, \theta) = \sum_{l=0}^{\infty} \frac{2l+1}{k} e^{im} \sin(\eta_l) P_l(\cos \theta) \quad (4)$$

and

$$\tan \eta_l = \frac{u(x_2)x_1j_l(kx_1) - u(x_1)x_2j_l(kx_2)}{u(x_2)x_1n_l(kx_1) - u(x_1)x_2n_l(kx_2)}, \quad (5)$$

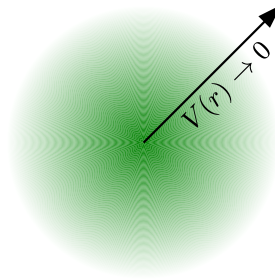


FIG. 3: For neutral helium, the potential goes to zero outside the atom.

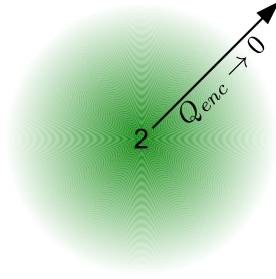


FIG. 4: For neutral helium, the enclosed/effective charge ranges from two (i.e., the nuclear charge) to zero outside the atom.

where  $\eta_l$  is called the phase shift and  $P_l(x)$  is the  $l$ th Legendre Polynomial [3, 4].  $x_1$  and  $x_2$  are points where the potential is effectively zero (i.e., where the boundary condition occurs). Each term in the summation is called a partial wave.

The idea is to solve Eq. (2) for each partial wave to a distance where the potential is effectively zero, yielding  $x_1$ ,  $x_2$ ,  $u(x_1)$ , and  $u(x_2)$ . Then, use Eq. (5) to find the corresponding phase shifts and Eq. (4) to find the scattering amplitude. Finally, use Eq. (1) to find the differential cross section.

### Screened Potential/Distorted Wave

The charge outside a neutral helium atom is, obviously, zero. Inside, however, the charge is a function of radial distance due to screening by electrons, as shown in Fig. 4. Using known approximations for the wave function of Helium, the charge distribution of the electrons can be found. To simplify the calculation, the electrons are assumed to be in spherically symmetric shells so that the Shell Theorem can be used. In addition, only the case where the radial distance of interest,  $r$ , is inside or outside both electrons is considered. The case where  $r$  is between two electron shells is ignored. Using this, the effective charge can be calculated as

$$Q(r) = Q_{enc}(r) = 2(1 - P(r_1 < r, r_2 < r)), \quad (6)$$

where  $P(r_1 < r, r_2 < r)$  is the probability that both electrons are inside the radial distance,  $r$ . By Gauss's Law, the screened potential is

$$V(r) = \frac{Q_{enc}(r)}{r}. \quad (7)$$

Solving the radial equation in Eq. (2) using this screened potential is solving by a distorted wave approach.

### Hylleraas Wave Function

One of the most accurate approximations for the wave function of helium is the Hylleraas expansion, which takes the form  $\psi_{He}(r_1, r_2, r_{12})$  when using parameter values No. 14 from Bonham and Kohl [5]. However, this is not easily integrated for the electron distribution. To make integration possible, a further assumption that  $r_1 = r_2 = r$  is made. In other words, it is assumed that the two electrons have the same radial distance from the center of the atom. From this assumption,  $r_{12} = r\sqrt{2}$ , on average. Then, the wave function has been converted to a function of one variable:  $\psi_{He}(r_1, r_2, r_{12}) \rightarrow \psi_{He}(r)$ . Integrating this wave function gives the probability of measuring both electrons at a radial distance of 0 to  $r$ :

$$P(r_1 < r, r_2 < r) = 4\pi \int_0^r r'^2 |\psi_{He}(r')|^2 dr'.$$

From Eq. (6), the charge distribution is

$$Q_{enc}(r) = 2 \left( 1 - 4\pi \int_0^r r'^2 |\psi_{He}(r')|^2 dr' \right). \quad (8)$$

Note when  $r \rightarrow \infty$ , the term in the parenthesis is zero due to the normalization of the wave function. Then, the effective charge is zero, as expected. When  $r \rightarrow 0$ , the term in the parenthesis is one. Then, the effective charge is the nuclear charge of two, as expected.

#### *Hartree-Fock Wave Function*

The Hartree-Fock wave function for helium takes the form  $\psi_{He}(r_1, r_2) = u_{1s}(r_1)u_{1s}(r_2)$ , where the 1s orbital,  $u_{1s}(r)$ , is given by  $u_{1s}(r) = (4\pi)^{-1/2} (Ae^{-\alpha r} + Be^{-\beta r})$ , with constants defined in Ref. [2]. Since this wave function is separable, the probability of both electrons being within a radial distance,  $r$ , is equal to the probability of one electron being within  $r$ , squared. In other words,

$$P(r_1 < r, r_2 < r) = \left[ 4\pi \int_0^r r'^2 |u_{1s}(r')|^2 dr' \right]^2.$$

From Eq. (6), the charge distribution is

$$Q_{enc}(r) = 2 \left( 1 - \left[ 4\pi \int_0^r r'^2 |u_{1s}(r')|^2 dr' \right]^2 \right). \quad (9)$$

Note this charge distribution yields the correct results of two when  $r \rightarrow \infty$  (due to normalization) and zero when  $r \rightarrow 0$ . The benefit of the Hartree-Fock wave function is that the wave function itself takes into account electron screening.

#### *Hydrogenic Wave Function*

The hydrogenic wave function for helium is the product of two hydrogen-like wave functions for a helium ion. That is,  $\psi_{He}(r_1, r_2) = \psi_H(r_1)\psi_H(r_2)$ , where  $\psi_H(r)$  is the ground state wave function for hydrogen-like helium. Since this is separable,

$$P(r_1 < r, r_2 < r) = \left[ 4\pi \int_0^r r'^2 |\psi_H(r')|^2 dr' \right]^2.$$

From Eq. (6), the charge distribution is

$$Q_{enc}(r) = 2 \left( 1 - \left[ 4\pi \int_0^r r'^2 |\psi_H(r')|^2 dr' \right]^2 \right). \quad (10)$$

Note this charge distribution yields the correct results of two when  $r \rightarrow \infty$  (due to normalization) and zero when  $r \rightarrow 0$ . The deficiency of the hydrogenic wave function is that it does not take into account electron screening in the wave function itself.

## COMPUTATIONAL METHOD

### Master-Slave Model

The high performance computing resources available at Los Alamos National Laboratory were used to calculate the differential cross sections. Multiple processors were organized into a master-slave model, where the first processor is logically designated the master and the remaining are logically designated slaves, as shown in Fig. 5. The master processor communicates with the slave processors and manages what they compute.

Continuing with Fig. 5, the program starts with the slave processors sleeping while the master processor sets up the calculation. The master processor gets the input parameters, such as the masses and charges of the proton-helium system and the number of terms to retain in Eq. (4). Then, it calculates the potential at equally spaced points,

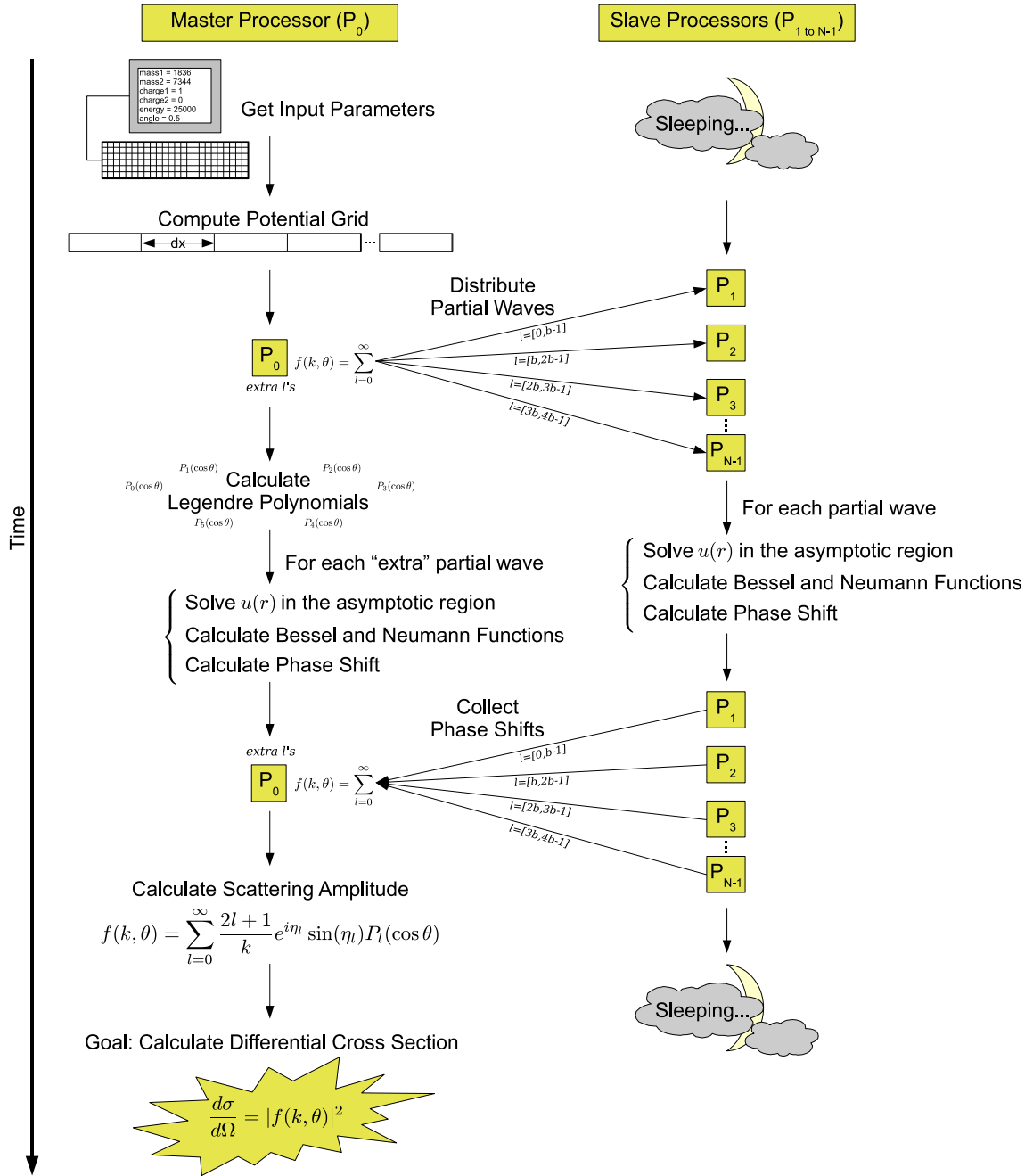


FIG. 5: Program flow for computing elastic differential cross sections using partial wave analysis.

which is used to solve the radial equation in Eq. (2). Afterwards, the master processor breaks the summation in Eq. (4) among the slave processors, distributing an equal range of partial waves to each of them. For each partial wave, a slave processor solves  $u(r)$  until the potential goes to zero, calculates the Bessel and Neumann functions, and finally computes the phase shift using Eq. (5). In the meantime, the master processor computes the Legendre polynomials and calculates the phase shifts for any partial waves that did not divide evenly into the slave processors.

Once all the phase shifts are calculated, the slave processors return them to the master processor. The master processor then calculates the scattering amplitude using Eq. (4). Finally, using Eq. (1), it calculates the differential cross section by squaring the scattering amplitude.

### Computing $u(r)$ Using Numerov's Method

Numerov's method states that differential equations of the form  $\left[\frac{d^2}{dx^2} + k^2\right]y(x) = S(x)$  can be approximated numerically by

$$\left(1 + \frac{h^2}{12}k_{n+1}^2\right)y_{n+1} - 2\left(1 - \frac{5h^2}{12}k_n^2\right)y_n + \left(1 + \frac{h^2}{12}k_{n-1}^2\right)y_{n-1} = \frac{h^2}{12}(S_{n+1} + 10S_n + S_{n-1}),$$

where  $h$  is the step size [6]. This constant step size yields conversions between indices and radial distances:

$$y_0 = y(0), y_1 = y(h), y_2 = y(2h), \dots, y_n = y(nh).$$

For the radial equation in Eq. (2),  $S = 0$ ,  $y(x) \rightarrow u(r)$ , and  $k^2 \rightarrow k^2 - \frac{l(l+1)}{r^2} - U = k^2 - \frac{l(l+1)}{(nh)^2} - U$ . Numerov's method then gives

$$u_n = \frac{2\left[1 - \frac{5h^2}{12}\left(k^2 - \frac{l(l+1)}{((n-1)h)^2} - U_{n-1}\right)\right]u_{n-1} - \left[1 + \frac{h^2}{12}\left(k^2 - \frac{l(l+1)}{((n-2)h)^2} - U_{n-2}\right)\right]u_{n-2}}{1 + \frac{h^2}{12}\left(k^2 - \frac{l(l+1)}{(nh)^2} - U_n\right)}. \quad (11)$$

Using this recursive relationship, it is straightforward to solve for  $u(r)$  until the potential is effectively zero. Any two points in this asymptotic region can be used for  $x_1$  and  $x_2$  in Eq. (5). To use Eq. (11), two starting points must be found. From boundary conditions, the wave function must be zero at  $r = 0$ . Thus,  $u(0) = u_0 = 0$ . However, this cannot be used as a starting point in Numerov's method since  $l(l+1)/(nh)^2$  is undefined for  $n = 0$ . Rather, the next two points,  $u_1$  and  $u_2$ , can be used to start the recursive relationship. They can be found by solving the radial equation in Eq. (2) using polynomial approximations. To begin, a new function,  $Z(r)$ , is introduced as a function of the potential:

$$Z(r) \equiv U(r) \cdot r = 2m \cdot V(r) \cdot r = 2m \cdot Q_{enc}(r), \quad (12)$$

where the last equality comes from Eq. (7). Since  $Q_{enc}(r)$  is known from Eqs. (8-10), it is known how to evaluate  $Z(r)$ . The first polynomial approximation is expressing  $Z(r)$  as

$$Z(r) \approx b_1 + b_{2p}r + b_3r^2 + b_4r^3. \quad (13)$$

Rearranging the radial equation in Eq. (2) for  $u'' = d^2u/dr^2$  and substituting Eq. (13) results in

$$\begin{aligned} u'' &= \left(\frac{l(l+1)}{r^2} + U - k^2\right)u \\ &= (l(l+1) + Ur^2 - k^2r^2) \frac{u}{r^2} \\ &= (l(l+1) + Zr - k^2r^2) \frac{u}{r^2} \\ &\approx (l(l+1) + b_1r + b_{2p}r^2 + b_3r^3 + b_4r^4 - k^2r^2) \frac{u}{r^2} \\ &= (l(l+1) + b_1r + b_2r^2 + b_3r^3 + b_4r^4) \frac{u}{r^2} \end{aligned} \quad (14)$$

where  $b_2 = b_{2p} - k^2$ . The second polynomial approximation is expressing  $u(r)$  as

$$u(r) \approx r^{l+1}(1 + a_1r + a_2r^2 + a_3r^3 + a_4r^4). \quad (15)$$

Plugging this (and its second derivative) into Eq. (14) and equating like powers of  $r$  yields the coefficients of Eq. (15) in terms of the coefficients of Eq. (13):

$$a_1 = \frac{b_1}{2l+2} \quad (16a)$$

$$a_2 = \frac{a_1b_1 + b_2}{4l+6} \quad (16b)$$

$$a_3 = \frac{a_1b_2 + a_2b_1 + b_3}{6l+12} \quad (16c)$$

$$a_4 = \frac{a_1b_3 + a_2b_2 + a_3b_1 + b_4}{8l+20}. \quad (16d)$$

In other words, if the  $b_n$ 's in Eq. (13) are known, then the coefficients for  $u(r)$  in Eq. (15) can be calculated. Then,  $u(r)$  can be used to approximate  $u_1 = u(h)$  and  $u_2 = u(2h)$ . To find these  $b_n$ 's,  $Z(r)$  is again approximated as a polynomial, this time of the form

$$Z(r) \approx a + b(r-h) + c(r-h)(r-2h) + d(r-h)(r-2h)(r-3h) + e(r-h)(r-2h)(r-3h)(r-4h). \quad (17)$$

These coefficients are easily found by evaluating  $Z(r)$  at  $r = h, 2h, 3h, 4h$ , and  $5h$ :

$$a = Z(h) \quad (18a)$$

$$b = \frac{Z(2h) - Z(h)}{h} \quad (18b)$$

$$c = \frac{Z(3h) - 2Z(2h) + Z(h)}{2h^2} \quad (18c)$$

$$d = \frac{Z(4h) - 3Z(3h) + 3Z(2h) - Z(h)}{6h^3} \quad (18d)$$

$$e = \frac{Z(5h) - 4Z(4h) + 6Z(3h) - 4Z(2h) + Z(h)}{24h^4}. \quad (18e)$$

Since it is known how to evaluate  $Z(r)$ , all these coefficients are known. Equating the two polynomial approximations for  $Z(r)$  in Eqs. (13) and (17), and comparing like powers of  $r$  gives the  $b_n$ 's in Eq. (13) in terms of the coefficients of Eq. (17):

$$b_1 = a - bh + 2ch^2 - 6dh^3 + 24eh^4 \quad (19a)$$

$$b_{2p} = b - 3ch + 11dh^3 - 50eh^3 \quad (19b)$$

$$b_3 = c - 6dh + 35eh^2 \quad (19c)$$

$$b_4 = d - 10eh. \quad (19d)$$

In summary,  $Z(r)$  from Eq. (12) can be used to find the coefficients,  $a-e$ , in Eq. (17) using Eqs. (18a-e). These can then be used to find the  $b_n$ 's in Eq. (13) using Eqs. (19a-d). From the  $b_n$ 's, the  $a_n$ 's in Eq. (15) can be found using Eqs. (16a-d). Since the  $a_n$ 's are the coefficients of  $u(r)$ , they can be used to approximate  $u_1$  and  $u_2$ , which are used as starting points in Numerov's method in Eq. (11).

### Legendre, Bessel, and Neumann Functions

There are well-known recursive relationships for the Legendre polynomials ( $P_n$ ), Bessel functions ( $j_l$ ), and Neumann functions ( $n_l$ ) that depend on the previous two terms:

$$\begin{aligned} P_{n+1}(x) &= \frac{(2n+1)xP_n(x) - nP_{n-1}(x)}{n+1} & P_0(x) &= 1 & P_1(x) &= x \\ j_{l+1}(x) &= \left(\frac{2l-1}{x}\right)j_l(x) - j_{l-1}(x) & j_0(x) &= \frac{\sin x}{x} & j_1(x) &= \frac{\sin x}{x^2} - \frac{\cos x}{x} \\ n_{l+1}(x) &= \left(\frac{2l-1}{x}\right)n_l(x) - n_{l-1}(x) & n_0(x) &= -\frac{\cos x}{x} & n_1(x) &= -\frac{\cos x}{x^2} - \frac{\sin x}{x} \end{aligned}$$

Since the first two terms are known, additional terms are easily calculated. However, the recursive relationships for Bessel and Neumann functions are only stable when the condition

$$\ln x > b_1 l^3 + b_2 l^2 + b_3 l + b_4 \quad (20)$$

is met, where the  $b_n$ 's are defined in Ref. [7]. From Eq. (5), the Bessel and Neumann functions are evaluated where the potential is effectively zero. However, it is not enough that the potential be zero. The points must be far enough such that Eq. (20) is also satisfied.

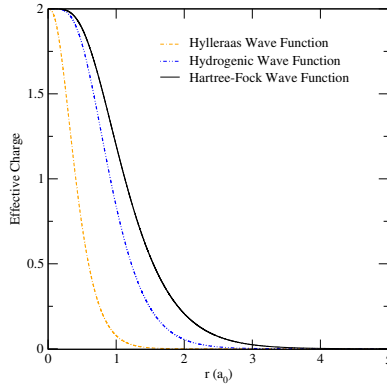


FIG. 6: Effective charge of neutral helium.

## NUMERICAL RESULTS

### Effective Charge

Using the Hylleraas, Hartree-Fock, and Hydrogenic ground state wave functions of helium, different effective charges were obtained using Eqs. (8-10), as shown in Fig. 6. Note the effective charge ranges from two near the nucleus to zero outside the atom. From these, the potential was calculated using Eq. (7).

### Elastic Differential Cross Sections

Elastic differential cross sections were calculated using these screened potentials for 25, 50, and 100 keV proton impact on neutral helium where 10,000 partial waves were retained in Eq. (4), and 5,000 points per wavelength were used in Numerov's method. The results are shown in Fig. 7, with experimental values and Born, Glauber, classical, and four-state calculations from Peacher *et al.* [8].

Immediately noticeable is that all the calculations are in disagreement with experiment in terms of magnitude.

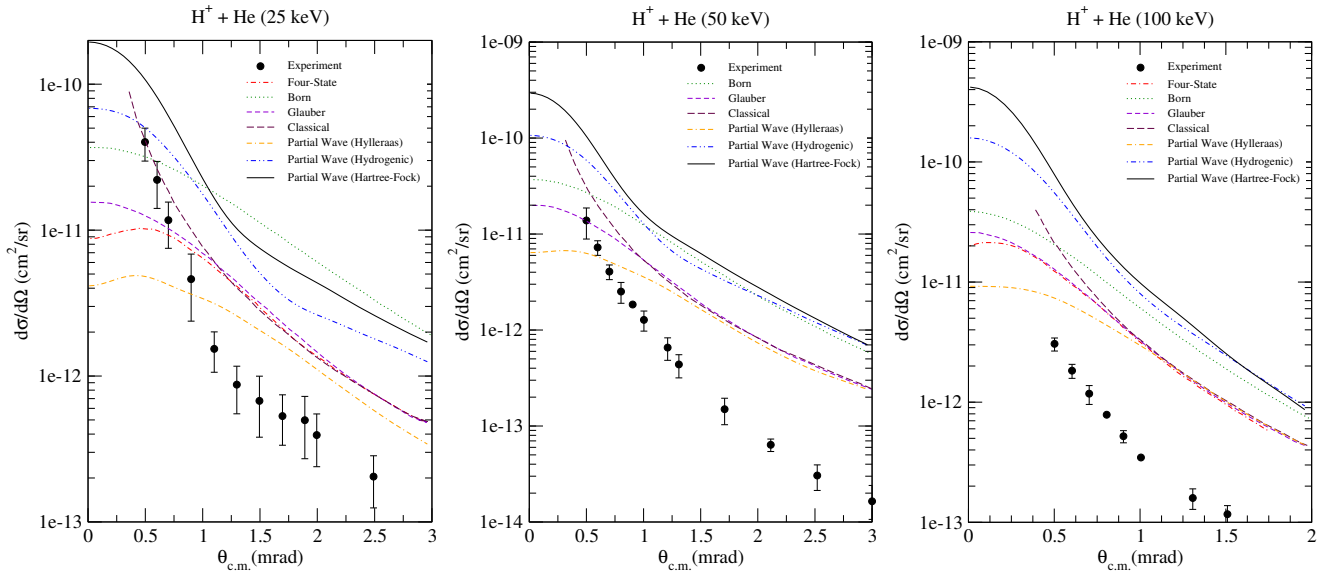


FIG. 7: Elastic differential cross sections for proton impact on neutral helium in the center-of-mass frame for a proton with laboratory energy of 25, 50, and 100 keV using 10,000 partial waves retained in Eq. (4) and 5,000 points per wavelength.

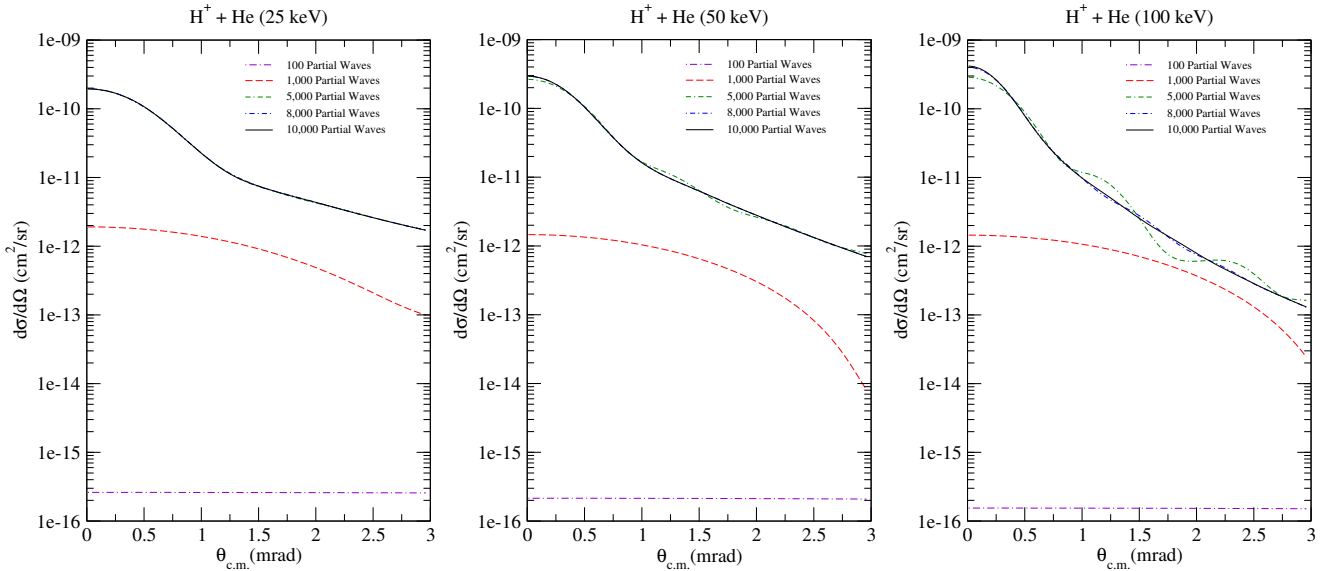


FIG. 8: Elastic differential cross sections for proton impact on neutral helium in the center-of-mass frame for a proton with laboratory energy of 25, 50, and 100 keV using a Hartree-Fock wave function for the distorted wave with different numbers of partial waves retained in Eq. (4).

This is expected, since measuring purely elastic differential cross sections is very difficult and inelastic channels may affect the experimental values. This was suggested by Peacher *et al.* when they discussed the discrepancy between experiment and theory for the four calculations they presented. This was later confirmed by Slim *et al.*, where calculations including inelastic channels matched the experimental values well, particularly in the 25 and 50 keV collisions [9]. Since the partial wave calculations also ignore inelastic channels, the discrepancy between experiment and theory in terms of magnitude is expected.

Although the magnitude of the experimental data may differ due to inelastic effects, the shape should be consistent. Importantly, in regard to this, the partial wave calculations are better than the four calculations provided by Peacher *et al.*, specifically for the Hartree-Fock wave function. The hydrogenic wave function also carries a similar shape to the Hartree-Fock wave function, as evident in the 25 keV case in Fig. 7, but is shifted to higher angles. The difference is likely due to the electron screening taken into account in the Hartree-Fock wave function, which is absent in the hydrogenic. The Hylleraas wave function is poor in matching the shape of the experimental data. Although it is the most accurate wave function of the three, the approximation that  $r_1 = r_2 = r$  likely made it inaccurate. This accuracy in matching the shape, at least for the Hartree-Fock wave function, suggests that partial wave analysis with a distorted wave treatment is more accurate than previous calculations.

Furthermore, the partial wave calculations are relatively fast. Each of the differential cross section calculations in Fig. 7 took roughly twenty minutes using thirty processors on a high performance computing cluster.

### Convergence of Differential Cross Sections

The number of terms needed for partial wave analysis scales with momentum. Since protons are fairly massive, it takes thousands of partial waves for the elastic differential cross sections to converge, as shown in Fig. 8. The 5,000 partial wave curve reflects this well. While it is converged for the 25 keV case, it is inaccurate for 100 keV. The 8,000 and 10,000 partial wave curves overlap at the three energies that were calculated, showing the converged answer.

The radial equation in Eq. (2) oscillates very quickly due to the mass of the system. As a result, thousands of points per wavelength are necessary to accurately calculate  $u(r)$ , as shown in Fig. 9. However, at just a few hundred points per wavelength, the result yields the general shape of the graph at the tail region. The 3,000, 5,000, and 8,000 point per wavelength curves overlap at the three energies that were calculated, showing the converged answer.

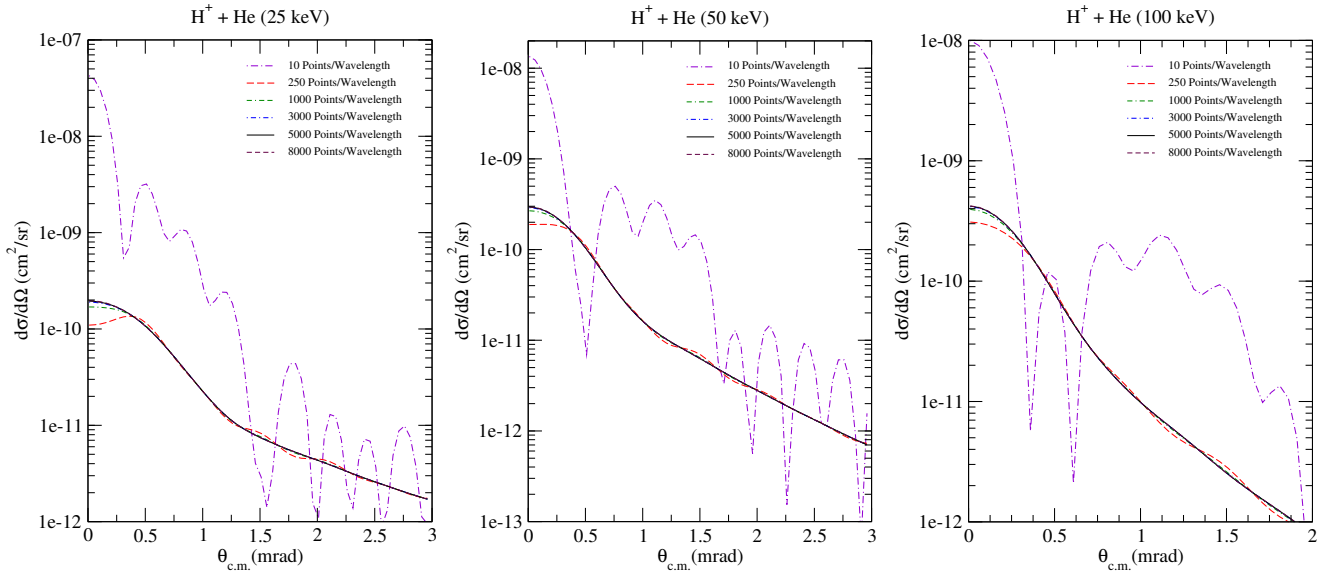


FIG. 9: Elastic differential cross sections for proton impact on neutral helium in the center-of-mass frame for a proton with laboratory energy of 25, 50, and 100 keV using a Hartree-Fock wave function for the distorted wave, 10,000 partial waves retained in Eq. (4), and different numbers of points per wavelength.

### Future Directions

Returning to the larger problem of heavy ion-impact ionization, the partial wave results suggest it is very feasible to calculate fully differential cross sections for heavy ions using today's computing resources. Partial wave analysis, often used in electron-impact ionization, can be extended to heavy ions in an accurate and reasonably fast manner.

Research supported by a NSF Research Experience for Undergraduates grant through the University of New Mexico in conjunction with funding from Los Alamos National Laboratory.

- 
- [1] M. Foster, J. L. Peacher, M. Schulz, and D. H. Madison, *Phys. Rev. Lett.* **97**, 093202 (2006).
  - [2] B. H. Bransden and C. J. Joachain, *Physics of Atoms and Molecules* (Pearson Education, Harlow, England, 2003), 2nd ed.
  - [3] T. E. Simos, *Int. J. Mod. Phys. C* **11**, 79 (2000).
  - [4] T. E. Simos, *Computers Math. Applic.* **42**, 833 (2001).
  - [5] R. A. Bonham and D. A. Kohl, *J. Chem. Phys.* **45**, 2471 (1966).
  - [6] S. E. Koonin and D. C. Meredith, *Computational Physics: Fortran Version* (Westview, Boulder, 1990).
  - [7] A. Jablonski, *J. Comput. Phys.* **111**, 256 (1994).
  - [8] J. L. Peacher, T. J. Kvale, E. Redd, P. J. Martin, D. M. Blankenship, E. Rille, V. C. Sutcliffe, and J. T. Park, *Phys. Rev. A* **26**, 2476 (1892).
  - [9] H. A. Slim, E. L. Heck, B. H. Bransden, and D. R. Flower, *J. Phys. B: At. Mol. Opt. Phys.* **24**, 2353 (1991).

# Simulation of the $L\alpha$ Spectra of Fe Ions

Tony Li

*Los Alamos Summer School REU Program, Los Alamos National Laboratory,  
Atomic and Optical Theory Group (T-4), Los Alamos, NM 87545, USA and  
Cornell University, Ithaca, NY 14853, USA*

Justin Oelgoetz

*Los Alamos National Laboratory, Applied Physics Division,  
PO box 1663, MS F663, Los Alamos, NM 87545, USA*

X-ray spectroscopy of highly charged ions is an important tool in the study of high-temperature plasmas, especially distant astrophysical plasmas. For example, in He-like ions, the relatively strong  $K\alpha$  spectral complex—lines arising from electron transitions between the  $1s2l$  and  $1s^2$  configurations—has been studied extensively and serves as an effective diagnostic of both temperature and electron density. Less attention has been directed toward the  $L\alpha$  spectral complex of He-like and Li-like ions, which results from transitions between the configurations  $1s3l$  and  $1s2l$ ,  $1s^23l$  and  $1s^22l$ , or  $1s2l3l$  and  $1s2l2l'$ . These  $L\alpha$  lines have lower photon energies, and as such may be more easily resolved by current instruments than the well known  $K\alpha$  complex. As they arise from the same ionization stages as the  $K\alpha$  complex, they could be used as alternative diagnostics, particularly for Fe and other heavier ions, since the  $K\alpha$  features of such ions are unresolvable by current X-ray satellites. Using the code ATOMIC developed at Los Alamos, we simulate both steady-state and time-dependent iron plasmas, focusing primarily on the  $L\alpha$  lines. The resulting spectra cleanly break into distinct regions of Li-like, He-like, and H-like spectral lines. We then analyze the temperature dependence of these lines, as well as potential spectral signatures of cooling or recombining plasma.

## I. INTRODUCTION

In highly ionized plasmas, particularly astrophysical plasmas, spectroscopic analysis serves as an important diagnostic of such conditions as temperature, density, and ionization states. In these plasmas, He-like ions with two bound electrons are common, as the closed inner K ( $n=1$ ) shell of such ion species tends to remain over the largest temperature range. Also common are H-like and Li-like ions, which consist of one and three bound electrons, respectively. Of special interest are the prominent spectral features of these ions, since generally, conditions of astrophysical objects are not directly observable except through their spectral signatures. In heavier and more highly charged species of these ions, the energies of the spectral lines tend to fall into the hard and soft X-ray ranges, and so X-ray spectroscopy is necessary to observe and analyze these lines.

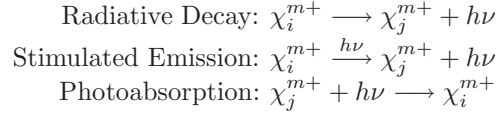
Previous work (see [4, 6, 10–17] among many others) has focused extensively on the features arising from the  $K\alpha$  spectra in He-like ions, which arise from radiative electron transitions from the L to K ( $n=2$  to  $n=1$ ) shells of the ion. Various diagnostics of plasma conditions have been proposed as a result of these studies. A particular example are the so-called G and R ratios, which have been developed, calculated, and observed for the spectra of various elements and under various astrophysical conditions. The quantities G and R are intensity ratios of specific and prominent spectral lines within the  $K\alpha$  spectra and are highly useful as temperature and density diagnostics, respectively.

Less attention has been directed towards the spectral features of the  $L\alpha$  transition series. These are emissions that result from transitions from the M to L ( $n=3$  to  $n=2$ ) shells. We are specifically interested in iron plasmas, because the  $K\alpha$  spectra of He-like iron is too high in photon energy to be resolvable by current X-ray telescopes. As the  $L\alpha$  transitions occur in approximately the 1 keV to 1.3 keV energy range, they have a hope of being resolved by current instrumentation on satellites such as the *Chandra* or *XMM-Newton*. As such, there may be features of the  $L\alpha$  spectra that can be used for alternative or corroborative diagnostics of plasma conditions. While some work on the  $L\alpha$  lines has been done (see for instance [5, 7, 8, 10, 11]) to our knowledge there are no systematic studies of these lines that span multiple ionization stages, nor are there studies presenting line ratios involving only  $L\alpha$  lines. Previous line ratio work [5, 7, 8] is based off comparing the intensity of the  $\Delta n = 0$ ,  $1s^22p^2P_{3/2}^0 \rightarrow 1s^22s^2S_{1/2}$  line to  $L\alpha$  lines [5, 7, 8]. Line ratios, such as the ones previously considered, composed of lines separated by large energies are especially susceptible to instrument calibration [5]; thus a ratio composed of only  $L\alpha$  lines could be of greater utility.

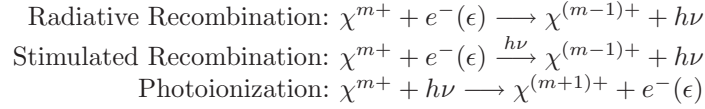
## II. THEORY

### A. Atomic Processes in Plasmas

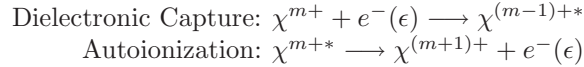
In astrophysical plasmas, a number of processes, both radiative and non-radiative, contribute to the population of different ionicities and energy levels. Processes that involve radiative energy transitions are responsible for producing the observable spectral lines. All atomic processes we have considered are listed here, presented in groups related by the principle of detailed balance.



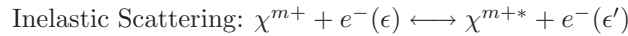
Radiative decay occurs when a bound electron spontaneously decays to a lower energy state, emitting a photon with energy equal to the difference between the final and initial states. Stimulated emission is the same process, but induced by an incident photon of the same energy. In the reverse direction is photoabsorption, in which a photon is absorbed and causes the electron to jump to a higher energy state.



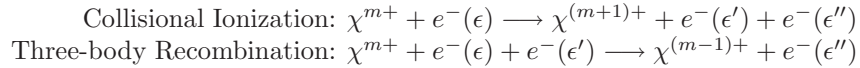
Radiative recombination occurs when a free electron becomes bound to an ion, emitting radiation in the process. Analogous to the previous case, this process can be induced by an incident photon with equal energy to the emitted photon. The process also occurs in the reverse direction as photoionization, in which an ion absorbs a photon with enough energy to free an electron.



Dielectronic capture occurs when an electron combines non-radiatively with an ion, becoming quasi-bound. That is to say, the energy of the electron and the ion combined will be greater than the ionization threshold. If an ion is already in such a state, the electron may be spontaneously released through the process of autoionization.



In inelastic scattering, an electron and an ion interact and exchange energy but do not recombine. This may also be referred to as electron-impact excitation and de-excitation.



Collisional ionization occurs when a free electron gives enough energy to a bound electron to push it above the ionization threshold, releasing it from its ion. In reverse, the process is three-body recombination.

## B. Collisional-Radiative Model

To calculate populations of each level and ionicity, every one of the aforementioned atomic processes must be taken into account. This amounts to solving the following rate equation for all relevant ionicities and levels:

$$\begin{aligned}
\frac{dN_{l,j}}{dt} = & \sum_{i(i>j)} N_{l,i} A_{i \rightarrow j} - N_{l,j} \sum_{i(i<j)} A_{j \rightarrow i} + W \sum_{i(i \neq j)} (N_{l,i} B_{i \rightarrow j}(\tilde{\rho}) - N_{l,j} B_{j \rightarrow i}(\tilde{\rho})) \\
& + N_e \sum_i N_{l-1,i} (\alpha_{l-1,i \rightarrow l,j}^{RR}(\tilde{\varepsilon}) + W \gamma_{l-1,i \rightarrow l,j}(\tilde{\rho}, \tilde{\varepsilon})) + W \sum_i N_{l+1,i} P_{l+1,i \rightarrow l,j}(\tilde{\rho}) \\
& - N_e N_{l,j} \sum_i (\alpha_{l,j \rightarrow l+1,i}^{RR}(\tilde{\varepsilon}) + W \gamma_{l,j \rightarrow l+1,i}(\tilde{\rho}, \tilde{\varepsilon})) - W N_{l,j} \sum_i P_{l,j \rightarrow l-1,i}(\tilde{\rho}) \\
& + \sum_i N_{l+1,i} \Gamma_{l+1,i \rightarrow l,j}^{AI} - N_{l,j} \sum_i \Gamma_{l,j \rightarrow l-1,i}^{AI} + N_e \sum_i N_{l-1,i} D_{l-1,i \rightarrow l,j}(\tilde{\varepsilon}) \\
& - N_e N_{l,j} \sum_i D_{l,j \rightarrow l+1,i}(\tilde{\varepsilon}) + N_e \sum_{i(i \neq j)} (N_{l,i} q_{i \rightarrow j}(\tilde{\varepsilon}) - N_{l,j} q_{j \rightarrow i}(\tilde{\varepsilon})) \\
& + N_e \sum_i N_{l+1,i} C_{l+1,i \rightarrow l,j}(\tilde{\varepsilon}) - N_e N_{l,j} \sum_i C_{l,j \rightarrow l-1,i}(\tilde{\varepsilon}) \\
& + N_e^2 \sum_i N_{l-1,i} \beta_{l-1,i \rightarrow l,j}(\tilde{\varepsilon}) - N_e N_{l,j} \sum_i \beta_{l,j \rightarrow l+1,i}(\tilde{\varepsilon})
\end{aligned} \tag{1}$$

Each term contains a rate coefficient to correspond to each process.  $A$  is the Einstein coefficient of radiative decay between two states. Similarly,  $B$  is the Einstein coefficient of absorption and stimulated emission. The  $\alpha^{RR}$  terms denote radiative recombination, the  $\gamma$  terms denote stimulated recombination, and the  $P$  terms denote photoionization. The autoionization rate is given by  $\Gamma^{AI}$ , while its inverse, dielectronic capture, is given by  $D$ . Electron-impact excitation and de-excitation is governed by  $q$ , collisional ionization by  $C$ , and three-body recombination by  $\beta$ . As it happens, in our particular study, we did not include a radiation field, so that some terms were set to zero (that is, the effects of stimulated emission, absorption, stimulated recombination, and photoionization were all neglected). The model included all fine structure levels resulting from the configurations  $nl$ ,  $1s^2$ ,  $1snl$ ,  $2snl$ ,  $2pnl$ ,  $1s^2nl$ ,  $1s2snl$ ,  $1s2pnl$ ,  $1s3snl$ ,  $1s3pnl$ , and  $1s3dnl$  ( $n \leq 10$ ,  $l \leq g$ ) as well as the bare nucleus, which spans the ionization stages Fe XXIV through Fe XXVI.

In order to calculate level populations, ionization balances, and spectral intensities, we use the ATOMIC code [9] developed at Los Alamos. However, running the code requires input data that must in turn be calculated from other physics codes. In particular, rate coefficients for all atomic processes must be obtained, which are found by integrating the atomic cross section over the electron energy distribution or the radiation field. The three codes used for this task, also developed at Los Alamos, are CATS, ACE, and GIPPER [2, 3]. CATS is responsible for the atomic structure and electron impact cross sections. Using CATS data, ACE improves upon the electron impact cross sections, while GIPPER calculates photoionization, autoionization, and collisional ionization processes [1].

Once all the preliminary data has been calculated, it is provided as input, along with necessary parameters such as electron temperature ( $T_e$ ), electron density ( $N_e$ ), and radiation field temperature. We can then provide a set of initial conditions and obtain a time-dependent solution, or we can solve for a steady-state situation, in which case the rate equations are all set to zero.

## C. Calculating Spectra

As all levels have been calculated in intermediate coupling, allowing for configuration interaction (CI), the only strict selection rules are that the parity of the state must change (even to odd or odd to even) and on the total angular

momenta, ( $\Delta J = 0, \pm 1$ ). As the photon itself has a spin of 1,  $J=0$  to  $J=0$  transitions are forbidden as the emitted photon carries away momentum (see [18]). As these Fe atoms are highly charged, and mixing is in general small, the strong lines will all follow the more restrictive set of LS coupling selection rules, in which CI is neglected. Thus we can also impose the following selection rules: L ( $\Delta L = 0 \pm 1$ ) and to a lesser extent the rule for S ( $\Delta S = 0$ ) in addition to only allowing single electron jumps and requiring that the electron jump have a  $\Delta l = \pm 1$ . With these rules in mind, the dipole-allowed  $L\alpha$  lines are depicted in Figures 1, 2, and 3.

After determining these allowed radiative transitions, we can obtain the emitted photon energies. Tables I–III list in ascending order those energies, obtained using CATS calculations of energy level data. The reader will notice some transitions where the selection rule  $\Delta S = 0$  is violated. These intercombination lines are in general weaker than those that do not violate the spin selection rule, and are caused by mixing between states of the same  $J$  but different spins due to spin-orbit coupling.

The intensities of these lines are calculated from the level populations ( $N_{l,j}$ ) found by solving equation (1) and the radiative decay rates via the simple relation

$$I(l, j \rightarrow l, k) = N_{l,j} A_{j \rightarrow k} . \quad (2)$$

Emission spectra ( $S$ ) are calculated from the line intensities ( $I$ ) and then applying a Doppler-broadened line profile to it using the equations

$$S(h\nu) = \sum_{l,j,k} I(l, j \rightarrow l, k) h\nu \frac{c\sqrt{m_i}}{2\pi k T_i} e^{-\frac{m_i c^2 (h\nu - \Delta E_{jk})^2}{2\Delta E_{jk}^2 k T_i}} , \quad (3)$$

where  $m_i$  and  $T_i$  are the ion mass and temperature respectively, and  $\Delta E_{jk}$  is the energy of the line produced by radiative decay from level  $j$  to  $k$ . This Doppler-broadened profile accounts for the broadening due to the thermal motion of the ions.

### III. RESULTS

We now analyze and discuss results for the spectral temperature dependence of steady-state plasmas, focusing on the  $L\alpha$  spectral range. From this, we note a line intensity ratio within the Li-like set of lines which could serve as a potential temperature diagnostic. Additionally, we present and discuss results for spectra from a recombining cooling plasma.

#### A. Steady-state Plasma

In the steady-state iron plasma, we set the electron density to  $10^{10}$  electrons/cm<sup>-3</sup> and looked at the spectra as a function of electron temperature, which varied logarithmically from  $8.617 \times 10^2$  eV to  $8.617 \times 10^4$  eV, or approximately  $10^7$  to  $10^9$  K. As mentioned, we included no radiation field. Upon matching the previously calculated transition energies with their respective peaks in the data, the spectra divides clearly into separate regions of Li-like, He-like, and H-like spectral lines, whose relative intensities at separate temperatures are shown in Figure 4. Figures 6, 7, and 8 show the individual spectra in more detail.

Note, also, in Figure 5, that the intensities of the Li-like lines are on the same order of magnitude as the Fe  $K\alpha$  lines. While the  $K\alpha$  data is simulated as well, since the Fe  $K\alpha$  complex cannot be resolved into its separate peaks, it is indeed observable, encouraging the prospect of using the  $L\alpha$  lines as an alternative temperature diagnostic.

Of particular note are the two highest-energy spectral lines in the Li-like range. In Figure 8, these correspond to the two peaks on the far right of the graph. These lines result from  $p$ -orbital to  $s$ -orbital transitions, and, as shown in Figures 9 and 10, they decrease more slowly with increasing temperature relative to the other line intensities. This behavior suggests a potential diagnostic ratio within the Li-like,  $L\alpha$  transitions. If we take the ratio of the  $S \leftarrow P$  line

intensities to the  $P \leftarrow D$  line intensities, or instead the  $S \leftarrow P$  to the  $P \leftarrow S$  transitions, then we obtain a quantity that varies fairly steadily and predictably with temperature. The temperature-dependence of these quantities are shown in Figure 11.

## B. Time-dependent Plasma

We also looked briefly at a transient cooling or recombining plasma. We first obtained a simulated iron plasma in steady state at  $T_e = 8.617 \times 10^4$  eV ( $10^9$  K), and step-decreased the electron temperature to  $T_e = 8.617 \times 10^2$  eV ( $10^7$  K). The resulting spectral signature, at various times, is shown in Figure 12. While the analysis is only preliminary, one can clearly see that the H-like lines are prominent initially, then the He-like lines, and finally the Li-like lines. Detailed study of the spectral signature of these lines is underway.

## IV. CONCLUSIONS

Using the ATOMIC code, we have simulated the  $L\alpha$  spectra for iron under both steady-state and cooling conditions. We have focused on the steady-state results, in which we have identified two ratios of interest within the Li-like lines of iron, one of the  $S \leftarrow P$  lines to the  $P \leftarrow D$  lines, and the other of  $S \leftarrow P$  lines to the  $P \leftarrow D$  lines. Observational data will certainly be needed to corroborate these results, but since these lines lie within the resolvable energy range of present technology, it is quite possible that either of these ratios may have practical diagnostic applications.

## V. ACKNOWLEDGMENTS

Special thanks to James Colgan, Sally Seidel, and especially Norm Magee for their roles in organizing, administering, and providing for the Los Alamos Summer School REU. Additional thanks to the University of New Mexico for hosting the program, as well as the NSF for providing the funding to make it possible.

- 
- [1] J. Abdallah, Jr, R. E. H. Clark, and R. D. Cowan. *Theoretical Atomic Physics Code Development V: Rate Equations for Plasmas in Non Local Thermodynamic Equilibrium*. Los Alamos National Lab, Los Alamos, NM, October 1990. LA-11926.
  - [2] J. Abdallah, Jr, R. E. H. Clark, J. M. Peek, and C. J. Fontes. Kinetics calculations for near ne-like ions. *Journal of Quantitative Spectroscopy & Radiative Transfer*, 51(1):1-8, 1994.
  - [3] J. Abdallah, Jr, H. L. Zhang, C. J. Fontes, D. P. Kilcrease, and B. J. Archer. Model comparisons for high-z non-lte steady-state calculations. *Journal of Quantitative Spectroscopy & Radiative Transfer*, 71(2-6):107-16, 2001.
  - [4] A. H. Gabriel and C. Jordan. Long wavelength satellites to the He-like ion resonance lines in the laboratory and the sun. *Nature*, 221:947-949, 1969.
  - [5] A. H. Gabriel and C. Jordan. *Case Studies in atomic collision physics*, volume II, chapter 4: Interpretation of spectral intensities from laboratory and astrophysical plasmas, pages 209-291. North-Holland Pub., Amsterdam, 1971.
  - [6] A.H. Gabriel and C. Jordan. Interpretation of solar helium-like ion line intensities. *Monthly Notices of the Royal Astronomical Society*, 145:241-248, 1969.
  - [7] E. Haug. Temperature-sensitive line ratios of the lithium-like ion O VI. *solar Physics*, 136(1):111-16, 1991.
  - [8] L. Heroux. A spectroscopic determination of electron temperature in a high temperature plasma. *Proceedings of the Physical Society*, 83:121-136, 1964.
  - [9] N. H. Magee, J. Abdallah, Jr, J. Colgan, P. Hakel, D. P. Kilcrease, S. Mazevet, M. Sherrill, C. J. Fontes, and H. L. Zhang. Los Alamos opacities: transition from LEDCOP to ATOMIC. In J. S. Cohen, S. Mazevet, and D. P. Kilcrease, editors, *Atomic Processes in Plasmas*. Fourteenth APS Topical Conference, Santa Fe, NM 2004, pages 168-179, New York, 2004. AIP conference proceedings No. 730, AIP.
  - [10] R. Mewe and E. H. B. M. Gronenschild. Calculated X-radiation from optically thin plasmas IV. Atomic data and rate coefficients for spectra in the range 1-270 Å. *Astronomy and Astrophysics Supplement Series*, 45:11-52, 1981.

- [11] R. Mewe, E. H. B. M. Gronenschild, and G. H. J. van den Oord. Calculated X-radiation from optically thin plasmas. V. *Astronomy and Astrophysics Supplement Series*, 62:197–254, November 1985.
- [12] R. Mewe and J. Schrijver. Helium-like ion line intensities: I - Stationary plasmas. *Astronomy and Astrophysics*, 65:99–114, April 1978.
- [13] R. Mewe and J. Schrijver. Helium-like ion line intensities: II - Non-stationary plasmas. *Astronomy and Astrophysics*, 65:115–121, April 1978.
- [14] J. Oelgoetz and A. K. Pradhan. The  $K\alpha$  complex of He-like iron with dielectronic satellites. *Monthly Notices of the Royal Astronomical Society*, 327:L42–L46, 2001.
- [15] J. Oelgoetz and A. K. Pradhan. The 6.7-keV  $K\alpha$  complex of He-like iron in transient plasmas. *Monthly Notices of the Royal Astronomical Society*, 354:1093–1102, 2004.
- [16] A. K. Pradhan. Recombination-cascade x-ray spectra of highly charged helium-like ions. *The Astrophysical Journal*, 288:824–830, 1985.
- [17] A. K. Pradhan and J. M. Shull. Density and temperature diagnostics of x-ray sources: line ratios for helium-like ions. *The Astrophysical Journal*, 249:821–830, 1981.
- [18] G. P. Rybicki and A. P. Lightman. *Radiative Processes in Astrophysics*, chapter 10: Radiative Transitions. John Wiley and Sons, Inc., New York, 1979.

TABLE I: Li-like Ion Transitions

| Transition   | Photon Energy (eV) |
|--|--------------------|
| $1s^2 2p (^2P_{3/2}) \leftarrow 1s^2 3s (^2S_{1/2})$ | 1085.6             |
| $1s^2 2p (^2P_{1/2}) \leftarrow 1s^2 3s (^2S_{1/2})$ | 1101.7             |
| $1s^2 2p (^2P_{3/2}) \leftarrow 1s^2 3d (^2D_{3/2})$ | 1109.0             |
| $1s^2 2p (^2P_{3/2}) \leftarrow 1s^2 3d (^2D_{5/2})$ | 1110.5             |
| $1s^2 2p (^2P_{1/2}) \leftarrow 1s^2 3d (^2D_{3/2})$ | 1125.1             |
| $1s^2 2s (^2S_{1/2}) \leftarrow 1s^2 3p (^2P_{1/2})$ | 1164.0             |
| $1s^2 2s (^2S_{1/2}) \leftarrow 1s^2 3p (^2P_{3/2})$ | 1168.8             |

TABLE II: He-like Ion Transitions

| Transition                               | Photon Energy (eV) |
|--|--------------------|
| $1s 2p (^1P_1) \leftarrow 1s 3s (^3S_1)$ | 1164.4             |
| $1s 2p (^1P_1) \leftarrow 1s 3s (^1S_0)$ | 1171.8             |
| $1s 2p (^1P_1) \leftarrow 1s 3d (^3D_2)$ | 1181.4             |
| $1s 2p (^3P_2) \leftarrow 1s 3s (^3S_1)$ | 1181.6             |
| $1s 2p (^1P_1) \leftarrow 1s 3d (^1D_2)$ | 1183.3             |
| $1s 2p (^3P_1) \leftarrow 1s 3s (^3S_1)$ | 1196.5             |
| $1s 2p (^3P_2) \leftarrow 1s 3d (^3D_2)$ | 1198.7             |
| $1s 2p (^3P_0) \leftarrow 1s 3s (^3S_1)$ | 1200.1             |
| $1s 2p (^3P_2) \leftarrow 1s 3d (^3D_3)$ | 1200.3             |
| $1s 2p (^3P_2) \leftarrow 1s 3d (^1D_2)$ | 1200.5             |
| $1s 2p (^3P_1) \leftarrow 1s 3s (^1S_0)$ | 1204.0             |
| $1s 2s (^1S_0) \leftarrow 1s 3p (^3P_1)$ | 1207.4             |
| $1s 2p (^3P_1) \leftarrow 1s 3d (^3D_1)$ | 1213.5             |
| $1s 2p (^3P_1) \leftarrow 1s 3d (^3D_2)$ | 1213.6             |
| $1s 2p (^3P_1) \leftarrow 1d 3d (^1D_2)$ | 1215.4             |
| $1s 2s (^1S_0) \leftarrow 1s 3p (^1P_1)$ | 1216.5             |
| $1s 2p (^3P_0) \leftarrow 1s 3d (^3D_1)$ | 1217.1             |
| $1s 2s (^3S_1) \leftarrow 1s 3p (^3P_0)$ | 1234.7             |
| $1s 2s (^3S_1) \leftarrow 1s 3p (^3P_1)$ | 1235.7             |
| $1s 2s (^3S_1) \leftarrow 1s 3p (^3P_2)$ | 1240.2             |
| $2s 2p (^1P_1) \leftarrow 2p 3p (^1D_2)$ | 1244.4             |
| $1s 2s (^3S_1) \leftarrow 1s 3p (^1P_1)$ | 1244.8             |

TABLE III: H-like Ion Transitions

| Transition                                 | Photon Energy (eV) |
|--|--------------------|
| $2p (^2P_{3/2}) \leftarrow 3s (^2S_{1/2})$ | 1273.2             |
| $2p (^2P_{3/2}) \leftarrow 3d (^2D_{3/2})$ | 1279.4             |
| $2p (^2P_{3/2}) \leftarrow 3d (^2D_{5/2})$ | 1281.5             |
| $2s (^2S_{1/2}) \leftarrow 3p (^2P_{1/2})$ | 1294.2             |
| $2p (^2P_{1/2}) \leftarrow 3s (^2S_{1/2})$ | 1294.6             |
| $2s (^2S_{1/2}) \leftarrow 3p (^2P_{3/2})$ | 1300.5             |
| $2p (^2P_{1/2}) \leftarrow 3d (^2D_{3/2})$ | 1300.8             |

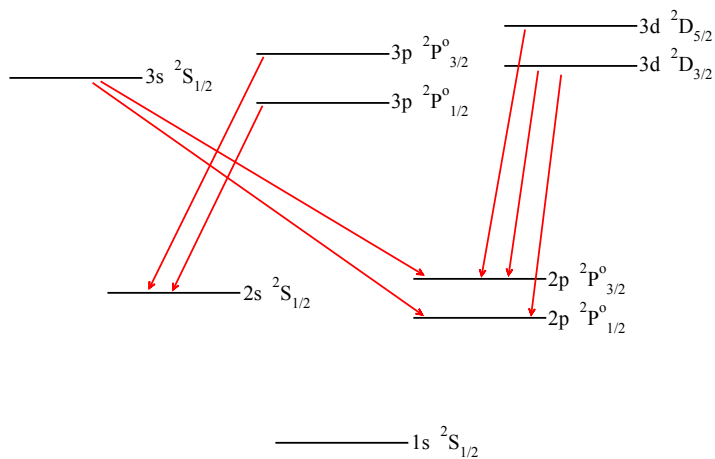


FIG. 1: Dipole-allowed  $L\alpha$  transitions in the H-like ion.

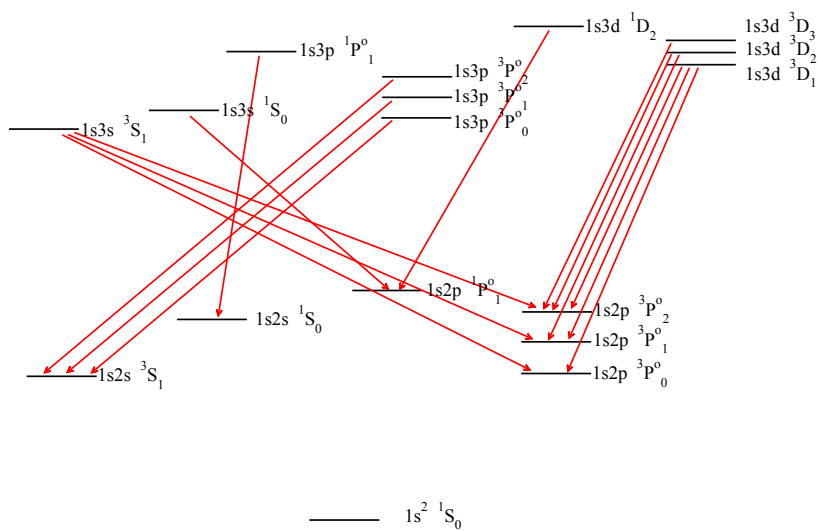


FIG. 2: Dipole-allowed  $L\alpha$  transitions in the He-like ion.

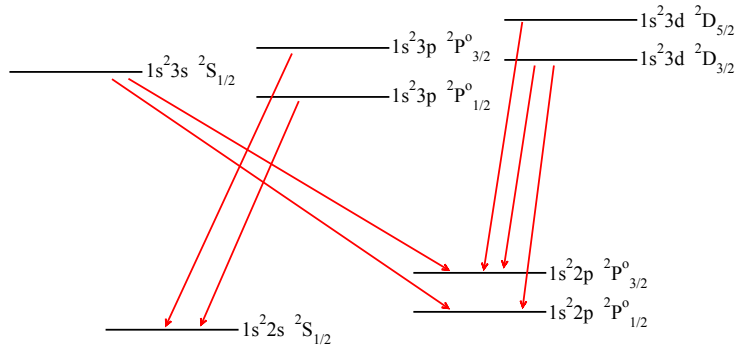


FIG. 3: Dipole-allowed  $L\alpha$  transitions in the Li-like ion.

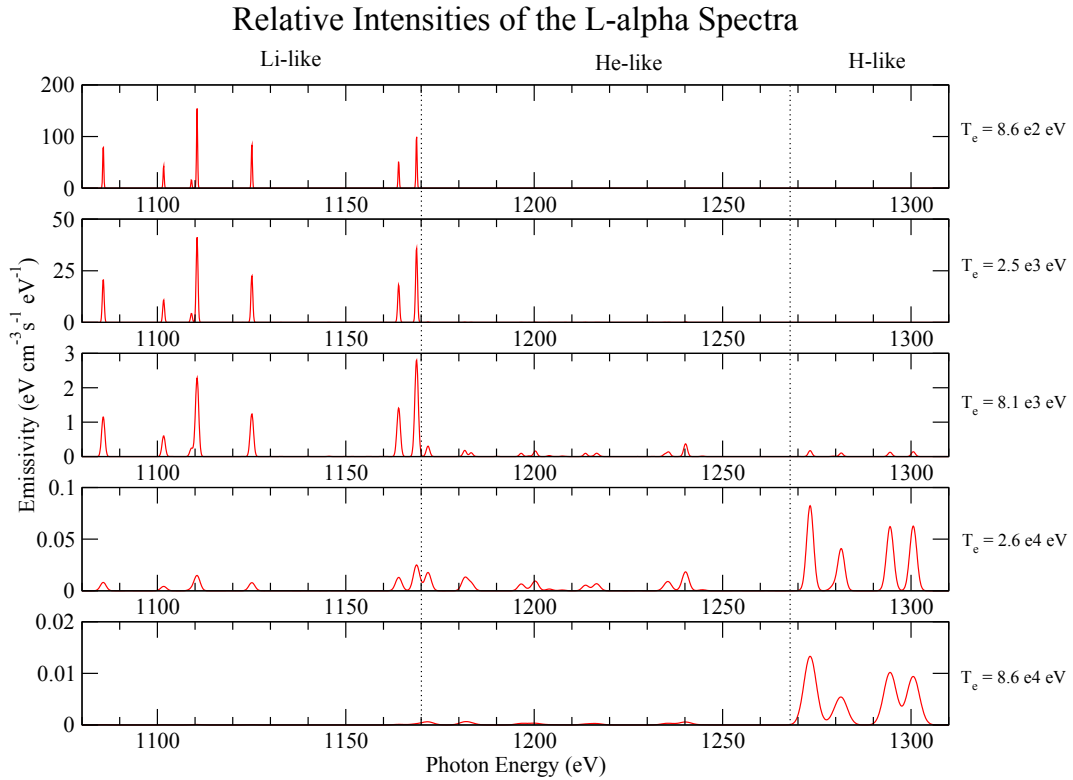


FIG. 4: The  $L\alpha$  spectra of iron at logarithmically spaced temperatures, from  $8.6 \times 10^2$  eV to  $8.6 \times 10^4$  eV, or  $10^7$  to  $10^9$  K. Note that the y-axis varies since the intensities on this graph are scaled relative to each other. The separate regions of Li-like, He-like, and H-like lines have been indicated.

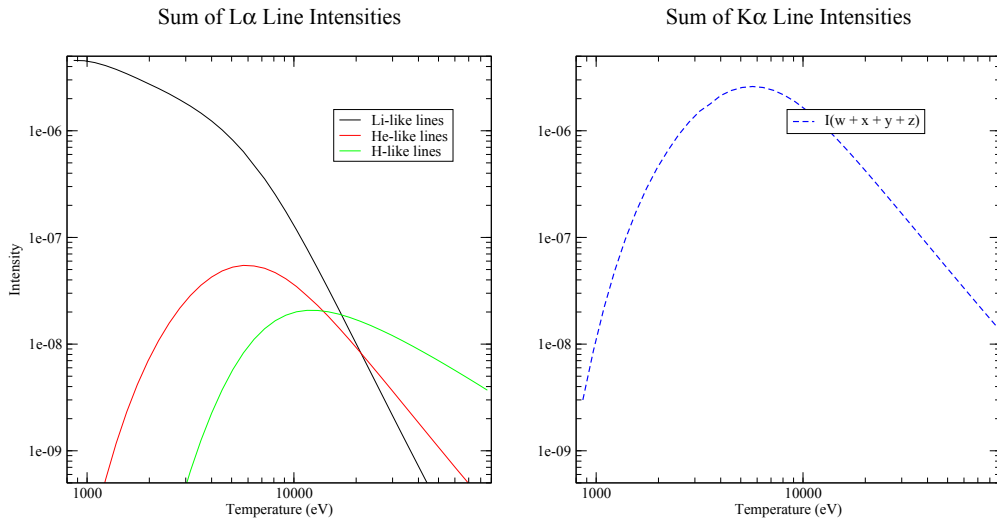


FIG. 5: Total spectral line intensities vs. temperature, on a log-log scale. Plotted on the left are summed line intensities of the  $L\alpha$  spectra, grouped into Li-like, He-like, and H-like lines. Plotted on the right are the sum of the intensities of the most prominent lines of the  $K\alpha$  spectra.

### Spectra of H-like Transitions

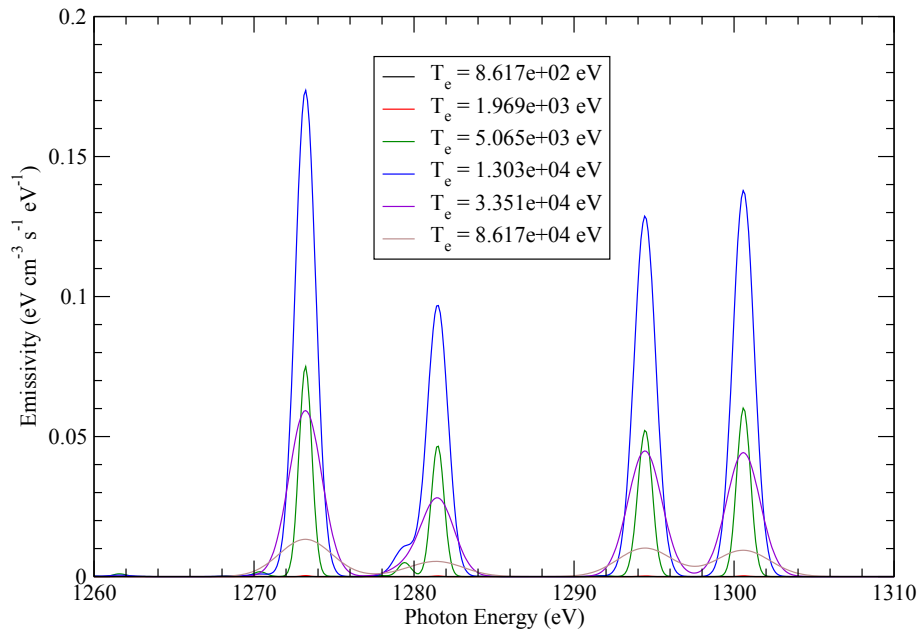


FIG. 6: Spectra of H-like ions

### Spectra of He-like Transitions

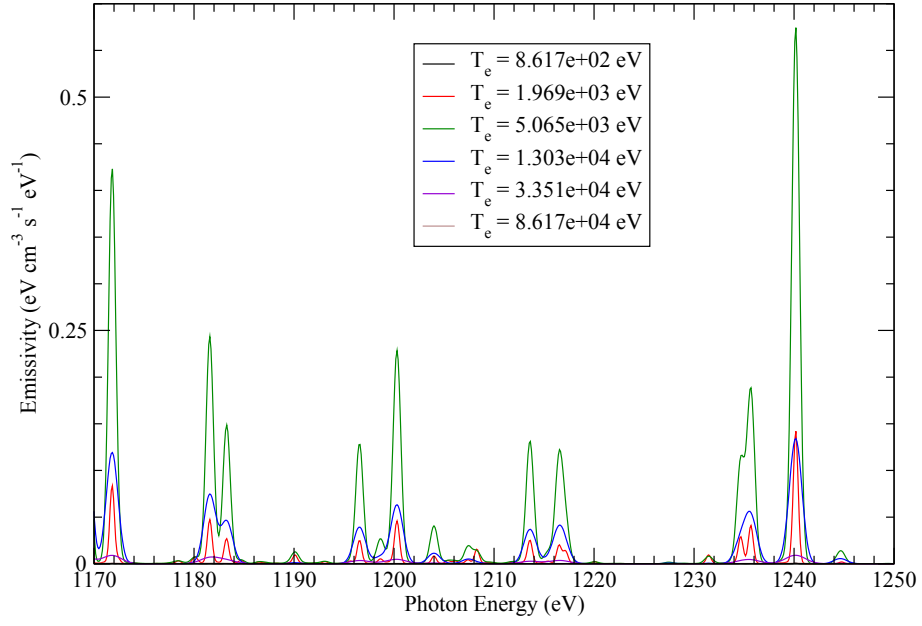


FIG. 7: Spectra of He-like ions

### Spectra of Li-like Transitions

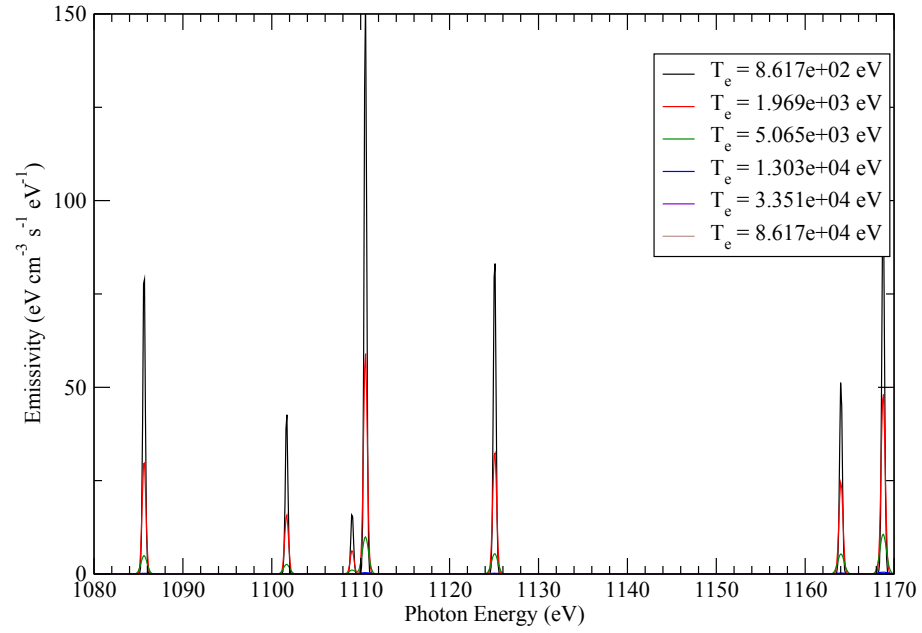


FIG. 8: Spectra of Li-like ions

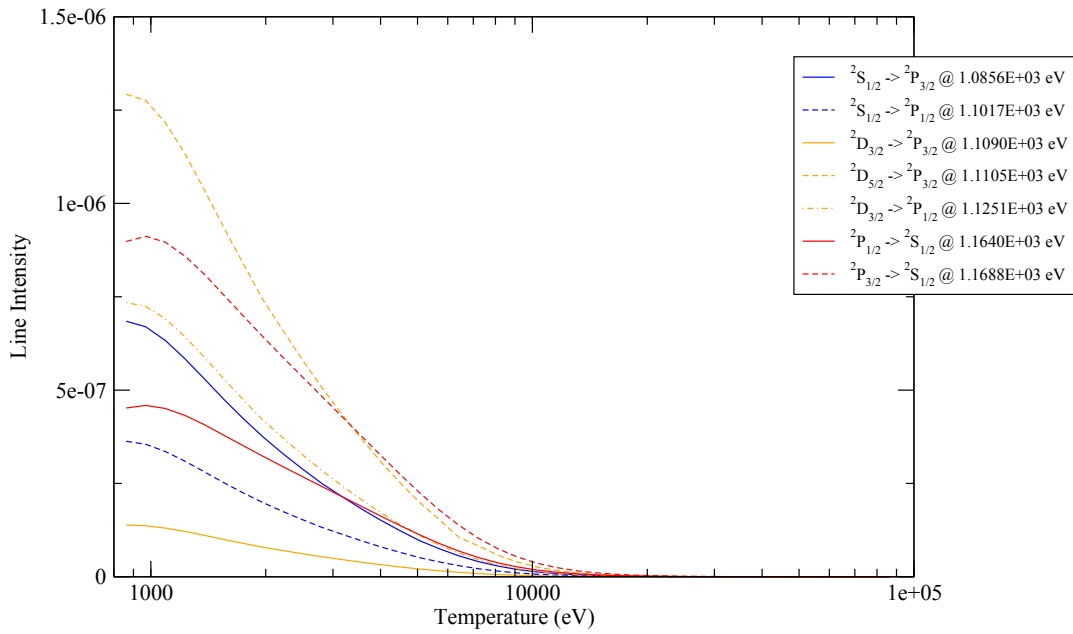


FIG. 9: Individual line intensities in the Li-like  $L\alpha$  spectra.

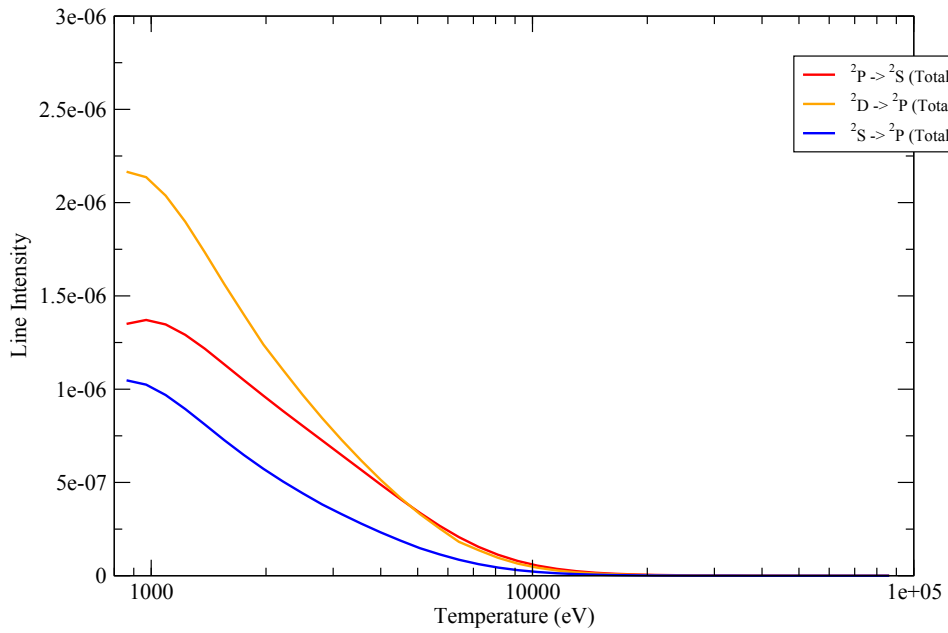


FIG. 10: Sum of line intensities in the Li-like  $L\alpha$  spectra.

### Line Intensity Ratios

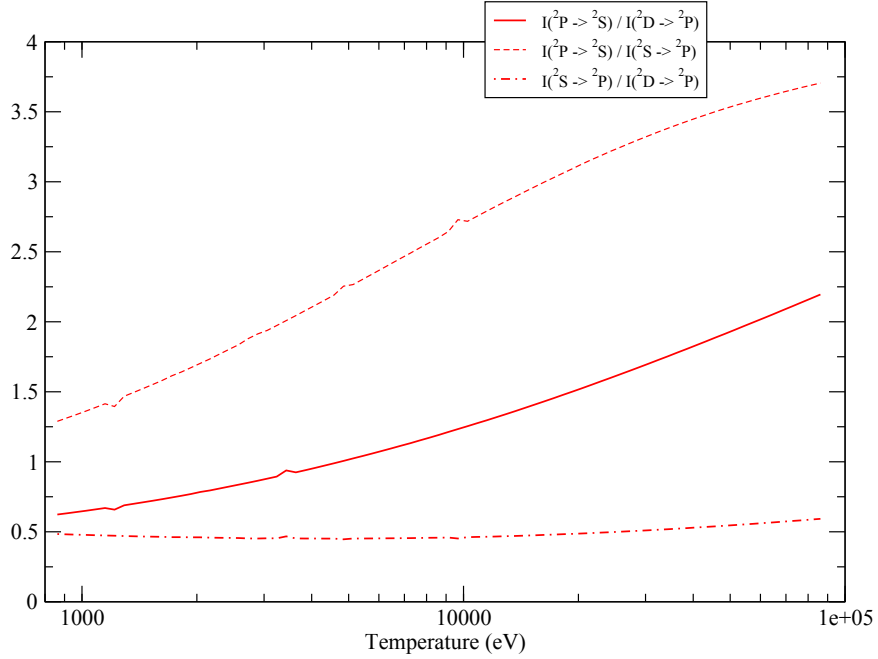


FIG. 11: Selected line ratios in the Li-like  $L\alpha$  spectra.

### Spectra of Cooling Fe Plasma

$T_e = 8.6e+04 \text{ eV}$  to  $T_e = 8.6e+02 \text{ eV}$

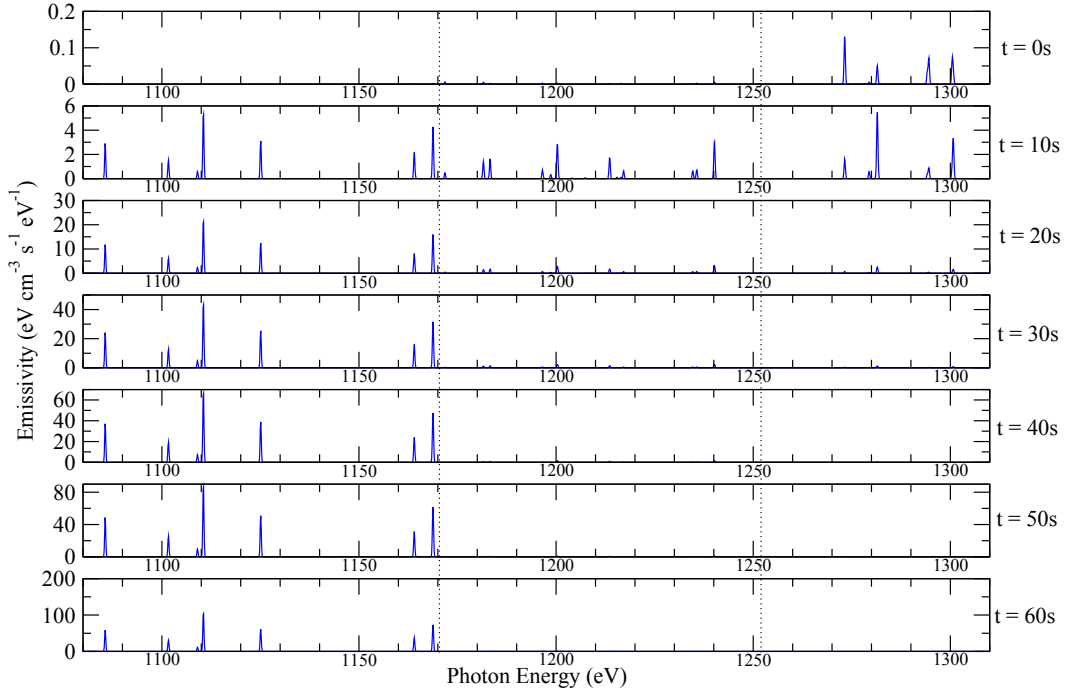


FIG. 12:  $L\alpha$  spectra of transient cooling plasma. The relative intensities of the H-like spectral lines are notably changed from the steady state.